12-2016

Dynamic Responses of Wheel-Rail Systems with Block Dampers

TzuYu Tseng
University of Nebraska-Lincoln, tzuyutseng@gmail.com

DYNAMIC RESPONSES OF WHEEL-RAIL SYSTEMS WITH BLOCK DAMPERS

by

TzuYu Tseng

A THESIS

Presented to the Faculty of

The Graduate College at the University of Nebraska

In Partial Fulfillment of Requirements

For the Degree of Master of Science

Major: Mechanical Engineering and Applied Mechanics

Under the Supervision of Professor Cho Wing Solomon To

Lincoln, Nebraska

December 2016

Dynamic Responses of Wheel-Rail Systems with Block Dampers

Tzu Yu Tseng, M.S.

University of Nebraska, 2016

Advisor: C. W. Solomon To

The wheel-rail interaction problem has been widely studied in the past few decades. In this problem, dynamic responses at the contact areas remain the central issue since they induce damage to the rail over time. In particular, the dynamic responses at the contact areas between the wheels and rails present difficulties in understanding and mathematical modeling. Even with the computer power one has today, its mathematical modeling employs the versatile numerical analysis method, the finite element method (FEM) remains a formidable challenge due to its extremely small contact areas and in turn the extremely high stress levels. In addition, friction at the contact areas is another challenge in the modeling. These extremely high stress levels and difficulties in modeling friction at the small contact areas lead to the simplified analytical and finite element (FE) models available in the literature. However, to-date, these simplified mathematical and computational models are far from satisfactory. Therefore, in the investigation reported here, simplified analytical and FE models are first studied in order to understand the

parameters of the models and to provide a foundation for more detailed studies. In these simplified analytical and FE models, the wheels are treated as traveling point loads.

Subsequently, a more detailed FE model employing three-dimensional (3D) finite elements for the wheel and rail is studied while the computed results are compared with those of the same FE model but with the wheel replaced by the traveling point loads. In this model, frictions at the contact areas are considered. In parallel, the effect of block dampers on the dynamic responses at the contact areas is studied. Various configurations of attaching the block dampers to the rail are considered. Conclusions are then drawn from the accuracy and efficacy of replacing the wheels by traveling point loads, and the effect on the dynamic responses of added block dampers to the rail.

ACKNOWLEDGMENTS

Firstly, I would like to thank my advisor Dr. C.W. Solomon To for his support, guidance, and being patient over these years. He gives me an interesting topic of the study and inspires me with different aspects. I am so glad and honor to do my thesis under Dr. C.W. Solomon To.

Secondly, I would also like to express my gratitude to Dr. Mehrdad Negahban and Dr. Benjamin Terry for being my examiners and giving me the different point of views for further studying.

Thirdly, I would like to thank our department secretary Kathie Hiatt for helping me to deal with some paper works for graduating. And I would like to thank my friends who have supported me in these years.

Finally, I would like to thank my family, my father, mother, and sister. No matter what decision I make, they always support me.

CONTENT

LIST OF FIGURES

LIST OF TABLES

CHAPTER 1 INTRODUCTION

Railway plays an important role during the industrial revolution and, nowadays, it has never stopped changing our lives. The innovation of railways is rapidly developing from the first steam locomotive appeared in 1804 [1.1]. The world's first steam locomotive ran on railway system in England at 8 km/hr. To date, the fastest speed of test railway system is at 603 km/hr which is based on the application of magnetic levitation or the so-called maglev with passengers in Japan in 2015. The fastest speed of commercial railway system is at 501.5 km/hr in China in 2003 [1.2]. Also, railway system is not only used for long distance travel but for short distance in the cities. Railway transportations provide an alternatively safe and clean way of travel in many countries. However, no matter how fast the speeds of trains are the railway companies have a major problem with maintaining their rail tracks. These companies not only spend a great amount of time and money on their maintenance but also create noises during the maintenance work at night. Therefore, how to reduce the times and, in turn, the cost of maintenance is a major challenge to the design and maintenance engineers. One approach to the challenge is by studying the dynamics and reducing the dynamic deflections of the rail system. This posts a major challenge in providing a relatively accurate and efficient dynamic model.

1.2 OBJECTIVES OF INVESTIGATION

One of the major goals of the present investigation is to provide a model wheel-rail system by using rail and concentrated traveling point loads. This, if proves to be applicable, will circumvent the great difficulty of providing a relatively accurate

computational model, typically applying the finite element method (FEM). The great difficulty is due to the fact that every wheel-rail system is under extremely high stresses at the contact areas between the wheels and rails. In the finite element (FE) model, to provide accurate representations of the contact areas, very small sizes of FE are necessary. In addition, to model the wheel posts another major challenge in the sense that one has to consider sliding and rotating.

The second major goal of the investigation is to perform a comparison study between the wheel-rail system and the rail with traveling point loads. In this part of the investigation, a procedure is established so that the rail with traveling point loads can replace the wheel-rail system. This, in turn, will reduce the computational cost drastically and circumvent the difficulty of dealing with extremely small FE sizes.

The final and third major goal of this investigation is to understand the dynamic responses of the wheel-rail system with and without block dampers. Block dampers which are simply mass blocks attached to the sides of the rail. The main idea of adding block dampers is to change significantly the natural frequencies of rail and reduce the dynamic responses. The effects of different locations and masses of block dampers on the dynamic responses are studied.

1.3 LITERATURE SURVEY

The literature survey of wheel-rail systems in this section is separated into two sub-sections. The first sub-section is concerned with beam theories for application to the railway model. It includes natural frequencies, and dynamics responses with traveling point load and moving mass. The second sub-section deals with applications of the FEM

in the wheel-rail modeling and response computations.

1.3.1 Beam Theories

The most common and relatively simple way to model the rail is by using beam theories. Euler-Bernoulli beam (EBB) and Timoshenko beam (TB) theories are applied. In Chapter 6 of [1.3], two types of vibrations were discussed. One is the low-frequency oscillation due to long wavelength and it usually comes from structure of rails and sleepers, and sometimes rail pad which are modeled as spring set connected between rail and sleeper. The other consists of irregularities due to short wavelength oscillations which occur when the wavelength of span is twice the width of sleeper. This is the so-called pined-pined resonance. In addition, because of the aspect ratio TB theory can give closer solution to measured data. A relatively comprehensive treatment of wheel-rail modeled by EBB with concentrated traveling point load can be found in the book by Fryba [1.4]. Analytical solution for simply-supported (SS) EBB with traveling point load is provided in this reference. In a similar work Young, et al. [1.5] dealt with dynamic interaction of vehicle-bridge system with applications to high-speed railways. For high-speed railways problem, reference [1.6], presented by Grassie, et al., is concerned with undergoing high frequency motion. The deficiency by using EBB under certain conditions was mentioned. In this reference, corrugation with amplitude and phase of contact force was studied. Beam under a moving load was reported by B. Mehri, et al. [1.7]. The approach of modeling traveling point load was using dynamic Green's function which is different from the method by Fryba. Many studies of rail by applying beam theories are concerned with one span only. In [1.8], Ichikawa, et al. presented a different approach for

solutions of EBB subjected to traveling point load. They believed their method could easily handle many conditions of continuous beams, such as non-uniform, multiple boundary conditions, and so on. In [1.9] the issue of contact forces in wheel-rail system was addressed by Ayasse and Chollet. Because of their complexities frictional forces at the contact areas are frequently disregarded, such that the simple Hertzian contact theory can be employed.

Owing to the fact that the distance between two consecutive sleepers does not satisfy the aspect ratio requirement of SS EBB theory, TB theory is widely used instead. Lin [1.10] pointed out the advantages of using TB theory and inaccuracy of applying EBB theory. In [1.11] Ruge and Brik examined results using EBB and TB on Winkler foundation. In [1.12] Kargarnovin and Younesian included the effects of Pasternak foundation with TB subjected to a moving load. Fourier transformation was employed. Uzzal, et al. [1.13] also used Pasternak foundation with moving load and moving mass. It was found that the moving mass had a larger effect than the moving load. In [1.14] Wu and Thompson studied the noise and the effect of nonlinearity.

1.3.2 Finite Element Method for Wheel-Rail Interaction

The approaches to the analysis of the wheel-rail problem, while can provide some useful results and insight, they cannot provide detail information at the contact areas and three-dimensional (3D) responses. In order to overcome these shortcomings, the versatile numerical technique, the Finite Element Method (FEM) has been widely employed. However, because of computational cost, some researchers applied simpler FE models for the wheel-rail interaction problem. For example, Wu [1.15] applied FE based on TB

theory for the rail study. In [1.16] Wu and Thompson applied TB finite element to study high-frequency lateral response. In this reference, multiple spans were considered. Beam FE model for the railway was studied in [1.17]. In [1.18] Ekevid found that when the speed of train or load exceeds the Rayleigh wave velocity larger vibration motion occurred.

Many detailed FE models for wheel-rail interaction problem have been investigated in the last three decades or so. For example, the wear problem of the lateral surface of wheel-rail system was investigated by Vyas and Gupta [1.190]. It was found that the impact force resulted from the flat zones of the rail wheel was twice as much as the normal rolling force. In [1.20] Sladkowski and Sitarz also studied the wear problem of the wheel-rail interaction in which the quasi-Hertz contact was assumed. In [1.21] Pieringer, et al. found that the contact force level of a 3D FE model is lower than that of a 2D FE model. In [1.22] K Nguyen, et al. used a 2D FE model since they have found that a 3D FE model was of large computational cost. Dinh [1.23] considered a two span 3D FE model. Esen [1.24] presented results of a study using the 3D FE model in which only the normal contact force was considered. Corrugation was examined.

1.4 ORGANIZATION OF PRESENTATIONS

In this thesis, there are six chapters. Chapter 1 includes background and motivation, objectives of the investigation, literature survey, and organization of presentation of this thesis. Chapter 2 deals with theoretical development. Analytical approaches applying beam theories and traveling point load are introduced. Finite element models employing beam theories and 3D solid elements are presented. Frictions at the contact areas are

included. Chapter 3 shows the details of wheel-rail modeling by the commercially available FE package, Abaqus. In Chapter 4, computed results and their verifications by those of analytical approaches are given. Computed results for the 3D FE wheel-rail system are compared with those of 3D FE rail and traveling point load model. In addition, it provides an approach to adjust the traveling point loads in order to provide computed results comparable to those of the wheel-rail system. Chapter 5 presents the applications of scaled traveling point load on the 3D FE rail model. Here in particular block dampers are included in the wheel-rail system. Effects of block dampers, and their locations are examined. Finally, in Chapter 6, it includes conclusions of the investigation and recommendations for future work.

CHAPTER 2 THEORETICAL DEVELOPMENT

In this chapter, models of wheel-rail interaction based on beam theories and finite elements (FE) are presented. The wheel-rail contact forces are modeled as traveling loads. In the FE models, the wheel-rail system without and with block dampers are considered. Similar to the beam models contact forces of the three-dimensional (3D) FE models are considered as traveling loads.

The organization of this chapter is the following. Section 2.1 is concerned with the rail modeled as beams. The beam theories applied are those due to Euler-Bernoulli and Timoshenko. Section 2.2 deals with the free vibration of undamped simply supported Euler-Bernoulli beam (EBB). Wrinkler's beam (WB) theory for a beam with the foundation is briefly introduced in Section 2.3. A simple model for wheel-rail interaction is presented in Section 2.4. For more realistic wheel-rail interaction investigation the FE models are considered in Section 2.5 in which the FE beam models and 3D finite element models using the 8-node brick element are included. Finally, the wheel-rail model with block dampers is considered in Section 2.6.

2.1 RAIL MODELS BY BEAM THEORIES

Simple analytical models of rail have been employed in the studies of wheel-rail interaction. In this section, vibration of beam structures is considered. The Euler-Bernoulli beam theory and the Timoshenko beam theory are considered in the following sub-sections.

2.1.1 Euler-Bernoulli Beam Theory

The basic assumptions of the Euler-Bernoulli beam (EBB) theory are that: (a) the aspect ratio of length to transversal dimension such as diameter of a circular cross-section or width a rectangular cross-section is greater than 10, (b) normal to the cross-section before deformation and after deformation remains unchanged, (c) the material is homogeneous and isotropic, and (d) it obeys Hooke's law. The governing partial differential equation of motion for transversal or lateral beam deflection $w(x,t)$ for uniform cross-section is given by [2.1]

$$EI\frac{\partial^4 w(x,t)}{\partial x^4} + \rho A\frac{\partial^2 w(x,t)}{\partial t^2} = q(x,t), \tag{2.1}$$

where, $EI = \text{flexural rigidity of the beam},$

$\rho = \text{density},$

$A = \text{area of cross} - \text{section of the beam},$

$\rho A = \text{the mass of the beam per unit length},$

$t = \text{time},$

$q(x,t) = \text{distributed load or load intensity on the beam.}$

Note that for simplicity damping in the beam is not included in this equation.

2.1.2 Timoshenko Beam Theory

In Timoshenko beam (TB) theory, it assumes the rotation of the area of cross-section of the beam and shear deformation of the beam. Its aspect ratio can be smaller than 10 and generally it is applied when accurate high natural frequencies are required. One general form of the equations of motion consists of two variables, namely, the lateral deflection $w(x,t)$ and shear deformation $\varphi(x,t)$. These equations are [2.2]

$$\rho A\frac{\partial^2 w(x,t)}{\partial t^2} - \ q(x,t) = \ \frac{\partial}{\partial x}\left[\kappa AG\left(\frac{\partial w(x,t)}{\partial x}\right) - \varphi(x,t)\right], \tag{2.2a}$$

$$\rho I\frac{\partial^2 \varphi(x,t)}{\partial t^2} = \ \frac{\partial}{\partial x}\left(EI\frac{\partial \varphi(x,t)}{\partial x}\right) + \kappa AG\left(\frac{\partial w(x,t)}{\partial x} - \varphi(x,t)\ \right). \tag{2.2b}$$

If the beam is linear, isotropic, homogeneous and of uniform cross-section, the last two equations can be combined to form a single one as [2.2]

$$EI\frac{\partial^4 w(x,t)}{\partial x^4} + \ \rho A\frac{\partial^2 w(x,t)}{\partial t^2} - \rho I\left(1 + \ \frac{E}{\kappa G}\right)\frac{\partial^4 w(x,t)}{\partial x^2 \partial t^2} + \ \frac{\rho^2 I}{\kappa G}\frac{\partial^4 w(x,t)}{\partial t^4}$$
$$= \ q(x,t) + \ \frac{\rho I}{\kappa GA}\frac{\partial^2 q(x,t)}{\partial t^2} \ - \ \frac{EI}{\kappa GA}\frac{\partial^2 q(x,t)}{\partial x^2}, \tag{2.3}$$

where $EI,,A,t,$ and $q(x,t)$ have already been defined in the foregoing,

$G =$ shear modulus, and

$\kappa =$ shear factor.

2.2 FREE VIBRATION OF UNDAMPED SIMPLY SUPPORTED EBB

In 2.1.1, the equation of motion for EBB was given. For free vibration excluding damping, it reduces to

$$EI\frac{\partial^4 w(x,t)}{\partial x^4} + \ \rho A\frac{\partial^2 w(x,t)}{\partial t^2} = \ \ 0, \tag{2.4}$$

or the if the area of cross-section is not uniform it can be rewritten as

$$-\ \frac{\partial^2}{\partial x^2}\left[EI\frac{\partial^2 w(x,t)}{\partial x^2}\right] = \ \rho A\ \frac{\partial^2 w(x,t)}{\partial t^2}. \tag{2.5}$$

After using separation of variables, the solution can be shown to be

$$w(x,t) = W(x)[Asin\,\omega t + Bcos\,\omega t], \tag{2.6}$$

in which $W(x)$ is given by

$$W(x) = C_1 sin\,\beta x + C_2 cos\,\beta x + C_3\,sinh\,\beta x + C_4\,cosh\,\beta x$$

where $A, B, C_1, C_2, C_3,$ and C_4 are constant and $\beta^4 = \frac{\omega^2\ \rho A}{EI}$.

The boundary conditions for simply supported (SS) beam are

$$W(x)|_{x=0} = 0,\ \left.\frac{\mathrm{d}^2W(x)}{\mathrm{dx}^2}\right|_{x=0} = 0,\ \ W(x)|_{x=L} = 0, \text{and}\ \left.\frac{\mathrm{d}^2W(x)}{\mathrm{dx}^2}\right|_{x=L} = 0,$$

with L being the length of the beam.

After applying the above boundary conditions, one has the solution for free vibration as [2.3].

$$w(x,t) = \sum_{n=1}^{\infty} C_n\ \ sin\left(\frac{n\pi}{L}x\right)\{A_n\ \ sin[\omega_n t] + B_n\ \ cos[\omega_n t]\}, \tag{2.7}$$

where C_n is constant, $\omega_n = \left(\frac{n\pi}{L}\right)^2\sqrt{\frac{EI}{\rho A}}$, and $n = 1, 2, 3\ \ \ldots, \infty$. The integer n is known as the modal number.

2.3 BEAM ON ELASTIC FOUNDATION

In practice, the rails rest on the track foundation which contains rail pads, fastening, sleepers, ballast, subballast, and subgrade, as shown in Figure 2.1[2.4]. The subgrade is usually used to represent the soil bed when it is under forces. For simplicity, it is commonly assumed that the relationship between forces and deformations is linear. When the displacement only appears in the loading zone, otherwise the displacement is equal to zero, the beams on elastic foundation can be modeled as series of springs connected between the beams and solid ground, as shown in Figure 2.2. This is the basis of Winkler beam (WB) theory [2.5].

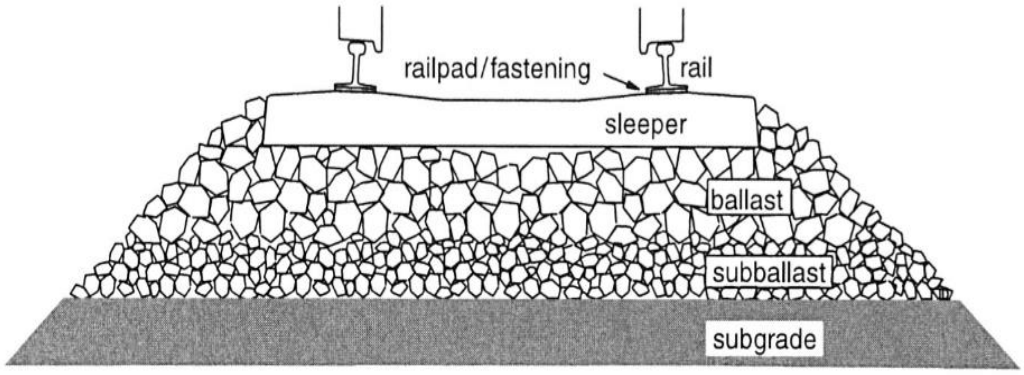

Figure 2.1 [2.3] Track structure with foundation.

The foundation modulus can be represented as

$$k_f = A_f k_s = b k_s$$

where $A_f =$ section area of the compressed foundation,

$k_s =$ soil stiffness coefficient, and

$b =$ width of the beam.

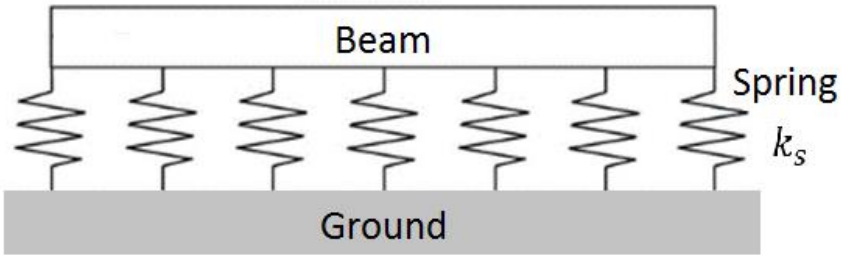

Figure 2.2 Model for Winkler beam.

The equation for free vibration of WB theory is therefore defined as [2.5]

$$-\ EI\frac{\partial^4 w(x,t)}{\partial x^4} + k_f w(x,t) = \ \rho A\frac{\partial^2 w(x,t)}{\partial t^2}. \tag{2.8}$$

This equation has the same form as Equation (2.5) except the additional term on the left-hand side (LHS). This term can simply be incorporated in the stiffness term of Equation (2.5) to give the new solution for the lateral deflection as

$$w_i(x,t) = W_i(x)(A_i sin\,\omega_i t + B_i cos\,\omega_i t), \tag{2.9}$$

where now $W_i(x)$ is governed by the fourth order differential equation

$$\frac{d^4 W_i(x)}{dx^4} - k_i^4 W_i(x) = 0 \tag{2.10}$$

in which ${k_i}^4 = \frac{(\rho A\omega_i^2 - k_f)}{EI}$, and

$$W_i(x) = C_{1i} sin\, k_i x + C_{2i} cos\, k_i x + C_{3i}\, sinh\, k_i x + C_{4i}\, cosh\, k_i x \tag{2.11}$$

where C_{1i}, C_{2i}, C_{3i}, and C_{4i} are constant and can be determined by applying the boundary conditions.

2.4 SIMPLE MODEL FOR WHEEL-RAIL INTERACTION

As pointed out in Chapter 1, to provide a realistic three-dimensional (3D) model for the wheel-rail interaction the issue of contact stresses is paramount and it incurs several major computational problems. For example, at the contact points, the stress levels are very high to the extent that the sizes of the finite elements are extremely small if one wishes to obtain reasonable numerical values of the stresses. This makes the computation of stresses very time consuming, if not computationally infeasible. On the other hand, many analytical models consider this contact problem by representing the rails as an EBB

or a TB and the contact point as Hertzian contact [2.6]. The latter does not include friction at the contact point and therefore is very different from reality.

In order to provide a means of including friction at the contact point between the wheel and rail, an analytical model for the wheel-rail interaction is to consider the SS EBB with a traveling load along with axial moving loads at the contact point. For simplicity, it is assumed that lateral and axial deformations are linear so that the principle of superposition can be applied, and the coupling effect between the axial and lateral deflections are disregarded such that this problem consists of two separate equations of motion. The first is the lateral deflection based on the EBB theory with a moving point load, and the second is the axial deflection governed by the second order partial differential equation with a moving load acting longitudinally. This latter longitudinal moving load represents the frictional force at the contact point.

2.4.1 Simply Supported EBB with Traveling Point Load

The case of lateral beam deflection with a moving load has been commonly applied in truck/car-bridge interaction problem [2.7], for example.

The equation of motion for this case is given by [2.7]

$$EI\frac{\partial^4 w(x,t)}{\partial x^4} + \quad \rho A\frac{\partial^2 w(x,t)}{\partial t^2} = P\delta(x-u), \tag{2.12}$$

where δ is the Dirac-delta function, P is the external traveling force, $u(t) = vt$ describes the position where the applied external force, and s is the constant velocity of the traveling load. A schematic diagram for this case is included in Figure 2.3. In this model the ends of the beam structure are assumed to be SS. That is, the boundary conditions at both ends of the beam structures are:

$$W(x)|_{x=0} = 0 \quad , \quad \left.\frac{\mathrm{d}^2 W(x)}{\mathrm{dx}^2}\right|_{x=0} = 0 \quad , \quad W(x)|_{x=L} = 0 \quad , \text{ and } \left.\frac{\mathrm{d}^2 W(x)}{\mathrm{dx}^2}\right|_{x=L} = 0,$$

And the initial conditions are:

$$w(x,0) = 0, \text{ and } \left.\frac{\partial w(x,t)}{\partial t}\right|_{t=0} = 0.$$

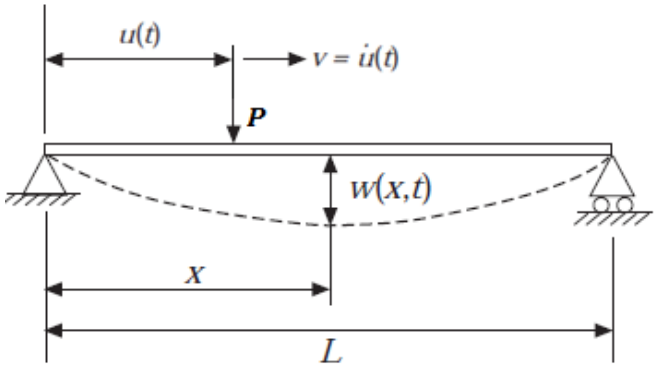

Figure 2.3 Simply-supported EBB subjected to a traveling point load.

The Dirac-delta function is given in the following:

$$\delta(x - vt) = \frac{dH(x)}{dx} \quad , \tag{2.13}$$

where $H(x)$ is called Heaviside function. Equation (2.13) simply means that the Dirac-delta function is equal to the distributional derivative of $H(x)$. The Dirac-delta function has the following relations with continuous function $f(x)$ in the intervals $< x_1, x_2 >$:

$$\int_{x_1}^{x_2} \delta(x - vt) f(x) dx = \begin{cases} 0, & vt < x_1 < x_2 \\ f(vt), & x_1 < vt < x_2 \\ 0, & x_1 < x_2 < vt \end{cases} \tag{2.14}$$

To solve Equation (2.12) with boundary and initial conditions, one uses the method of integral transformation. It starts with Equation (2.12) multiplied by $sin\frac{n\pi x}{L}$ and integrated with respect to x from 0 to L. Then, from fundamental relations of Laplace-Carson integral transformation [2.7], it one can obtain the following relations:

$$W(n,t) = \int_0^L w(x,t) sin\frac{n\pi x}{L} dx, \qquad n = 1,2,3, \ldots$$

$$v(x,t) = \frac{2}{L}\sum_{n=1}^{\infty} W(n,t)\, sin\frac{n\pi x}{L}, \tag{2.15}$$

where $W(n,t)$ is the sine transform of $w(x,t)$.

Taking the sine integral transforming, Equation (2.12) becomes

$$\frac{n^4\pi^4}{L^4} EI \;\; W(n,t) + \rho A \;\; \ddot{W}(n,t) = P sin\frac{n\pi vt}{L}, \tag{2.16}$$

and the angular frequency of n-th mode of vibration of SS EBB is the same as that in Section 2.2. That is, $\omega_n = \left(\frac{n\pi}{L}\right)^2 \sqrt{\frac{EI}{\rho A}}$.

The n-th natural frequency is described as

$$f_n = \frac{\omega_n}{2\pi}, \tag{2.17}$$

and also the angular velocity is related to the constant velocity of the traveling load by

$$\omega = \frac{\pi v}{L}. \tag{2.18}$$

Now, Equation (2.16) can be rewritten as

$$\ddot{W}(n,t) + \;\; {\omega_n}^2 \;\; W(n,t) = \frac{P}{\rho A} sin \;\; n\omega t, \tag{2.19}$$

and Equation (2.19) can be solved by using the method of Laplace-Carson integral transformation [2.7],

$$W^*(n,p) = p\int_0^{\infty} W(n,t) e^{-pt} dt,$$

$$W(n,t) = \frac{1}{2\pi i}\int_{a_0-i\infty}^{a_0+i\infty} e^{tp}\frac{W^*(n,p)}{p}\,dp, \tag{2.20}$$

where the parameter p is a variable in the complex plane and a_0 in the second relation signifies that the integration is carried out along a straight line parallel to the imaginary axis lying to the right of all the singularities of the function of the complex variable $\frac{e^{tp}}{p}$.

Therefore, after applying the Laplace-Carson integral transformation [2.7], Equation (2.19) becomes

$$p^2W^*(n,p) + \omega_n{}^2\ W^*(n,p) = \left(\frac{Pn\omega}{\rho A}\right)\frac{1}{p^2 + \omega_n{}^2}\ . \tag{2.21}$$

The transformed solution is

$$W^*(n,p) = \frac{Pn\omega}{\rho A}\left(\frac{1}{p^2+n^2\omega^2}\right)\left(\frac{1}{p^2+\omega_n{}^2}\right)\ . \tag{2.22}$$

By using the relation from Equation (2.20) and Equation (2.15), the original solution of SS EBB subjected with traveling point load with constant velocity is [2.8]

$$w(x,t) = w_0\sum_{n=1}^{\infty} sin\left(\frac{n\pi x}{L}\right)\frac{1}{n^2(n^2-\alpha^2)}\left[sin(n\omega t) - \frac{\alpha}{n}sin(\omega_n t)\right], \tag{2.23}$$

where w_0 is the deflection at mid-span of the beam with static load P at $x = \frac{L}{2}$.

The approximated value given by [2.7] is

$$w_0 = \frac{PL^3}{48EI}, \tag{2.24}$$

and α is the characteristic relating to the effect of velocity as

$$\alpha = \frac{v}{v_{critical}} = \frac{vL}{\pi}\sqrt{\frac{\rho A}{EI}}\ . \tag{2.25}$$

2.4.2 Uniform Bar with Traveling Axial Load

The vibration of a uniform bar with a moving horizontal load is applied to account for the moving friction force at the contact point. The case is shown in Figure 2.4.

The equation of motion is given

$$E\frac{\partial^2 U(x,t)}{\partial x^2} - \quad \rho\frac{\partial^2 U(x,t)}{\partial t^2} = \mu P\delta(x-u), \tag{2.26}$$

where $U(x,t)$ or simply U is displacement (longitudinal displacement) at x, μ is the kinematic coefficient of friction, and the remaining symbols have already been defined in the foregoing. The boundary conditions of a simply supported bar undergoing axial deformation are the same as a fixed-fixed cable or string. They are:

$$U(x,t)|_{x=0} = 0, \text{ and } U(x,t)|_{x=L} = 0,$$

and the initial conditions are:

$$U(x,0) = 0, \text{ and } \frac{\partial U(x,0)}{\partial t}\Big|_{t=0} = 0.$$

Also, the steps in the solution process are similar to those presented in Sub-section 2.4.1.

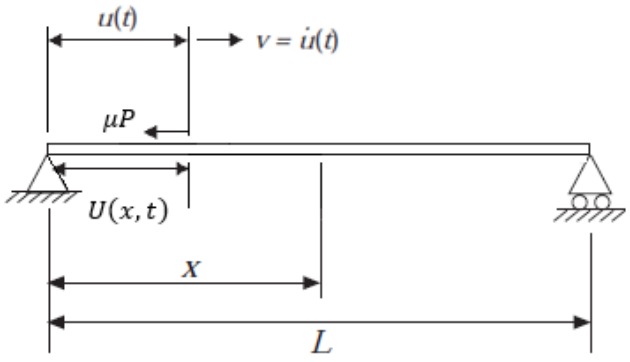

Figure 2.4 Traveling friction force on uniform bar.

2.5 FINITE ELEMENT MODELS FOR WHEEL-RAIL INTERACTION

The analytical models considered in the foregoing are relatively simple and are confined to simple loadings. However, when models with more realistic loadings or models involved with practical geometrical configurations are required one usually resorts to the versatile numerical approach, the finite element method (FEM). As reviewed in Chapter 1, finite element (FE) models for wheel-rail interaction can be loosely divided into two classes. The first class is concerned with the relatively simple cases of representing the rail as EBB or TB finite elements and the wheel as a traveling point load. The second class consists of the detailed models of wheel-rail interaction using three-dimensional (3D) finite elements. In this section, an example of the first class of models is introduced in Sub-section 2.5.1 while the 3D FE model of the second class is outlined in Sub-section 2.5.2.

2.5.1 Beam Finite Element Model of Wheel-Rail Interaction

To limit the scope of the present investigation, small deformations are considered such that linear models are adequate. In the FE analysis (FEA) the linear equation of motion for a simple wheel-rail interaction model is given by

$$[M]\{\ddot{q}\} + [C]\{\dot{q}\} + [K]\{q\} = \{F\}, \tag{2.27}$$

where $[M]$ is the assembled mass matrix, $[C]$ is the assembled damping matrix, $[K]$ is the assembled stiffness matrix, and $\{F\}$ is the assembled generalized forcing vector. For example, $[M]$ is assembled by making use of the EBB element matrices whereas $[K]$ is assembled by applying the EBB element stiffness matrices [2.8]. For direct reference and completeness, the beam element mass and stiffness based on the EBB theory and TB theory are included in the following sub-sections.

2.5.1.1 Element mass and stiffness matrices based on EBB Theory

For simplicity, the beam finite element considered here has 2 nodes with 2 degrees-of-freedom (dof) per node. The nodal dof are the displacement and angular displacement or rotation. Based on the EBB theory, its stiffness and mass matrices are, respectively given by [2.9]

$$[k_e] = \frac{EI}{l^3}\begin{bmatrix} 12 & 6l & -12 & 6l \\ 6l & 4l^2 & -6l & 2l^2 \\ -12 & -6l & 12 & -6l \\ 6l & 2l^2 & -6l & 4l^2 \end{bmatrix}, \tag{2.28}$$

$$[m_e] = \frac{\rho Al}{420}\begin{bmatrix} 156 & 22l & 54 & -13l \\ 22l & 4l^2 & 13l & -3l^2 \\ 54 & 13l & 156 & -22l \\ -13l & -3l^2 & -22l & 4l^2 \end{bmatrix}, \tag{2.29}$$

where l is the element length, and the subscript *e* denotes the element number.

2.5.1.2 Element mass and stiffness matrices based on TB Theory

As pointed out in Section 2.1 when the aspect ratio is less than 10 the EBB theory is no longer applicable and therefore the TB theory is applied instead. In this case, an additional nodal dof is introduced such that the element stiffness and mass matrices [2.10] for a uniform TB are, respectively defined as

$$[k_e] = [k_B] + [k_S] = \frac{EI}{l}\begin{bmatrix} k_{11B} & k_{12B} & k_{13B} & k_{14B} & k_{15B} & k_{16B} \\ & k_{22B} & k_{23B} & k_{24B} & k_{25B} & k_{26B} \\ & & k_{33B} & k_{34B} & k_{35B} & k_{36B} \\ & & & k_{44B} & k_{45B} & k_{46B} \\ & \textit{symmetrical} & & & k_{55B} & k_{56B} \\ & & & & & k_{66B} \end{bmatrix}$$
$$+\frac{\kappa_s GAl}{6}\begin{bmatrix} 0 & 0 & 0 & 0 & 0 & 0 \\ & 0 & 0 & 0 & 0 & 0 \\ & & 2 & 0 & 0 & 1 \\ & & & 0 & 0 & 0 \\ & \textit{symmetrical} & & & 0 & 0 \\ & & & & & 2 \end{bmatrix} \tag{2.30}$$

$k_{11B} = \frac{12}{l^2} = -k_{14B} = k_{44B};\ \ k_{12B} = \frac{6}{l} = -k_{13B} = k_{15B} = -k_{16B} = -k_{24B} = k_{34B} = -k_{45B} = k_{46B};\ \ k_{22B} = 4 = k_{52B};\ \ k_{23B} = -3 = k_{26B} = -k_{33B} = k_{35B} = -k_{36B} = -k_{56B} = -k_{66B};\ \ k_{25B} = 2$, where I is the second moment of area of the cross-section of the beam, G is shear modulus, κ_s is shear correction factor given by [2.11], $[k_B]$ is associated with bending, and $[k_S]$ is due to shear.

$$[\ m_e] = [m_B] + [m_R] = \frac{\rho A l^3}{420}\begin{bmatrix} m_{11B} & m_{12B} & m_{13B} & m_{14B} & m_{15B} & m_{16B} \\ & m_{22B} & m_{23B} & m_{24B} & m_{25B} & m_{26B} \\ & & m_{33B} & m_{34B} & m_{35B} & m_{36B} \\ & & & m_{44B} & m_{45B} & m_{46B} \\ & \textit{symmetrical} & & & m_{55B} & m_{56B} \\ & & & & & m_{66B} \end{bmatrix}$$

$$+\frac{\rho I l}{420}\begin{bmatrix} m_{11R} & m_{12R} & m_{13R} & m_{14R} & m_{15R} & m_{16R} \\ & m_{22R} & m_{23R} & m_{24R} & m_{25R} & m_{26R} \\ & & m_{33R} & m_{34R} & m_{35R} & m_{36R} \\ & & & m_{44R} & m_{45RR} & m_{46R} \\ & \textit{symmetrical} & & & m_{55R} & m_{56R} \\ & & & & & m_{66R} \end{bmatrix}, \qquad 2.31)$$

$m_{11B} = \frac{156}{l^2} = m_{44B},\quad m_{12B} = \frac{22}{l} = -m_{13B} = -m_{45B} = m_{46B},\quad m_{14B} = \frac{54}{l^2},\ m_{22B} = 4 = -m_{23B} = m_{33B} = m_{55B} = -m_{56B} = m_{66B},\quad m_{15B} = \frac{-13}{l} = -m_{16B} = -m_{24B} = m_{34B},\quad m_{25B} = -3 - m_{26B} = -m_{35B} = m_{36B}\ ;\ m_{11R} = \frac{504}{l^2} = -m_{14R} = m_{44R},\quad m_{12R} = \frac{42}{l} = m_{15R} = -m_{24R} = -m_{45RR},\quad m_{13R} = \frac{-252}{l} = m_{16R} = -m_{34R} = -m_{46R},\quad m_{22R} = 56 = m_{55R},\quad m_{23R} = -21 = m_{26R} = m_{35R} = m_{56R},\ m_{25R} = 14,\quad m_{33R} = 126 = m_{36R} = m_{66R},$

where $[m_B]$ is associated with bending and $[m_R]$ is due to rotary inertia.

2.5.2 Three-Dimensional Finite Element Model of Wheel-Rail System

A general 3D FE model of wheel-rail interaction is challenging in the sense that it possesses two major issues. The first issue is to do with the computation effort required, whereas the second issue is concerned with the physical problem of modeling the contact

between the moving wheel and rail. While there are many approaches available in the literature [2.12, 2.13] a particularly relevant and important review was presented by Wriggers and Zavarise [2.12].

To limit the scope of the present investigation the matrix equation of motion for a general wheel-rail interaction system is defined by [2.12]

$$[M]\{\ddot{q}\} + \{R(q)\} + \{R^c(q)\} = \{F\} \tag{2.32}$$

where $\{R(q)\}$ defines the so-called stress divergence term that includes nonlinearities due to large deformations, $\{R^c(q)\}$ is the residual due to contact, and the remaining symbols have already been defined in Equation (2.27). The contact term in Equation (2.32) is further divided into two sub-classes, namely, the smooth contact case and the non-smooth contact case.

Computationally, Equation (2.32) requires a great amount of effort as reviewed in Chapter 1 and in many cases it is infeasible. In order to overcome this major difficulty the present investigation has confined to cases with linear deformations and the term $\{R^c(q)\}$ is replaced by a forcing vector that contains multiple moving point loads. In turn, Equation (2.32) reduces to the form given by Equation (2.27). Thus, the 3D finite element model for wheel-rail interaction in the present investigation applies a 3D finite element that is available in many commercial FEA computer packages. This 3D finite element is included in the following for simplicity, completeness, and direct reference. This simple 3D or solid finite element has 8 nodes with 3 dof per node and known as the linear brick element [2.14]. The schematic diagram of this element is shown in Figure 2.5 [2.14]. The shape functions are given by

$$N_i = \frac{1}{8}(1 + \xi\xi_i)(1 + \eta\eta_i)(1 + \zeta\zeta_i), \qquad i = 1 \ldots 8, \tag{2.33}$$

where ξ, η, and ζ are the natural co-ordinates while the subscript i denotes the nodal number. The values of ξ_i, η_i, and ζ_i are given in Table 2.1.

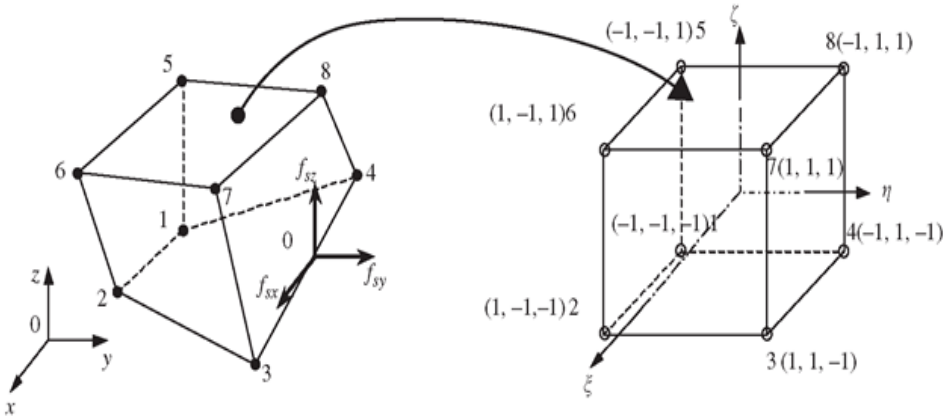

Figure 2.5 Eight-node brick element.

Table 2.1 Nodal co-ordinates for 8-node brick element.

i	ξ_i	η_i	ζ_i
1	– 1	–1	–1
2	1	–1	–1
3	1	1	–1
4	–1	1	–1
5	–1	–1	1
6	1	–1	1
7	1	1	1
8	–1	1	1

Therefore, the matrix of shape functions can be determined to be

$$[N] = \begin{bmatrix} 1 & 0 & 0 \\ 0 & 1 & 0 \\ 0 & 0 & 1 \end{bmatrix} N_i, \qquad i = 1, 2, \dots, 8 \tag{2.34}$$

and the strain matrix is given by

$$[B] = \boldsymbol{L}\ [N], \tag{2.35}$$

where $\boldsymbol{L}$ is the linear differential operator and not to be confused with the length of the beam structure.

The mass matrix of this brick element is given as [2.14]

$$[m_e] = \int_V \rho[N]^T[N]dV = \int_{-1}^{1}\int\int \rho[N]^T[N]\ |J|\, d\,\xi\, d\,\eta\, d\,\zeta, \tag{2.36}$$

where | J | is the determinant of the Jacobian matrix,

$$[\ J\ ] = \begin{bmatrix} \frac{\partial x}{\partial \xi} & \frac{\partial y}{\partial \xi} & \frac{\partial z}{\partial \xi} \\ \frac{\partial x}{\partial \eta} & \frac{\partial y}{\partial \eta} & \frac{\partial z}{\partial \eta} \\ \frac{\partial x}{\partial \zeta} & \frac{\partial y}{\partial \zeta} & \frac{\partial z}{\partial \zeta} \end{bmatrix}, \tag{2.37}$$

where x, y, and z are the Cartesian co-ordinates.

The corresponding element stiffness matrix for a brick of orthotropic material has first been explicitly given by Melosh [2.15] as

$$[k_e] = \int_V [B]^T[D][B]dV = \int_{-1}^{1}\int\int [B]^T[D][B]\ |\ J\ |\ \ d\,\xi\, d\,\eta\, d\,\zeta, \tag{2.38}$$

where $[D]$ is the elastic property matrix. The details of the explicit element stiffness matrix are not included here for brevity. However, it may be appropriate to point that this element exhibits locking behavior. Of course, to circumvent this behavior higher order

3D finite elements are preferred. But the latter is relatively expensive to employ since considerably more computer memory is required in the computation. Therefore, in the present investigation, the element derived by Melosh is adopted.

2.5.3 Dynamic Characteristics of Wheel-Rail System

Before the computation responses from matrix Equation (2.27), the eigenvalue solution has to be addressed first. This is important in that the computed eigenvalues or natural frequencies and eigenvectors or mode-shapes of the beam or 3D FE representations of the rail system can be compared with those from the analytical solution. For simplicity, the effect of the rotation of the wheel is disregarded and only the dynamic characteristics of the rail are obtained in the present studies. The eigenvalue solution is obtained by considering the free vibration analysis of the system. That is, the free vibration of the wheel-rail system is obtained by the following matrix equation

$$[M]\{\ddot{q}\} + [K]\{q\} = \{0\}. \tag{2.39}$$

By applying $\{q\} = \{Q\}e^{i\omega t}$, the last equation reduces to

$$(\ -\ \omega^2[M] + [K]\ )\{Q\} = \{0\} \tag{2.40}$$

in which ω is the angular frequency and $\{Q\}$ is the vector of amplitudes of displacement. By writing $\lambda = \omega^2$ such that Equation (2.40) becomes

$$(\ -\lambda\ [M] + [K]\ )\{Q\} = \{0\}. \tag{2.41}$$

The characteristic values or eigenvalues of Equation (2.41) is determined by solving the characteristic or frequency equation

$$|\ -\ \lambda\ [M] + [K]| = 0. \tag{2.42}$$

For the present investigation, $[M]$ and $[K]$ are positive definite and therefore, there are *n* eigenvalues with *n* corresponding eigenvectors, where *n* is the order of the matrix $[M]$.

2.5.4 Three-Dimensional Finite Element Model of Wheel-Rail Interaction

In the present investigation, the matrix equation of motion of the 3D FE model of wheel-rail interaction is given by

$$[M]\{\ddot{q}\} + [C]\{\dot{q}\} + [K]\{q\} = \{F_o \delta(x - vt)\} \tag{2.43}$$

in which F_o is the vector of applied loads where friction forces at the contact points are included. The damping matrix $[C]$, in general, consists of two parts. One is the damping due to the material and the other is associated with the rotation of the wheels. This latter matrix is skew symmetric and is called the gyroscopic matrix [2.16]. The remaining symbols have already been defined in Equation (2.39).

2.6 FINITE ELEMENT MODELS FOR WHEEL-RAIL WITH BLOCK DAMPERS

As stated previously one of the main objectives of the present investigation is to investigate the responses in the wheel-rail interaction without or with block dampers. The effects of the block dampers on the responses of the wheel-rail interaction is to be studied, in addition to the treatment of contact forces as traveling point loads. Owing to the relatively large mass and stiffness of every block damper, the attached block dampers essentially modify the distributed nature of the rail. This, in effect, changes the assembled mass and stiffness matrices of the rail. However, the form of the matrix equation of motion for the wheel-rail system with block dampers is the same as that given by Equation (2.39). For simplicity and in order to reduce the amount of computational effort the block dampers are represented by the 8-node brick finite element introduced in Section 2.5.

CHAPTER 3 WHEEL-RAIL MODEL BY FEM SOFTWARE

In order to provide a more realistic model for the analysis of wheel-rail interaction, commercially available FEM software, such as Abaqus, ANSYS, COMSOL Multiphysics, and much more can be employed. However, in the present investigation Abaqus [3.1] is employed since it is relatively easy to implement in a high-end laptop or engineering workstation.

To analyze the complicated system of wheel and rail, there are several simplifications that are commonly applied. First, the wheel is treated as a rotation disk (see, Appendix 3A). Second, the standard UIC60 (this is the commonly used European standard where 60 denotes the mass of the rail in kg/m) rail is assumed to be an I-beam (see, Appendix 3B). Third, owing to the last two assumptions, the angle of wheel-rail interaction is not included in the studies.

To further limit the scope of the present investigation in which one of the main objectives was to study and explore the replacement of the wheel/rail interaction or wheel/rail contact action by a traveling load, only vertical and transversal deflections are considered in the first phase of the investigation. In addition, friction at the contact point is included. This is believed to be more realistic than the Hertzian contact model adopted by many researchers in the past. During the second phase of the investigation, simple block dampers have been attached to the rail so that their effect on the deflections of the rail can be examined. Of course, more refined FE models for the wheel and rail can be investigated but it is outside the scope of the present investigation.

3.1 GEOMETRICAL AND MATERIAL PROPERTIES OF WHEEL AND RAIL

The simplified cross-sectional geometrical properties of the UIC60 rail are indicated in Figure 3.1(a) in which the dimensions are in m. The total length of this experimental rail is 4.2 m. The wheel is simplified as a disk with a center hole and depth is 0.036. The sketch of this wheel model is presented in Figure 3.1(b).

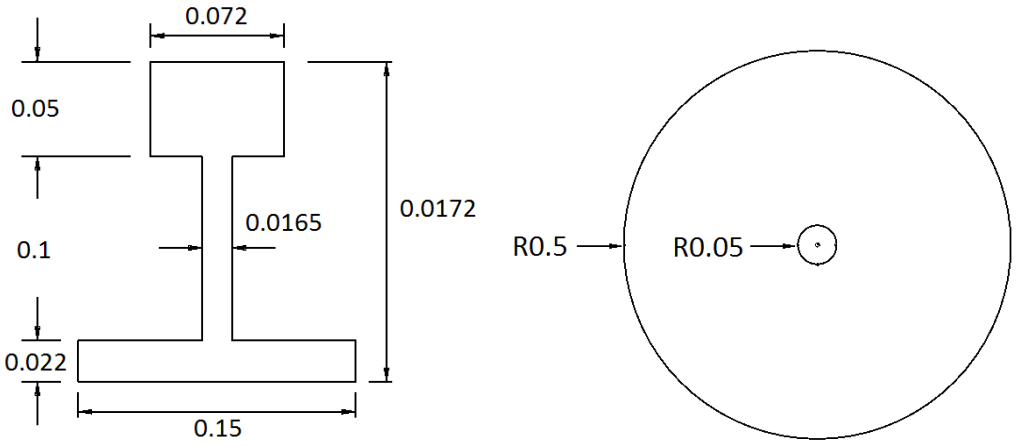

Figure 3.1 Geometrical dimensions of rail and wheel:
(a) I-beam model for rail, and (b) circular disk for wheel (in meter).

The material properties for the rail, wheel, and block damper are: Young's modulus E = 2.1×10^{11} Pa, Poisson ratio $\nu = 0.3$, and density $\rho = 7850$ $\frac{\text{kg}}{\text{m}^3}$.

3.2 PROCESS OF FE MODEL IN WHEEL-RAIL INTERACTION

In wheel-rail interaction studies, the typical process of constructing the finite element (FE) model is to separate into two steps. The first step is called pre-loading. It computes the deformations and stresses which are caused by applying the loading before the wheel

traveling and it is used to make sure that the wheel reaches the steady-state of rolling. The second step of the process is the initialization of deformation at the first time step and solving the moving loading problem by the explicit time-marching scheme [3.2]. The time step size is different from step to step in the time-marching scheme. For the first step, it is set to 1 ms. For the second time step the following equation is used

$$t_2 = \frac{4\ (m)}{speed}\ . \tag{3.1}$$

Initially, the wheel is located at 0.1 m from the departing end of the rail. Thus, the total distance of traveling in the second step is 4 m since the total length of the rail is 4.2 m.

3.3 IMPLICIT AND EXPLICIT TIME-MARCHING SCHEMES

Similar to many commercially available FEA packages Abaqus have several dynamic analysis procedures. In order to analyze the problem efficiently, the finite element dynamics explicit time scheme has been adopted for the present investigation. This is because there are several important features in this particular scheme. For example, when the system has a short dynamics response time and large discontinuity, it is efficient to employ the explicit time numerical integrating scheme since it is known to be unconditionally stable. Further, various choices for contact modeling are available. For the explicit time numerical integration scheme, one has to select a small time step size in order to provide a stable solution. In this regard, the critical time step size is governed by the following relation [3.3]

$$\Delta t = \frac{2}{\omega_{max}} \quad , \quad \omega_{max} = \frac{2}{l_e}\sqrt{\frac{E}{\rho}} \quad , \tag{3.2, 3.3}$$

where Δt is the time step size (s),

l_e is the length of the element (m),

ρ is the density (kg/m^3), and

ω_{max} is the highest natural frequency of the system.

As long as the time step is chosen slightly smaller than the critical time step size defined in Equation (3.2) the solution will be stable. A typical value has been suggested to be 98 or 95% of the critical [3.4].

In the FE model that adopts the explicit time scheme, the critical time step size, $\Delta t = 1.933 \times 10^{-6}$ s since for the above wheel-rail system Young's modulus is 2.1×10^{11} Pa, the density of the material 7850 kg/m^3, and smallest length of the element 0.01 m. Clearly, this time step size is very small and therefore for response computation the explicit time scheme is generally preferred for efficient computation.

3.4 BOUNDARY CONDITIONS

In the present investigation, the boundary conditions for the rail between consecutive sleepers are assumed to be simply-supported (SS) or hinged. More specifically, the present wheel rail model has the following features.

(1) With reference to Figure 3.2, the width of every sleeper is 0.2 m (6 sleepers are indicated in Figure 3.2).

(2) The length between two simply supported sleepers is 0.6 m (there are 5 spans with 6 SS sleepers as shown in Figure 3.3).

(3) The wheel is placed at 0.1 m from the starting end of the rail for the pre-loading step.

(4) The external force is 100kN. It is calculated from Superliner [3.5]. Each car is 74

tons with two four-wheel sets plus the weight of the capacity of passengers.

(5) The kinematic friction coefficient between wheel and rail is 0.3.

(6) The FE contact model assumes the penalty contact method [3.6].

(7) The relation between velocity and angular velocity is

$$v = r \times \omega \ .$$

(8) There are 8 different velocities of the train/wheel in every case considered in the computation. That is,

$$v = 10m, \qquad m = 1, 2, 3, \ldots 6, \qquad (m/s).$$

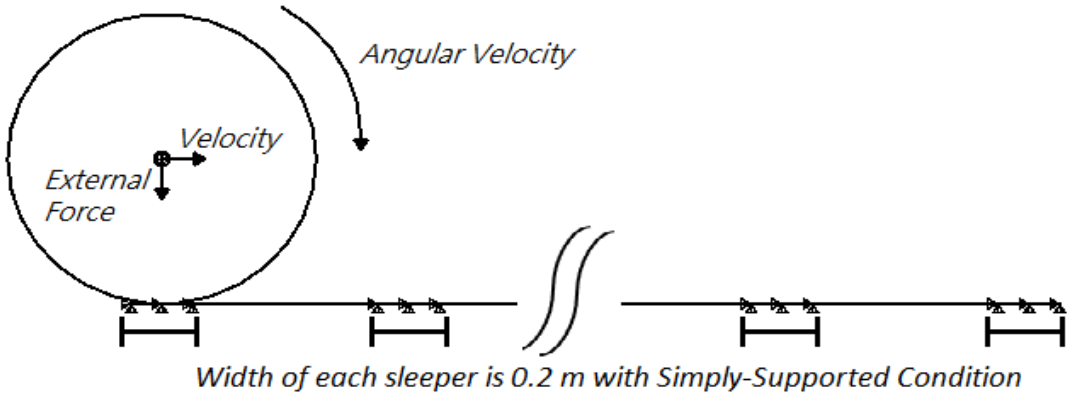

Figure 3.2 Wheel-rail model with boundary conditions indicated.

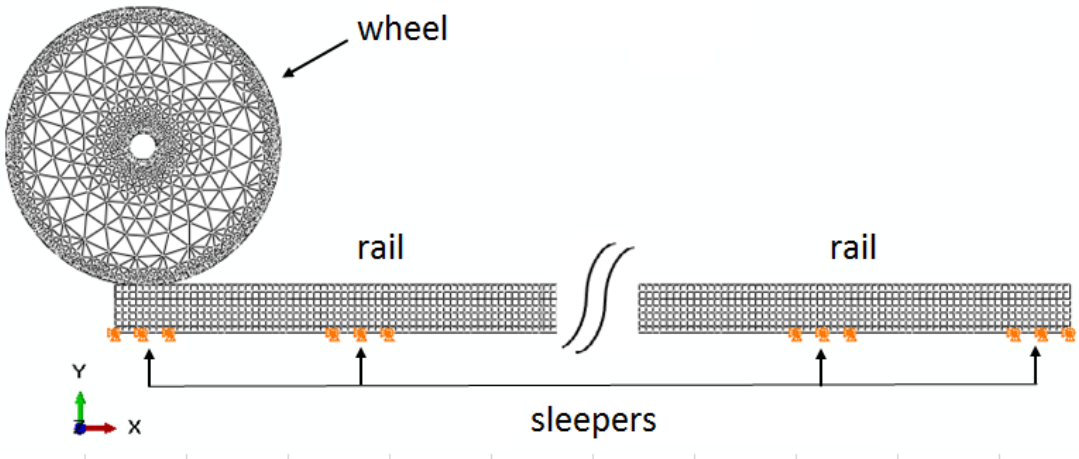

Figure 3.3 Finite element wheel-rail model with boundary conditions.

3.5 ELEMENT SIZE AND MESH

As mentioned in Section 3.3 in the foregoing, the critical time step size for explicit time scheme was obtained as $\Delta t = 1.933 \times 10^{-6}$ s which implies that in order to provide sufficiently accurate computational results the size of the elements at the contact point between the wheel and rail would be extremely small. The size of the element also leads to other problems when the contact point is rotating. The problem appears when the size of the rolling part is not small enough. For example, when the rail (or disk) is model as I shape beam and after a particular mesh is chosen, using element type C3D8 which is the 8 node lower order 3D element available in Abaqus [3.7], such that the element size is insufficiently small in accordance with Equation (3.3), then the computed displacement histories exhibit jumping (no contacts) phenomenon. Clearly, this phenomenon is not present in reality. To provide a visual appreciation of such a phenomenon three different sizes of the 3D element are presented in Table 3.1 in which element size means its largest dimension of that element. Recall that the 3D solid finite element employed in the present investigation is identified as type C3D8. As can be observed from this table the two coarser meshes start to experience no contact at 2 ms.

The effect of element size on Jumping (no contacts) phenomenon.

In Table 3.2 the element size and corresponding critical time step size are given so as to provide an appreciation of the smallness of the critical time step size for the computation applying the explicit time marching scheme.

Element C3D4, which is a 4-node tetrahedral element, is applied on wheel model due to partition. Rail model is still by using C3D8 element.

Table 3.1 Evolution of different mesh sizes for wheel-rail model with jumping (no contact).

Element size (cm)		5	2.5	1
Time (ms)	0	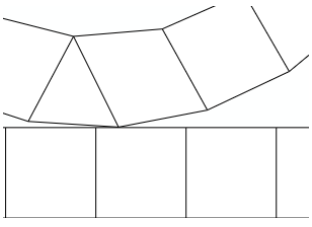	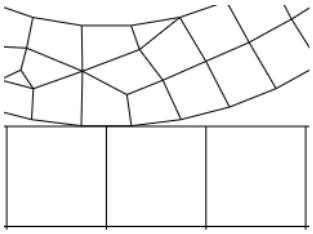	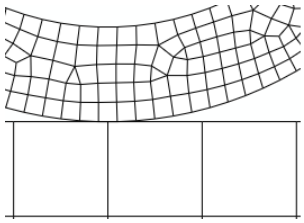
	2	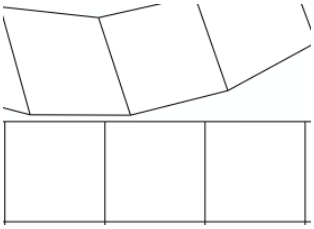	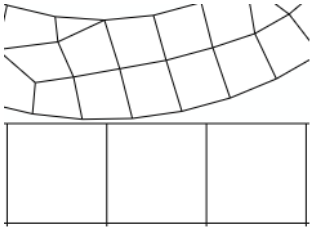	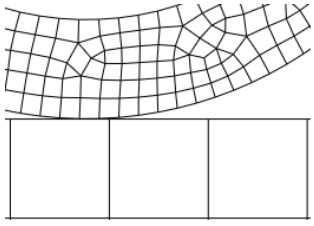
	5	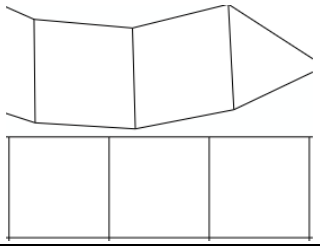	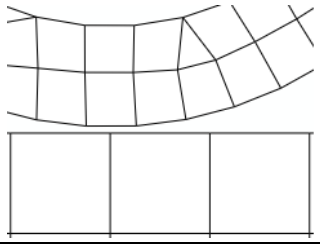	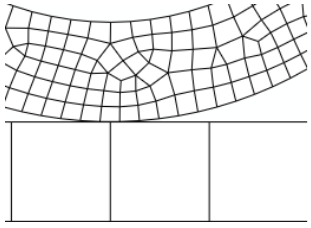

Table 3.2 Relationship between element size and time step size.

Element size (m)	0.05	0.025	0.01
Critical Δt (s)	9.667×10^{-6}	4.834×10^{-6}	1.933×10^{-6}

CHAPTER 4 WHEEL-RAIL INTERACTION MODELS WITHOUT BLOCK DAMPERS

This chapter is divided into two main parts. The first part is concerned with the determination of the important dynamic characteristics, such as the natural frequencies and mode-shapes of the rails. The second part deals with the evaluation of the responses of wheel-rail interaction models. No block dampers attached to the rails are included in this chapter.

The first part is therefore concerned with the eigenvalue solution and is included in Section 4.1 in which the rail is represented as a SS EBB, TB, and 3D FE model applying the 8 node brick element introduced Chapter 2. The second part that includes the modeling of the wheel-rail contact problem as a traveling point load, is presented in Section 4.2. It is further been sub-divided into three components. The first component deals with the analytical solution of the responses of the SS EBB under a traveling point load. The second component presents the responses of the 3D FE model under similar traveling point load and in this component friction forces are included in the analysis. The third component shows the unscaled traveling point load and the modification of vertical and friction forces by scaling amplitude of each node. In addition, the results of 3D FE rail model with unscaled and scaled traveling point load are compared with 3D FE wheel-rail model, are presented in Section 4.3.

4.1 EIGENVALUE SOLUTION OF RAIL MODELS

The eigenvalue solution is concerned with the determination of the natural frequencies and mode-shapes of the dynamic system. In this section, the rail is modeled as a SS EBB, TB, and 3D FE representation.

Analytical solution for the SS EBB is included in Sub-section 4.1.1. Computed results applying the FEM are presented in Sub-section 4.1.2 in which the EBB finite element, TB finite element, and 3D finite element models are studied and compared. The discussion is included in Sub-section 4.1.3.

4.1.1 Solution by EBB Theory

As presented in Chapter 2, the natural frequencies of the SS EBB are given by $\omega_n = \left(\frac{n\pi}{L}\right)^2 \sqrt{\frac{EI}{\rho A}}$. The geometrical properties of this EBB are: length L = 0.6 m, cross-section area of the beam $= 8.55 \times 10^{-3}$ $\mathbf{m^2}$, and the second moment of area of the cross-section $I = 3.42354 \times 10^{-5}$ $\mathbf{m^4}$. The material properties are: Young's modulus of elasticity $E = 2.1 \times 10^{11}$ Pa, Poisson ratio ν = 0.3, and density ρ = 7850 kg/m^3. While many natural frequencies and mode-shapes of this rail model can be calculated, for brevity, only the first six mode-shapes and natural frequencies are presented in Figure 4.1 and Table 4.1, respectively.

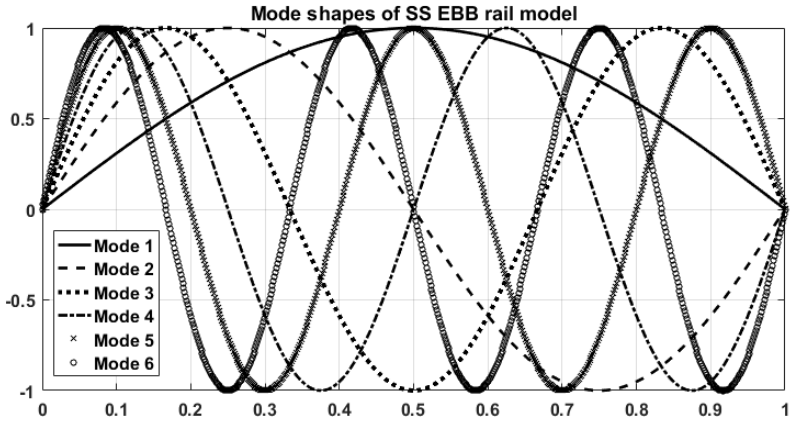

Figure 4.1 First six mode-shapes of SS EBB rail model.

Table 4.1 First six natural frequencies of SS EBB.

Mode number	**EBB (Exact) (Hz)**	**EBB element (B23) (Hz)**	**TB element (B21) (Hz)**
1	1428	1394	1074
2	5712	5575	2936
3	12852	12545	4836
4	22848	22306	6701
5	35701	34849	8537
6	51410	50180	10354

4.1.2 Computed Results of Beam Element and Solid Element Models

In the FE models, beam elements based on the EBB theory and TB theory, and 3D solid element are employed. The mass and stiffness matrices of the beam elements have

already been presented in Sub-sections 2.5.1.1 and 2.5.1.2. Table 4.1 and Figure 4.2 (a) through (f) show the first six natural frequencies and mode shapes by using EBB element (which is identified as B23 in Abaqus; henceforth, the notation inside the parentheses is referred to the identification in Abaqus) and TB element (B21). Table 4.2 and Figure 4.3 (a) through (l) show the first twelve natural frequencies and mode shapes by using the solid element (C3D8).

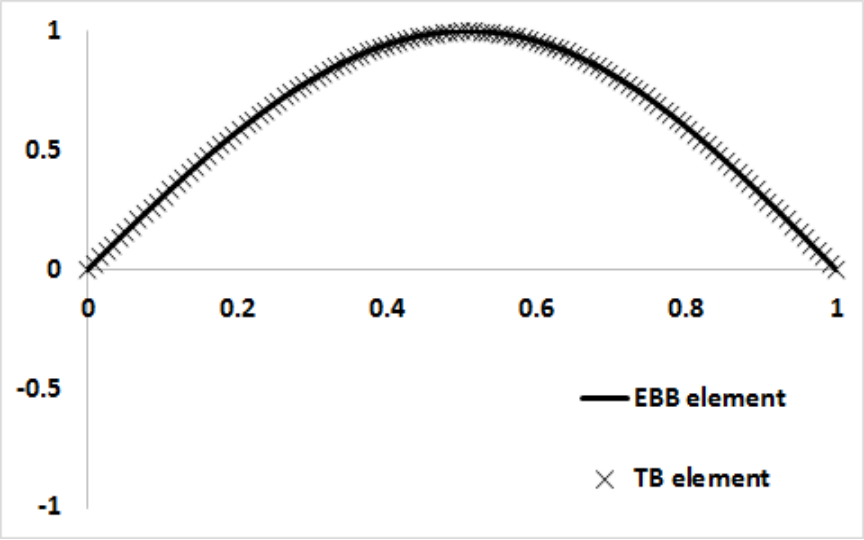

Figure 4.2 (a)

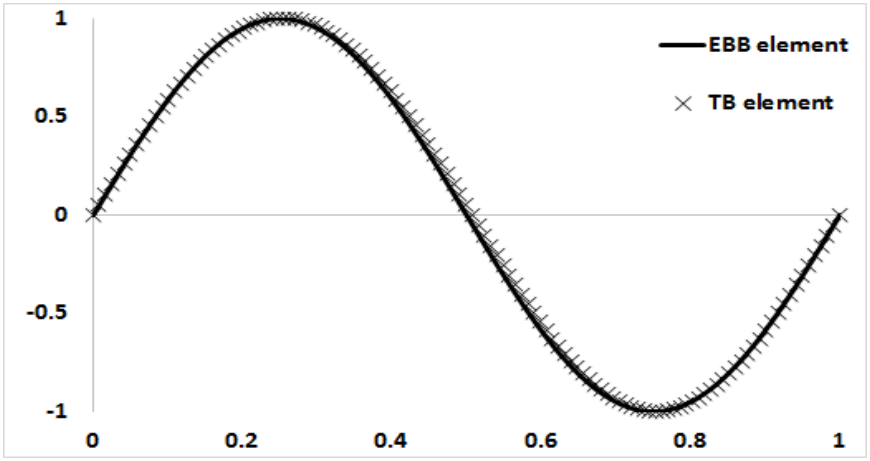

Figure 4.2 (b)

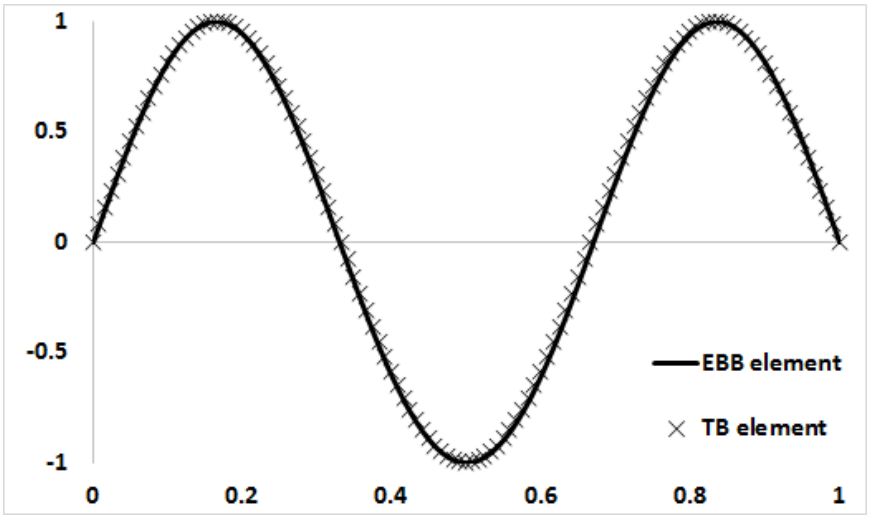

Figure 4.2 (c)

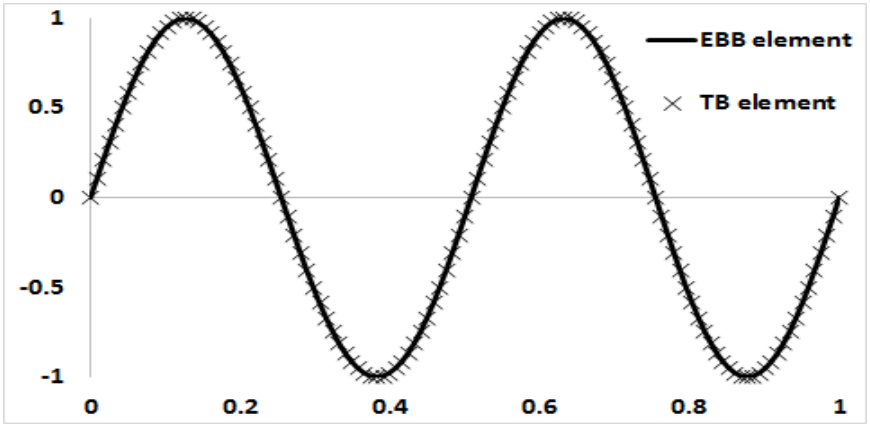

Figure 4.2 (d)

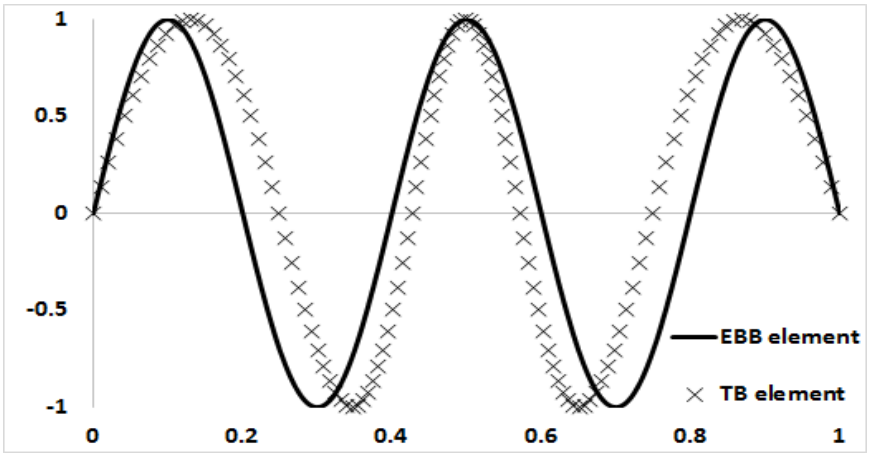

(e)

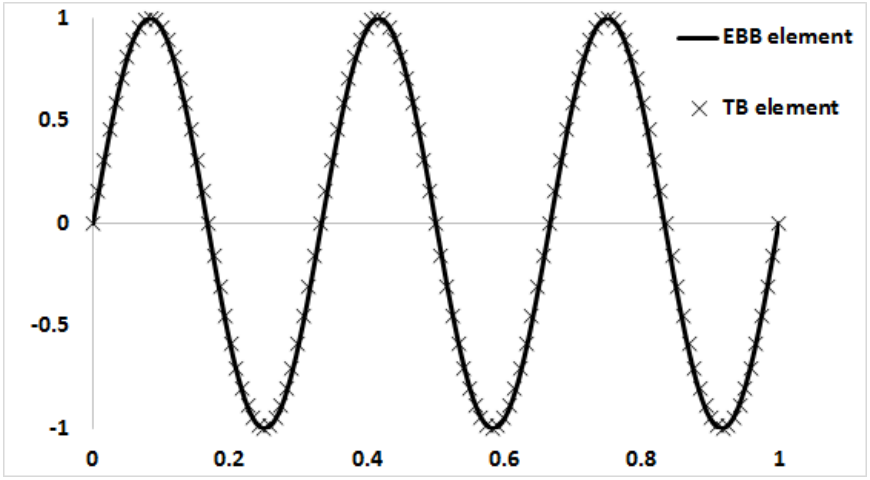

(f)

Figure 4.2 First six mode-shapes of beam element models:

(a) Mode 1, (b) Mode 2, (c) Mode 3, (d) Mode 4, (e) Mode 5, and (f) Mode 6.

Table 4.2 First twelve natural frequencies of FE solid element.

Mode number	**(Hz)**	Mode number	**(Hz)**
1	260	7	1776
2	679	8	2044
3	1044	9	2176
4	1125	10	2601
5	1292	11	2972
6	1760	12	3057

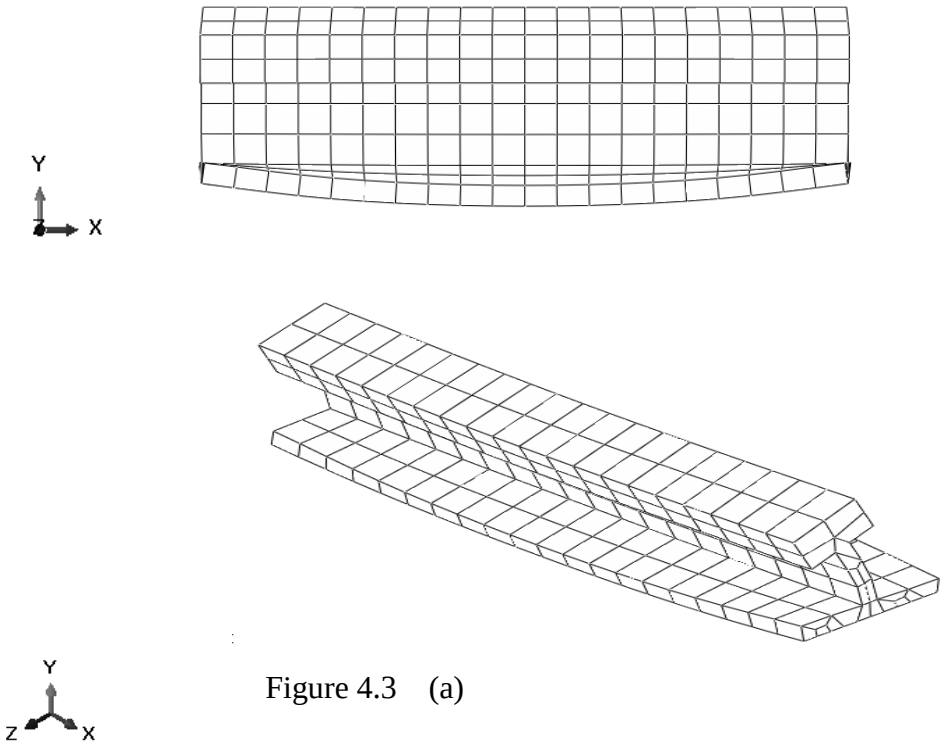

Figure 4.3 (a)

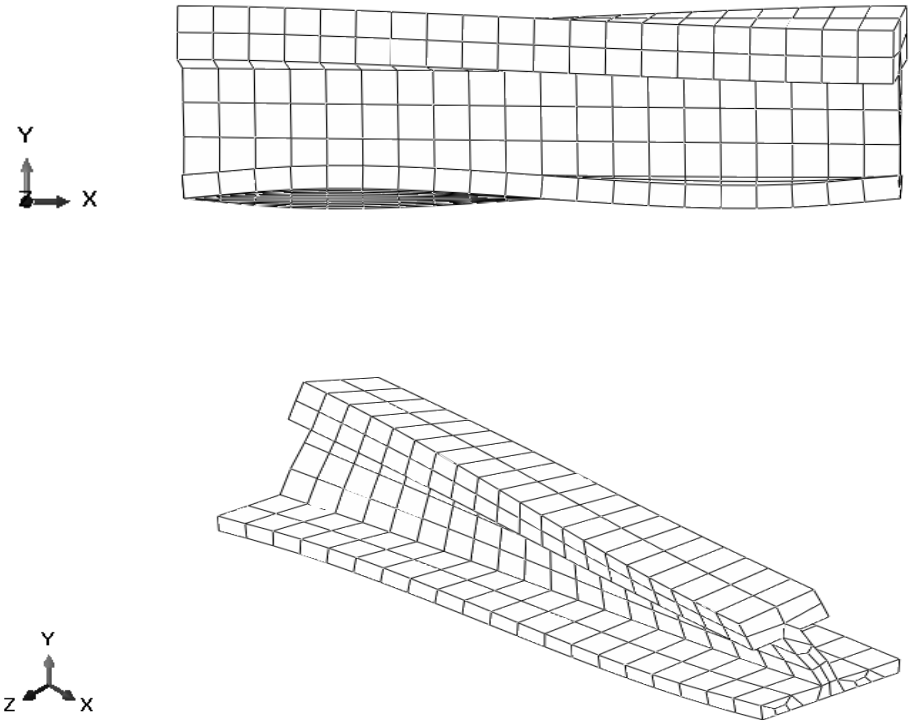

Figure 4.3 (b)

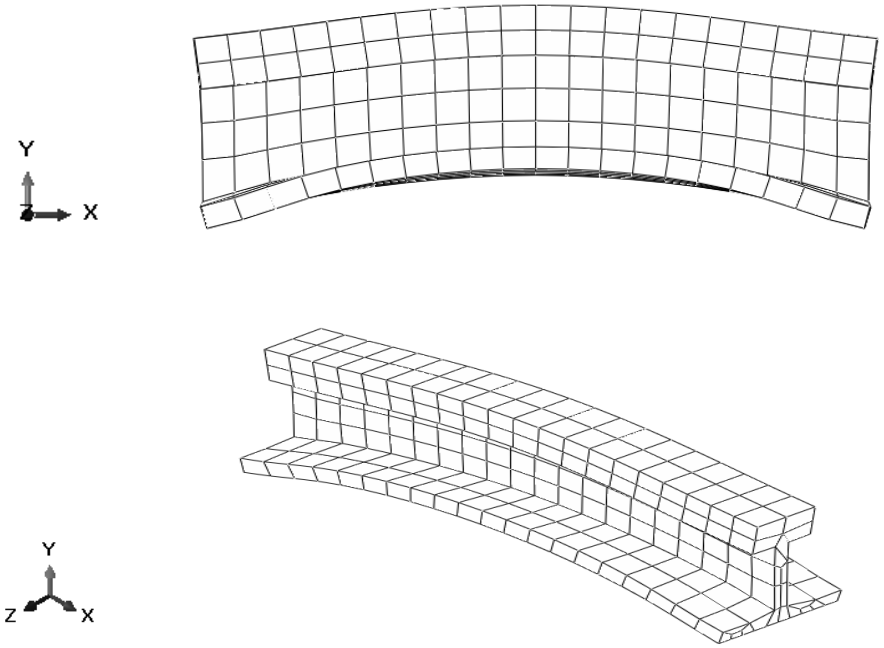

Figure 4.3 (c)

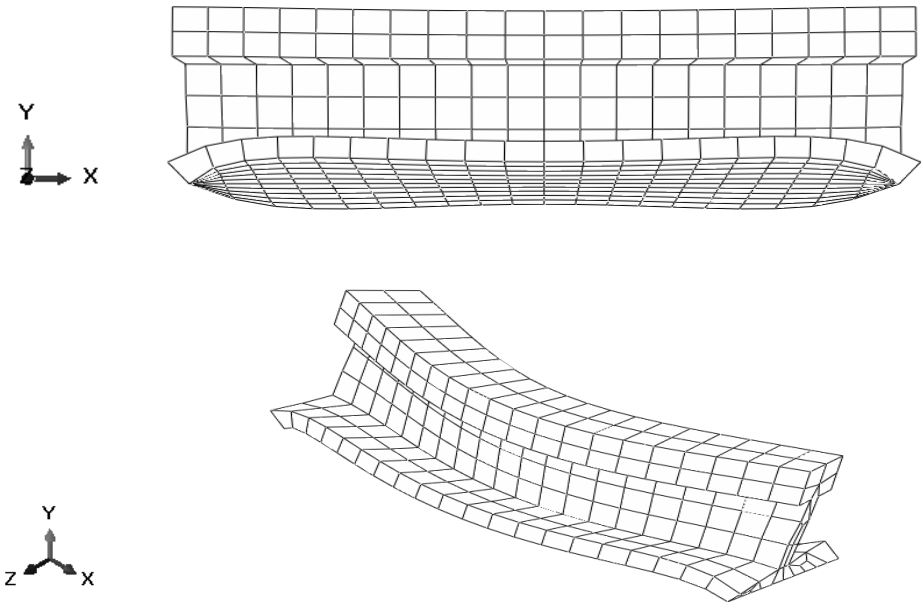

Figure 4.3 (d)

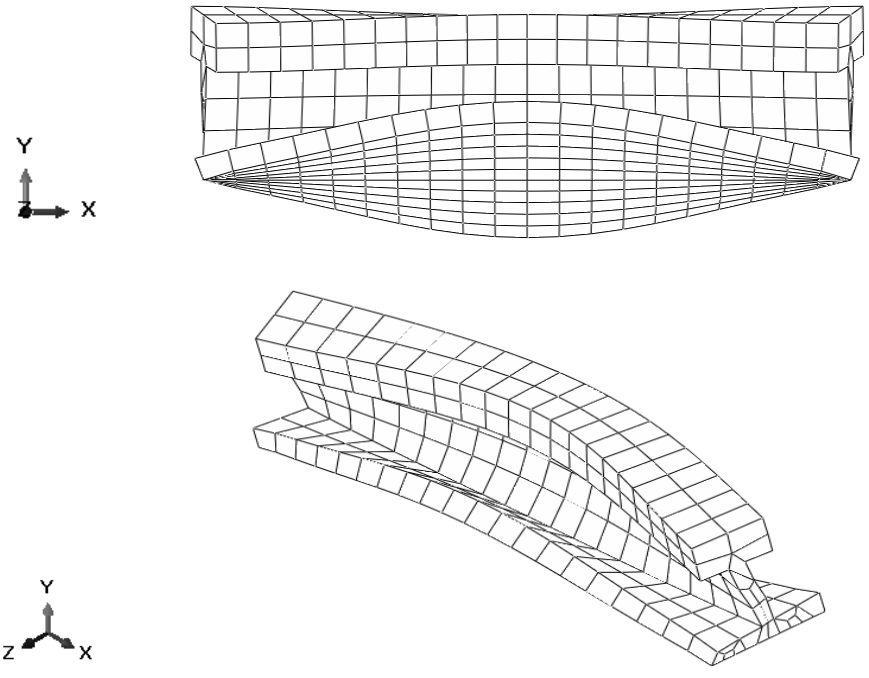

Figure 4.3 (e)

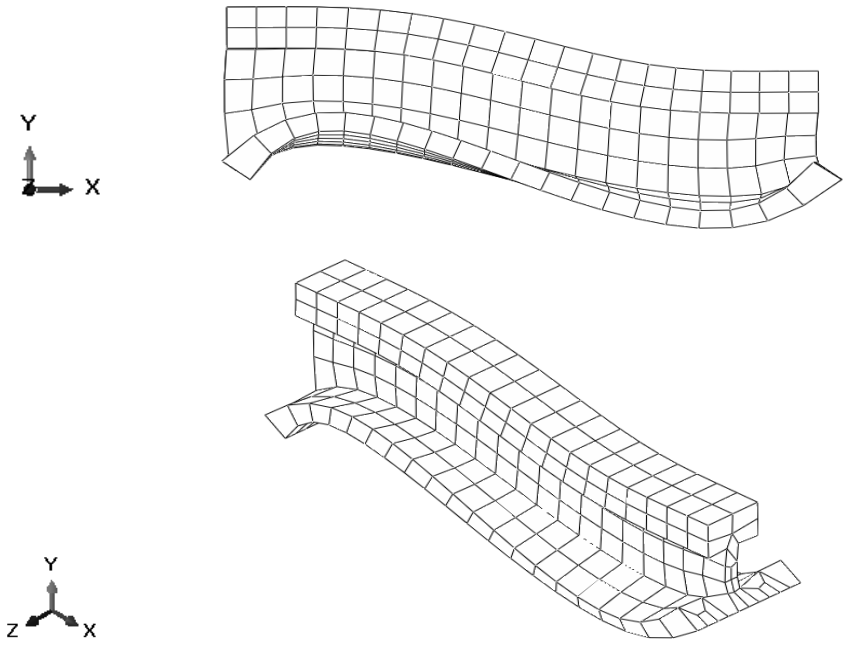

Figure 4.3 (f)

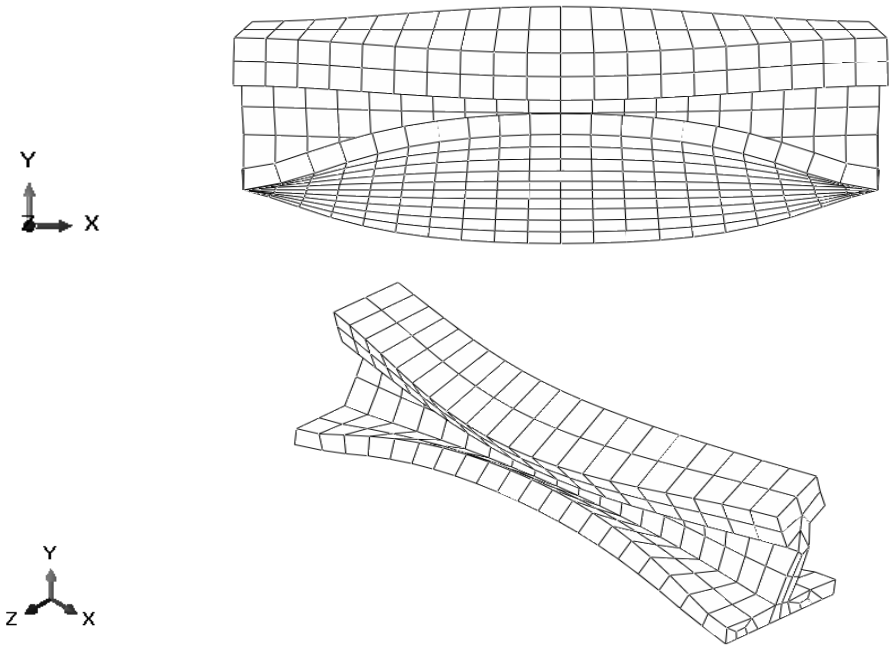

Figure 4.3 (g)

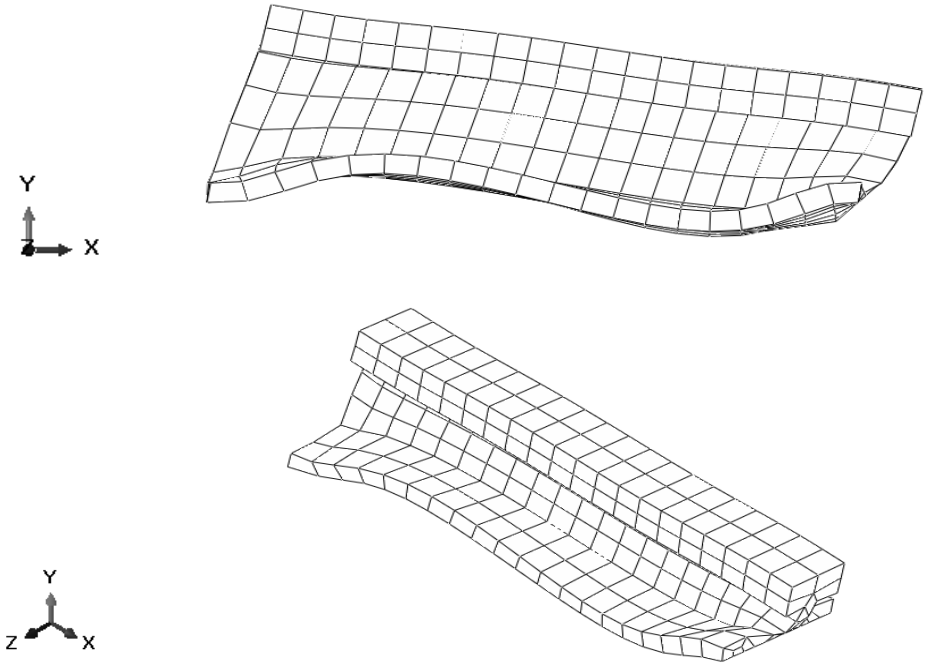

Figure 4.3 (h)

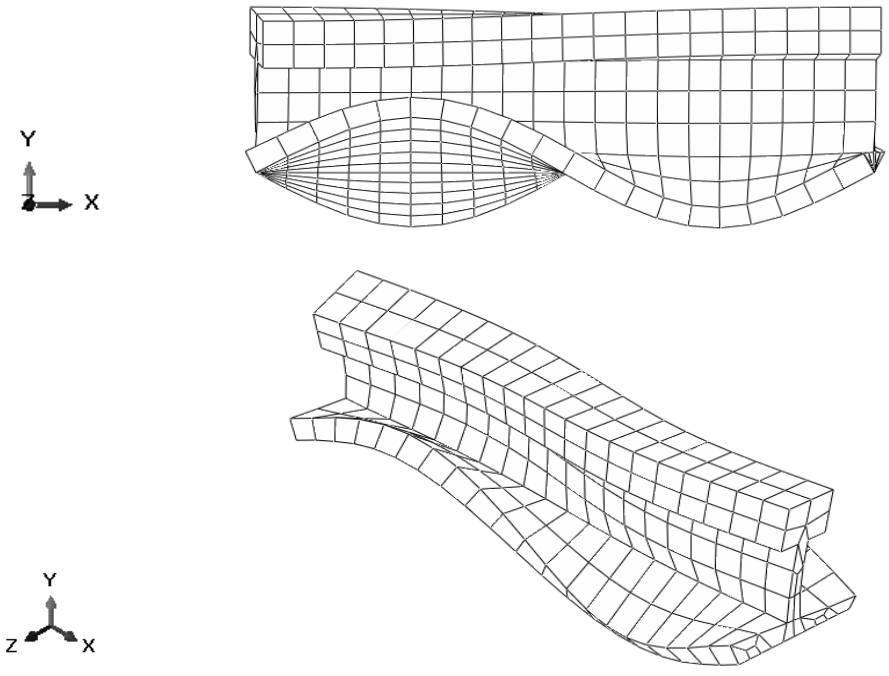

Figure 4.3 (i)

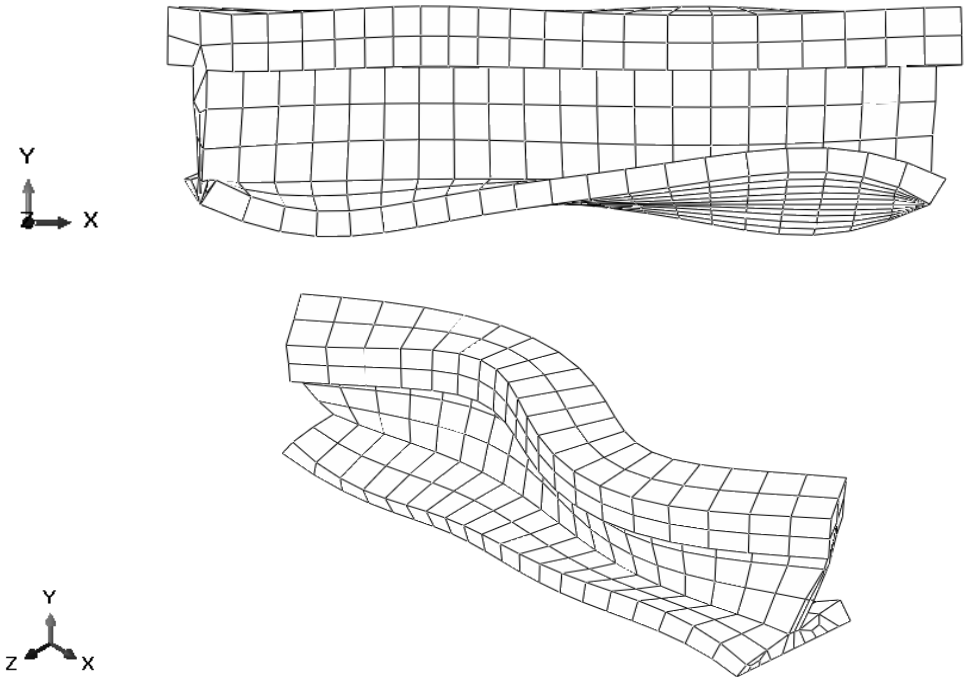

Figure 4.3 (j)

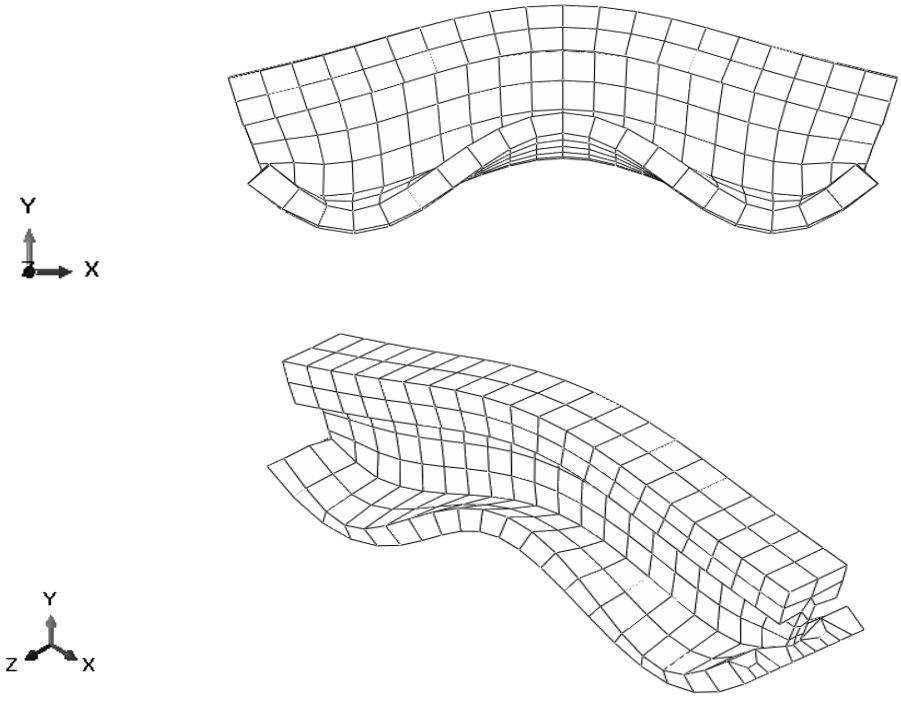

Figure 4.3 (k)

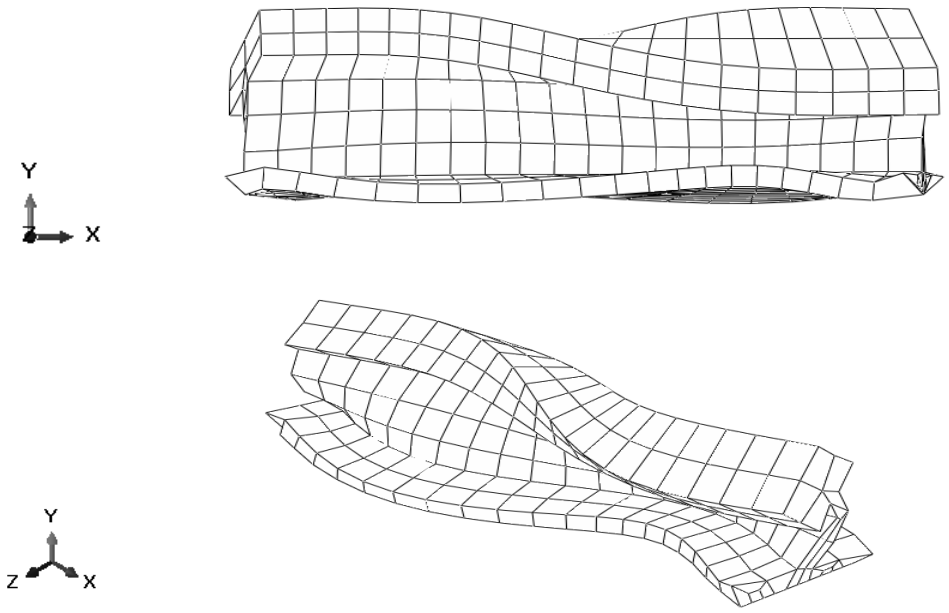

(l)

Figure 4.3 First twelve mode-shapes of solid element (C3D8) model:
(a) Mode 1, (b) Mode 2, (c) Mode 3, (d) Mode 4, (e) Mode 5, (f) Mode 6,
(g) Mode 7, (h) Mode 8, (i) Mode 9, (j) Mode 10, (k) Mode 11, and (l) Mode 12.

4.1.3 Discussion

With reference to the results presented in the foregoing, the EBB exact natural frequencies are close to the corresponding FE model as expected. The differences of first six natural frequencies between those using the EBB element and exact solutions are, respectively, 2.5%, 2.4%, 2.4%, 2.4%, 2.4%, and 2.4%, with respect to the exact EBB solution. However, these natural frequencies are significantly different from those using the TB FE model, and the 3D brick element model. This indicates that the TB and 3D FE models are close approximations to the actual rail whose aspect ratio is L/D = 3.48, where D is the largest dimension of the cross-section area of the rail.

4.2 RESPONSES OF RAIL DUE TO TRAVELING POINT LOAD

As presented in Chapter 2, the contact problem of the wheel-rail interaction model is treated as a SS structure with a traveling point load. The SS structure is represented by the EBB beam element and the 3D brick element. The main objectives are (a) to study analytically the responses of the EBB under a moving point load, and (b) to compute the responses of the EBB beam element and the 3D FE model for a similar traveling point load. The analytical and numerical responses of the simple EBB model are included in Sub-section 4.2.1 while the responses of the 3D FE model are computed and presented in Sub-section 4.2.2.

4.2.1 Analytical and FE Models of Rail with a Traveling Point Load

The essential objectives of the studies reported in this sub-section are (a) to introduce the detailed steps in implementing the traveling point load for the computation of responses of the SS EBB structure, and (b) to provide similar results using the FE EBB element. To satisfy the aspect ratio criterion for EBB theory, the following geometrical properties of the rail model are: length L = 0.6 m, width of cross-section b = 0.03 m, height of area of cross-section h = 0.03 m, the aspect ratio is 20, and the second moment of area of the cross-section $= 6.75 \times 10^{-8}$ m^4. The material properties are: Young's modulus of elasticity $E = 2.1 \times 10^{11}$ Pa, Poisson ratio ν = 0.3, and density ρ = 7850 kg/m^3.

Before the responses along the length of the FE SS EBB structure are computed the responses obtained analytically are considered first. From the results in Sub-section 2.4.1, the transversal deflection at mid-span of the beam, $w_0 = \frac{2MgL^3}{\pi^4 EI}$, where Mg is the

point load applied at mid-span or at $x = \frac{L}{2}$. In the case of a traveling load, the steps in the response computations are presented in the following.

Firstly, *Mg* is the vertical point load applied on the beam. To express into the dimensionless quantities, it is convenient to normalize the deflection by the mid-point static deflection which, in this case, the point load is 125 kN, is $w_0 = 3.9\times10^{-2}$ m, and the dimensionless time, $\tau = \frac{t}{\left(\frac{L}{v}\right)}$.

Secondly, Equation (2.17) is a summation series. It can be chosen as many modes as required. However, Equation (2.17) shows that when n is large, the value of $\frac{\alpha}{n^2(n^2-\alpha^2)}$ will be small. Therefore, in this case, the largest number n is chosen as 5.

The dimensionless responses computed by using the analytical solution are plotted in Figures 4.5 through 4.7. Note that in these figures the computed responses for n = 1 and n = 5 are very close.

Now, the responses of the SS EBB structure approximated by the FEM are considered. The traveling point load acting on the discretized SS EBB structure is dealt with first. As in the analytical model presented in the foregoing, for the point load to move along the length of the beam structure it is required to assign different amplitudes of the load at different stations along the length of the beam structure. For the present FE model, the traveling load is only considered when it passes the specific node. To illustrate this, Figure 4.8 may be helpful. For example, if the point load *F* is traveling with a constant speed v through Node $i =$ 1, 2, 3, and 4 (in this particular example) the length of the 2 node EBB element is $\frac{L}{3}$, which comes from the length of span L being divided by three 2 node EBB elements. Therefore, the times for the traveling point load to reach

Nodes $i =$ 1, 2, 3, and 4 are given by

$$t_i = \frac{L}{3}\left(\frac{i-1}{v} \right). \tag{4.1}$$

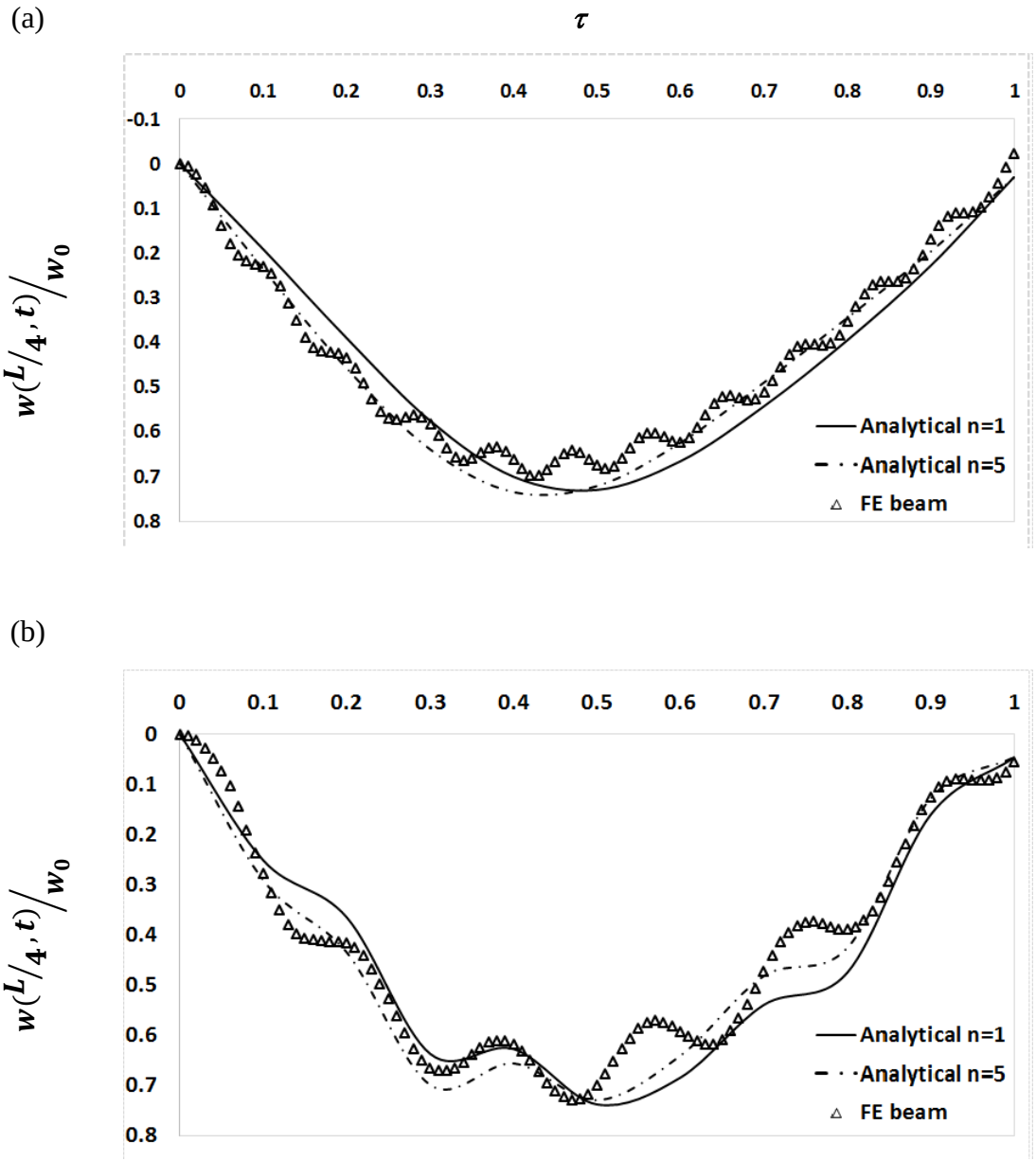

Figure 4.5 Normalized responses at a quarter-point from starting end of SS EBB (x =0.15 m): (a) v = 10 m/s, and (b) v = 20 m/s.

(c)

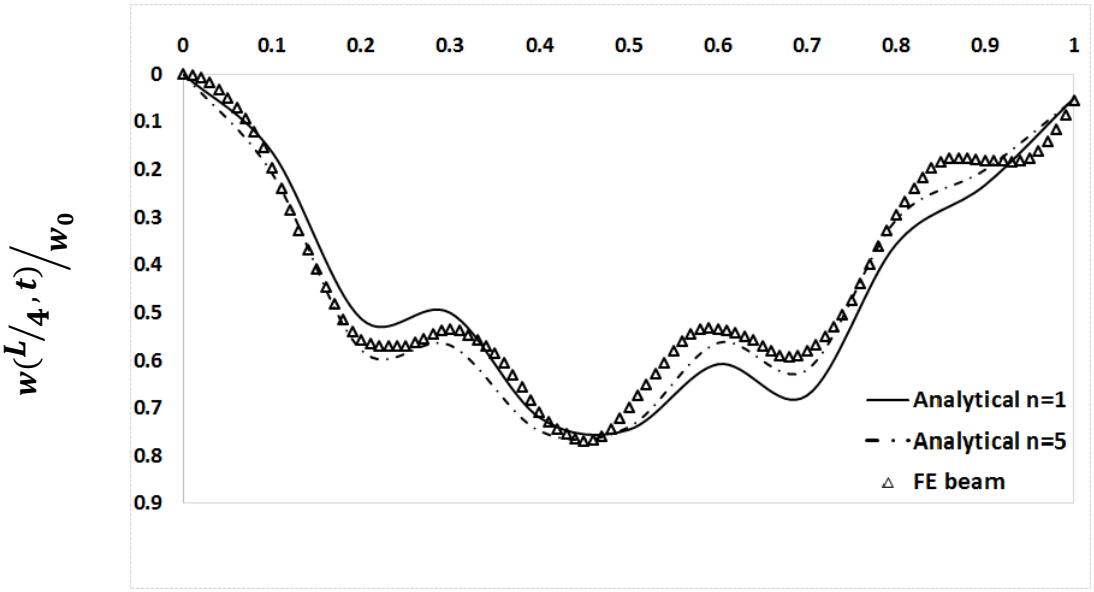

(d)

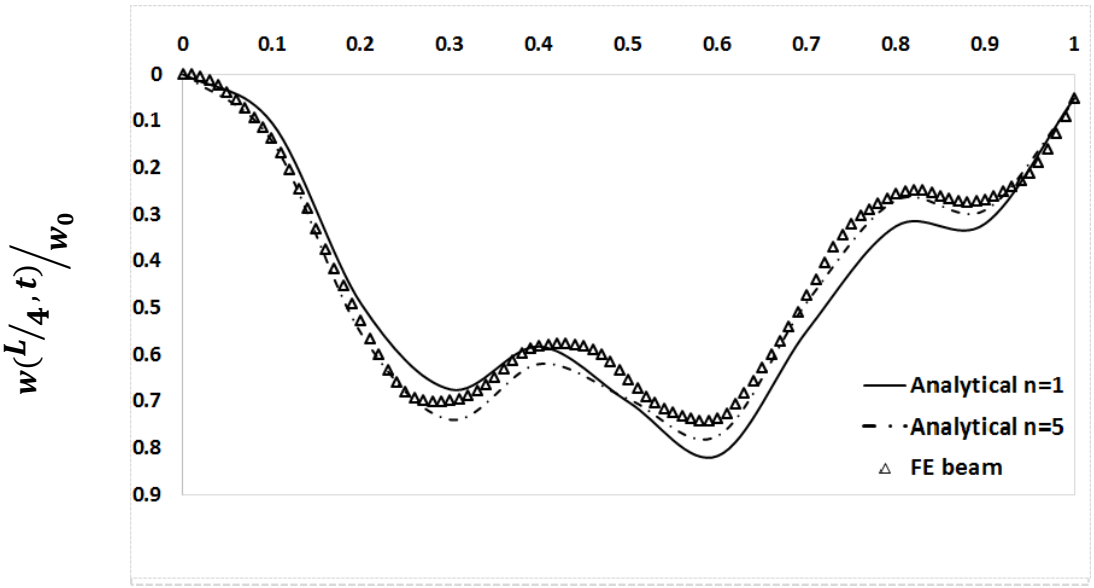

Figure 4.5 Normalized responses at a quarter-point from starting end of SS EBB (x =0.15 m): (c) v = 30 m/s, and (d) v = 40 m/s.

(e)

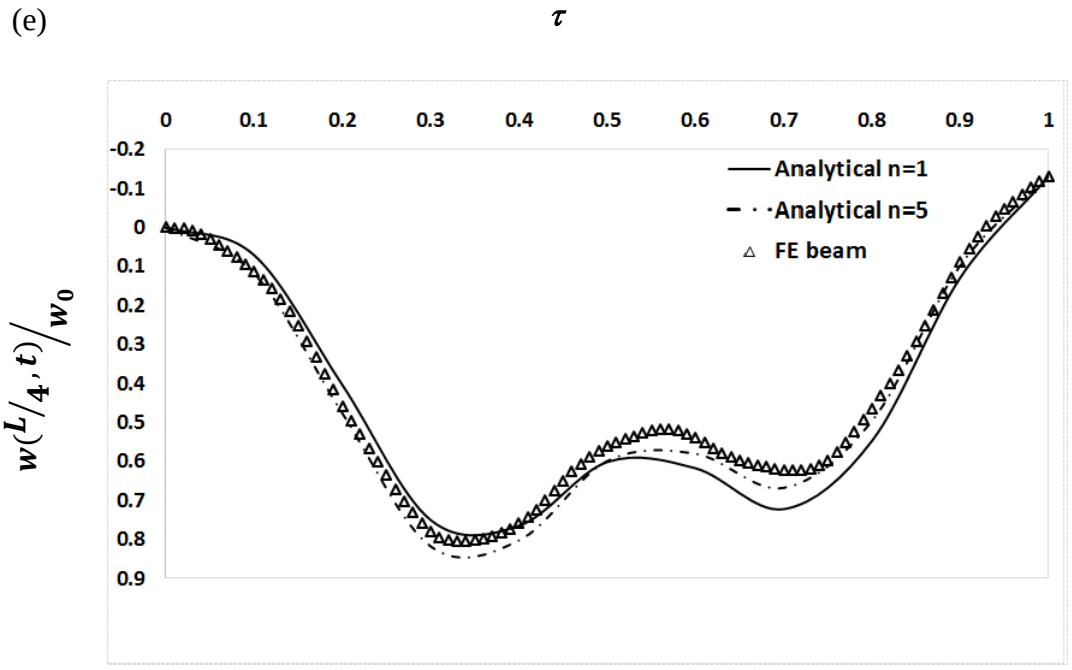

(f)

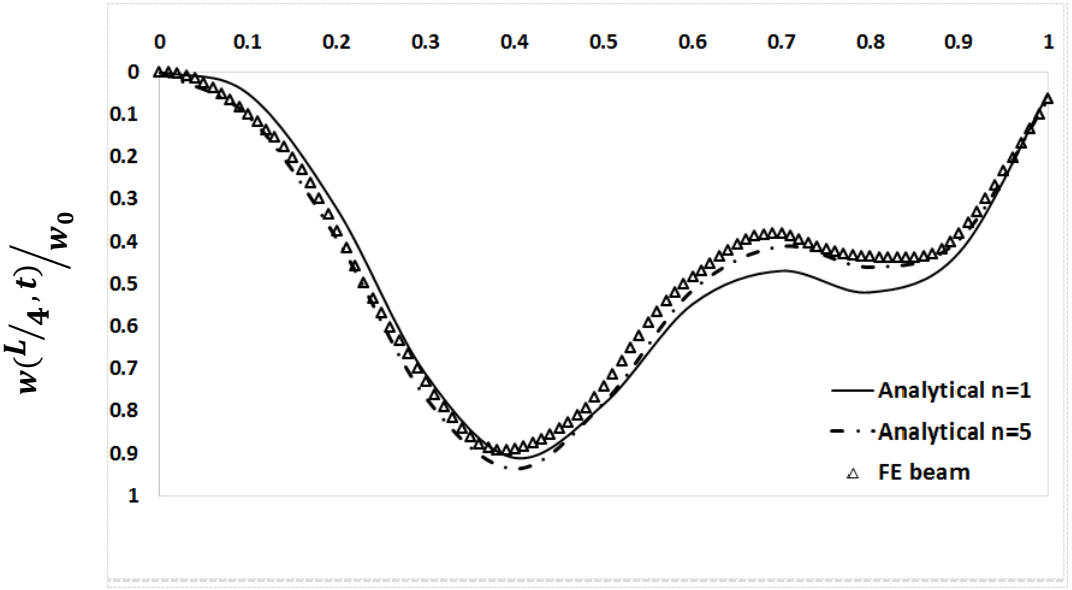

Figure 4.5 Normalized responses at a quarter-point from starting end of SS EBB (x =0.15 m): (e) v = 50 m/s, and (f) v = 60 m/s.

(a)

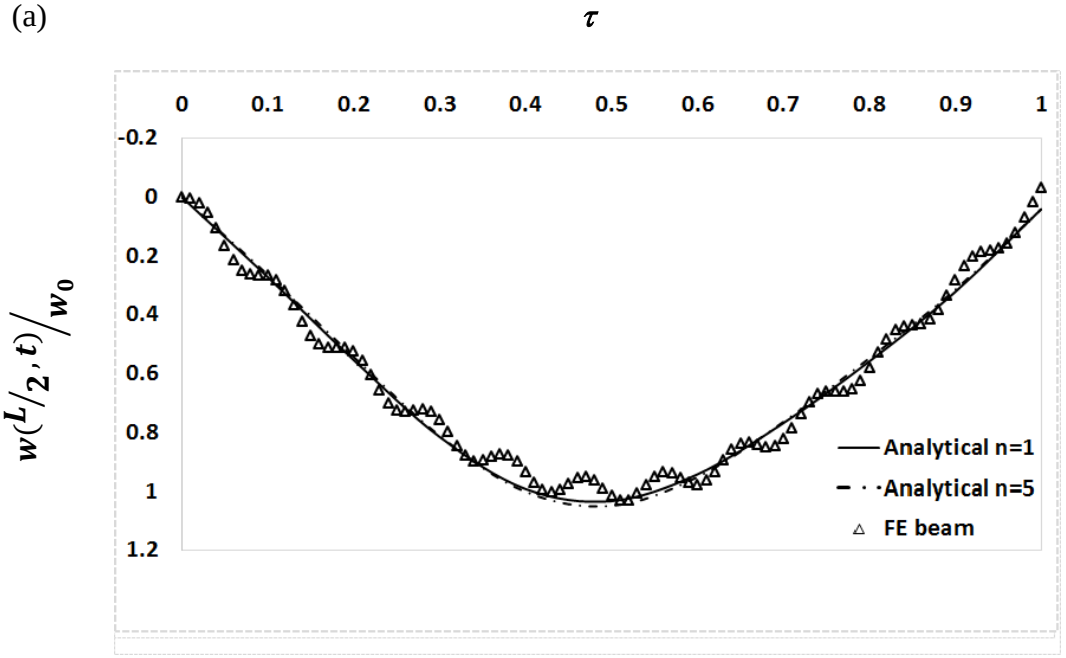

(b)

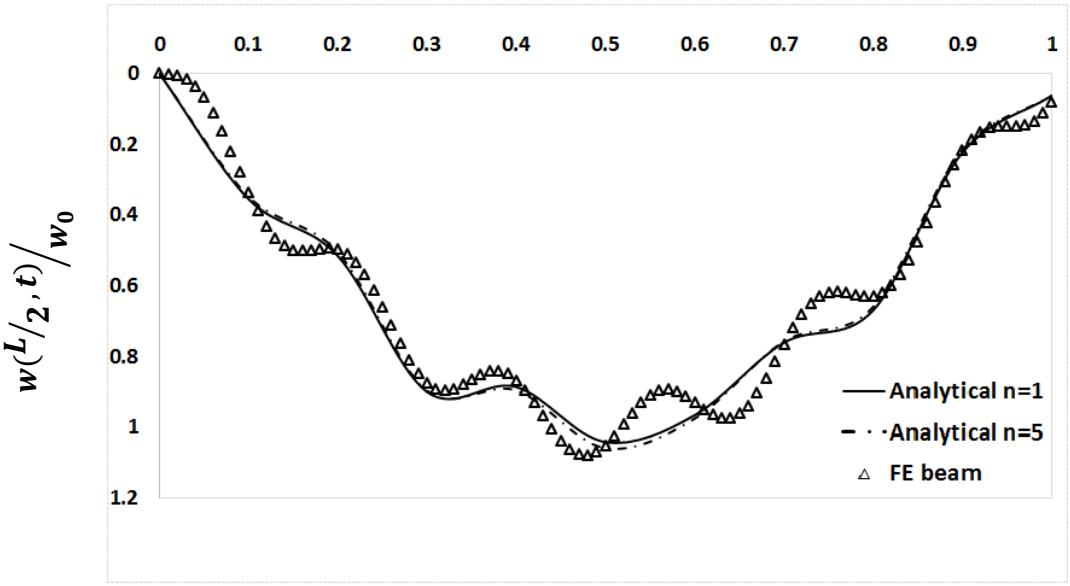

Figure 4.6 Normalized responses at mid-point from starting end of SS EBB (x = 0.30 m): (a) v = 10 m/s, and (b) v = 20 m/s.

(c)

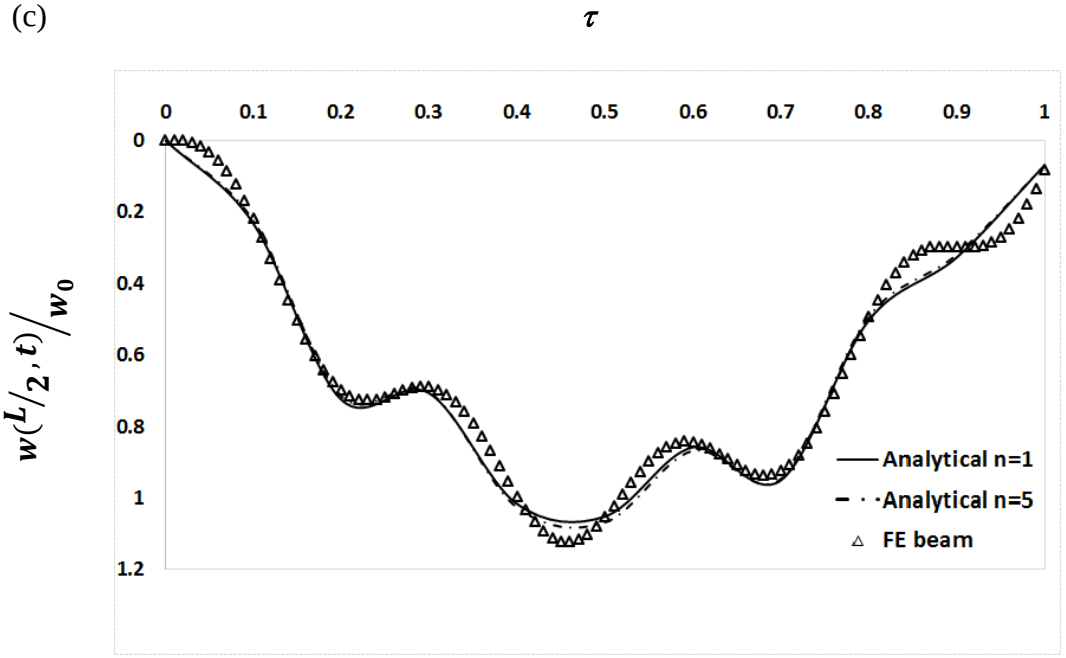

(d)

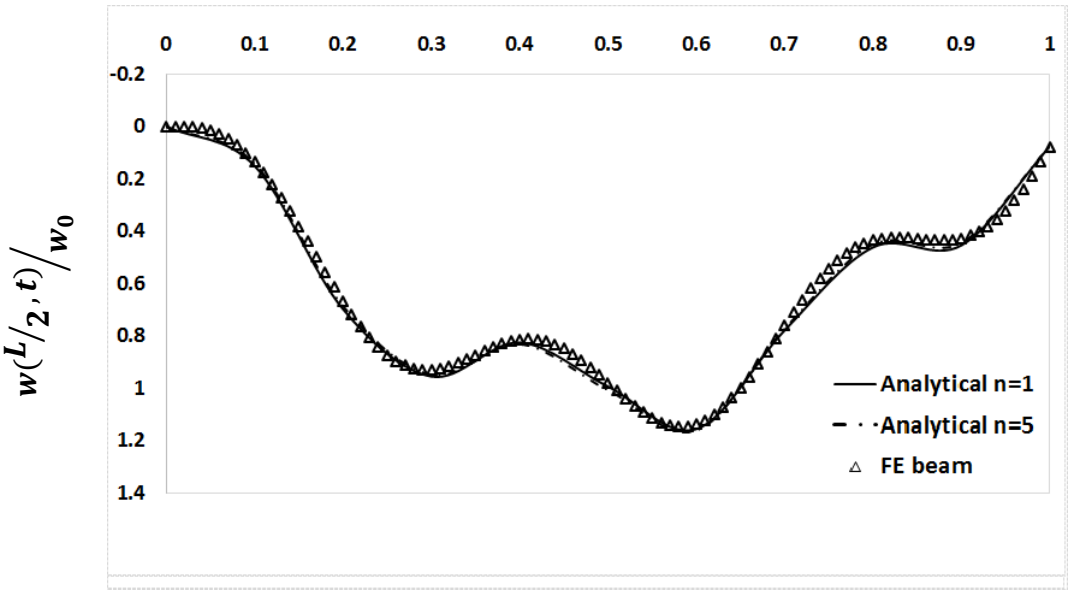

Figure 4.6 Normalized responses at mid-point from starting end of SS EBB (x = 0.30 m): (c) v = 30 m/s, and (d) v = 40 m/s.

(e)

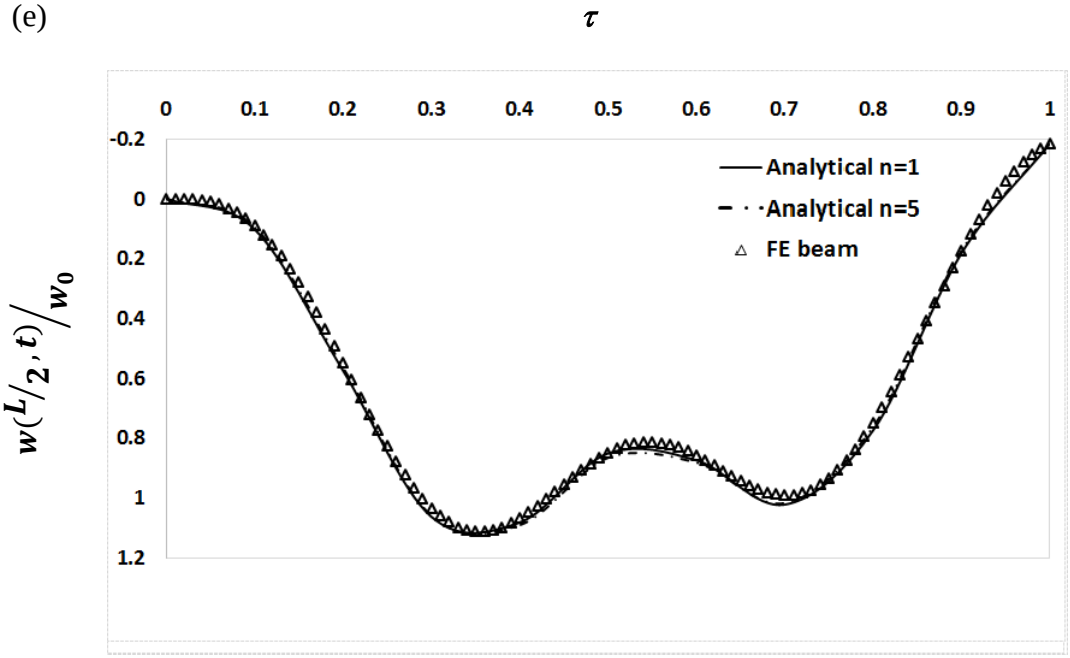

(f)

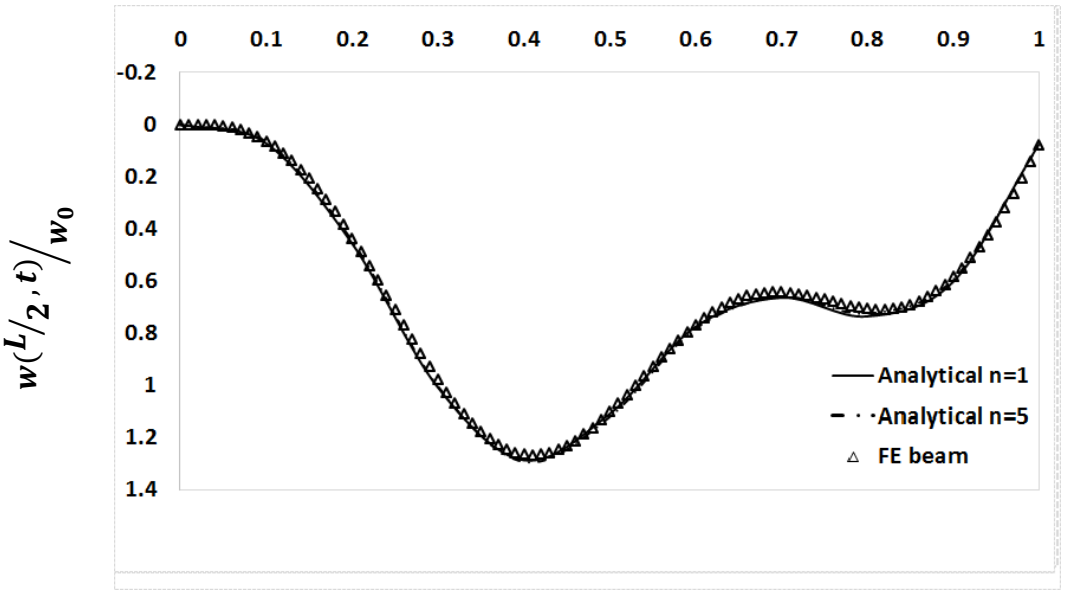

Figure 4.6 Normalized responses at mid-point from starting end of SS EBB (x = 0.30 m): (e) v = 50 m/s, and (f) v = 60 m/s.

(a)

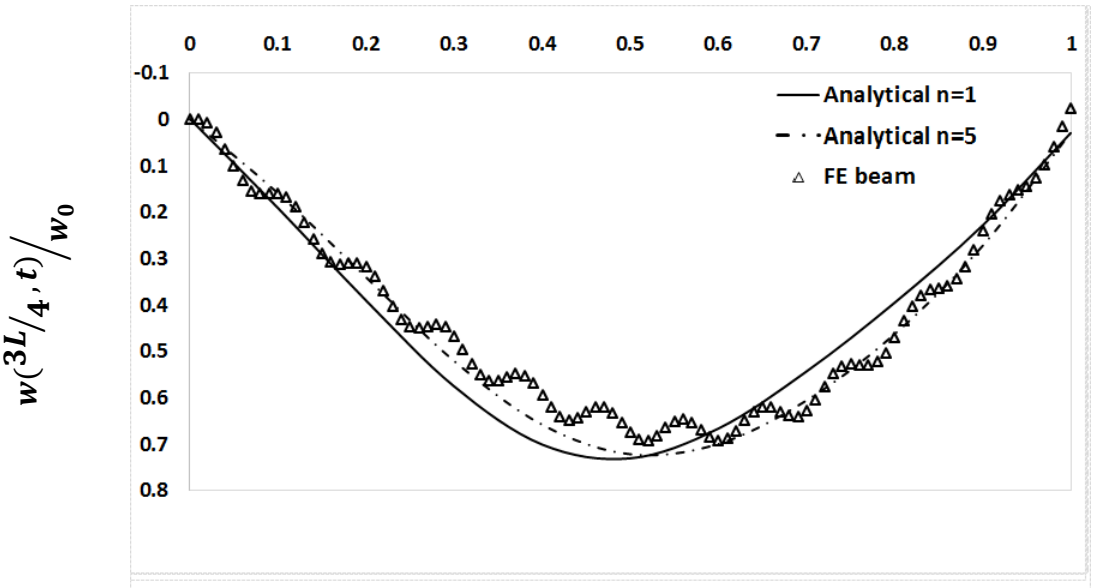

(b)

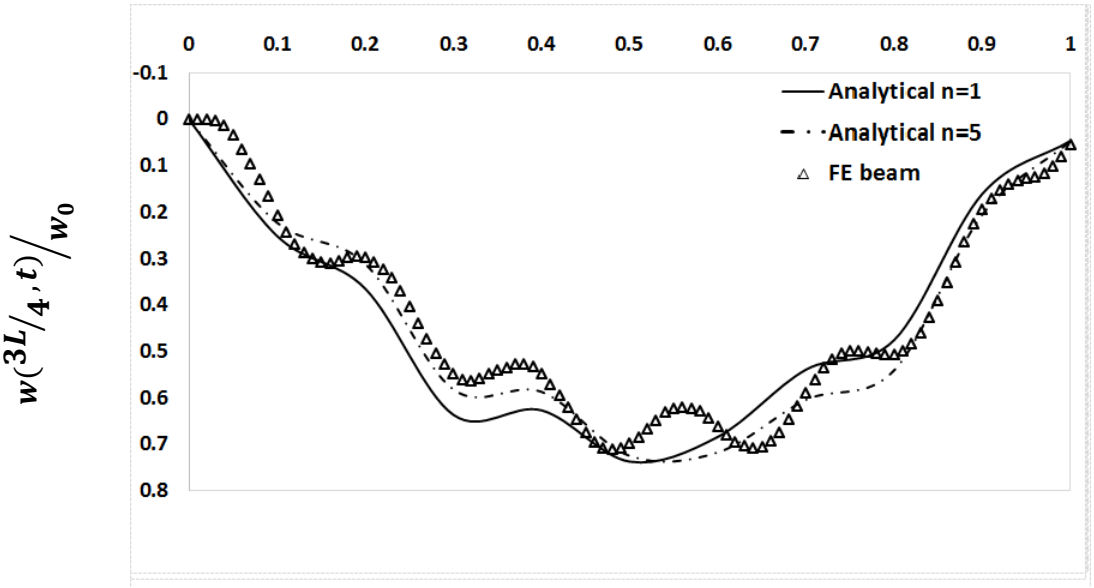

Figure 4.7 Normalized responses at the third quarter-point from starting end of SS EBB (x = 0.45 m): (a) v = 10 m/s, and (b) v = 20 m/s.

(c)

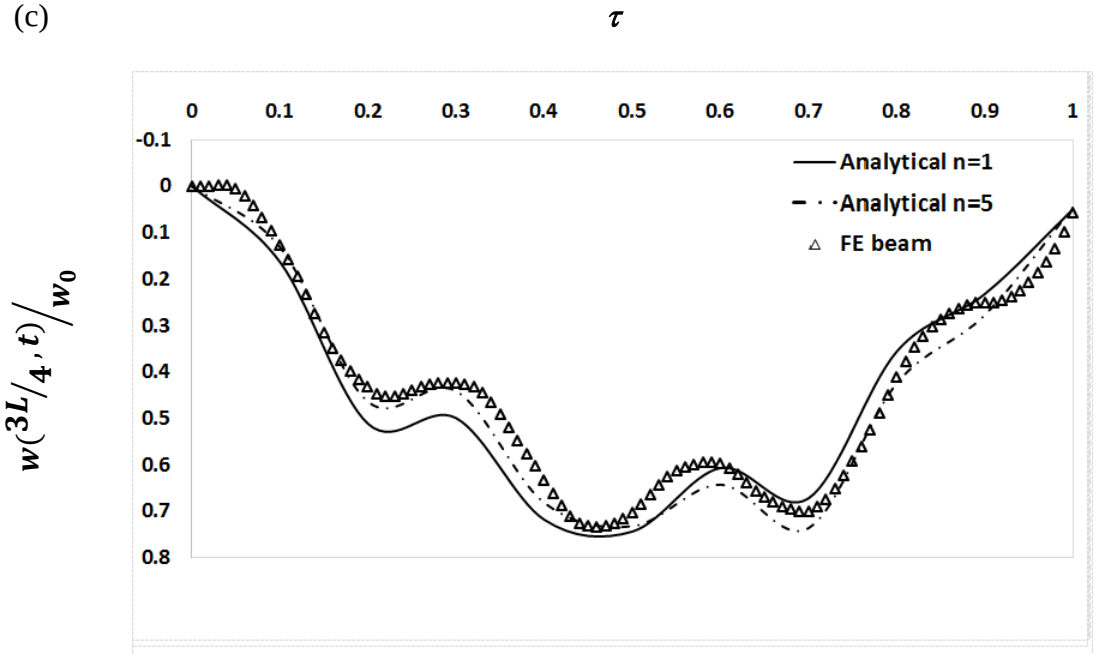

(d)

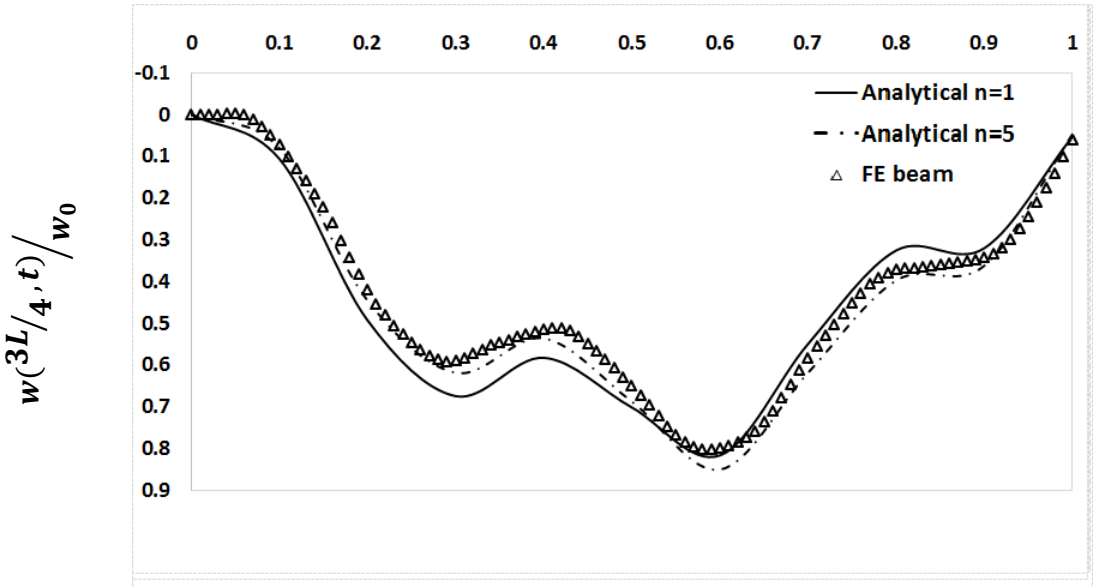

Figure 4.7 Normalized responses at the third quarter-point from starting end of SS EBB (x = 0.45 m): (a) v = 30 m/s, and (b) v = 40 m/s.

(e)

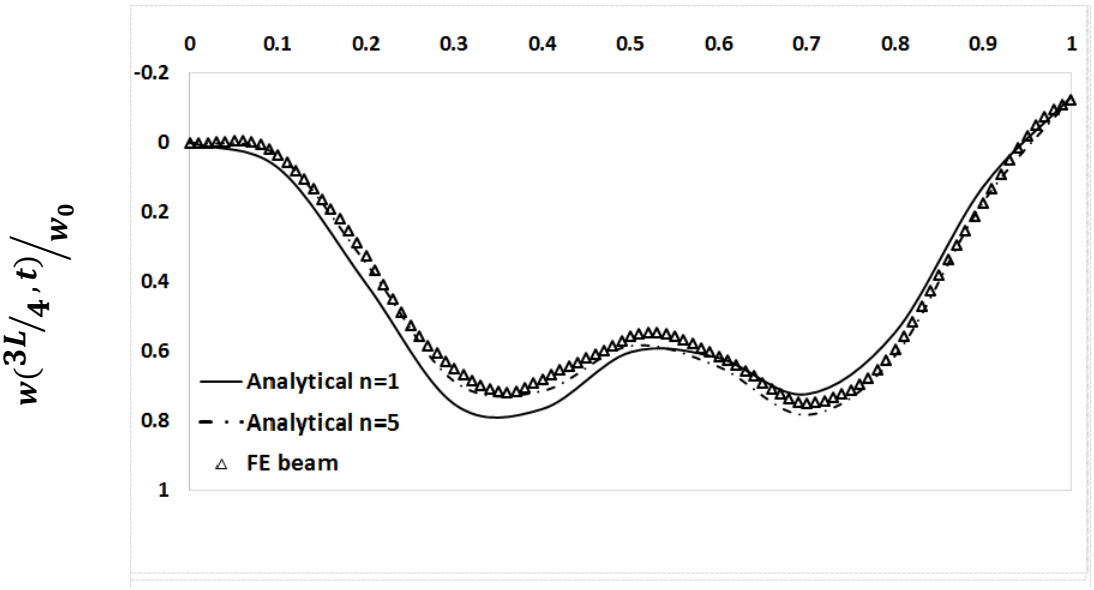

(f)

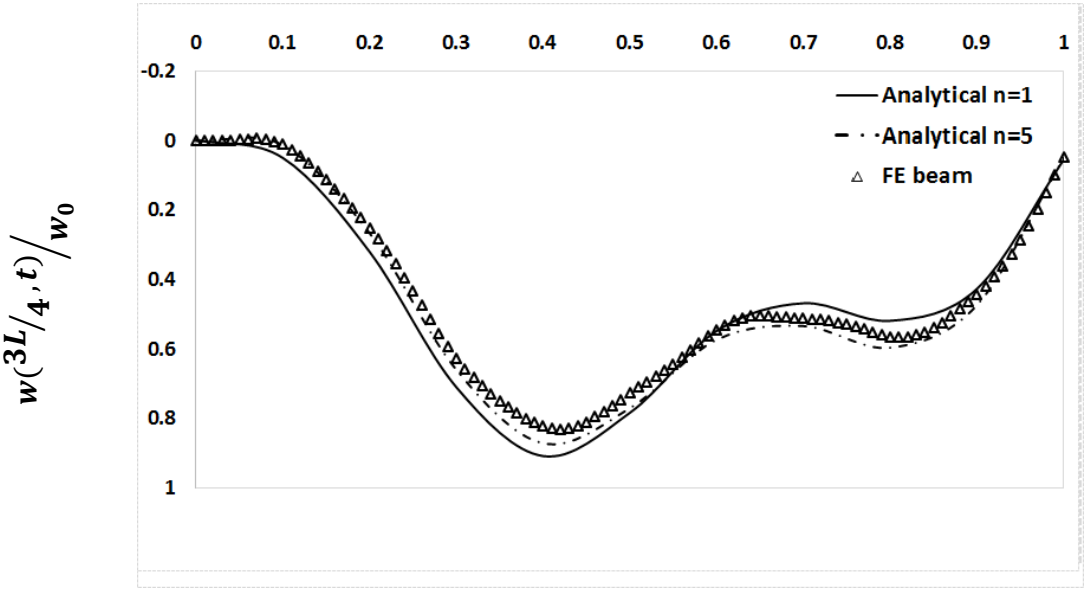

Figure 4.7 Normalized responses at the third quarter-point from starting end of SS EBB (x = 0.45 m): (a) v = 50 m/s, and (b) v = 60 m/s.

For the SS beam structure approximated by N EBB elements, the time is given by

$$t_i = \frac{L}{N}\left(\frac{i-1}{v} \right), \qquad (4.2),$$

where $i = 1, 2, 3, \ldots, N$.

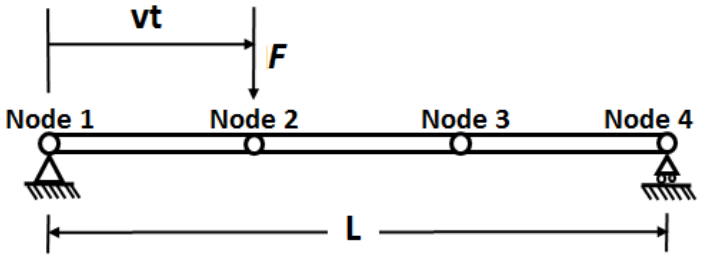

Figure 4.8 Three beam element representation of one SS beam structure.

The time and amplitude of the traveling point load for the 3 element case are included in Table 4.3. It includes the modifications of the starting node and ending node of the SS EBB FE model. In this table, the time and amplitude values under the nodal numbers are the time and force amplitudes applied at the nodes. Similarly, Table 4.4 provides the time and force amplitude values for the case of beam structure represented by *N* elements.

Table 4.3 Time and amplitude of traveling point load at Node 1 to Node 4.

	Node 1		Node 2			Node 3			Node 4	
Time	0	$\frac{L}{3v}$	0	$\frac{L}{3v}$	$\frac{2L}{3v}$	$\frac{L}{3v}$	$\frac{2L}{3v}$	$\frac{L}{v}$	$\frac{2L}{3v}$	$\frac{L}{v}$
Amplitude	1	0	0	1	0	0	1	0	0	1

Table 4.4 Time and amplitude for beam structure represented by *N* elements.

	Node 1		Node 2			Node n	
Time	t_1	t_2	$t_{i\ -1}$	t_i	t_{i+1}	$t_{n\ -1}$	t_n
Amplitude	1	0	0	1	0	0	1

Computed responses by the SS EBB FE model are included in Figures 4.5 through 4.7 for direct comparison to those of the analytical EBB solutions. It should be pointed out that the FE EBB results and those by the analytical EBB solutions are very close to each other.

4.2.2 Computed Results of 3D FE model with Traveling Point Load

In this sub-section, the time and force amplitude values considered in the last sub-section are applied to the 3D FE model. Thus, Table 4.4 is applied to the path of traveling vertical force along the (X_1, Y_1, Z_1) to (X_N, Y_N, Z_N) straight line. In the present case, it is (0, 0, 0) to (0.6, 0, 0), where the unit is in m. That is, (0, 0, 0) is the starting node and (0.6, 0, 0) is the ending node (See, Figure 4.9). To provide a more realistic representation of the wheel-rail interaction problem, friction is included in the present FE model. The friction force is considered to be equal to the product of the normal or vertical point load and the kinematic coefficient of friction, $\mu = 0.3$ in the present investigation. In the most general mathematical model for friction force it is considered as Coulomb friction and therefore it is represented by the signum function such that

$$sgn(\dot{x}) = \begin{cases} -1, & \dot{x} < 0 \\ 0, & \dot{x} = 0 \\ +1, & 0 < \dot{x} \end{cases} \tag{4.3}$$

The signum function is illustrated in Figure 4.10. Computationally it is difficult to operate on this function as it has a discontinuity at $\dot{x} = 0$. Therefore, it is generally approximated as that shown in Figure 4.11. This approximation is known as regularization. The computed responses applying the 3D solid element model are plotted in Figures 4.12 through 4.14.

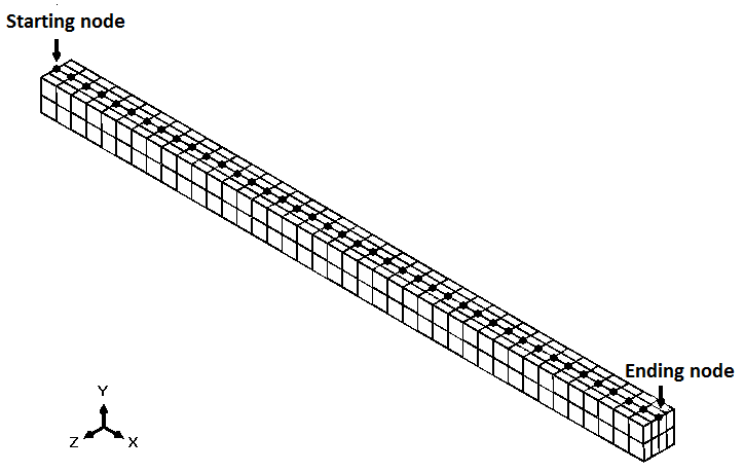

Figure 4.9 Finite element 3D model for traveling point load.

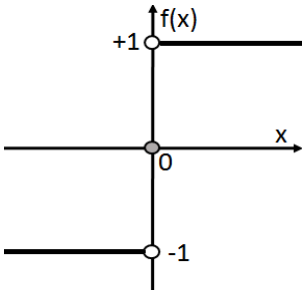

Figure 4.10 Signum function f(x).

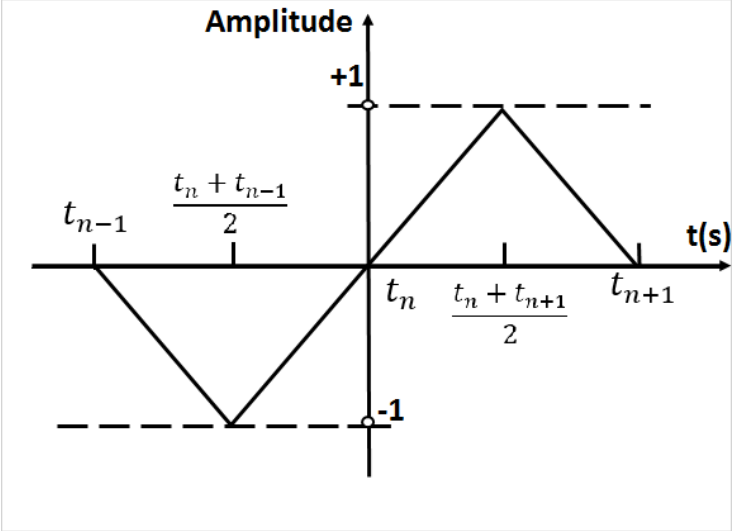

Figure 4.11 Regularization of signum function in discrete time steps.

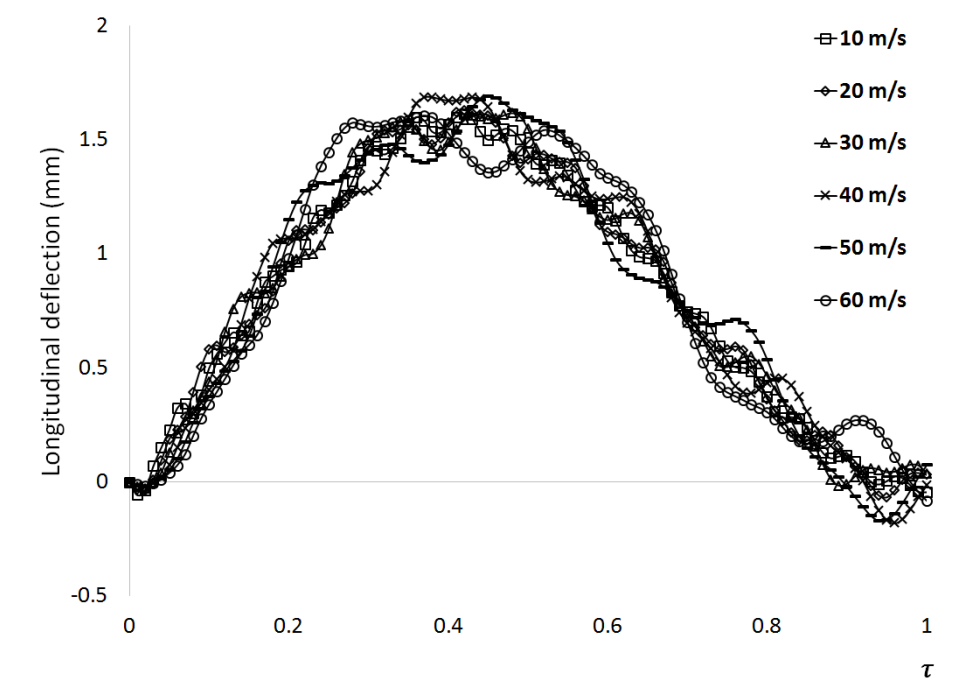

Figure 4.12(a) Longitudinal responses at quarter-point from starting node.

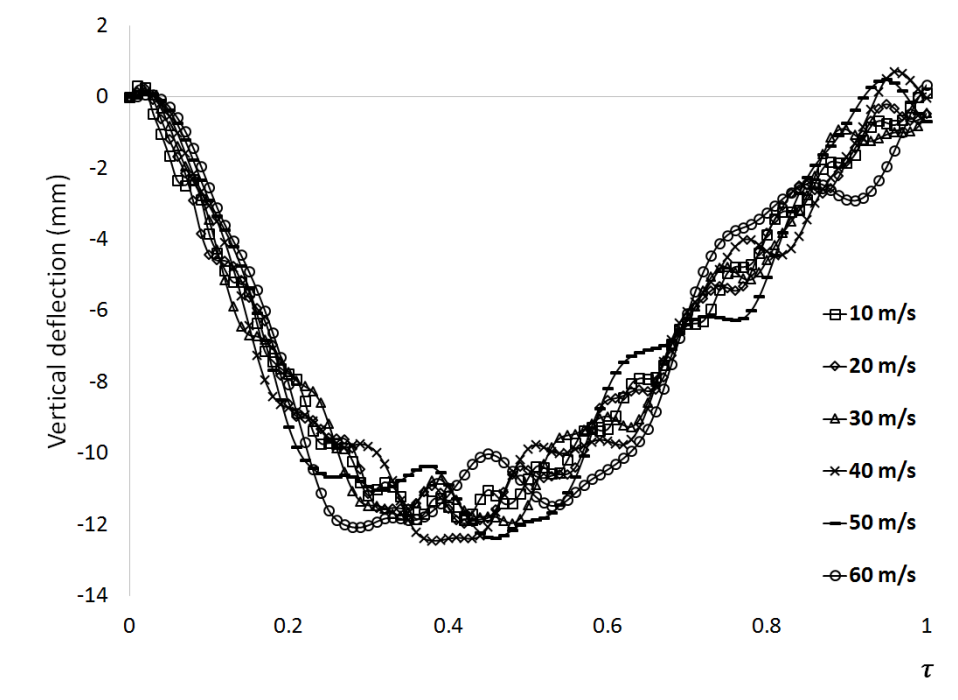

Figure 4.12(b) Vertical responses at quarter-point from starting node.

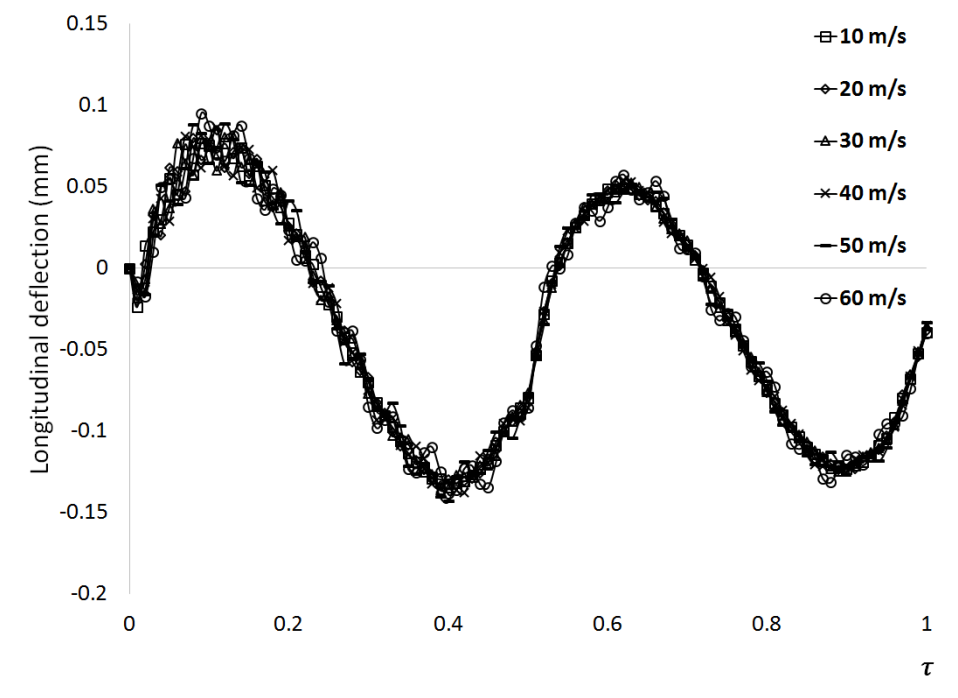

Figure 4.13(a) Longitudinal responses at middle span..

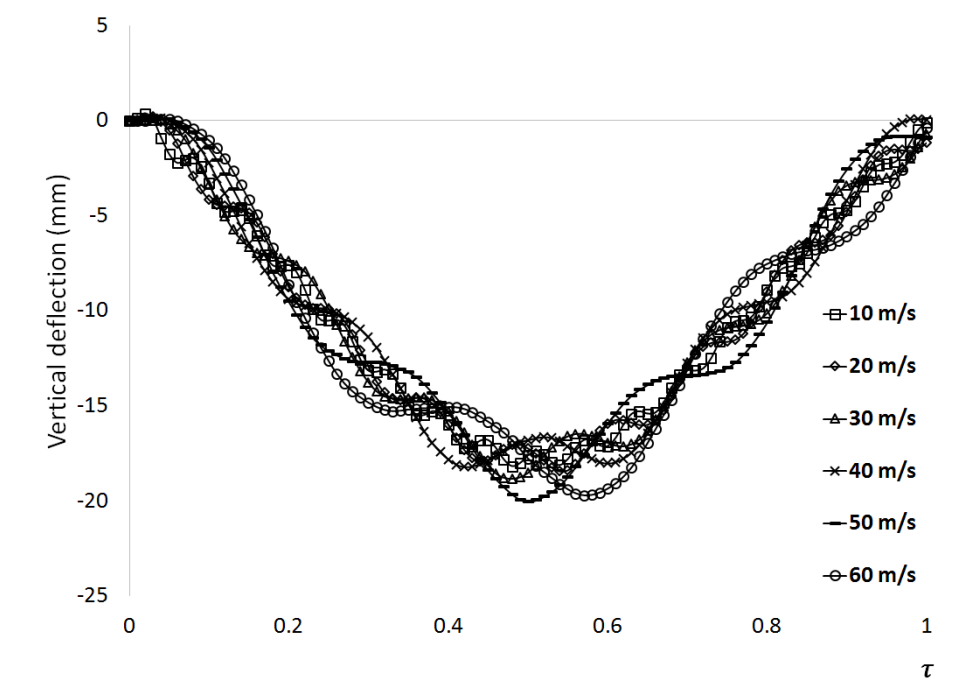

Figure 4.13(b) Vertical responses at middle span.

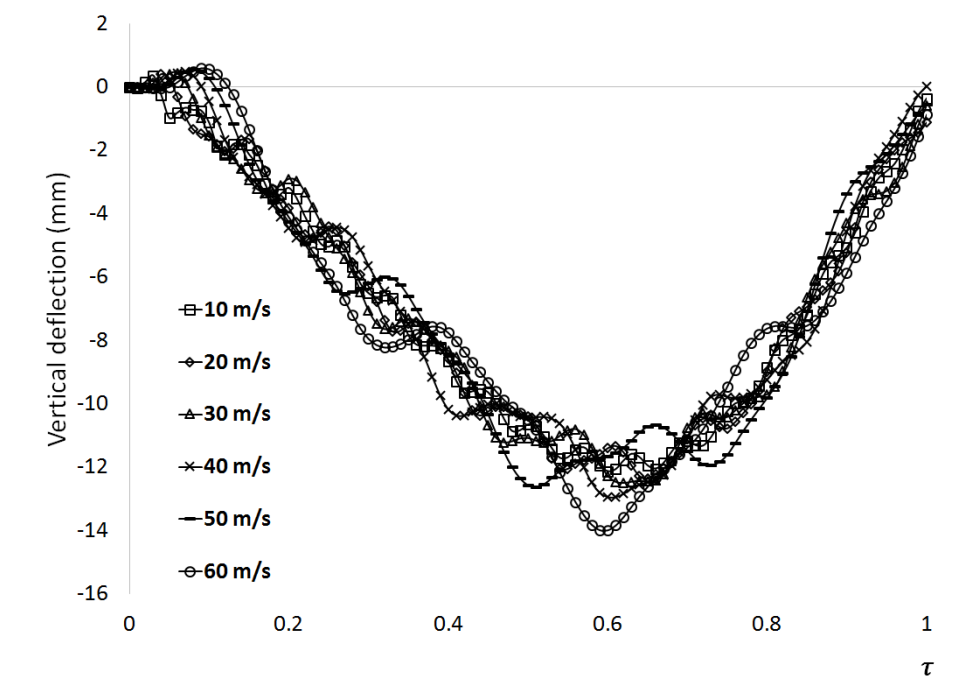

Figure 4.14(a) Longitudinal responses at quarter-point from ending node

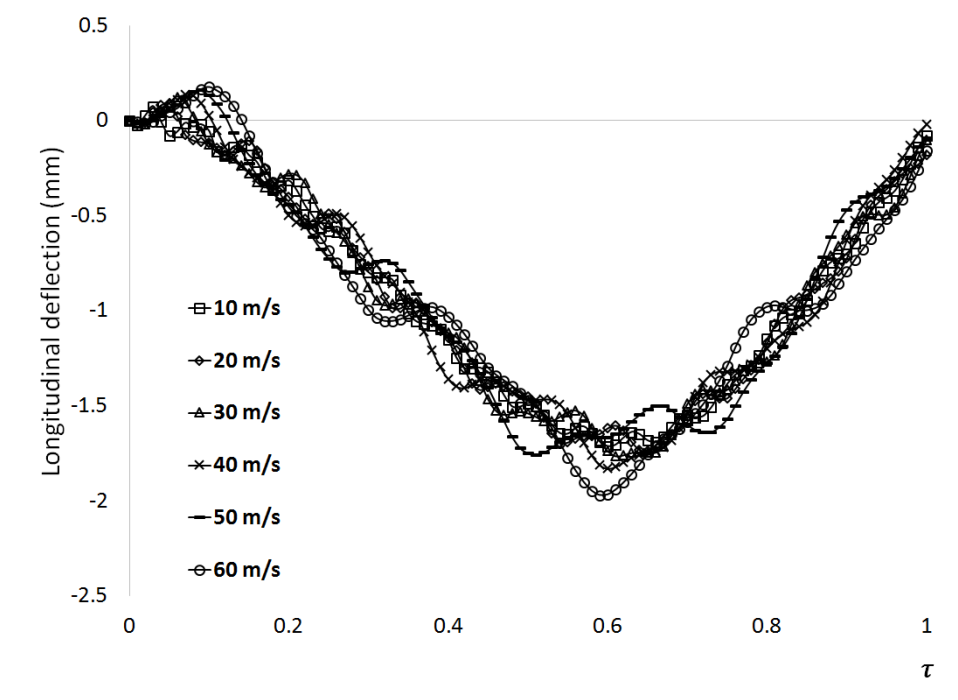

Figure 4.14(b) Vertical responses at quarter-point from ending node

4.2.3 Discussion

Computed results of deflection on FE SS EBB shows quite closed to analytical results. In addition, when the analytical results include more natural frequency into Equation 2.23, the results are more closed to FE SS EBB. It gives strong verification of the method of modeling traveling point load is correct. In 3D FE model, it does not show the different shapes due to various velocities obviously. The problem of this case is owing to input velocities which are much smaller than critical velocity. The relation between input velocity and critical velocity is defined as α which is presented in Equation 2.25. By using the analytical solution of SS EBB, the critical velocity is up to 235 m/s in this case. α in these cases are very small which is 0.04, 0.085, 0.12, 0.17, 0.21 and 0.25 with respect to 10 m/s to 60 m/s.

4.3 COMPUTED RESULTS OF 3D FE RAIL MODEL WITH TRAVELING POINT LOAD

With the traveling point load in foregoing, it presents the traveling point load on 3D FE rail model. In order understanding the responses of rail wheel-rail model. Here, the traveling point load is based on a real case which is 100kN for vertical force and with the friction force 30kN.

4.3.1 Comparison of 3D FE Rail with Traveling Point Load Model and 3D FE Wheel-Rail Model

In the traveling point load (TPL) case considered in Sub-section 4.2.2 above the TPL path is along the central line, as indicated in Figure 4.9. Since in practice, the contact is not at a point but rather a small area and therefore more TPL paths are required in the computation. For simplicity and symmetry, therefore three TPL paths along the global *X*-axis are chosen in the present studies. These paths with the nodal DOF indicated in small red integers and partial wheel and rail are shown in Figures 4.15 in which the first, second, and third paths are shown in Figures 4.15(a), 4.15(b), and 4.15(c), respectively.

(a)

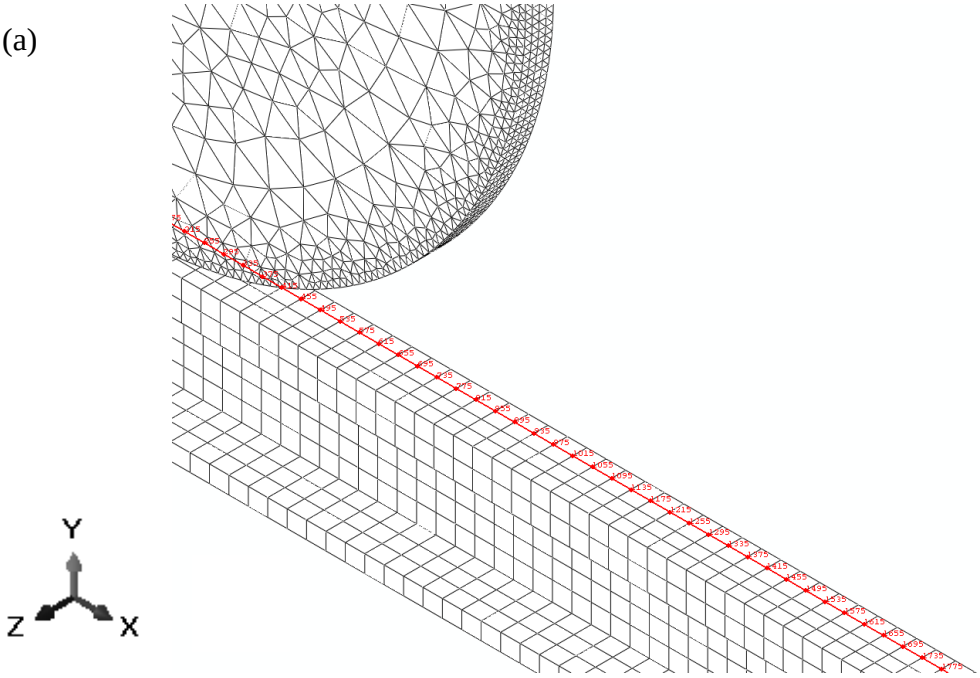

(b)

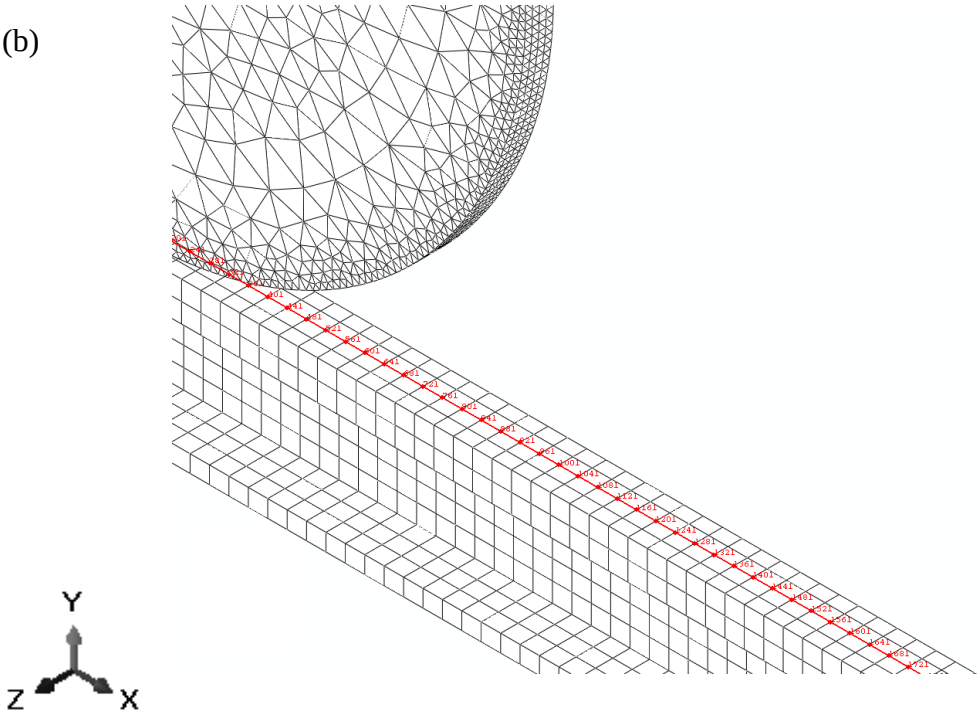

(c)

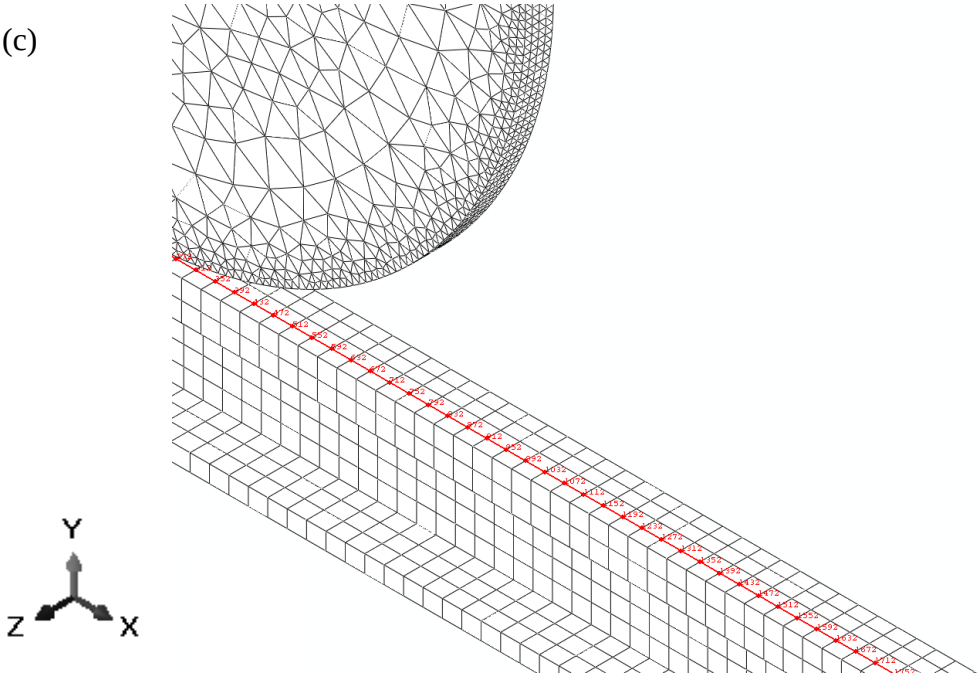

Figure 4.15 Wheel and rail contact paths: (a) Path 1, (b) Path 2, and (c) Path 3.

As mentioned in Chapter 3, in the 3D FE wheel-rail model, there are two main steps in the computation process. The first step is for pre-loading the wheel and inputting the forces. The second step is for the wheel to start rotating and moving along the rail. The time for the first step is 1.0 ms and the time for the second step is based on the speed of wheel such that the time in the present case is $\frac{4.0\ m}{v\ (m/s)}$ since the entire length of the present wheel-rail model is 4.2 m. Representative computed results are selected from the 9 points shown in Figure 4.16. The first 3 points (Points 1, 2, and 3) correspond to the quarter, middle, and third quarter distances from the starting end of the second span. Points 4, 5, and 6 correspond to the quarter, middle, and third quarter distances from the starting end of the third span while Points 7, 8, and 9 correspond to those of the fourth

span. Note that in the present model the rail was divided into 5 equal spans as illustrated in Figures 3.2 and 3.3. Since the corresponding results along Paths 1 and 3 are close to those of Path 2, as shown in Figures 4.17 and 4.18, and to reduce the amount of computed data only those along Path 2. The velocity of 3D FE wheel-rail mode and 3D FE rail model shown in Figure 4.17 and 4.18 is 10 m/s.

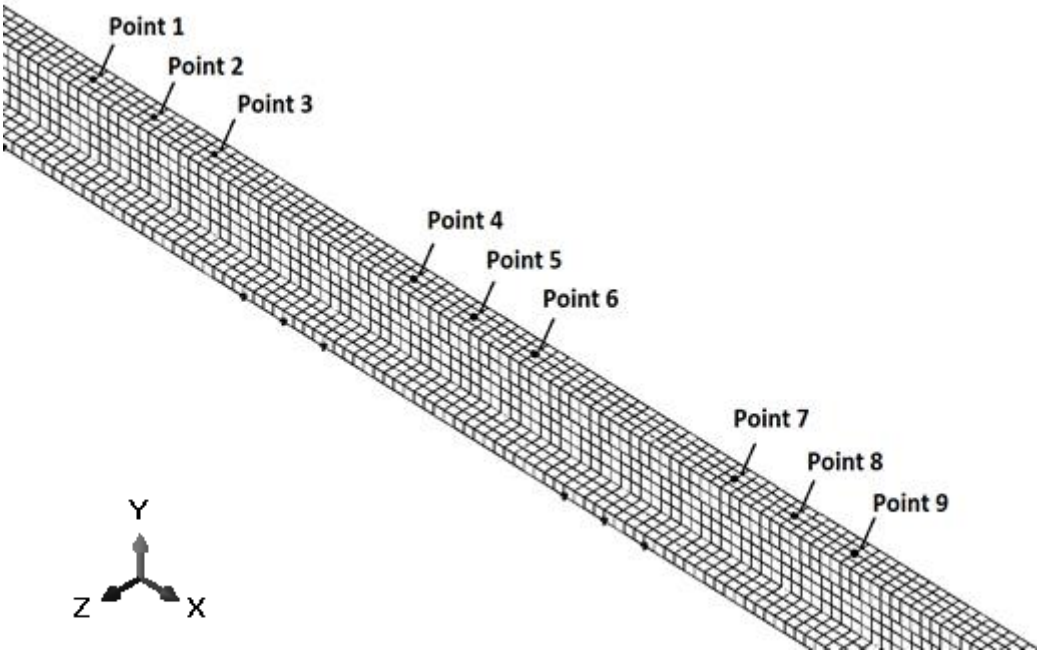

Figure 4.16 Locations of 9 selected points.

The computed results for the 3D FE wheel-rail model, denoted by “WRM”, and those of the 3D FE rail with TPL model, denoted by TPL, are plotted in Figures 4.19 through 4.24. For brevity, only computed results at Points 4, 5, and 6 are included.

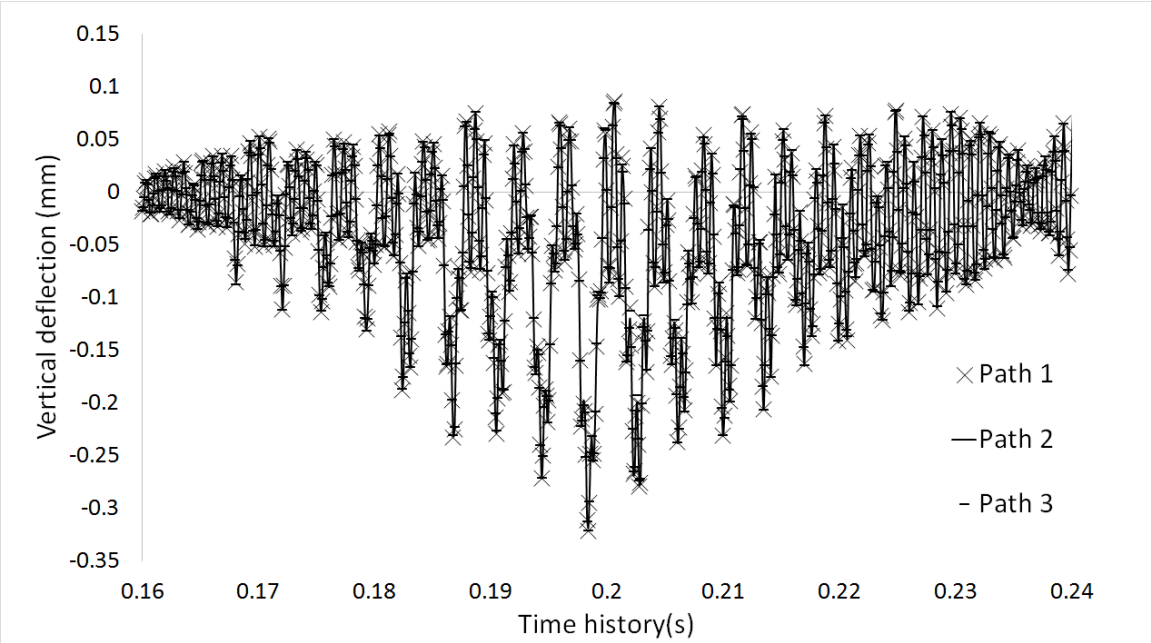

Figure 4.17 Vertical deflections of 3D FE wheel-rail model.

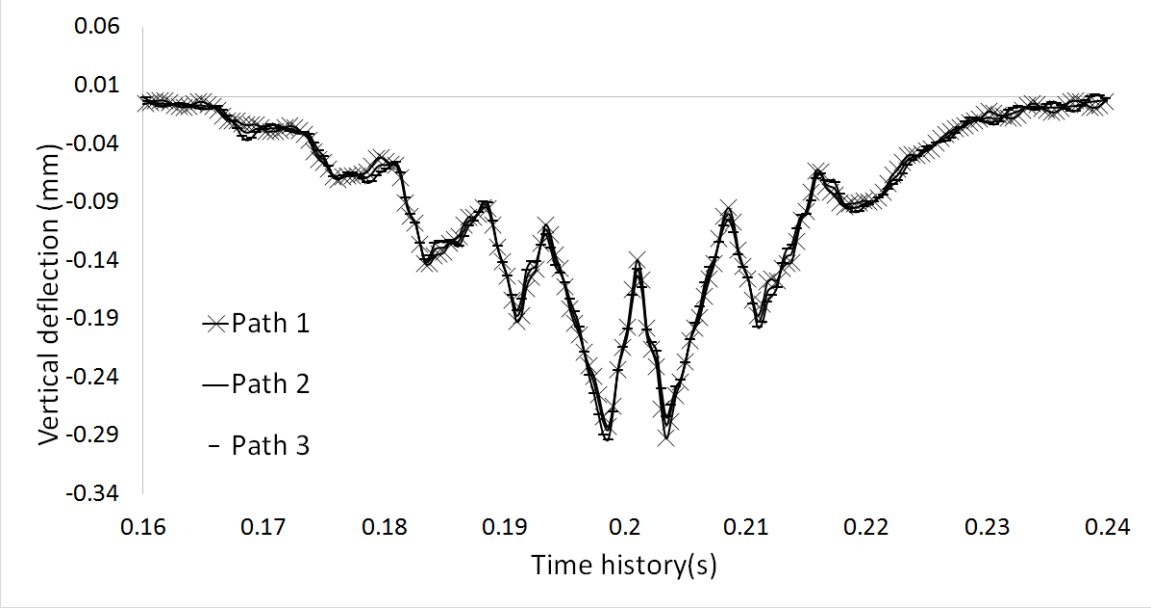

Figure 4.18 Vertical deflections 3D FE rail model with TPL.

(a)

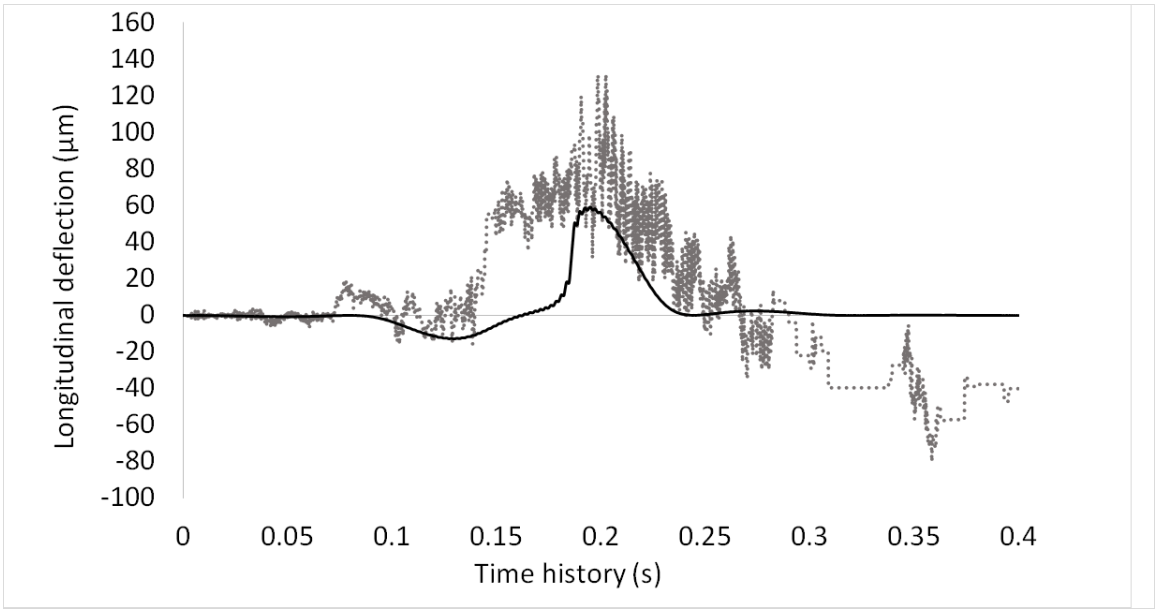

(b)

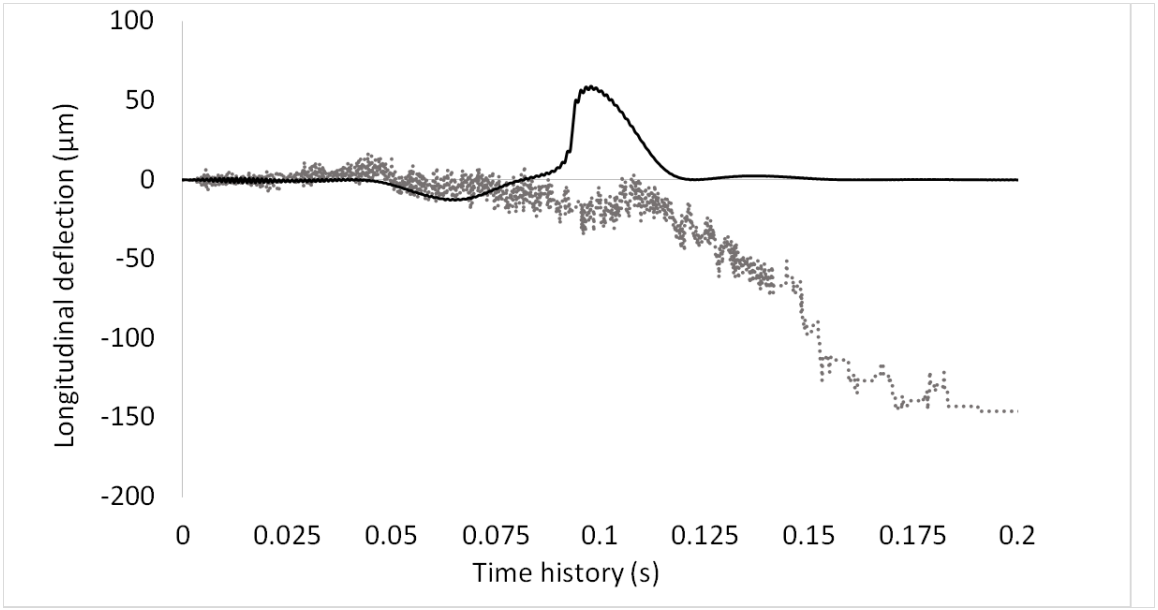

Figure 4.19 Longitudinal deflection at Point 4: —, TPL; …, WRM; (a) $v = 10\ \frac{m}{s}$, and (b) $v = 20\ \frac{m}{s}$.

(c)

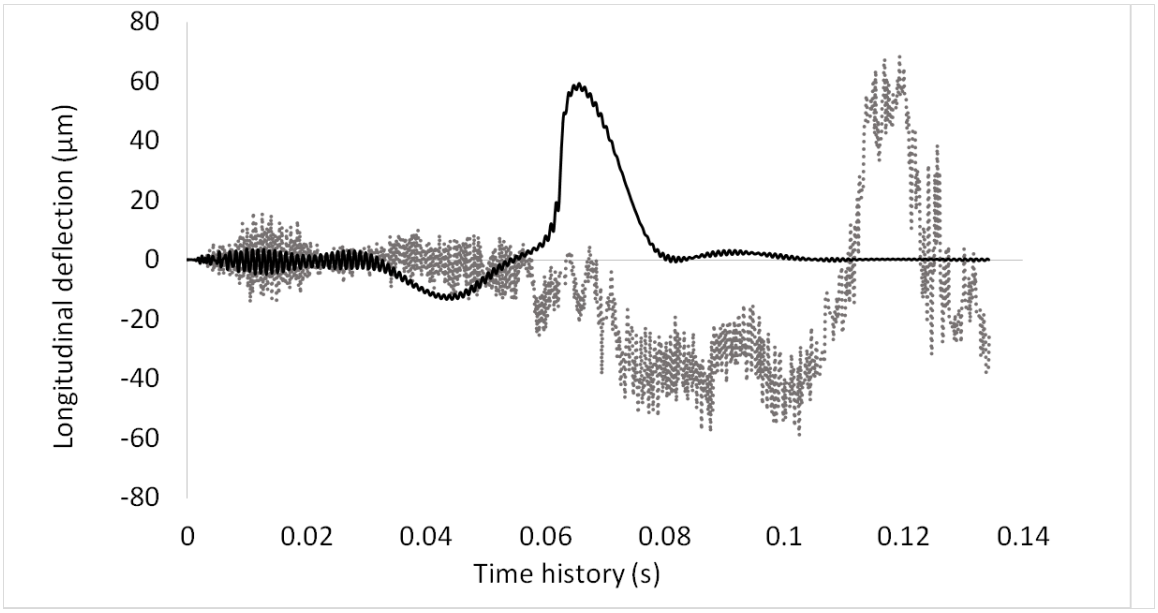

(d)

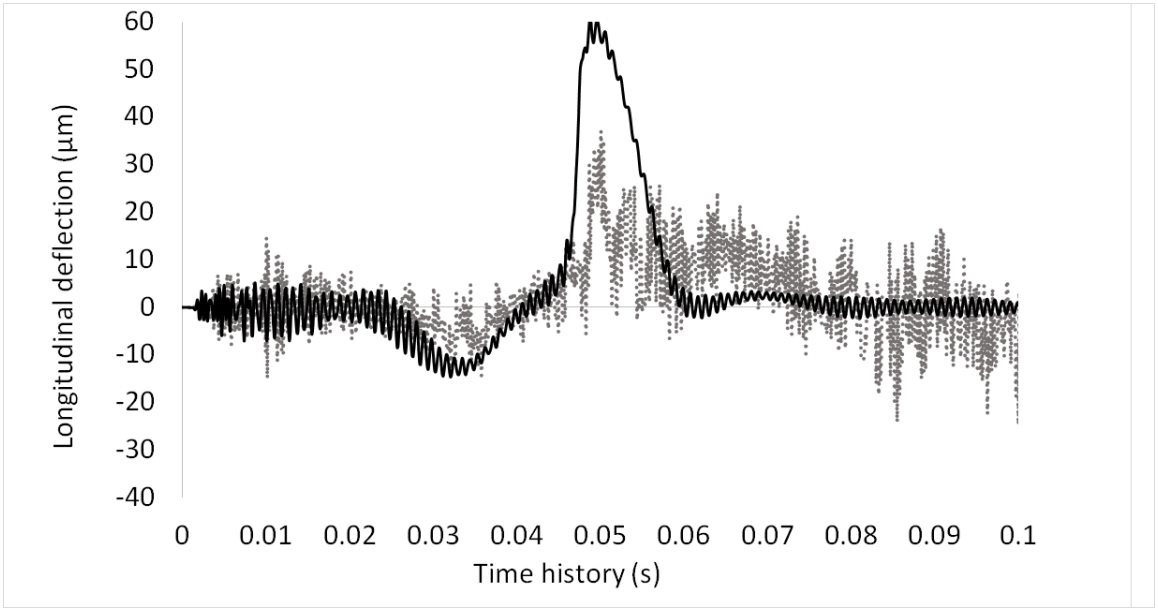

Figure 4.19 Longitudinal deflection at Point 4: —, TPL; …, WRM; (c) $v = 30 \ \frac{m}{s}$, and (d) $v = 40 \ \frac{m}{s}$.

(e)

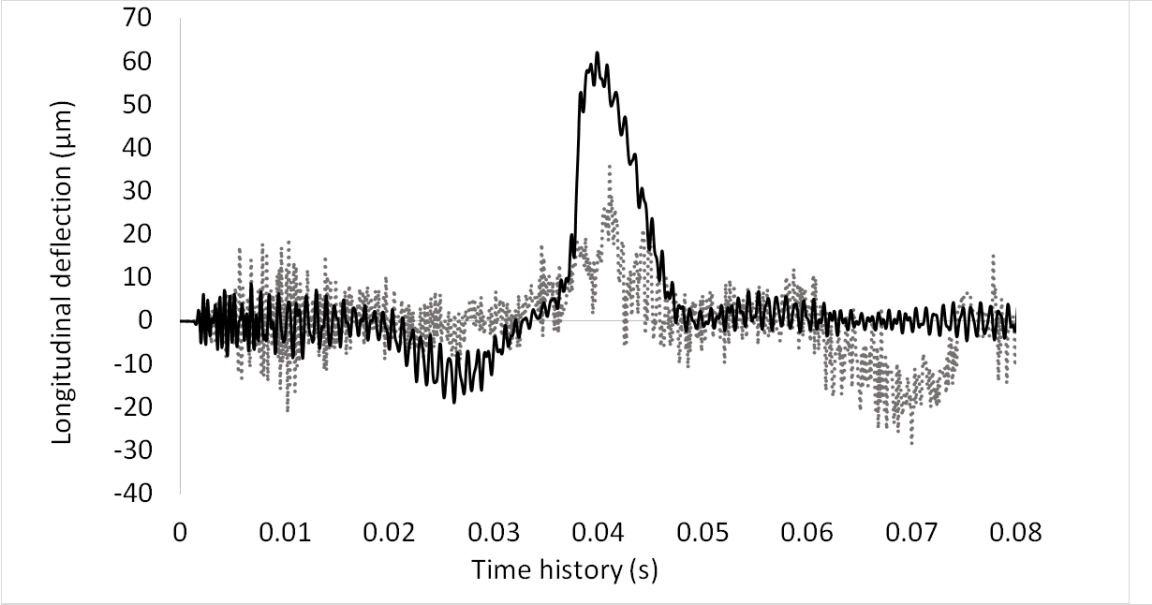

(f)

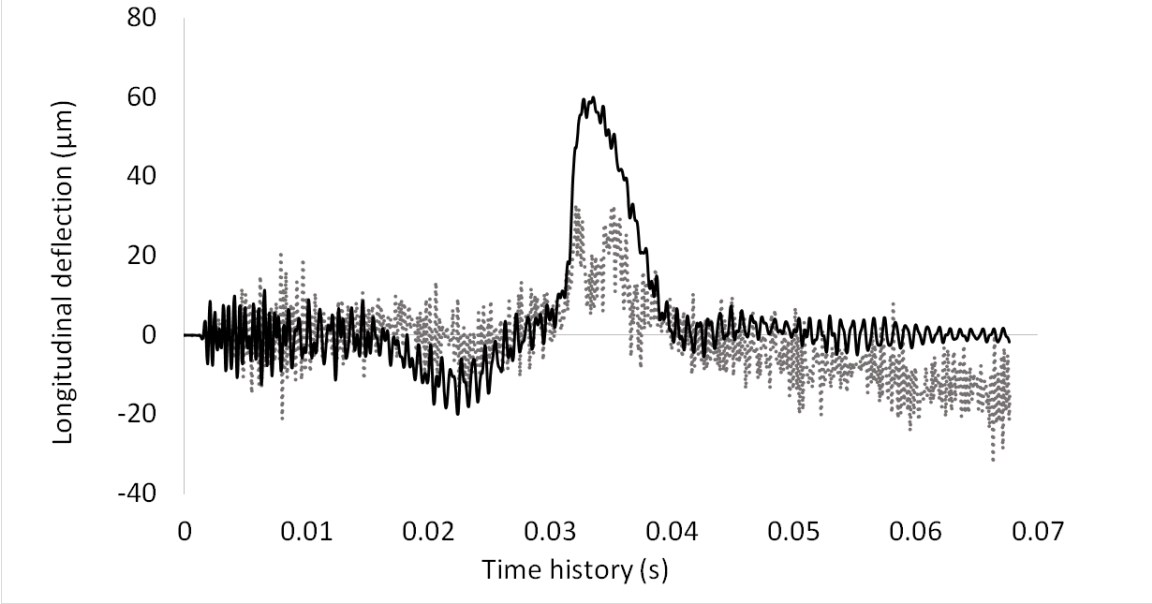

Figure 4.19 Longitudinal deflection at Point 4: —, TPL; …, WRM; (e) $v = 50 \ \frac{m}{s}$, and (f) $v = 60 \ \frac{m}{s}$.

(a)

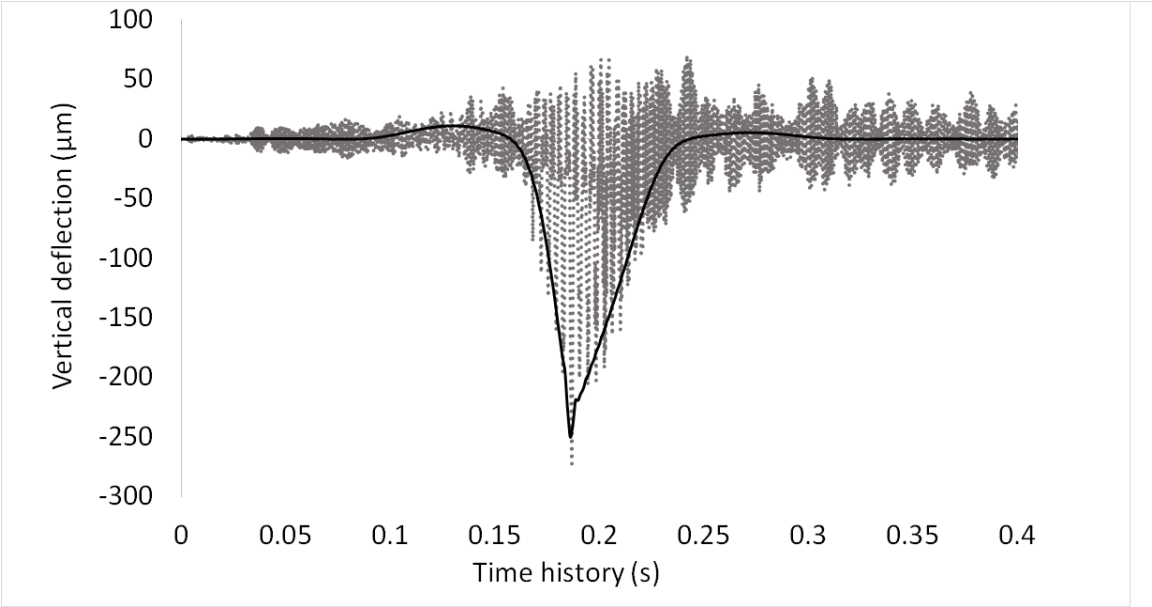

(b)

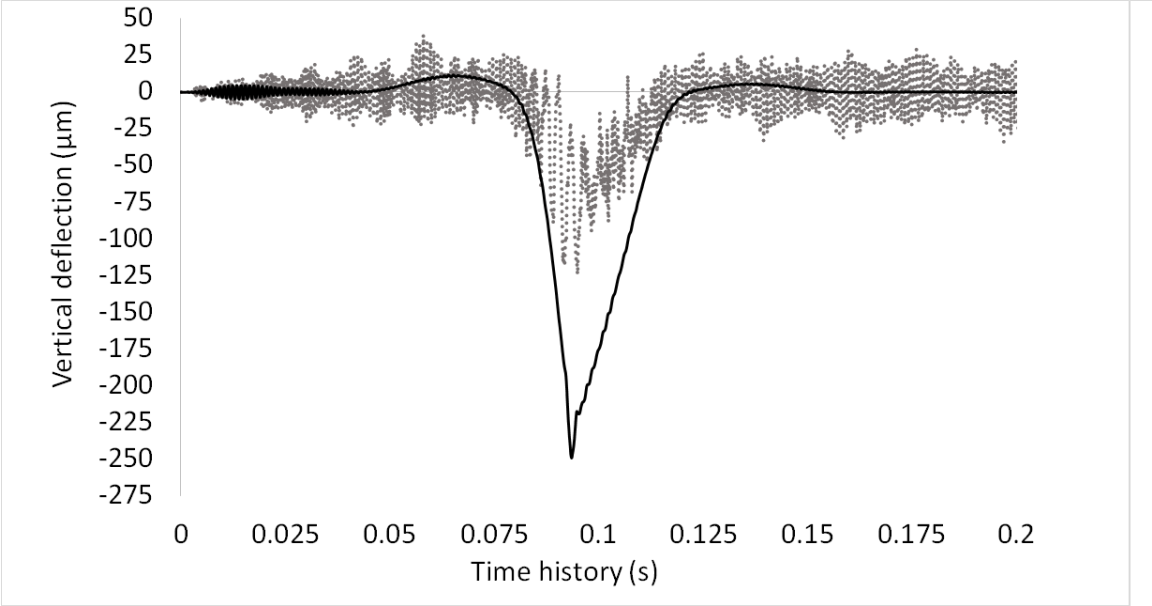

Figure 4.20 Vertical deflection at Point 4: —, TPL; …, WRM; (a) $v = 10\ \frac{m}{s}$, and (b) $v = 20\ \frac{m}{s}$.

(c)

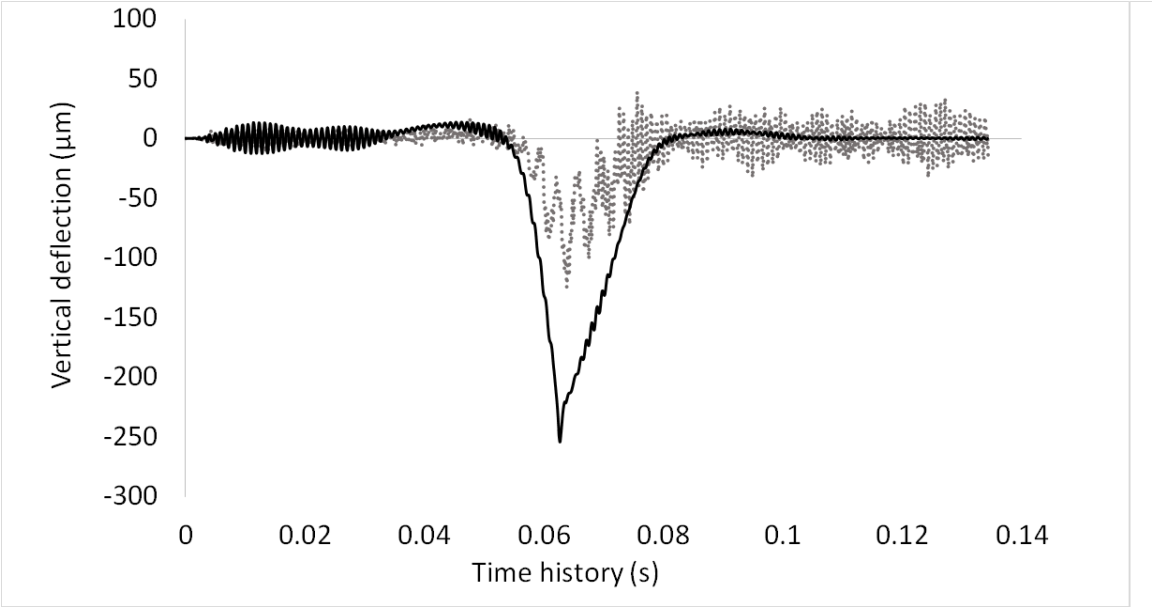

(d)

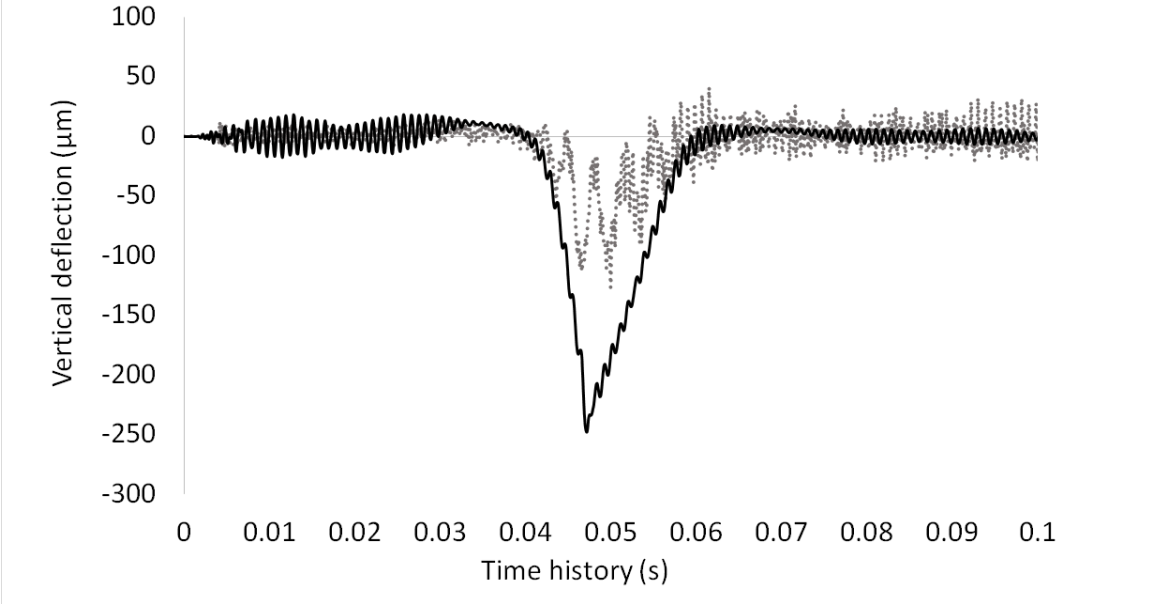

Figure 4.20 Vertical deflection at Point 4: —, TPL; …, WRM; (c) $v = 30\ \frac{m}{s}$, and (d) $v = 40\ \frac{m}{s}$.

(e)

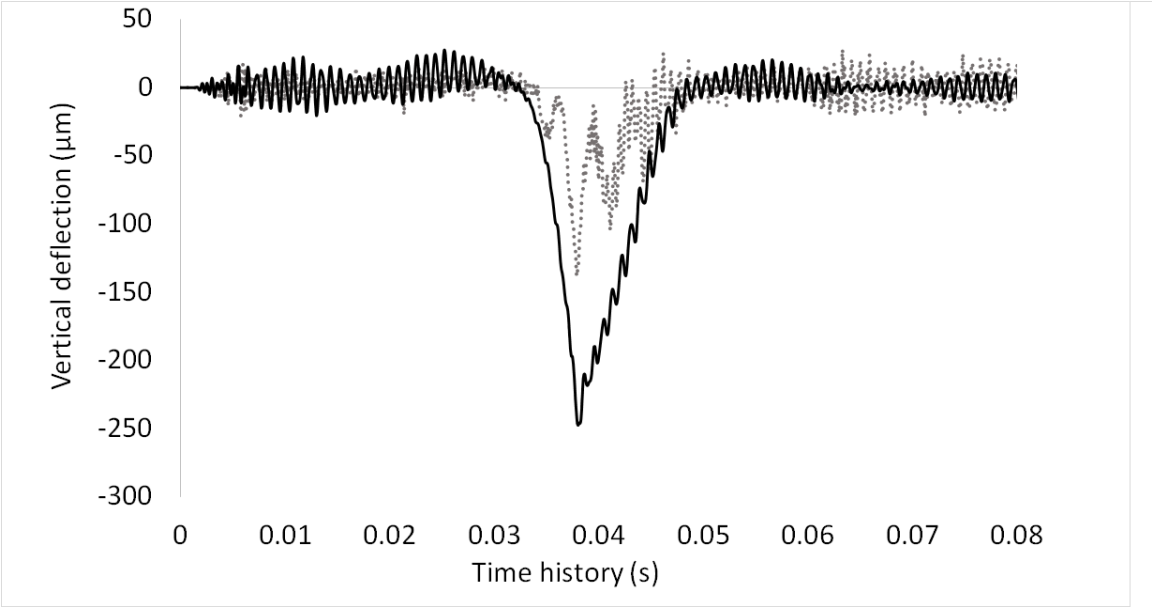

(f)

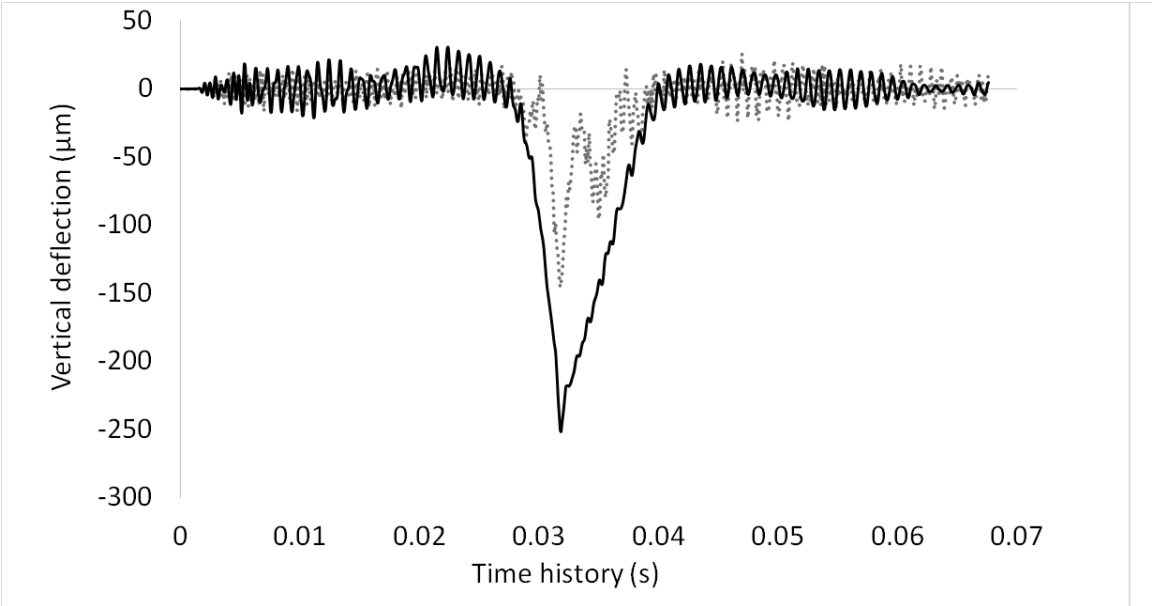

Figure 4.20 Vertical deflection at Point 4: —, TPL; …, WRM; (e) $v = 50 \ \frac{m}{s}$, and (f) $v = 60 \ \frac{m}{s}$.

(a)

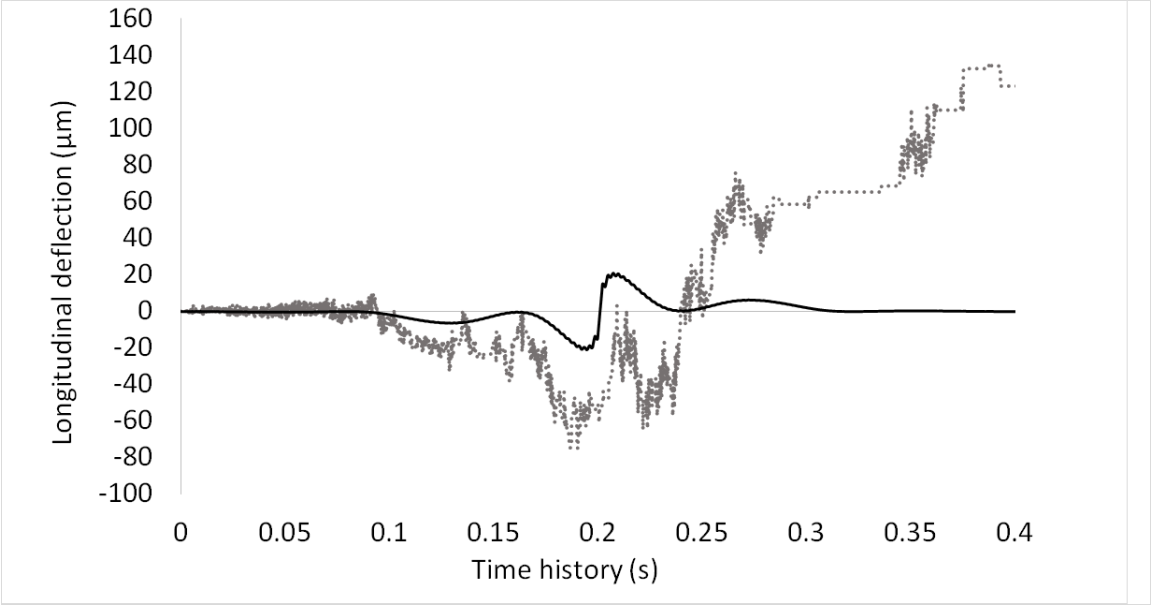

(b)

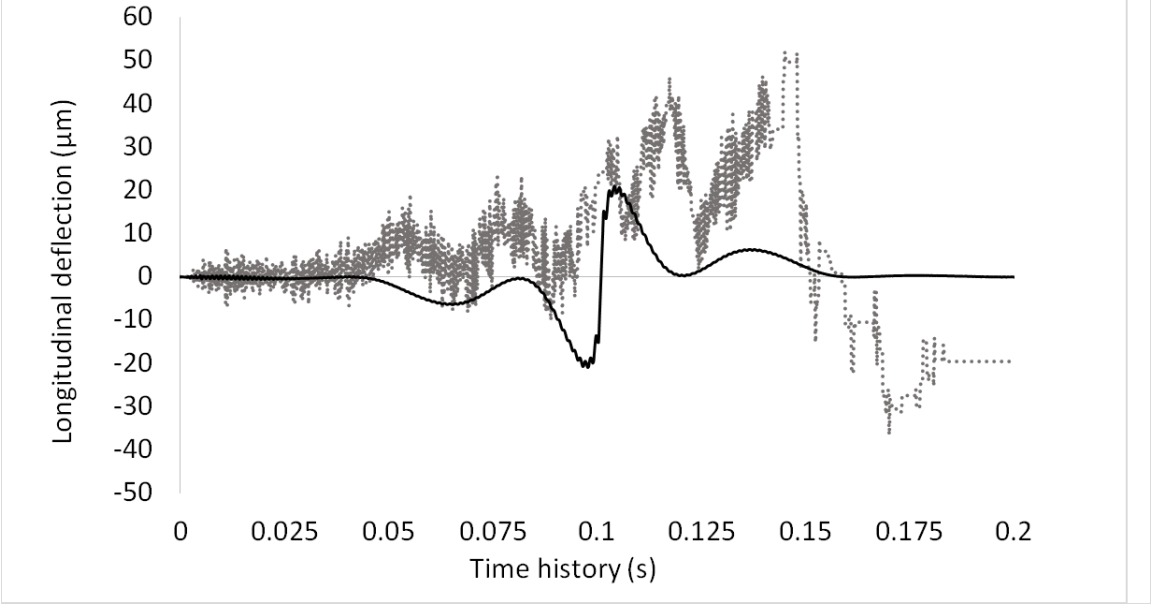

Figure 4.21 Longitudinal deflection at Point 5: —, TPL; …, WRM; (a) $v = 10\ \frac{m}{s}$, and (b) $v = 20\ \frac{m}{s}$.

(c)

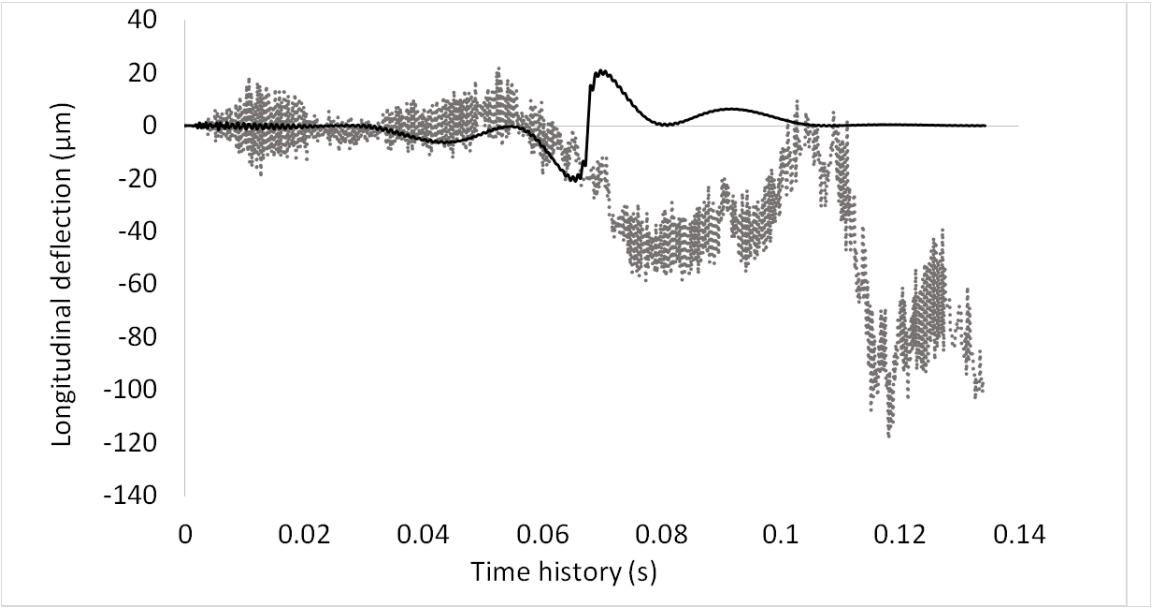

(d)

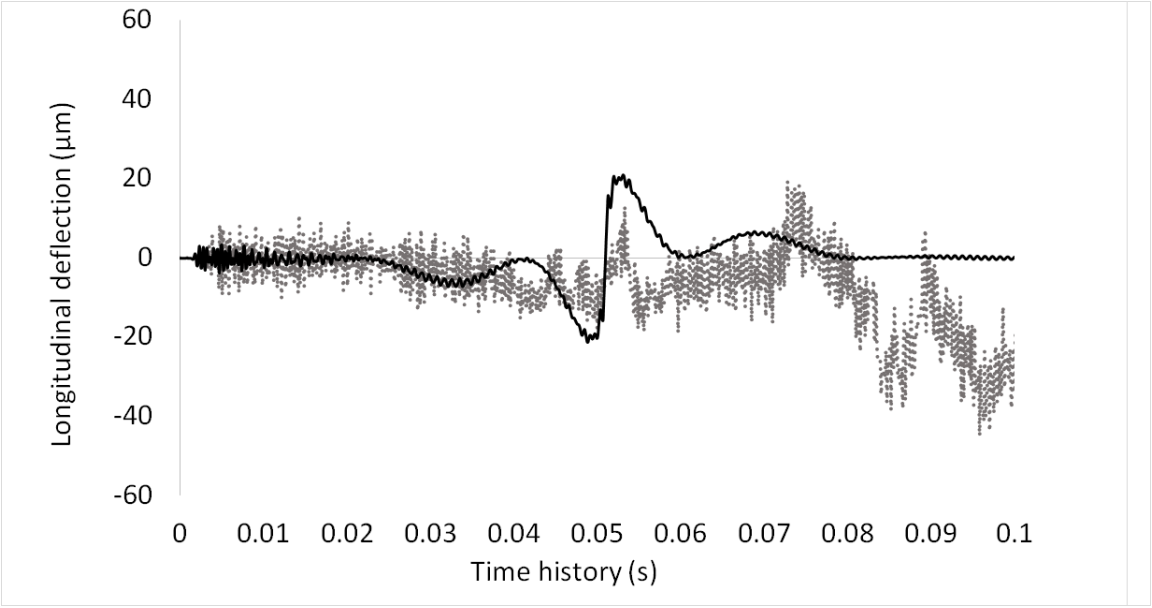

Figure 4.21 Longitudinal deflection at Point 5: —, TPL; …, WRM; (c) $v = 30\ \frac{m}{s}$, and (d) $v = 40\ \frac{m}{s}$.

(e)

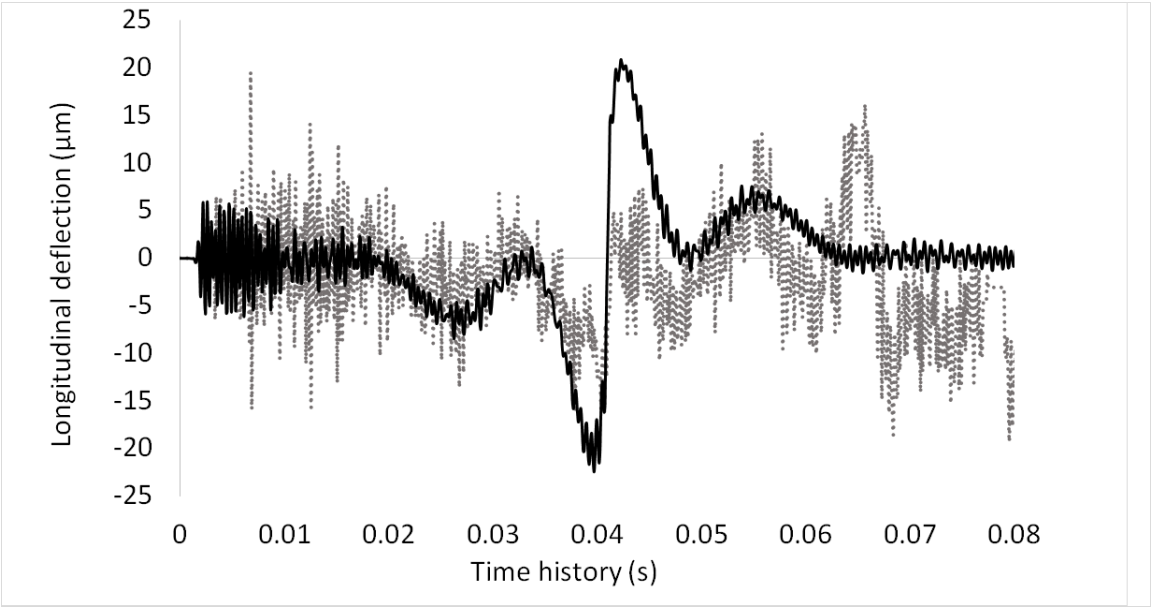

(f)

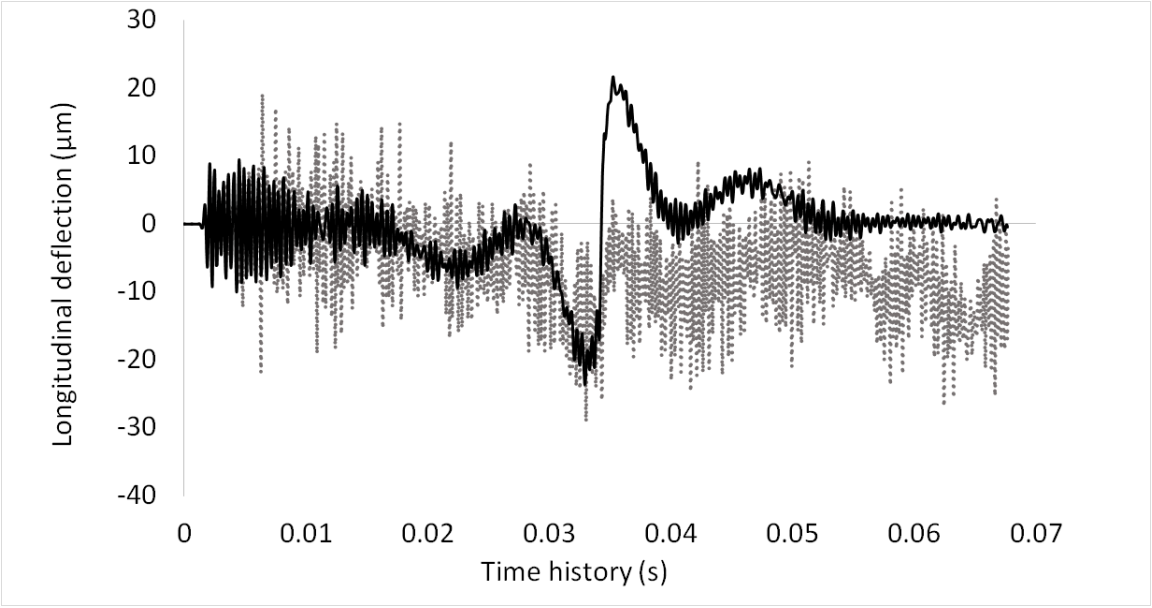

Figure 4.21 Longitudinal deflection at Point 5: —, TPL; …, WRM; (e) $v = 50\ \frac{m}{s}$, and (f) $v = 60\ \frac{m}{s}$.

(a)

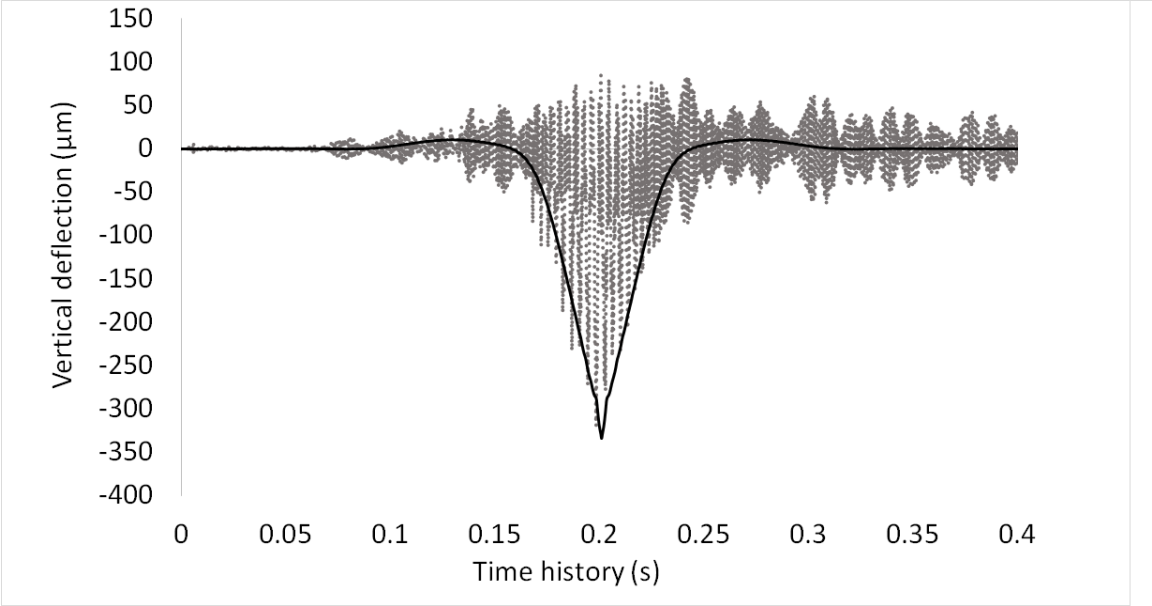

(b)

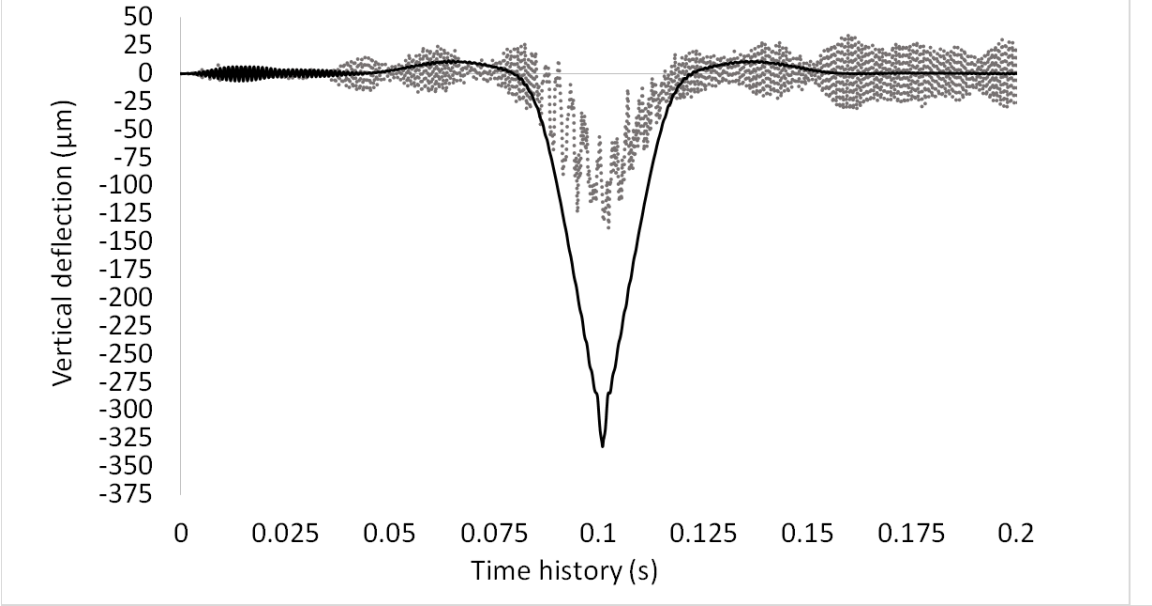

Figure 4.22 Vertical deflection at Point 5: —, TPL; …, WRM; (a) $v = 10\ \frac{m}{s}$, and (b) $v = 20\ \frac{m}{s}$.

(c)

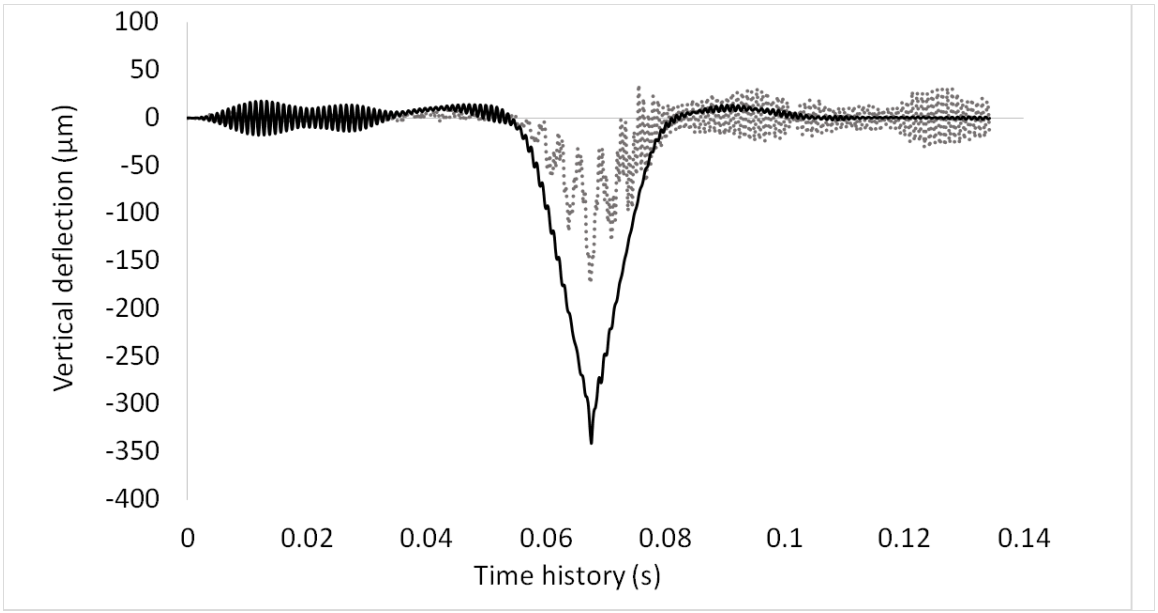

(d)

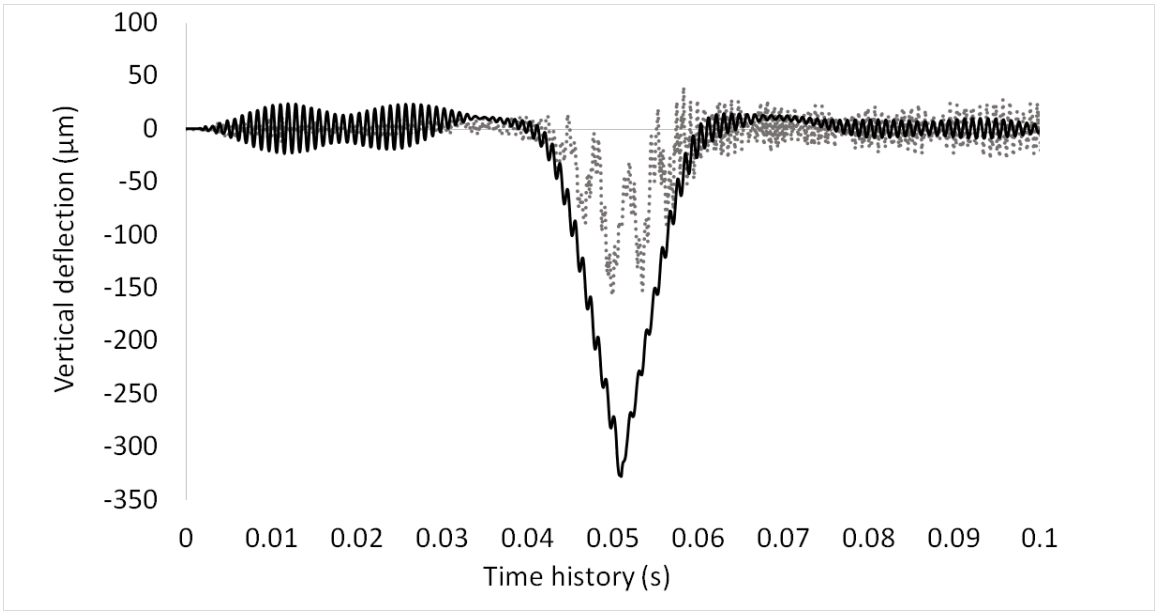

Figure 4.22 Vertical deflection at Point 5: —, TPL; …, WRM; (c) $v = 30 \ \frac{m}{s}$, and (d) $v = 40 \ \frac{m}{s}$.

(e)

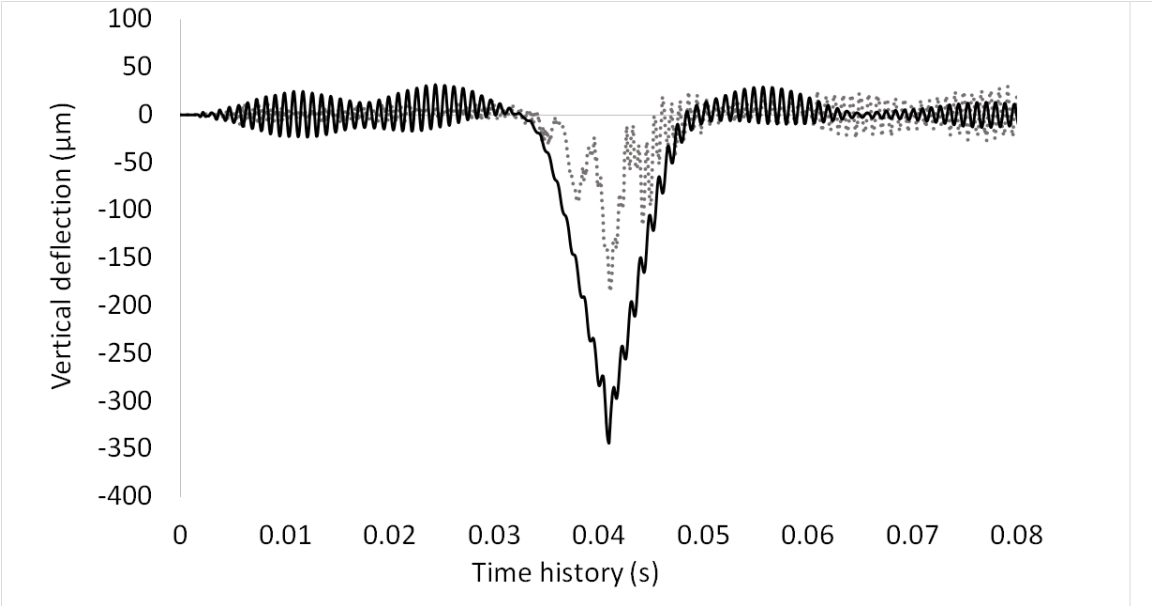

(f)

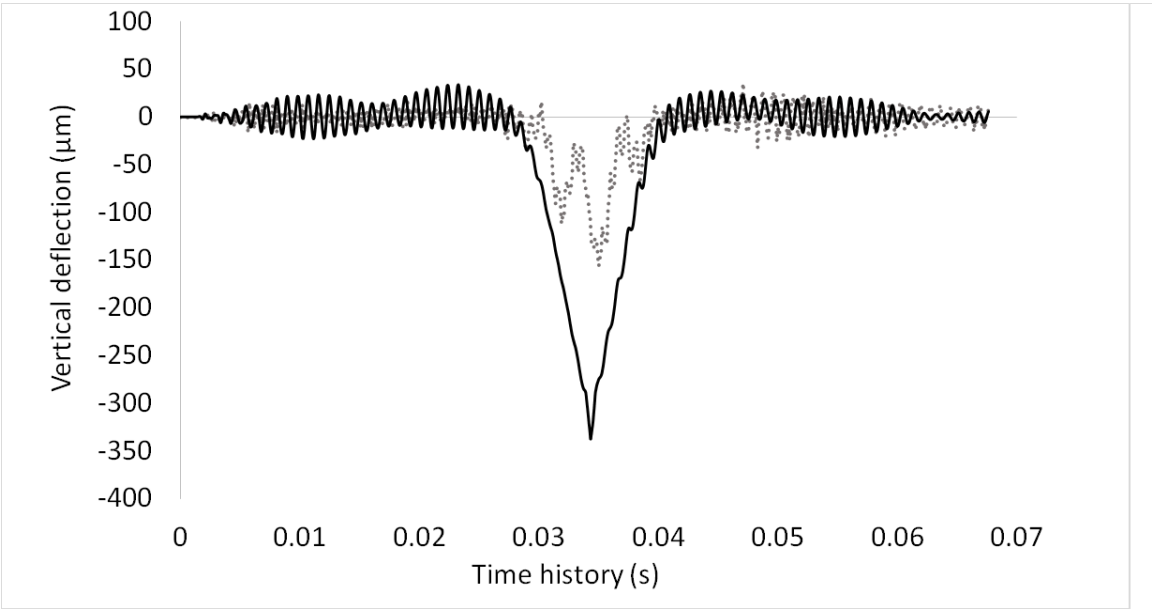

Figure 4.22 Vertical deflection at Point 5: —, TPL; …, WRM; (c) $v = 50 \ \frac{m}{s}$, and (d) $v = 60 \ \frac{m}{s}$.

(a)

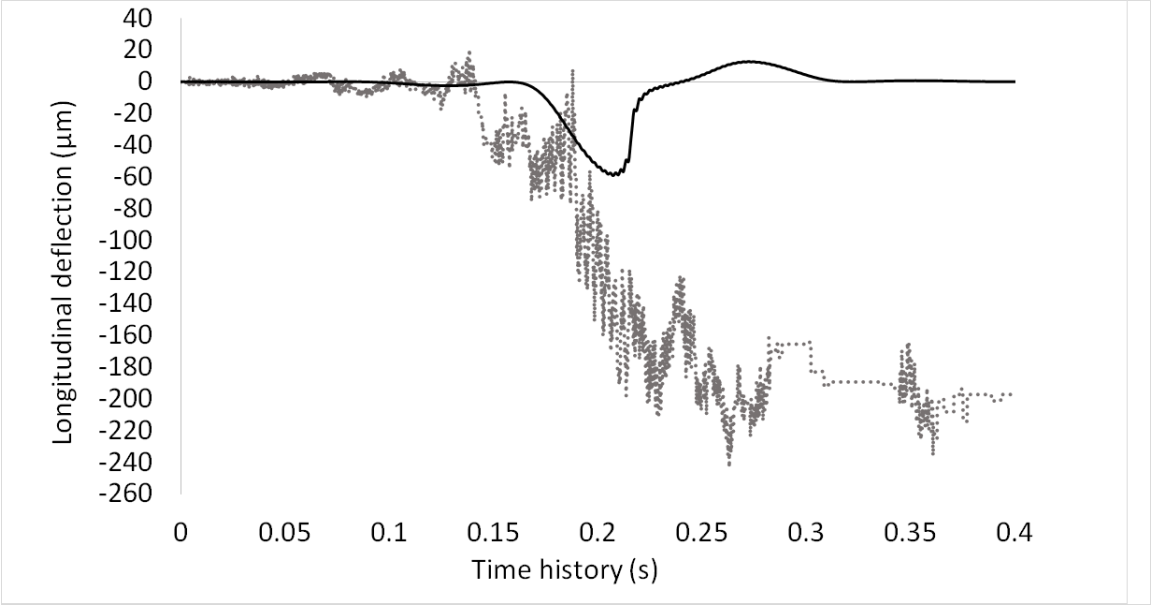

(b)

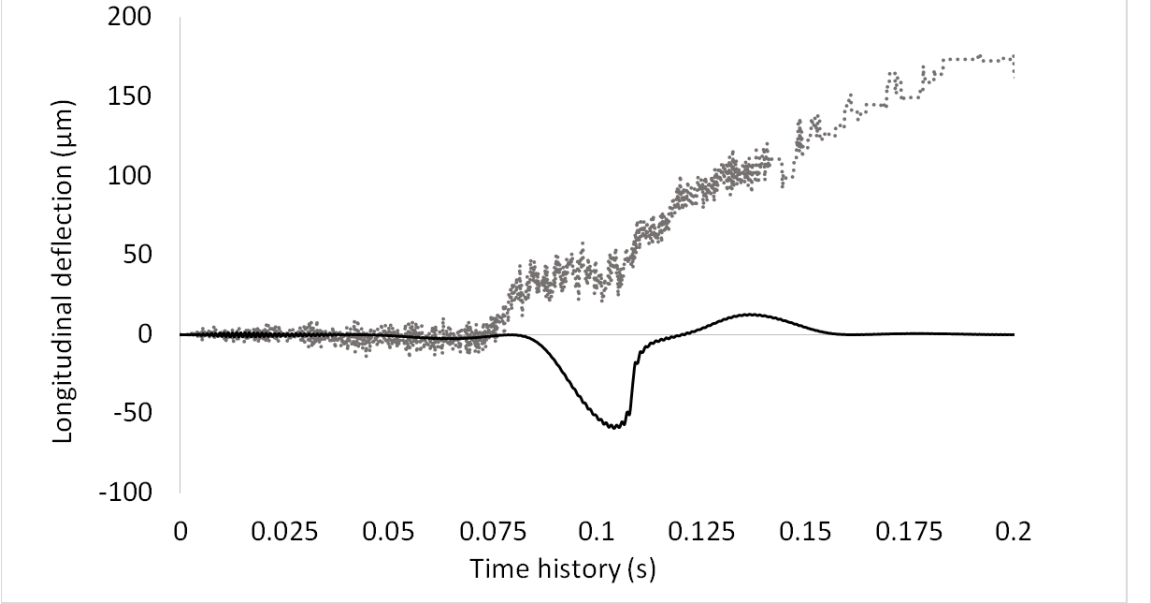

Figure 4.23 Longitudinal deflection at Point 6: —, TPL; …, WRM; (a) $v = 10\ \frac{m}{s}$, and (b) $v = 20\ \frac{m}{s}$.

(c)

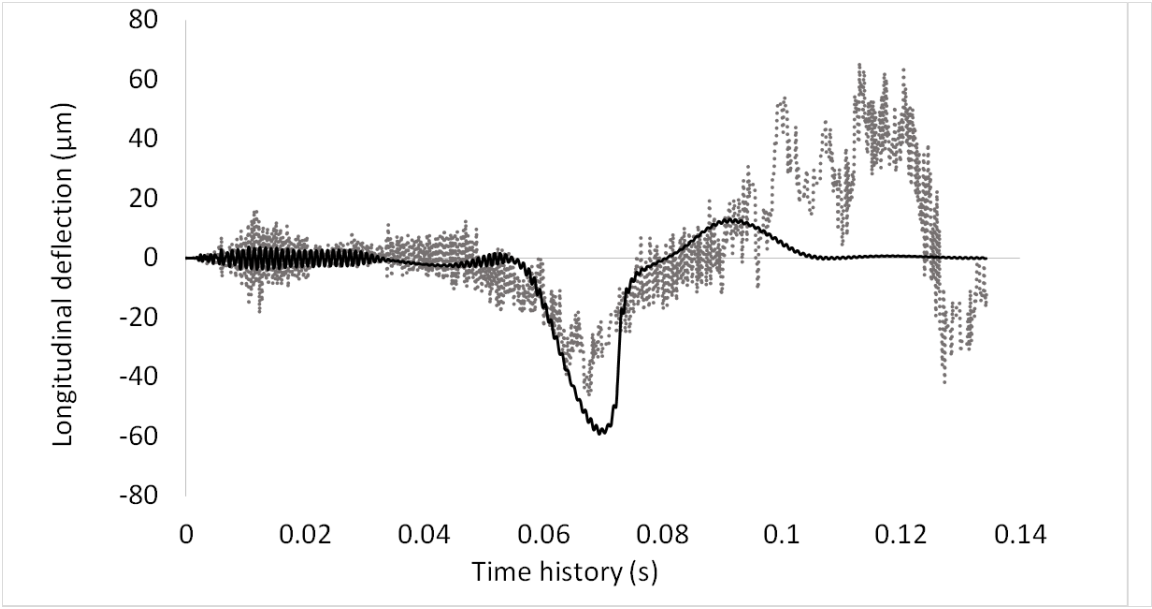

(d)

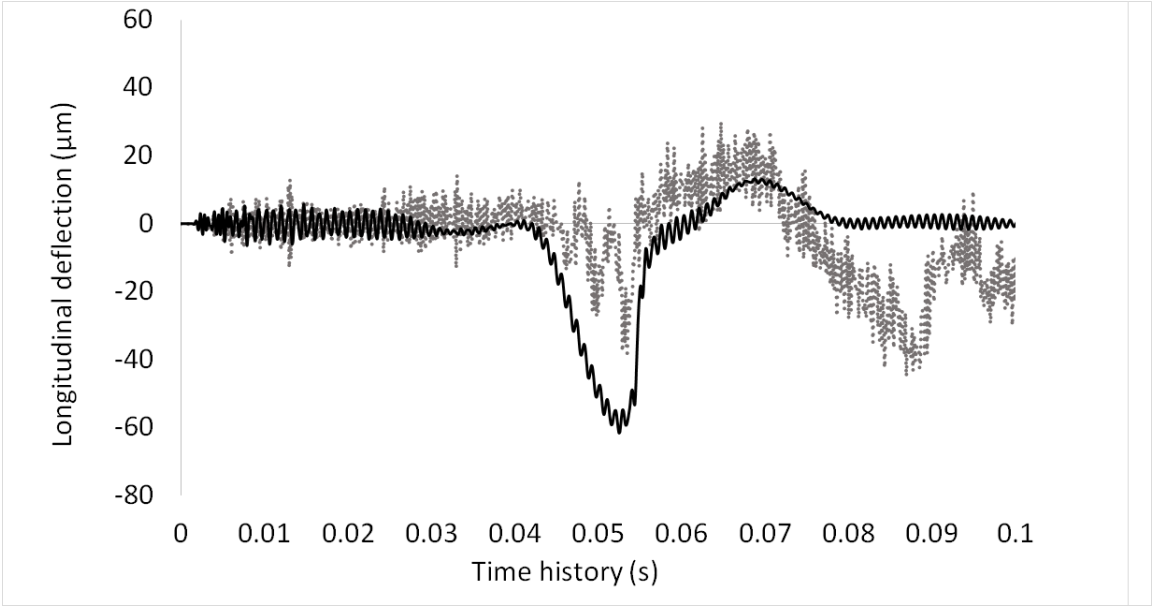

Figure 4.23 Longitudinal deflection at Point 6: —, TPL; …, WRM; (c) $v = 30 \ \frac{m}{s}$, and (d) $v = 40 \ \frac{m}{s}$.

(e)

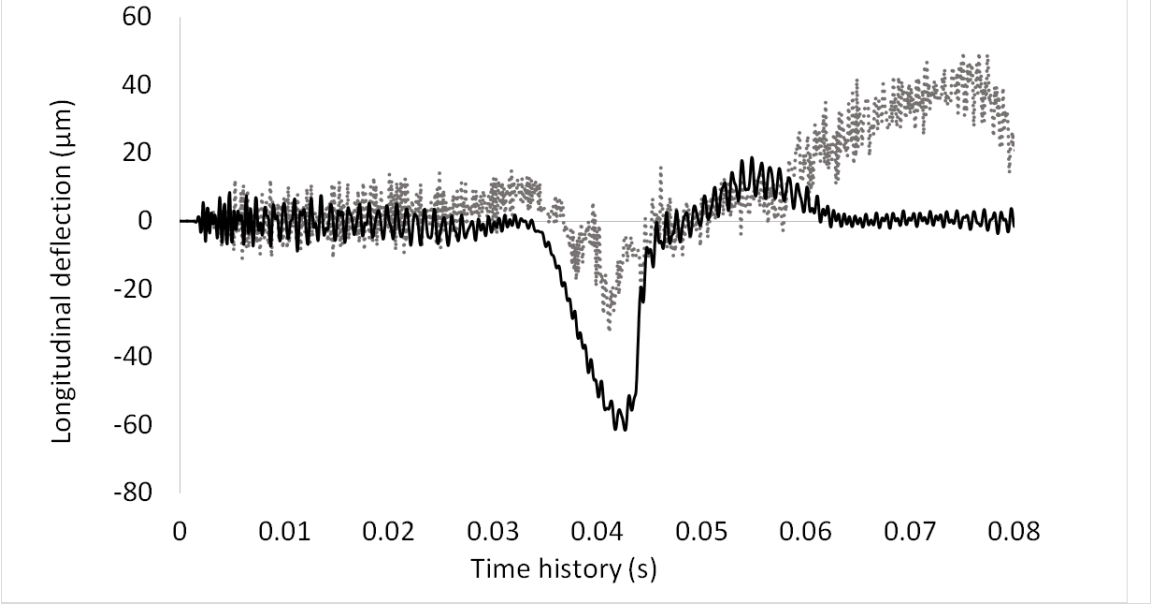

(f)

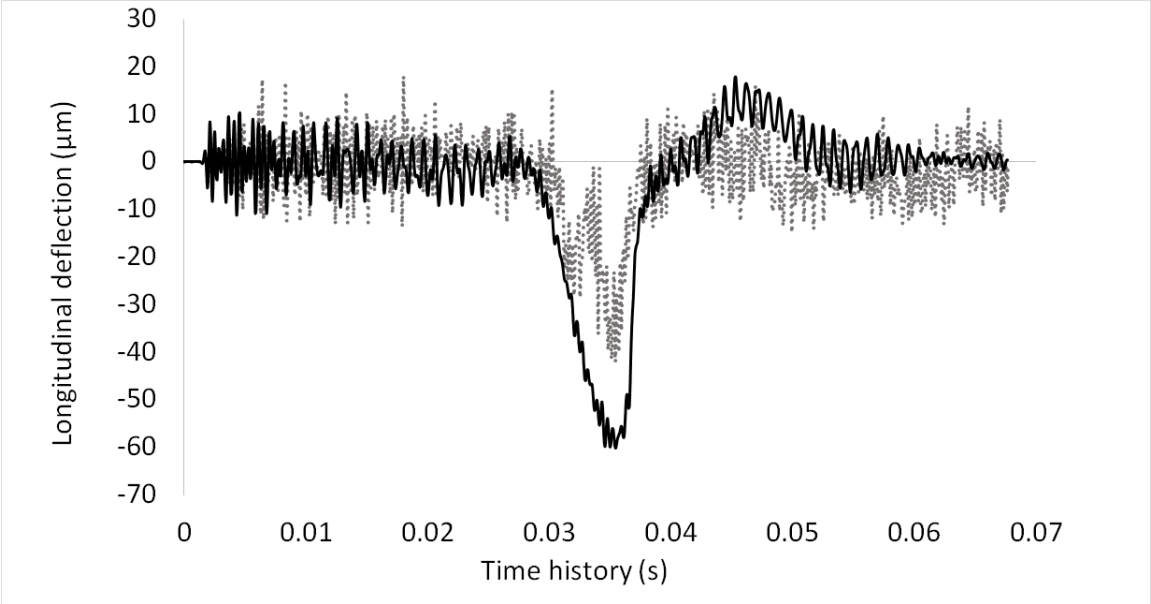

Figure 4.23 Longitudinal deflection at Point 6: —, TPL; …, WRM; (e) $v = 50\ \frac{m}{s}$, and (f) $v = 60\ \frac{m}{s}$.

(a)

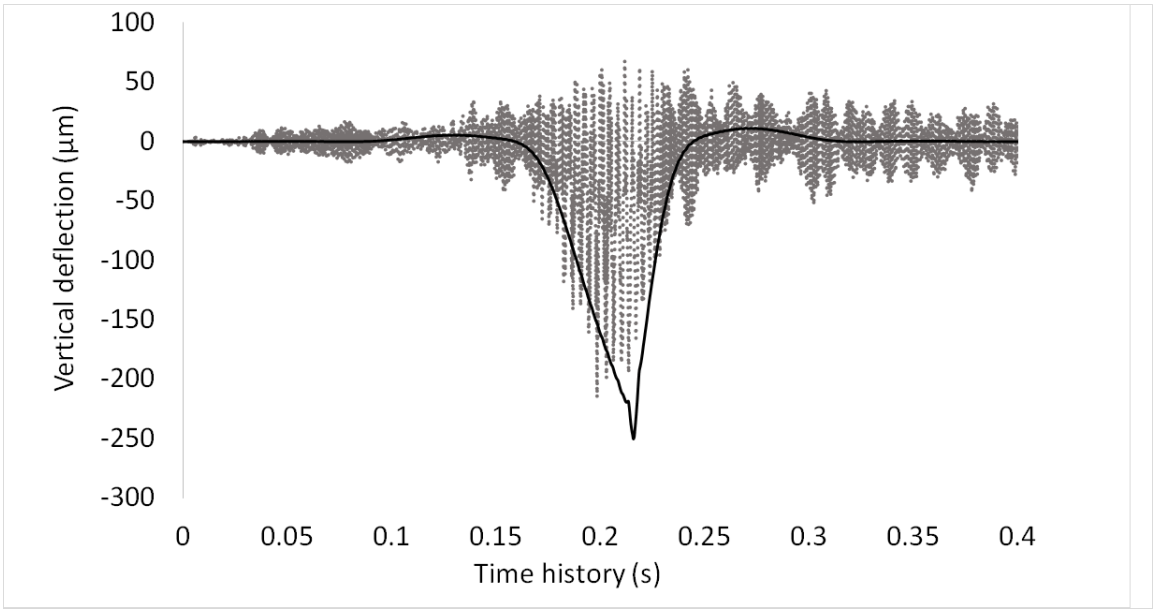

(b)

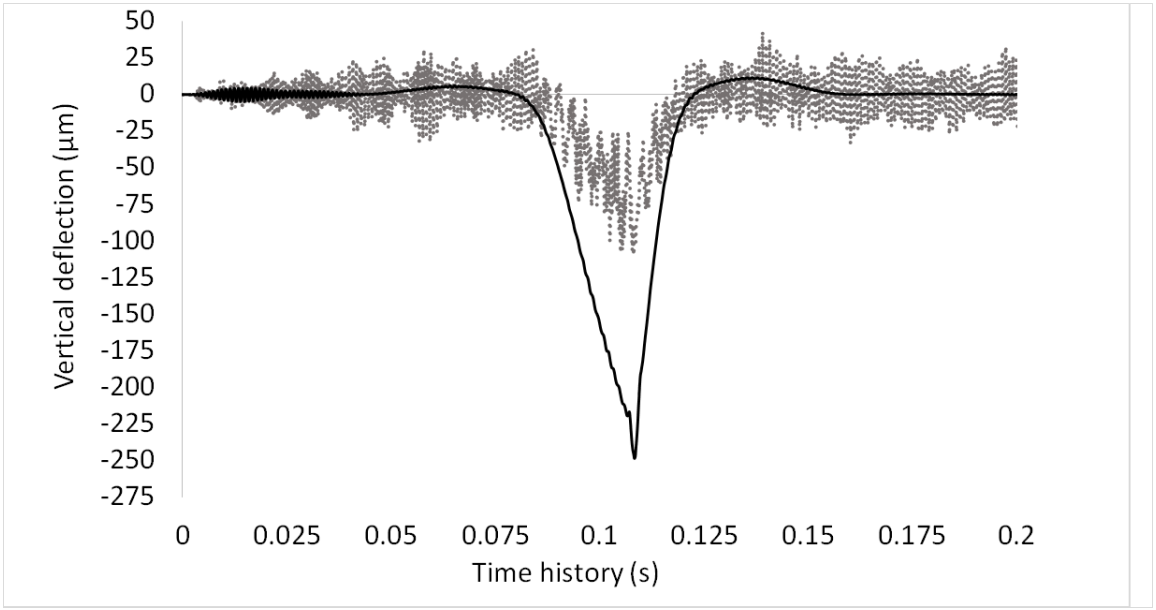

Figure 4.24 Vertical deflection at Point 6: —, TPL; …, WRM;

(a) $v = 10 \ \frac{m}{s}$, and (b) $v = 20 \ \frac{m}{s}$.

(c)

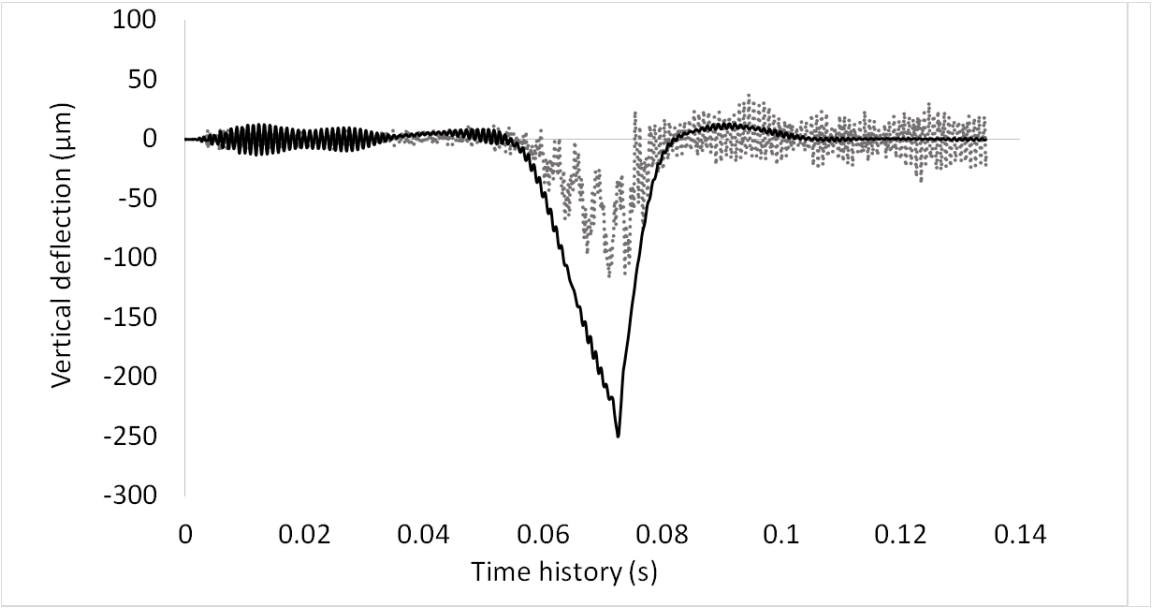

(d)

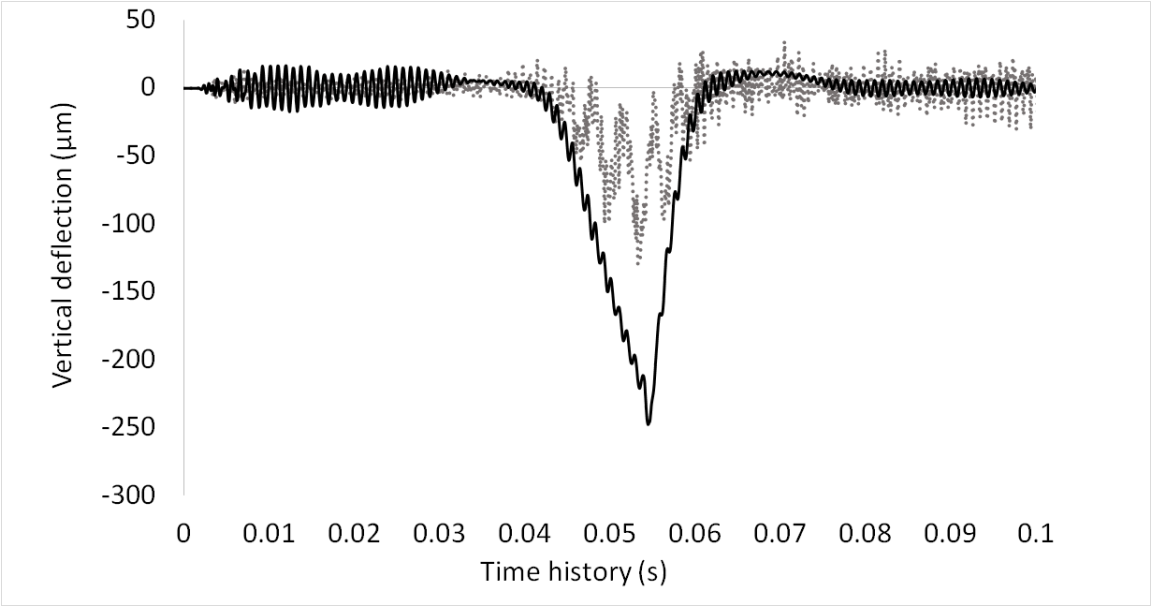

Figure 4.24 Vertical deflection at Point 6: —, TPL; …, WRM; (c) $v = 30\ \frac{m}{s}$, and (d) $v = 40\ \frac{m}{s}$.

(e)

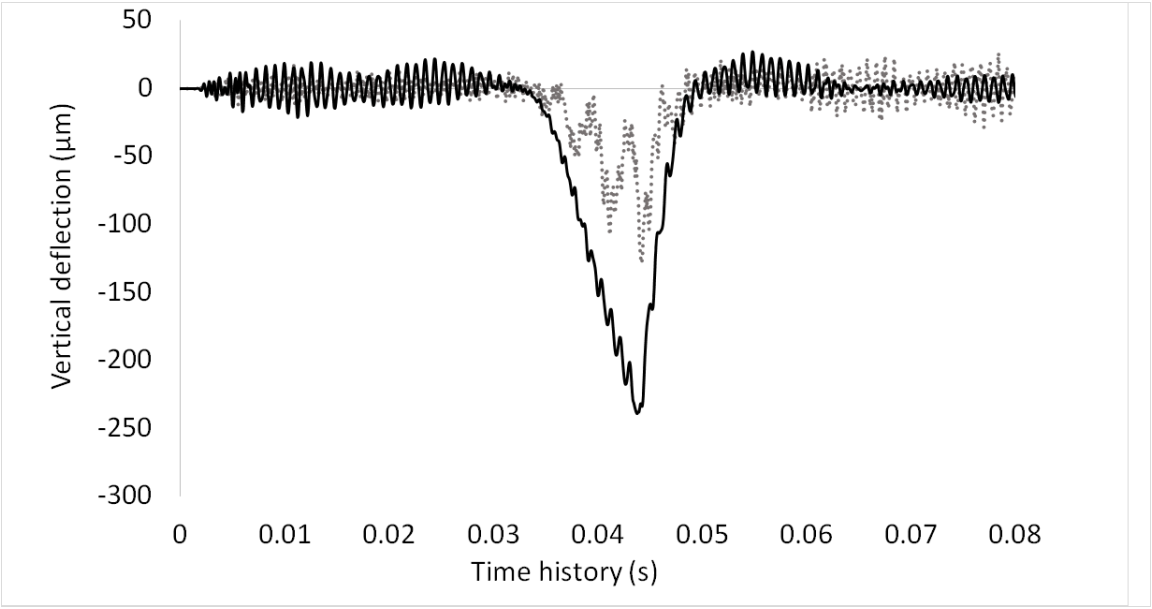

(f)

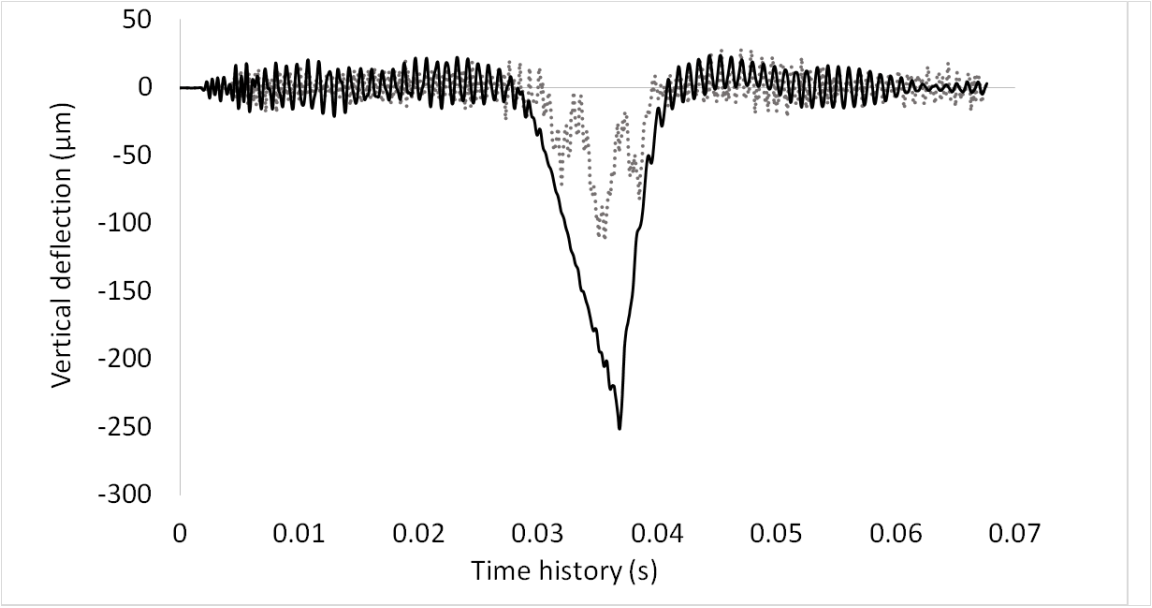

Figure 4.24 Vertical deflection at Point 6: —, TPL; …, WRM; (e) $v = 50\ \frac{m}{s}$, and (f) $v = 60\ \frac{m}{s}$.

4.3.2 Modification of Traveling Point Load By Scaling Amplitude

With the observed significant differences between the computed results of 3D FE rail with TPL model and those of the 3D FE wheel-rail model, it shows a large difference between these two at some points and speeds. In order understanding the reason why TPL cannot model FE wheel-rail well, it needs to consider the different contact force which is due to wheel-rail interaction. Therefore, the input TPL needs to follow the results of contact normal force and contact shear force on the surface of rail from 3D FE wheel-rail model. In 3D FE wheel-rail model, every contact point has different contact normal and shear force. Therefore, the scaling amplitudes should be collected from Path 1, Path2 and Path3 by searching the maximum and minimum shear force and the minimum normal force of each node on the paths. Then, the shear force and normal force collected from the nodes on contact paths are divided by 30 kN and -100kN, respectively. The 30kN is calculated by normal force multiplied by friction coefficient 0.3, and the reason why keeping it positive is due to the amplitude of friction force in the foregoing is +1 and -1. Therefore, input friction force follows the amplitude only. Also, keeping normal force negative is due to the contact normal force which always shows negative. Thus, the amplitude of input normal force is only positive. The Figure 4.25 illustrates the simple way to get the amplitudes.

The response of scaled TPL on 3D FE rail model are plotted and compared with FE wheel-rail model through Figure 4.26 to 4.31.(a)

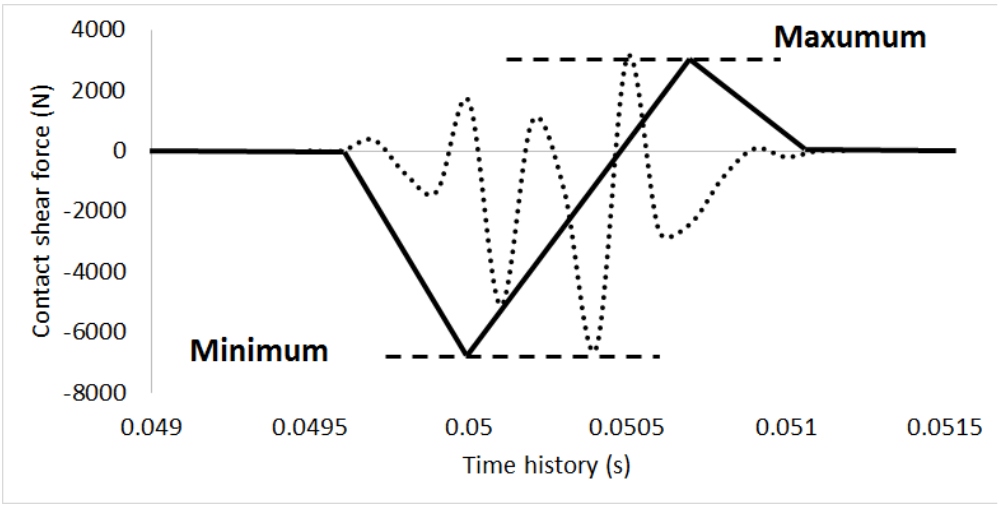

(b)

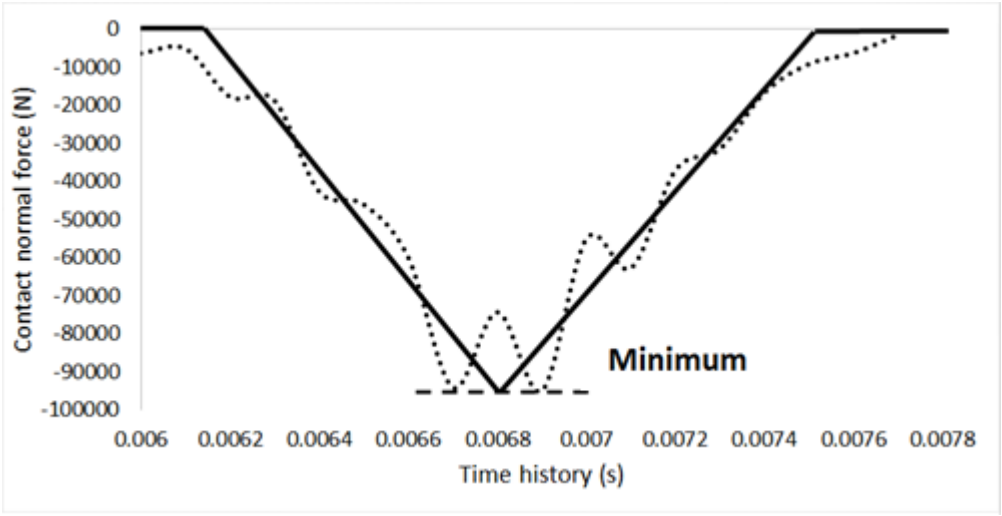

Figure 4.25 Normal and shear (longitudinal) forces from FE wheel-rail model: (a) shear force, and (b) normal force.

(a)

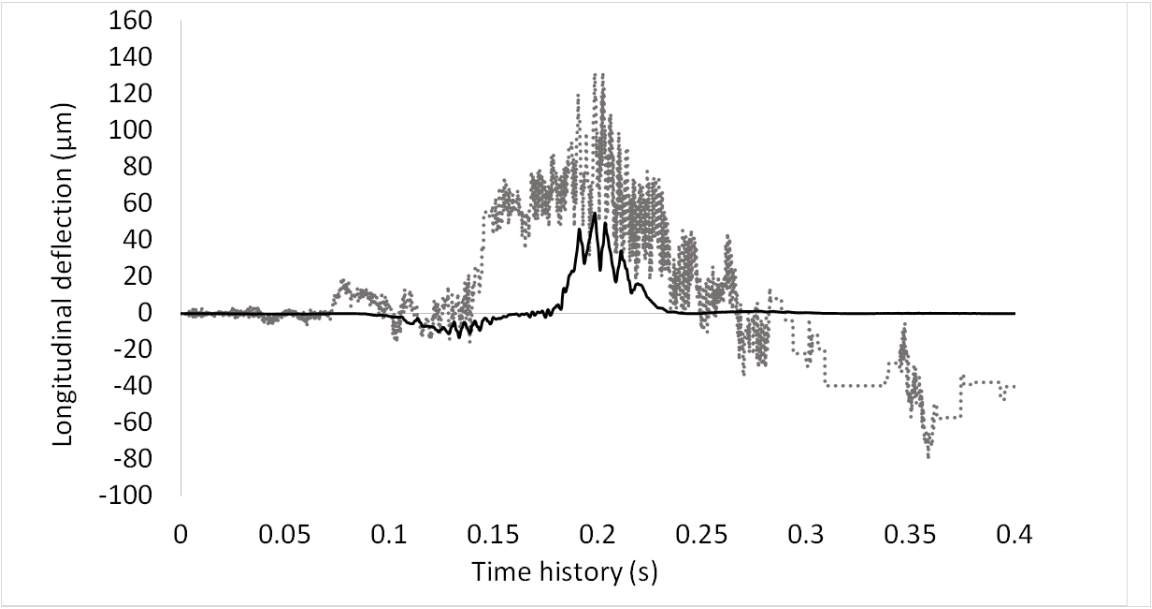

(b)

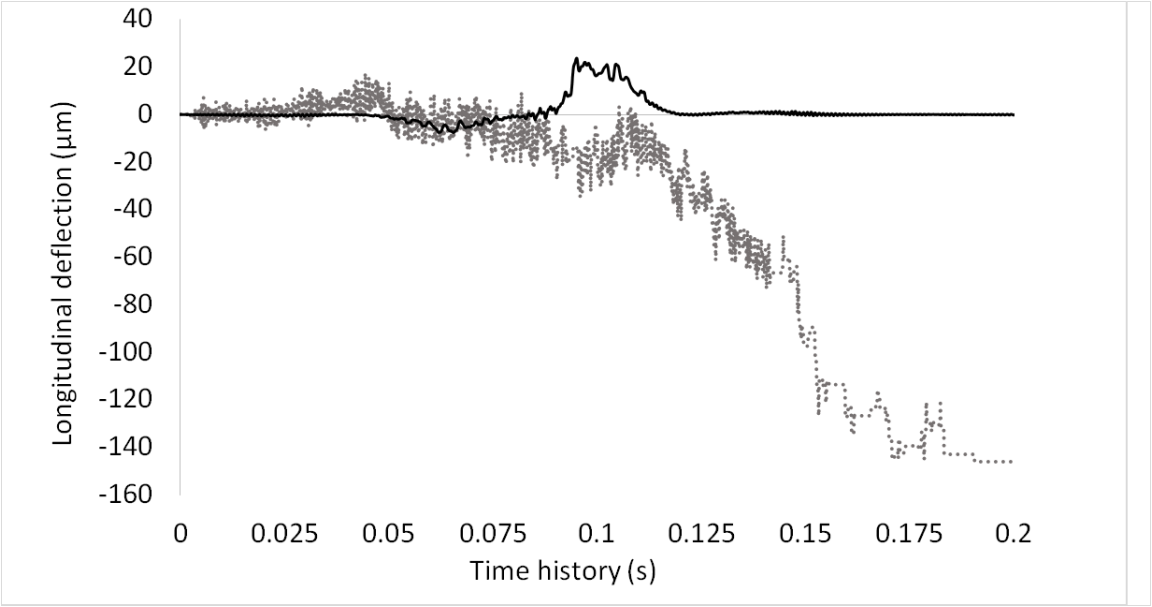

Figure 4.26 Longitudinal deflection at Point 4: —, Scaled TPL; …, WRM; (a) $v = 10 \ \frac{m}{s}$, and (b) $v = 20 \ \frac{m}{s}$.

(c)

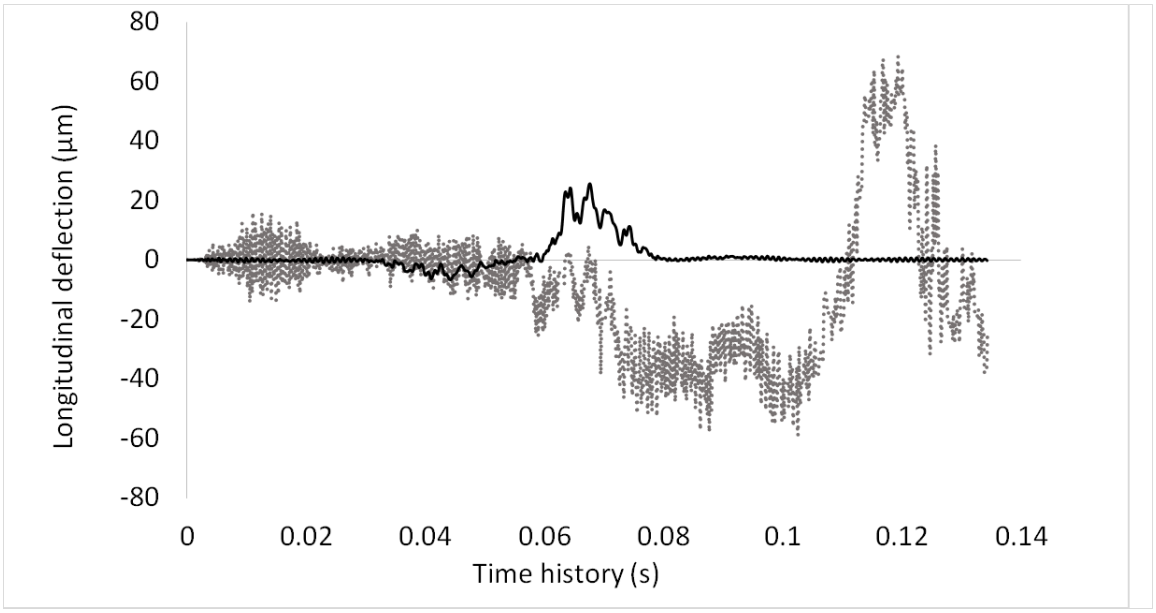

(d)

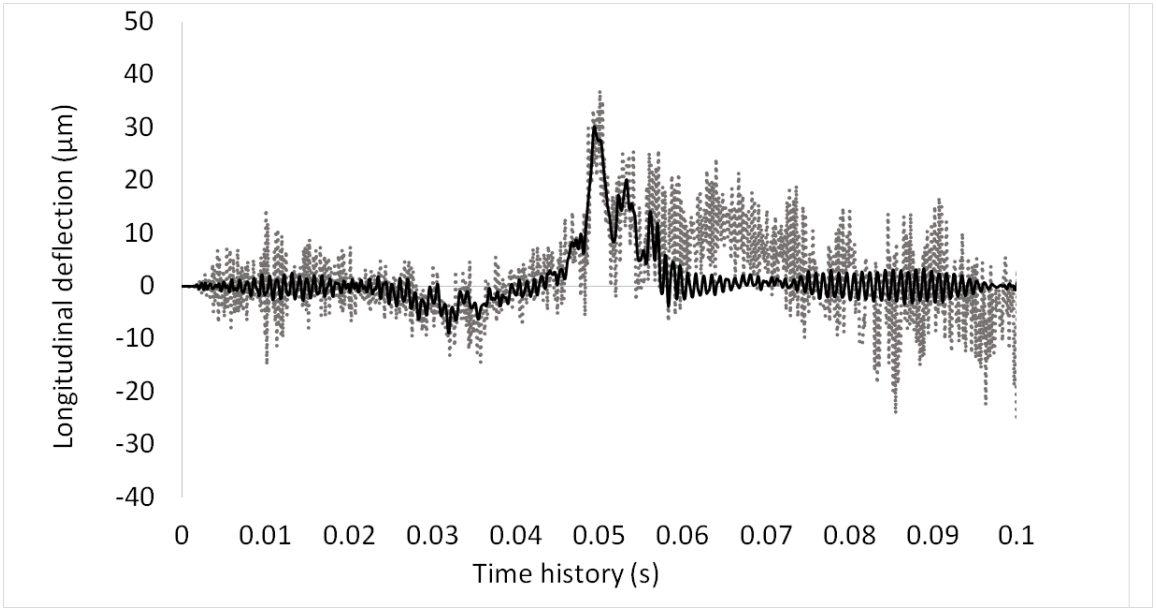

Figure 4.26 Longitudinal deflection at Point 4: —, Scaled TPL; …, WRM; (c) $v = 30 \ \frac{m}{s}$, and (d) $v = 40 \ \frac{m}{s}$.

(e)

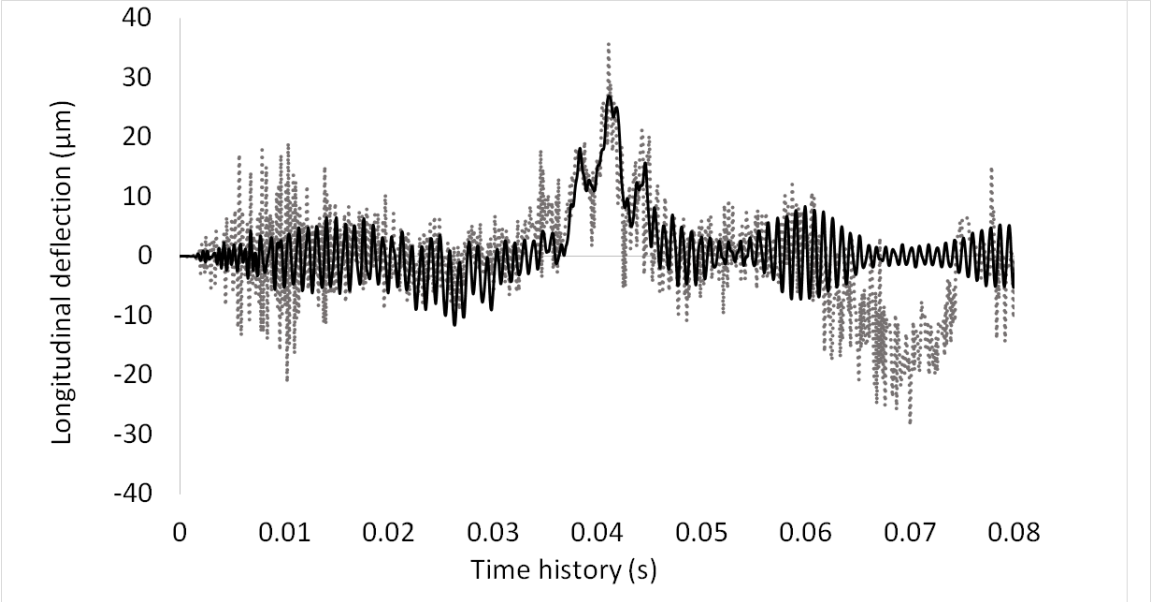

(f)

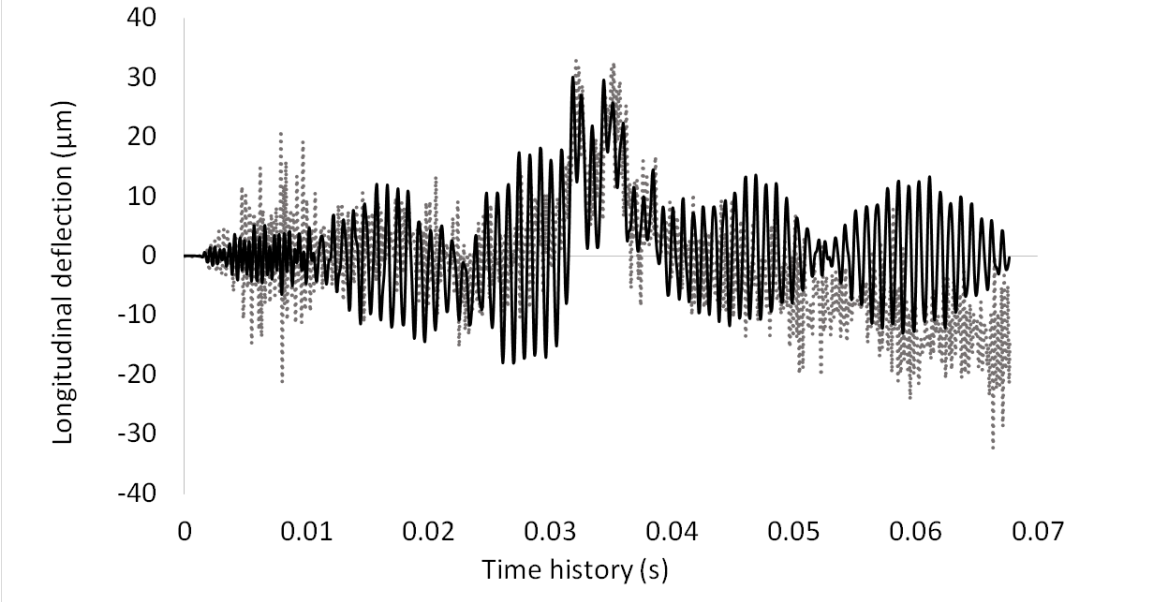

Figure 4.26 Longitudinal deflection at Point 4: —, Scaled TPL; …, WRM; (e) $v = 50 \ \frac{m}{s}$, and (f) $v = 60 \ \frac{m}{s}$.

(a)

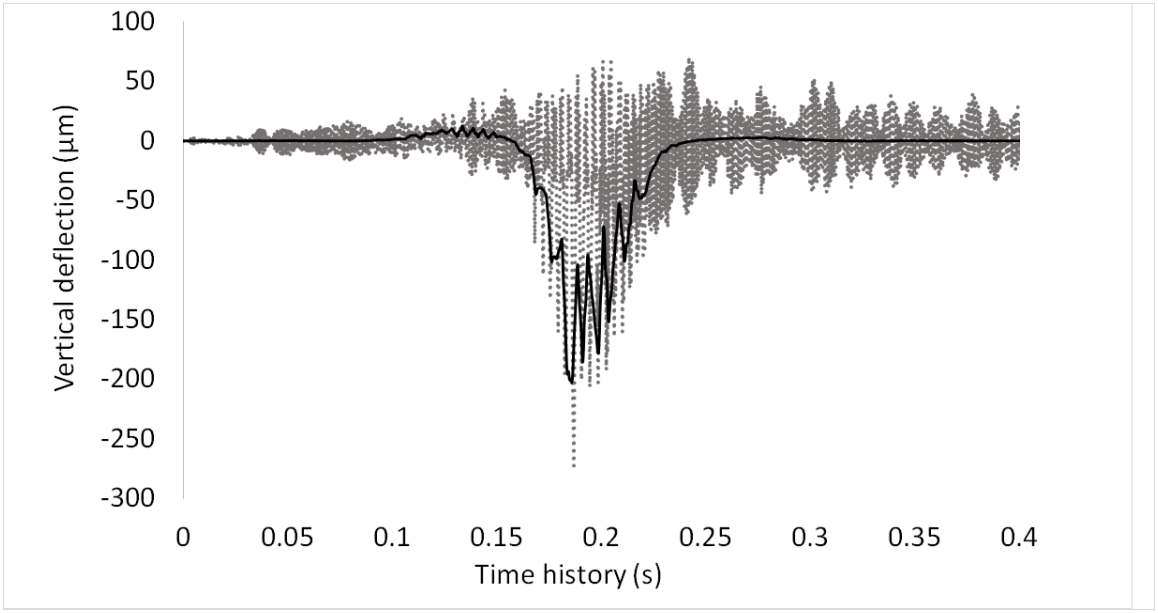

(b)

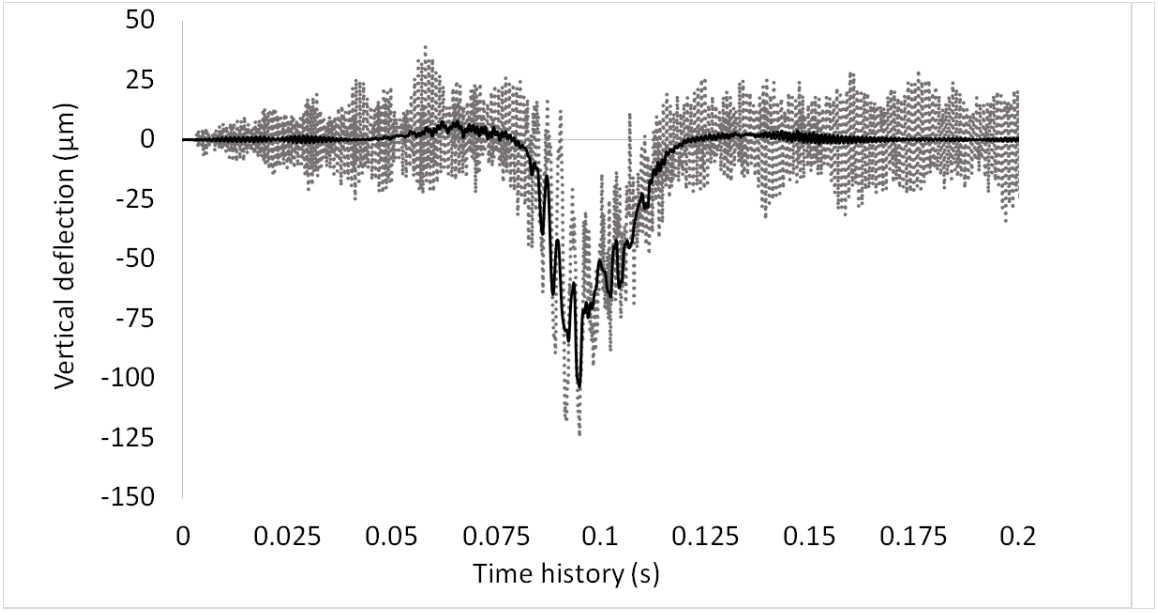

Figure 4.27 Vertical deflection at Point 4: —, Scaled TPL; …, WRM; (a) $v = 10\ \frac{m}{s}$, and (b) $v = 20\ \frac{m}{s}$.

(c)

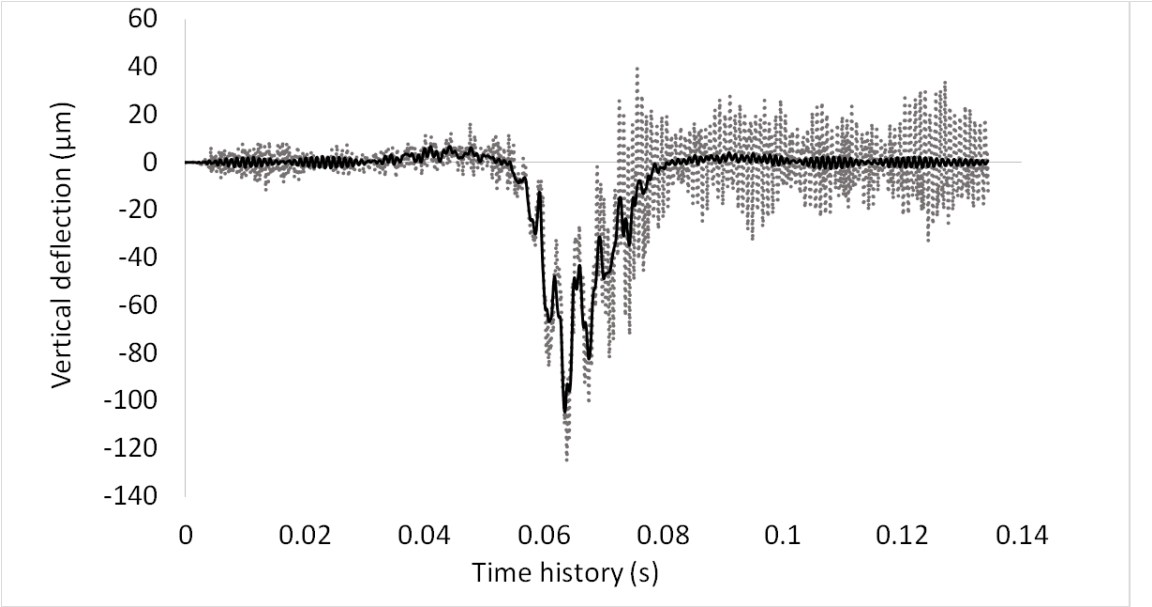

(d)

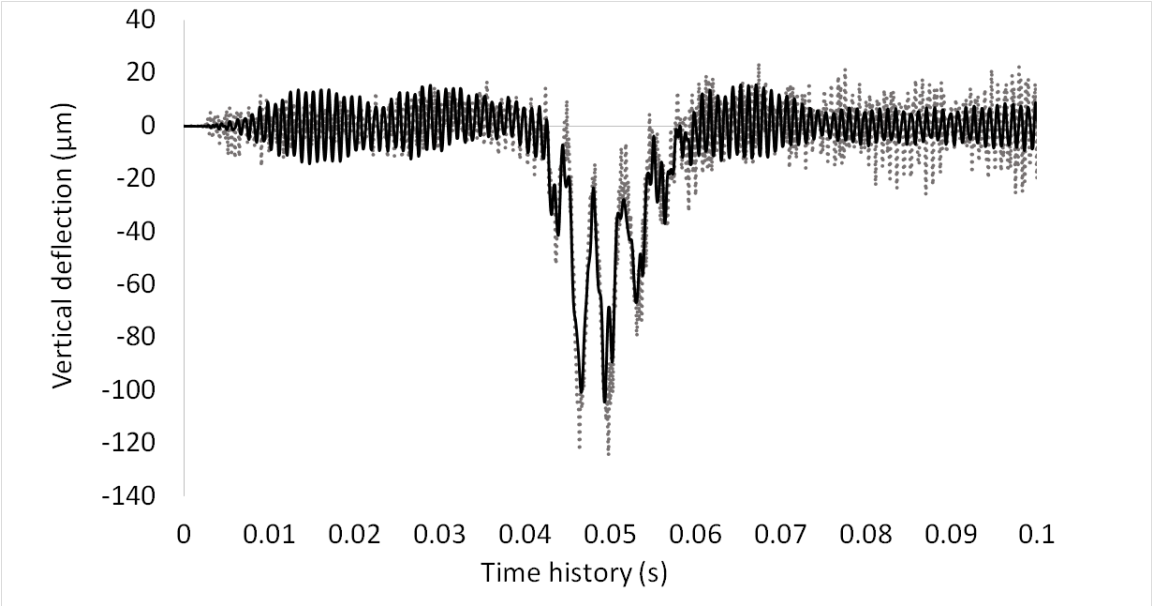

Figure 4.27 Vertical deflection at Point 4: —, Scaled TPL; …, WRM; (c) $v = 30\ \frac{m}{s}$, and (d) $v = 40\ \frac{m}{s}$.

(e)

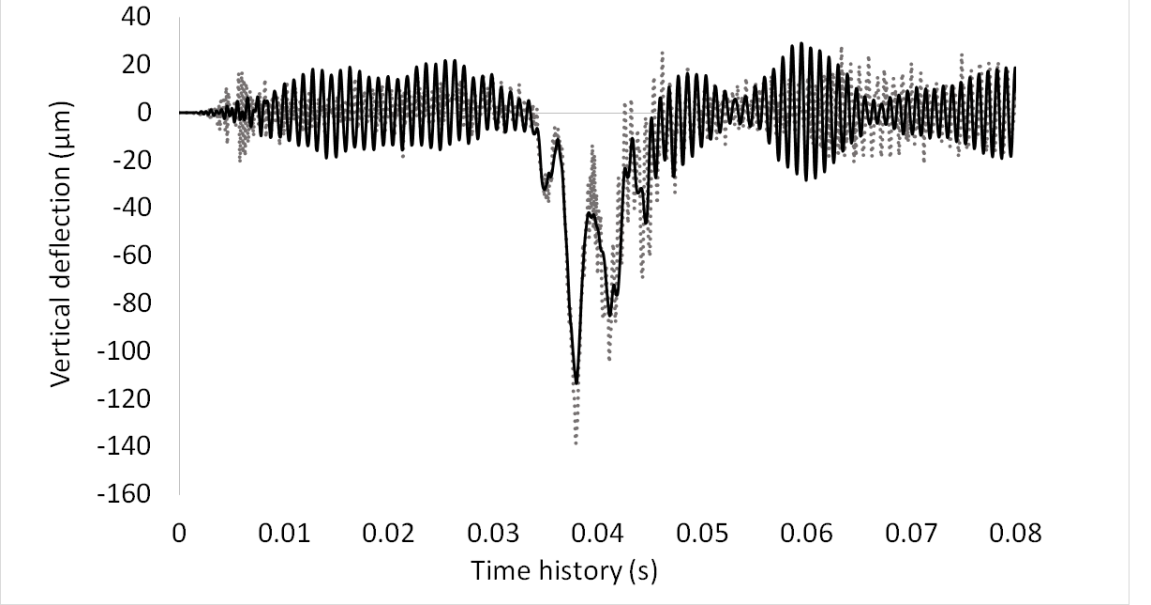

(f)

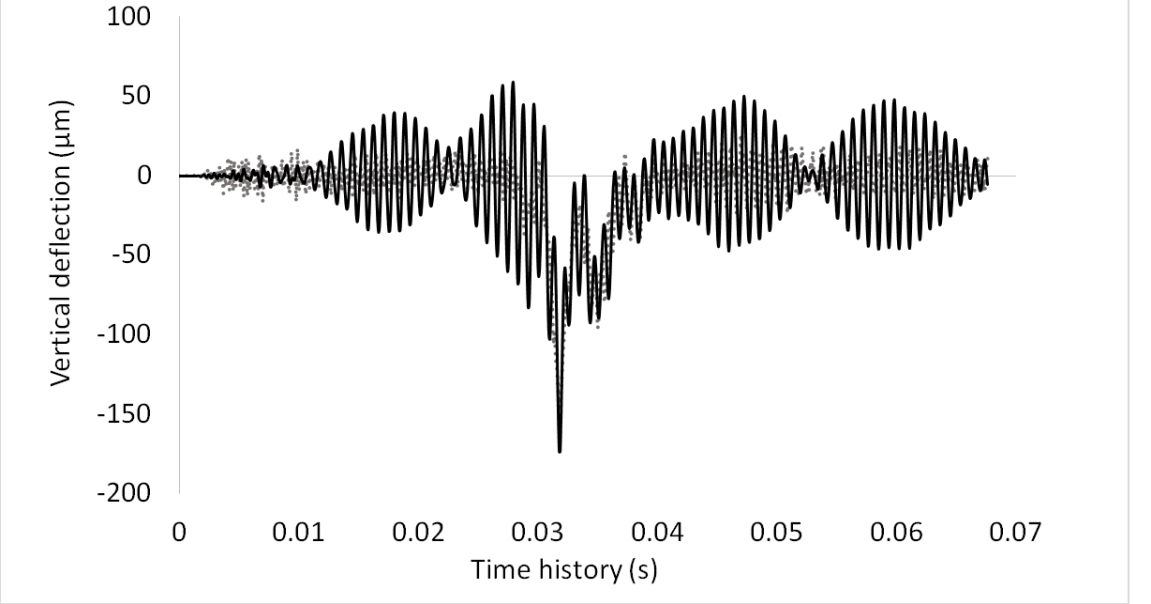

Figure 4.27 Vertical deflection at Point 4: —, Scaled TPL; …, WRM; (e) $v = 50\ \frac{m}{s}$, and (f) $v = 60\ \frac{m}{s}$.

(a)

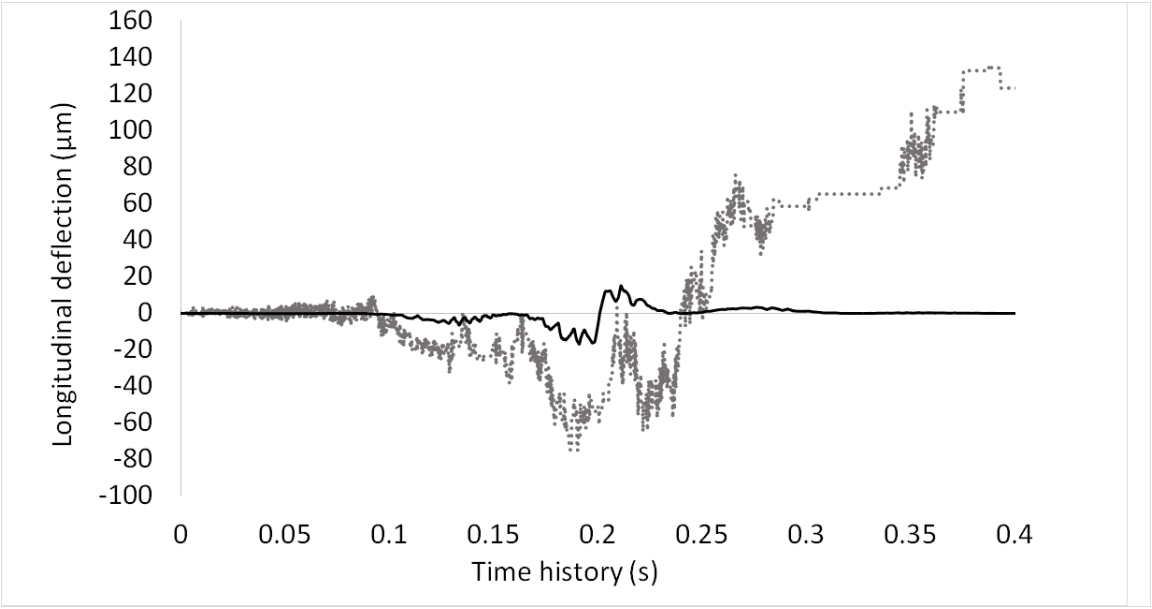

(b)

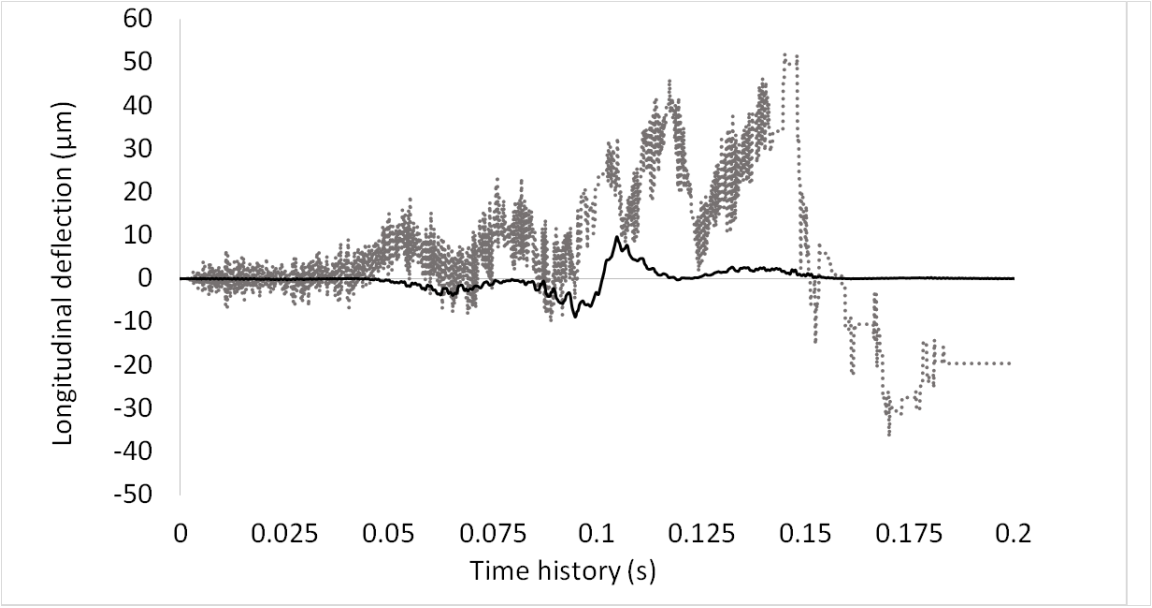

Figure 4.28 Longitudinal deflection at Point 5: —, Scaled TPL; …, WRM; (a) $v = 10\ \frac{m}{s}$, and (b) $v = 20\ \frac{m}{s}$.

(c)

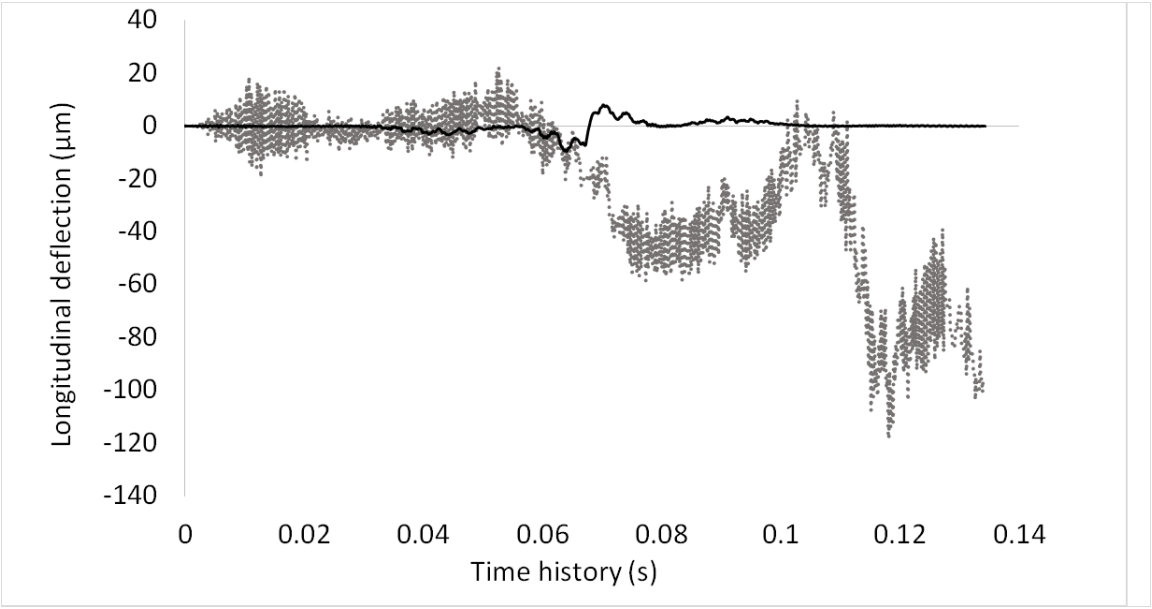

(d)

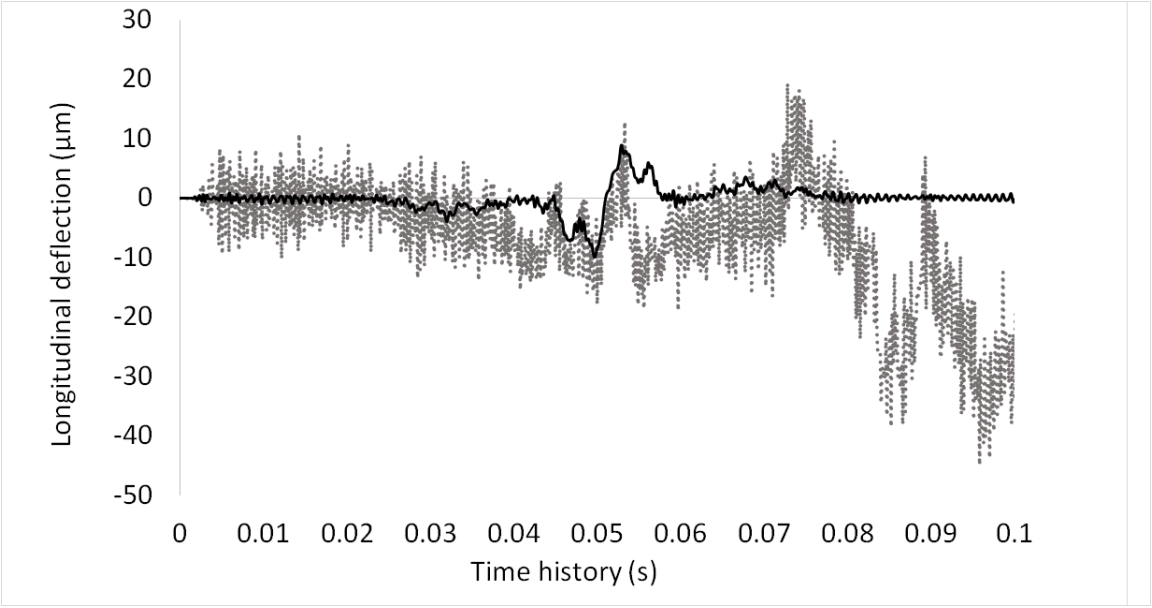

Figure 4.28 Longitudinal deflection at Point 5: —, Scaled TPL; …, WRM; (c) $v = 30 \ \frac{m}{s}$, and (d) $v = 40 \ \frac{m}{s}$.

(e)

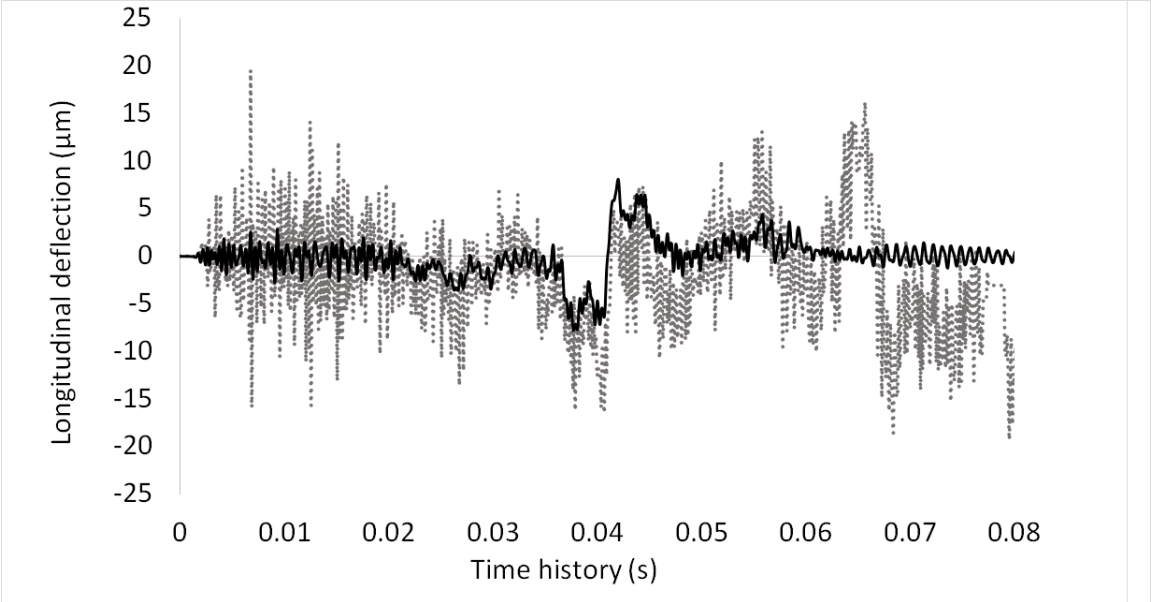

(f)

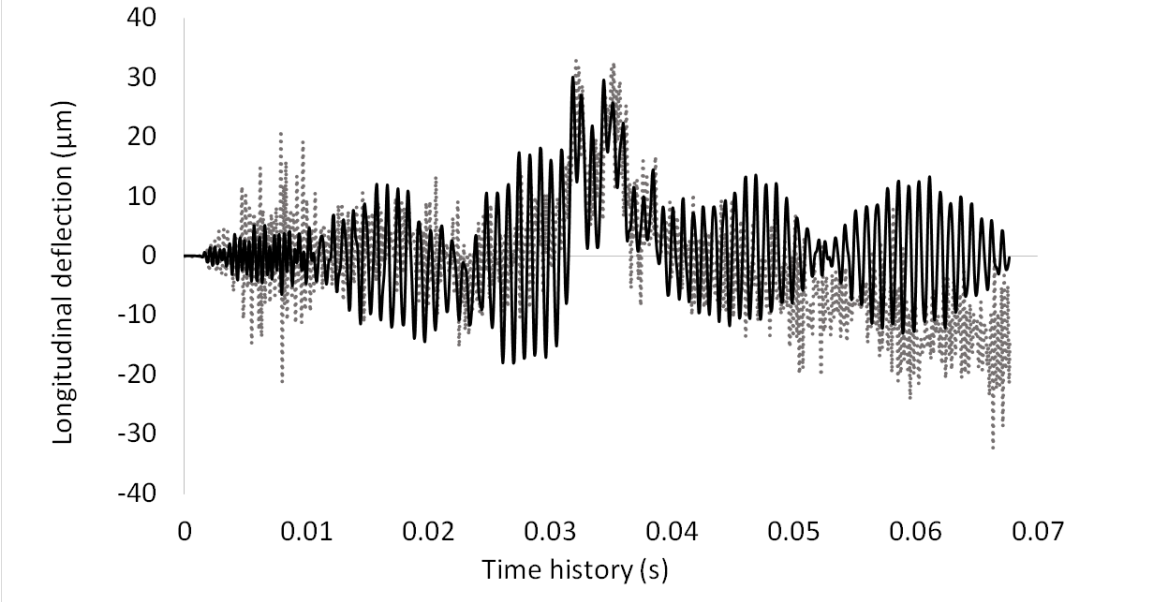

Figure 4.28 Longitudinal deflection at Point 5: —, Scaled TPL; …, WRM; (e) $v = 50 \ \frac{m}{s}$, and (f) $v = 60 \ \frac{m}{s}$.

(a)

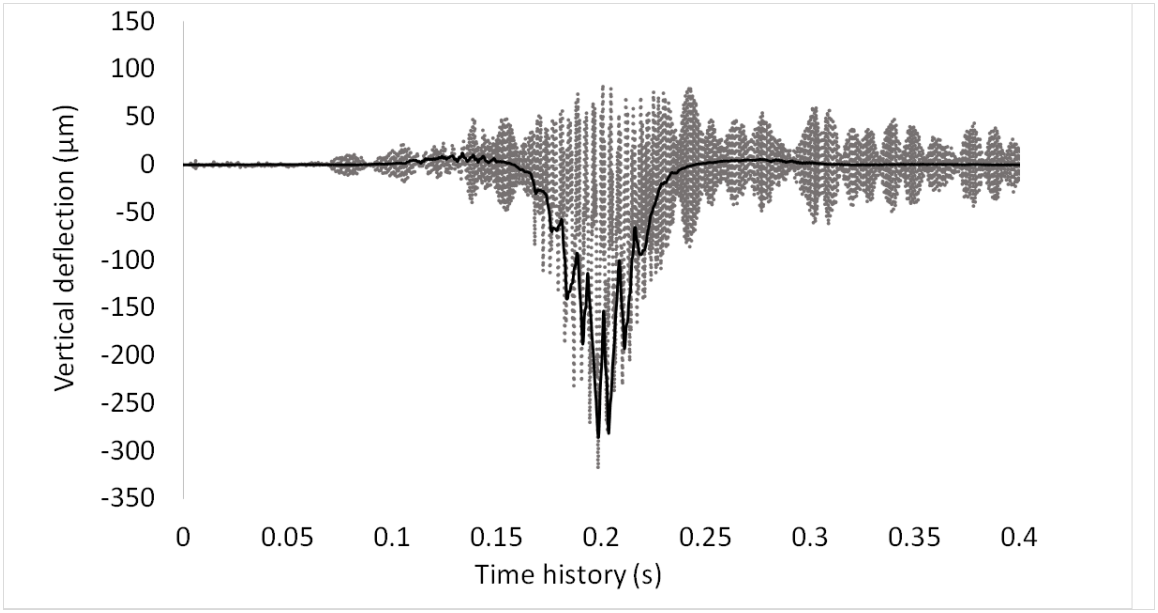

(b)

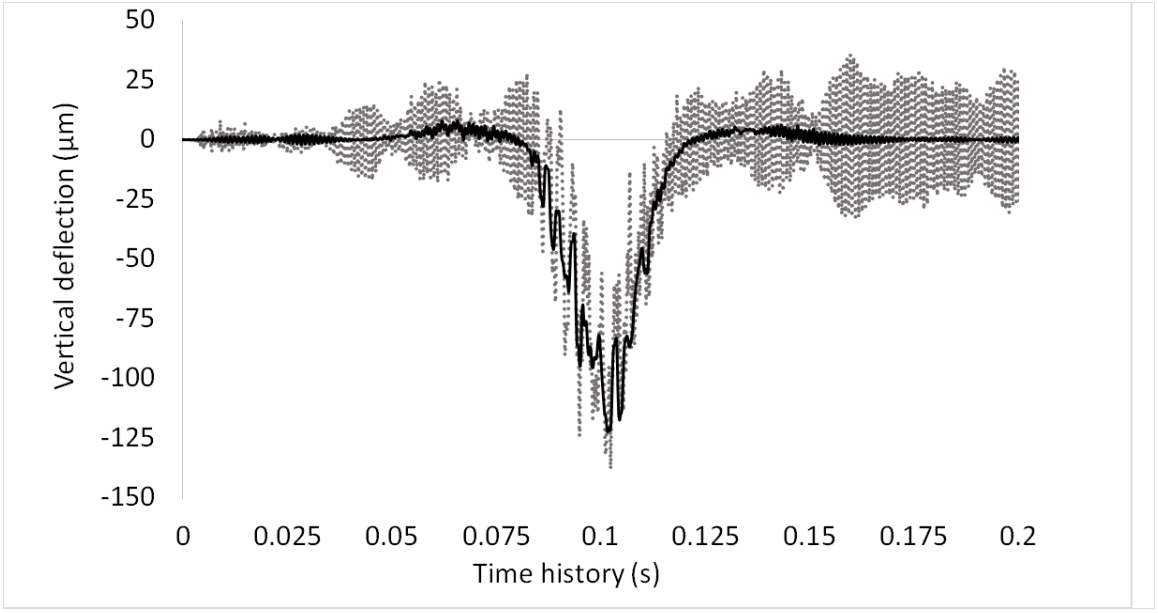

Figure 4.29 Vertical deflection at Point 5: —, Scaled TPL; …, WRM; (a) $v = 10\ \frac{m}{s}$, and (b) $v = 20\ \frac{m}{s}$.

(c)

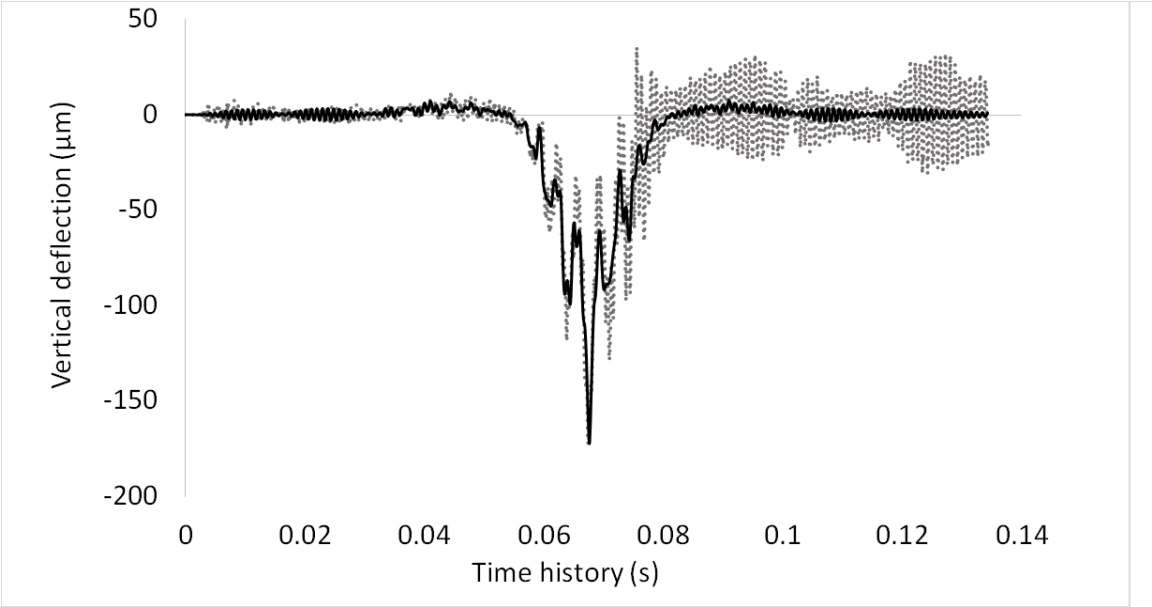

(d)

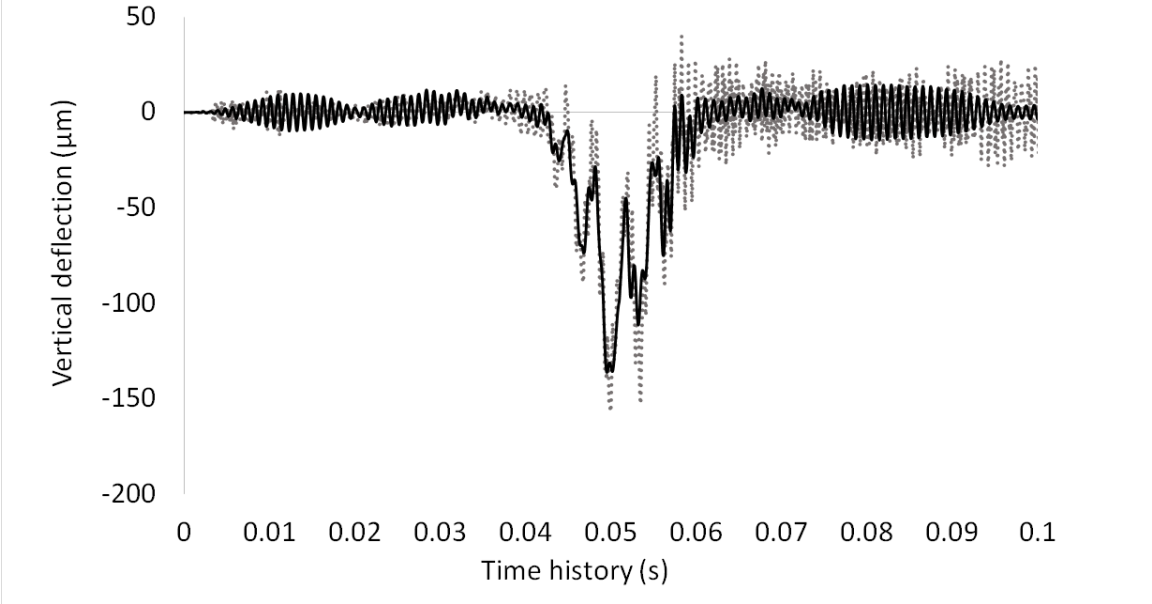

Figure 4.29 Vertical deflection at Point 5: —, Scaled TPL; …, WRM; (c) $v = 30\ \frac{m}{s}$, and (d) $v = 40\ \frac{m}{s}$.

(e)

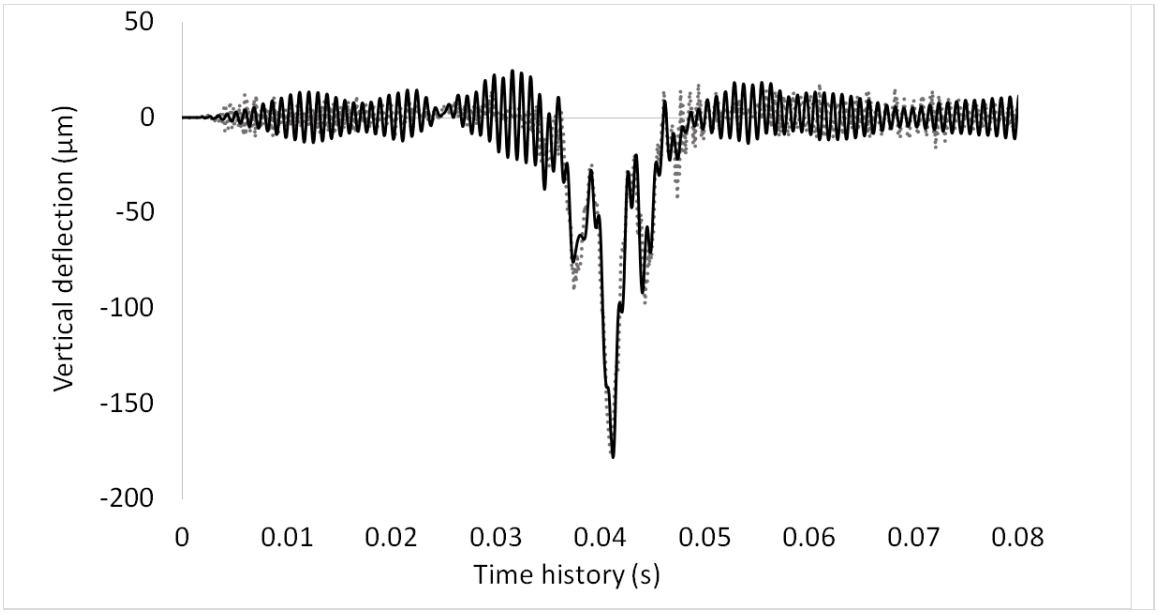

(f)

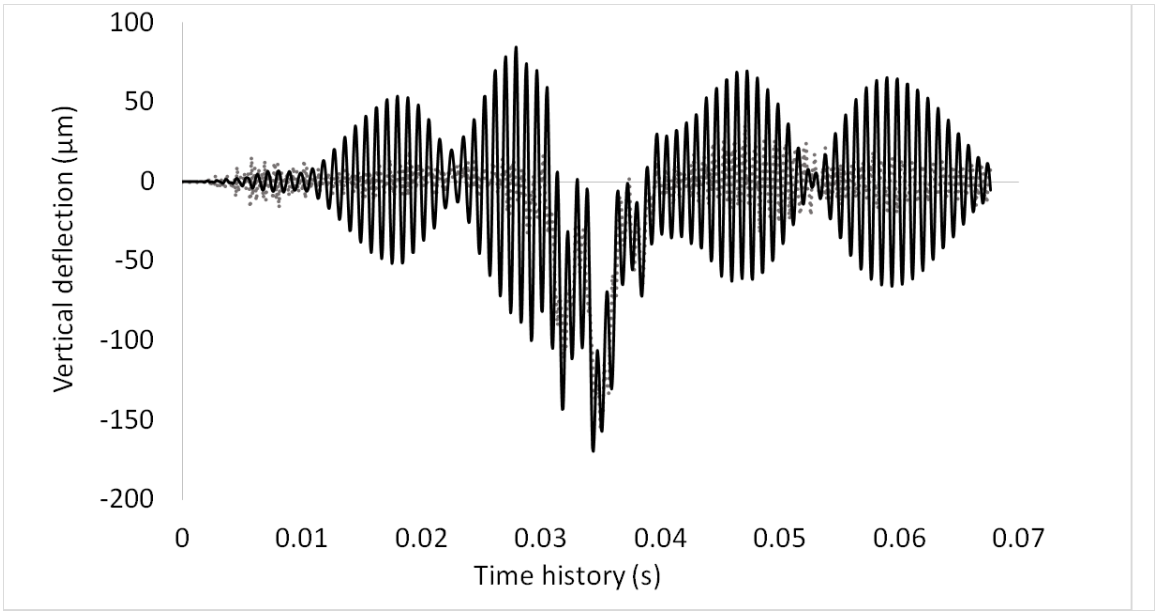

Figure 4.29 Vertical deflection at Point 5: —, Scaled TPL; …, WRM; (e) $v = 50\ \frac{m}{s}$, and (f) $v = 60\ \frac{m}{s}$.

(a)

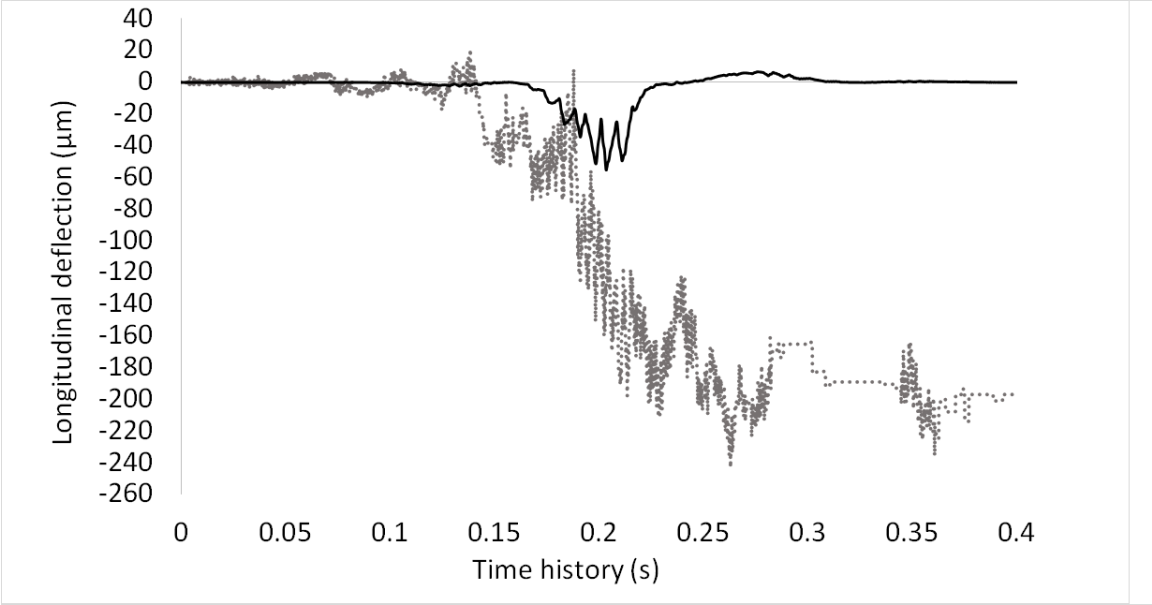

(b)

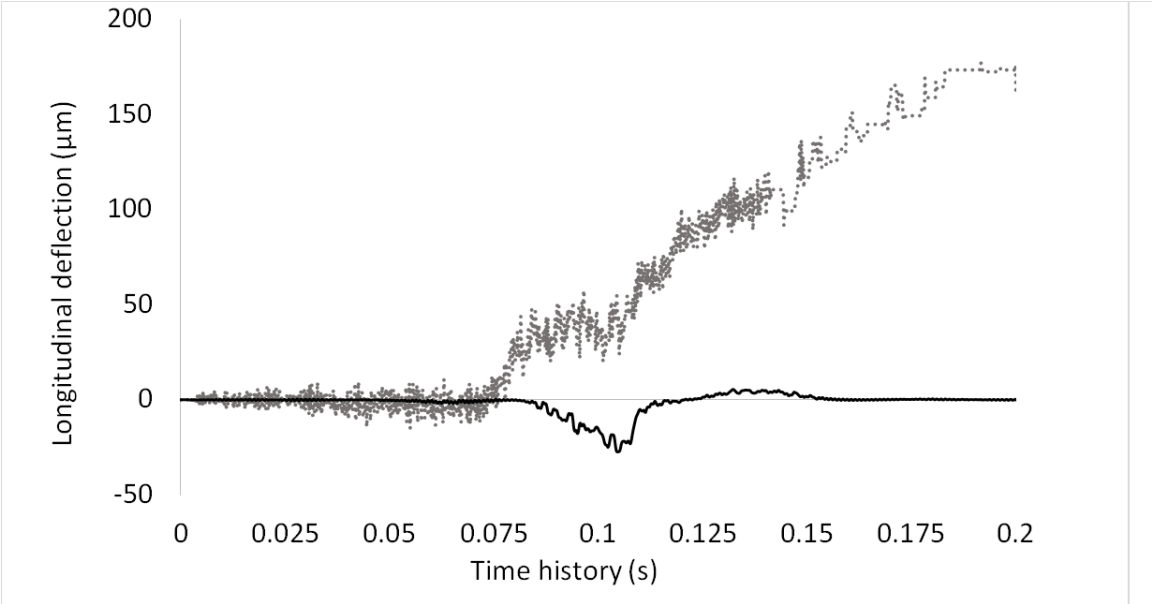

Figure 4.30 Longitudinal deflection at Point 6: —, Scaled TPL; …, WRM; (a) $v = 10\ \frac{m}{s}$, and (b) $v = 20\ \frac{m}{s}$.

(c)

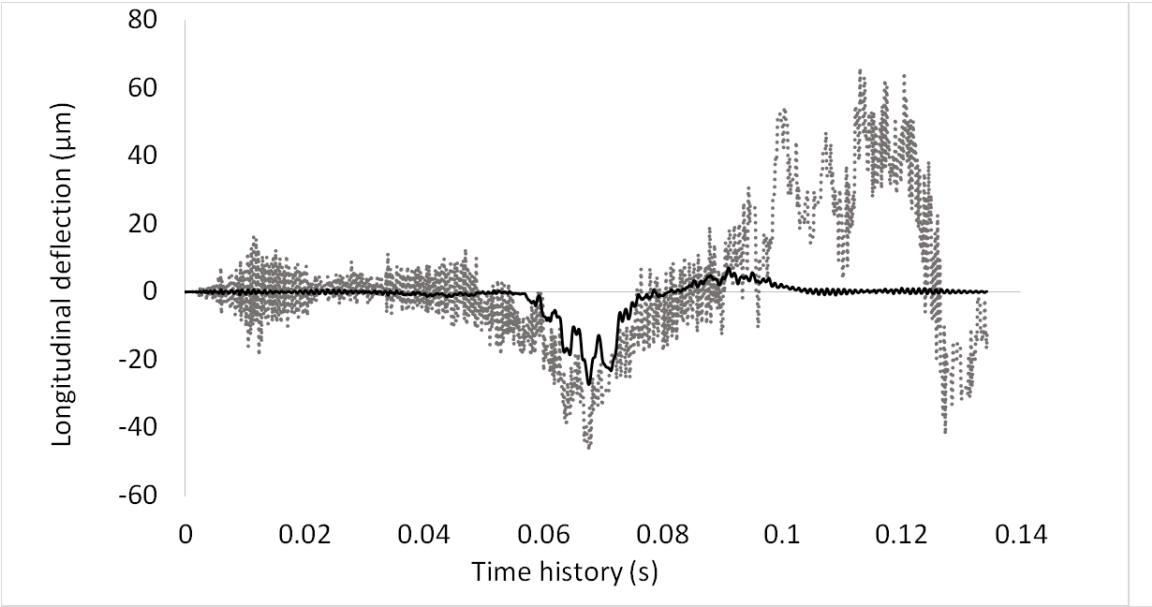

(d)

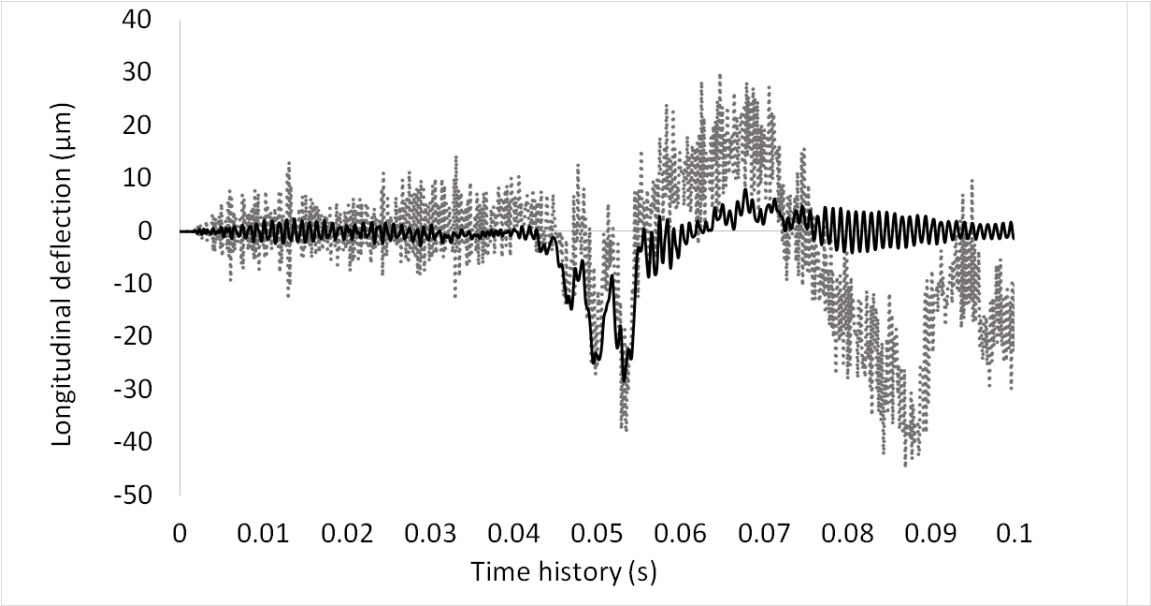

Figure 4.30 Longitudinal deflection at Point 6: —, Scaled TPL; …, WRM; (c) $v = 30 \ \frac{m}{s}$, and (d) $v = 40 \ \frac{m}{s}$.

(e)

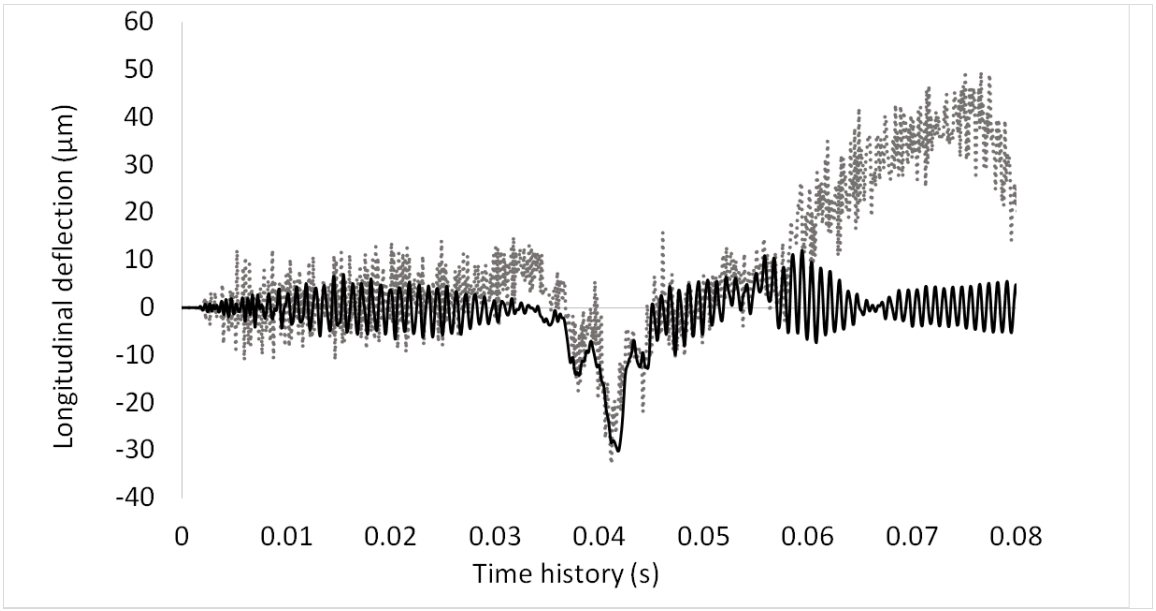

(f)

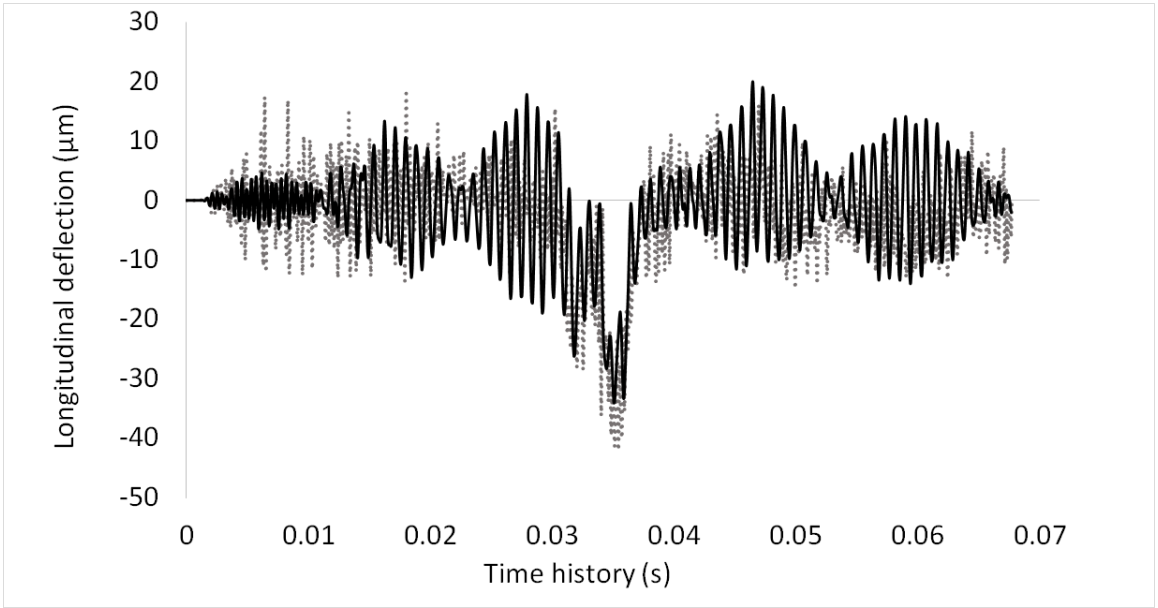

Figure 4.30 Longitudinal deflection at Point 6: —, Scaled TPL; …, WRM; (e) $v = 50 \ \frac{m}{s}$, and (f) $v = 60 \ \frac{m}{s}$.

(a)

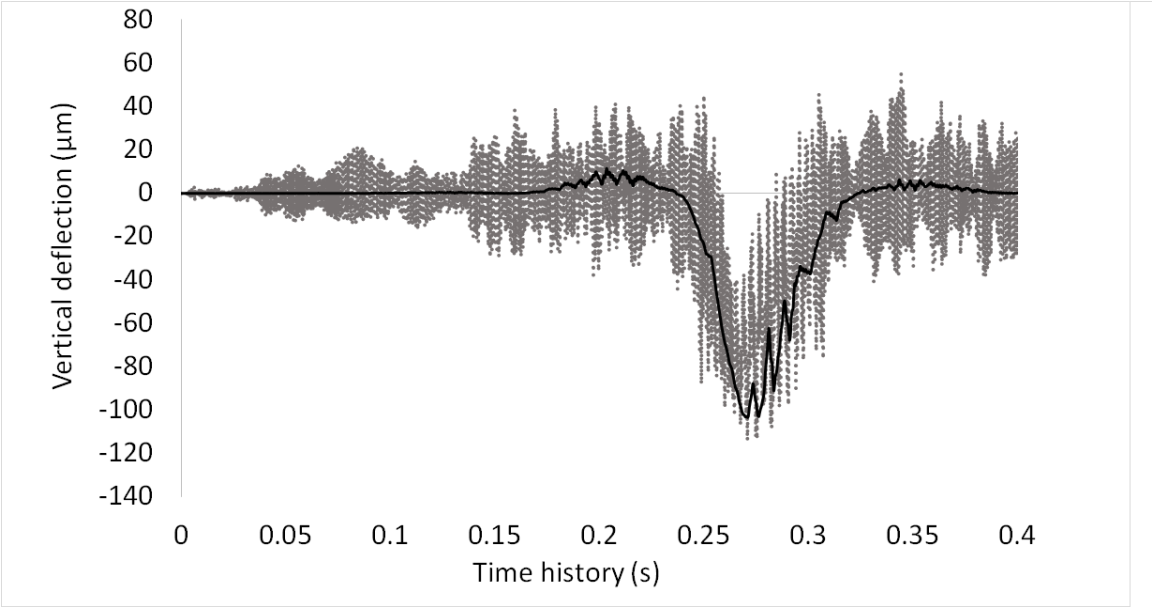

(b)

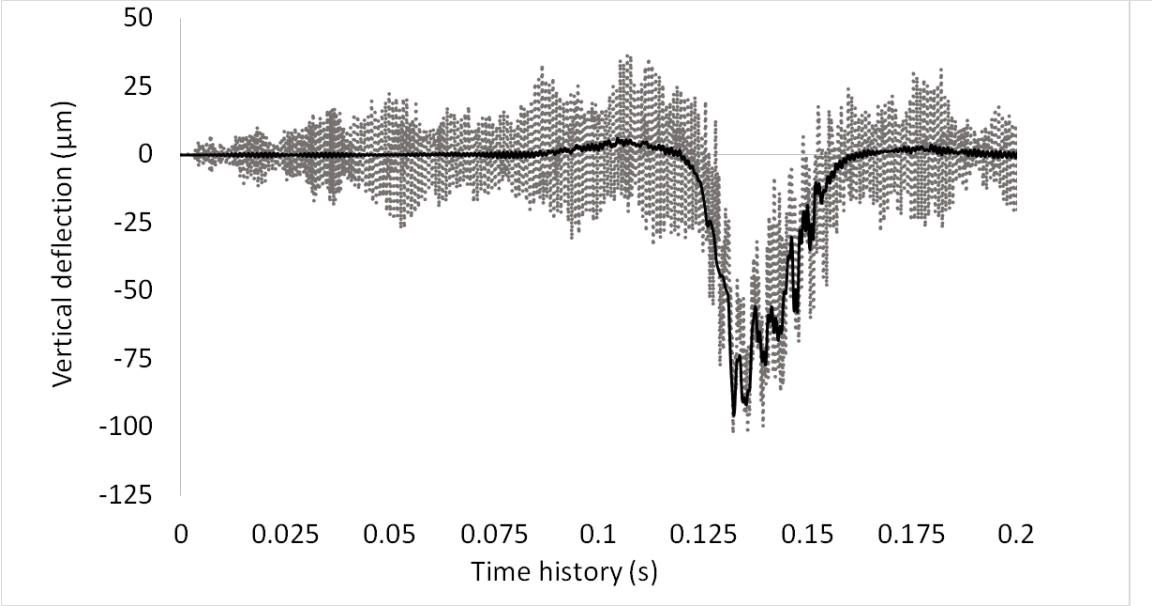

Figure 4.31 Vertical deflection at Point 6: —, Scaled TPL; …, WRM; (a) $v = 10\ \frac{m}{s}$, and (b) $v = 20\ \frac{m}{s}$.

(c)

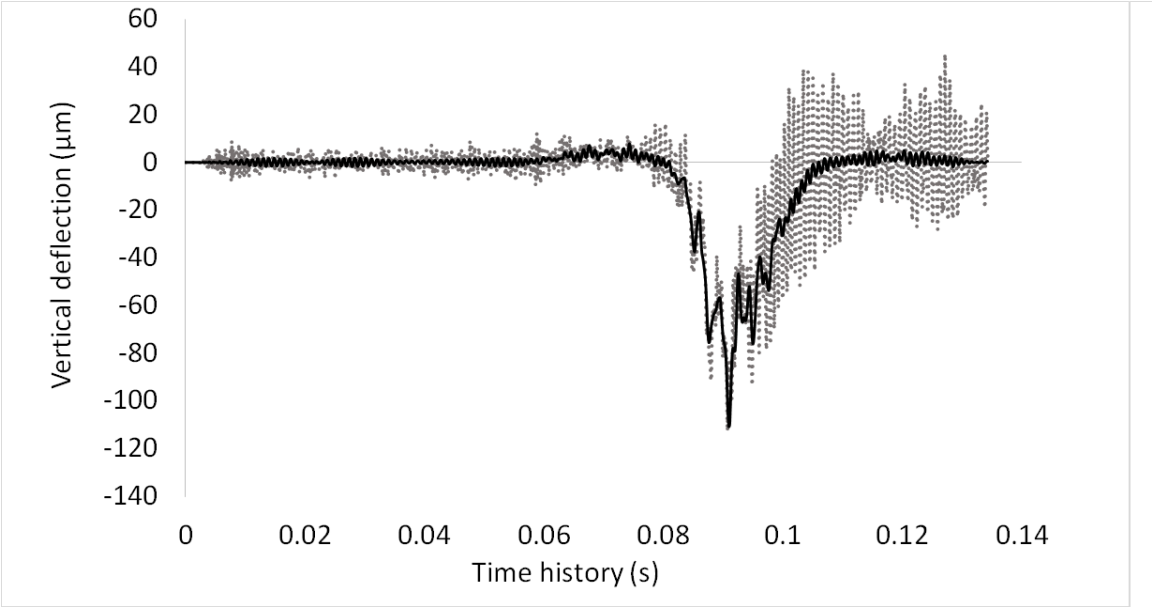

(d)

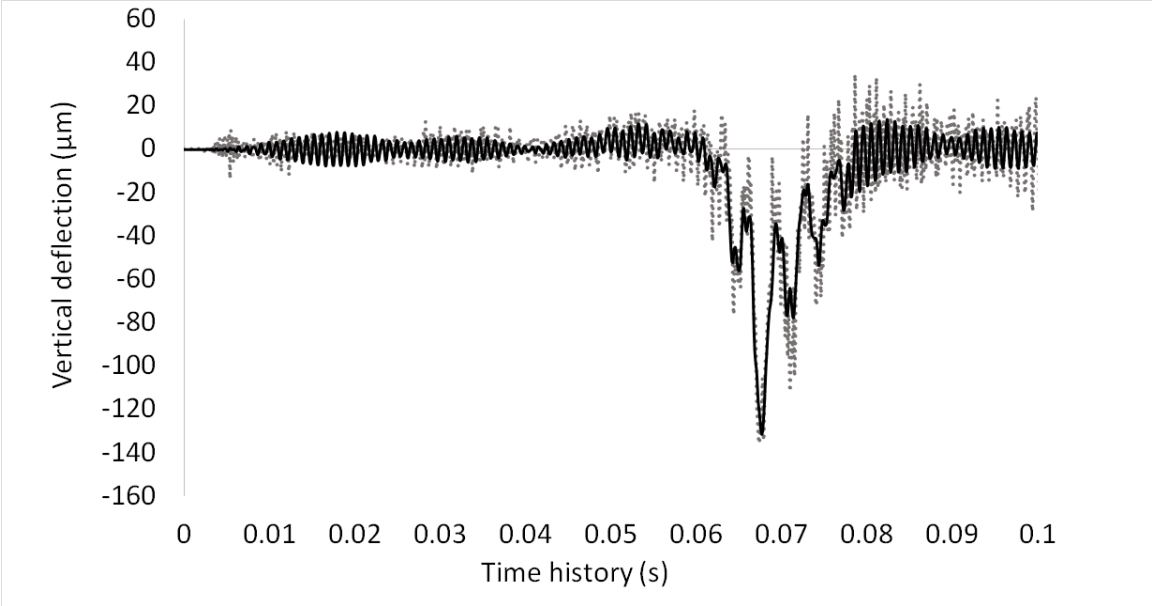

Figure 4.31 Vertical deflection at Point 6: —, Scaled TPL; …, WRM; (c) $v = 40\ \frac{m}{s}$, and (d) $v = 30\ \frac{m}{s}$.

(e)

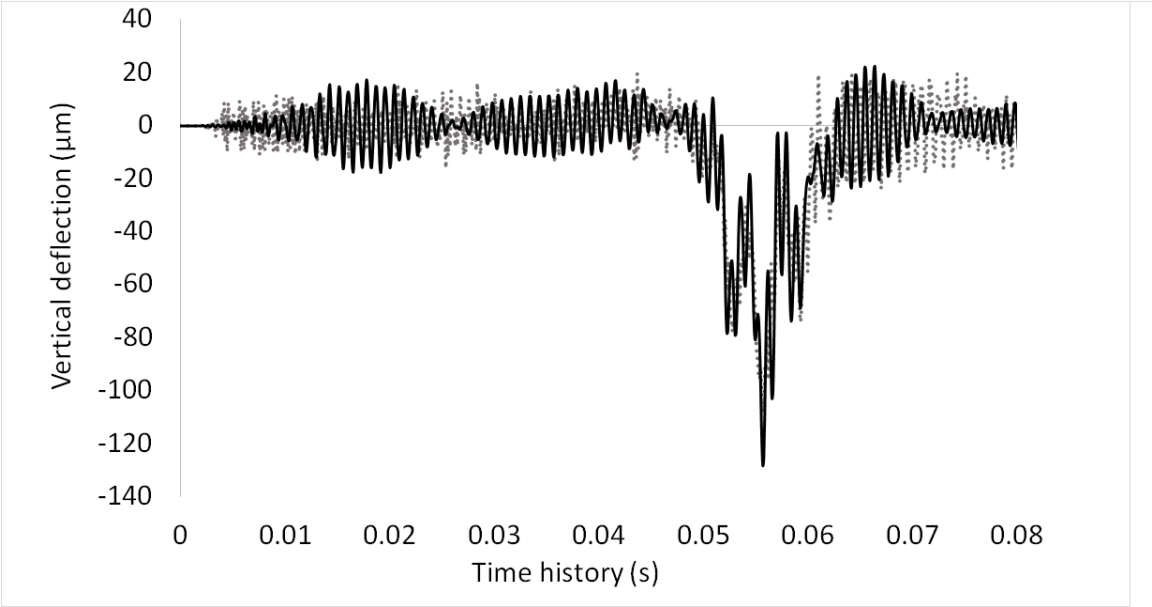

(f)

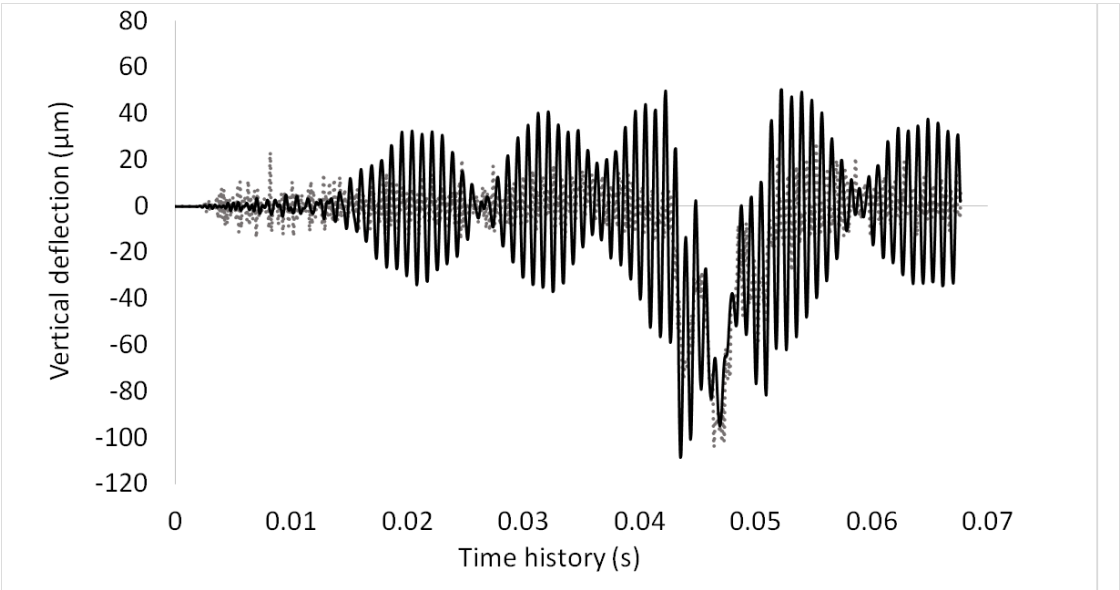

Figure 4.31 Vertical deflection at Point 6: —, Scaled TPL; …, WRM; (e) $v = 50\ \frac{m}{s}$, and (f) $v = 60\frac{m}{s}$.

4.3.3 Discussion

Although the difference still appears in longitudinal deflection at some specific speeds, such as 10 m/s, 20 m/s, and 30 m/s, the vertical deflection from the scaled TPL is much closer to the 3D FE WRM than the non-scaled TPL results. However, the vertical deflection from non-scaled TPL is closed to the FE WRM at 10 m/s as indicated in Figure 4.24(a). On the other hand, the results presented in Figure 4.32 indicated that the average amplitudes of the vertical forces are independent of the speed starting around 23 m/s. In this figure, the results for Paths 1 and 3 are close to each other because they are obtained from the equidistant nodal points on both sides of Path 2.

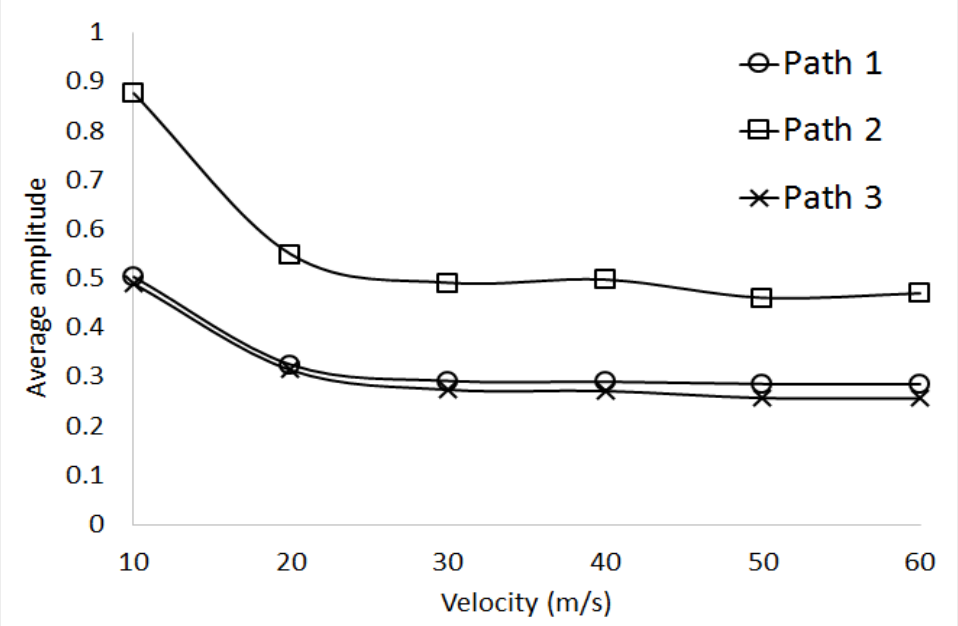

Figure 4.32 Relation between average amplitudes of vertical forces and speed for 3D FE wheel-rail model.

The computed average maximum and minimum shear forces are shown in Figure 4.33. In the latter, the results for Paths 1 and 3 are close to each other for the same reason as for the results in Figure 4.32.

(a)

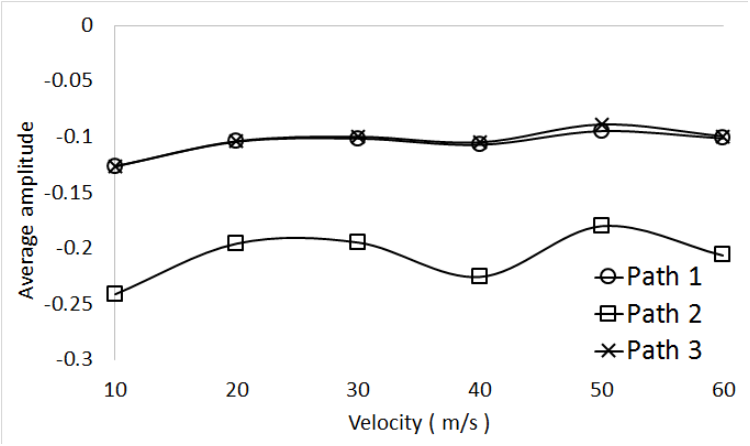

(b)

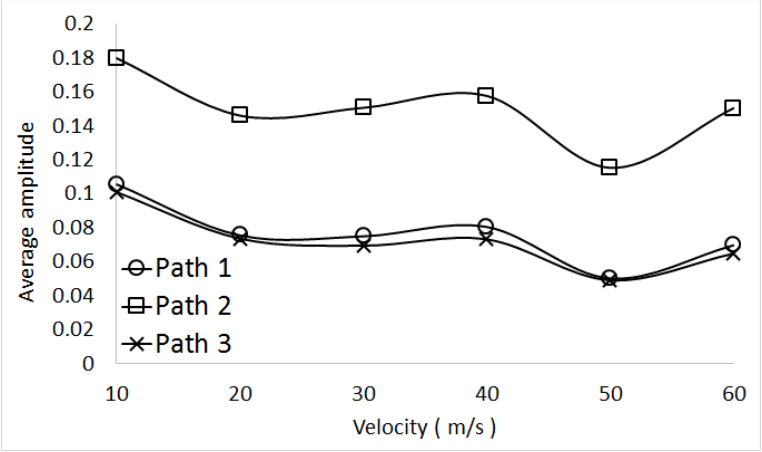

Figure 4.33 Relation between average amplitudes of shear forces and speed: (a) average minimum shear forces, and (b) average maximum shear forces.

CHAPTER 5 RAIL MODELS WITH BLOCK DAMPERS

Periodically, the train companies need to maintain rails and the main part of the maintenance involves with machining some sections of the rail. Such a maintenance is usually performed at night when the train system is closed. However, it takes time and the process is expensive. If vibration amplitude of the rail is large, maintenance becomes more frequent. Therefore, how to reduce the vibration of rail is important from the economical and safety points of view. Among various approaches the method of adding mass block dampers or simply called block dampers has been suggested recently. The philosophy behind this approach seems to be that of the so-called tuned mass damper (TMD) in earthquake-resistant design in which a single degree-of-freedom (dof) mass-dashpot-and-spring system is attached to the primary building structure so that the response of the building or system may be reduced. In the case of railway vibration reduction by attaching mass block dampers (BD), there are very limited number of studies reported in the literature. Therefore, there is a need for further understanding the effect of adding BD on the dynamic responses of the rail. To reduce the amount of computation and therefore cost the approach of replacing the 3D FE wheel-rail system by the 3D FE rail with scaled TPL is adopted in this chapter. The focus of the studies in this chapter is therefore in the comparison of computed results between the scaled TPL model without BD to that with BD. Another main objective in this chapter is the study of the effect of the locations of BD on dynamic responses. The total mass of the BD is also of interest.

5.1 MODELING 3D FE RAIL MODEL WITH BLOCK DAMPERS

In Sub-section 4.3.2, it was observed that the scaled TPL can approximately represent the 3D FE wheel-rail model. This is particular true of the results of the vertical deflection. In this section, the effects of BD on the responses of the scaled TPL model is investigated. For adding BD to the 3D FE rail model, the BD are attached to the rail or the so-called constrained by “tie” in the context of Abaqus. From Abaqus documentation [5.1], tie constraint is by forming two surfaces tied together. In addition, each nodal value such as displacement, temperature, pore pressure or electrical potential on slave surface has the same values of the master surface. Also, tie constraint allows rapid transitions in element mesh density within the model. The discretization method of tie constraint is surface-to-surface formulation. The reason to choose this method is avoiding stress noise at the tied interfaces. It is important for adding BD without bringing more irrelevant results into the modified model.

5.1.1 Dimension of Block Dampers

Dimensions of BD are related to the length of rail span which is 0.6 m in the rail system chosen. By adding the BD the total mass of the rail system changes without changing the rail itself. Therefore, the dimensions of BD are restricted by the length of rail span and the height of rail. In addition, owing to considering the effects of the total mass of BD with respect to the rail mass, the same location needs to be added with different masses of BD. To study the effects of different total mass at the same location on the 3D FE rail model, the only variable is the length. Table 5.1 shows the dimensions of three types of BD.

Table 5.1 Dimensions of three types of BD in different locations.

Type	*1*			*2*			*3*		
Width (cm)	*4.45*								
Length (cm)	*30*			*15*			*10*		
Height (cm)	*6*	*7*	*8*	*6*	*7*	*8*	*6*	*7*	*8*
% rail mass	*22*	*26*	*30*	*22*	*26*	*30*	*22*	*26*	*30*
Location	*Location 1*			*Location 2*			*Location 3*		
Number of BD	*10*			*20*			*30*		

5.1.2 Locations of Block Dampers on 3D FE Rail Model

To study the effects of different locations with same total mass of BD, the total mass of BD needs to be kept the same at each location. Figure 5.1 illustrates the different locations. In Figure 5.1(a) one Type 1 BD on both sides of the single span is identified as “Location 1”. The different total percentages of mass of BD with respect to that of the rail are 22%, 26%, and 30% rail mass. In Figure 5.1(b) two Type 2 of BD on both sides of the rail are called “Location 2”. The different total percentages of the mass of BD with respect to that of the rail are 22%, 26%, and 30% rail mass. In Figure 5.1(c) three Type 3 of BD on both sides are referred to as “Location 3”. The different total percentages of the mass of BD with respect to that of the rail are also 22%, 26%, and 30% rail mass.

(a)

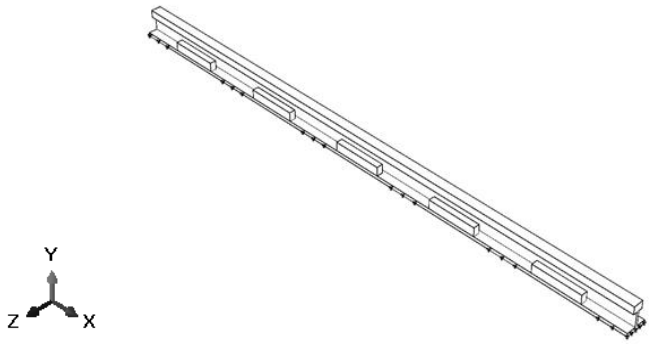

(b)

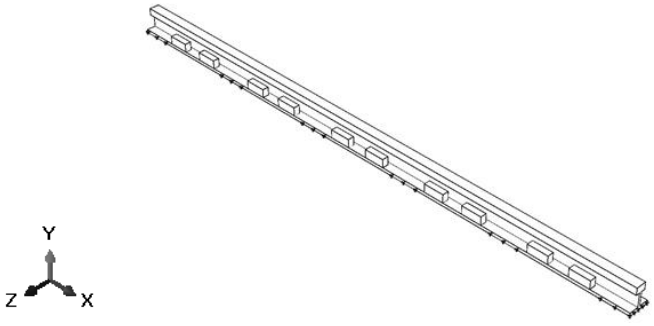

(c)

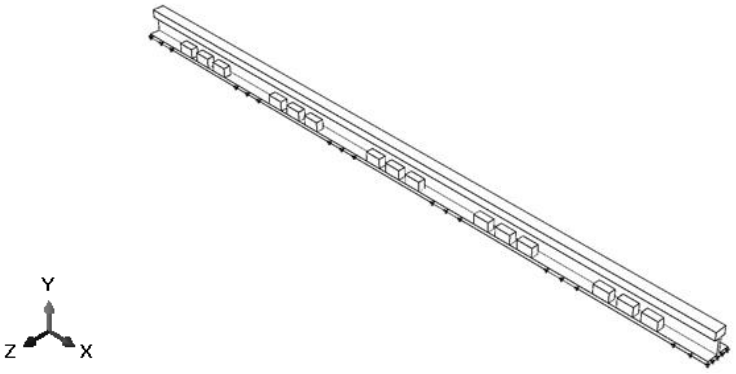

Figure 5.1 Three different locations for placing BD:

(a) Location 1, (b) Location 2, and (c) Location 3.

5.2 RESULTS OF 3D FE RAIL MODEL WITH BLOCK DAMPERS

In the computational process and by making use of the scaled TPL to represent the 3D FE wheel-rail model, BD is added to the 3D FE rail model. It should be mentioned there are many computed deflections and only representative ones are presented in this section. The chosen points for computed results are Points 4, 5, and 6 (see, Chapter 4). In every case the speeds of the train or TPL are 10, 20, 30, 40, 50, and 60 m/s. The following sub-sections are concerned with the effects of every specific case. For the vertical deflection, because computed results of the scaled TPL model showing the largest magnitude of deflection being negative, the results of the same rail model with BD should be negative. For the longitudinal deflection, it involves with maximum and minimum deflections due to friction, and therefore, the 3D FE results also show corresponding maximum and minimum values of deflections. This is consistent with the fact that friction force between the wheel and rail behaves in a matter best described by the signum function. The computed results of the effects of BD are presented in Sub-suctions 5.2.1 and 5.2.2.

5.2.1 Effects of Block Dampers at Different Locations

In the forging section, it was mentioned that the same total mass of BD at different locations was maintained. This helps to understand the effects of BD at different locations. Therefore, the following table shows the comparison of results of the same total mass of BD at different locations for the case with BD and that without BD. Tables 5.2 through 5.4, and Figures 5.2 through 5.10 show the percentages of difference with respect to the 3D FE rail model with scaled TPL.

Table 5.2 Percentages of difference between model with and without BD at Point 4:
(a) Maximum longitudinal deflection, and (b) Minimum longitudinal deflection.

(a) Speed	22 % of rail mass			26 % of rail mass			30 % of rail mass		
	Location 1	Location 2	Location 3	Location 1	Location 2	Location 3	Location 1	Location 2	Location 3
10 m/s	-3.98381	1.094515	2.37507	-6.15523	1.635306	2.103024	-9.62568	2.192929	-0.1651
20 m/s	-1.34384	-2.55261	0.189227	-1.56845	-2.11815	2.431086	-2.86985	0.74327	5.475921
30 m/s	15.31996	20.70944	36.63167	18.40437	1.18612	17.9551	-11.4938	37.80618	7.542432
40 m/s	-4.52392	5.289607	0.259703	1.583953	-2.33574	10.47015	-1.20089	1.625306	14.33492
50 m/s	11.04954	27.16866	1.901505	-4.9392	5.558813	6.128171	1.904284	6.037687	15.1671
60 m/s	-2.16138	15.76267	3.019394	20.75725	0.496167	9.70925	0.631073	6.666701	-5.37732
(b) Speed	22 % of rail mass			26 % of rail mass			30 % of rail mass		
	Location 1	Location 2	Location 3	Location 1	Location 2	Location 3	Location 1	Location 2	Location 3
10 m/s	-4.59563	-0.73345	-0.80112	-4.17286	-0.40453	-2.12551	0.633845	-2.6395	3.159938
20 m/s	-2.92788	-2.70113	0.502613	-2.16685	-3.08045	6.211932	-5.89007	-1.49419	-0.49529
30 m/s	46.33259	170.4245	205.8832	38.33509	57.18718	104.5183	87.26754	181.9376	88.00651
40 m/s	25.40295	-7.87023	25.07794	12.66589	2.892155	30.22657	-14.8597	16.60347	-12.8761
50 m/s	-24.8407	-4.84047	-29.4814	-20.2254	2.61156	-17.0714	-18.2033	-29.9313	-16.2511
60 m/s	-41.8347	-31.4305	-34.7012	-28.868	-26.2453	-35.8268	-32.2932	-32.0959	-27.2921

Table 5.2 Percentages of difference between model with and without BD at Point 4:
(c) Minimum vertical deflection.

(c) Speed	22 % of rail mass			26 % of rail mass			30 % of rail mass		
	Location 1	Location 2	Location 3	Location 1	Location 2	Location 3	Location 1	Location 2	Location 3
10 m/s	-0.16647	-1.80671	0.241565	-0.25541	-1.54626	0.032667	0.220809	-1.39288	0.758295
20 m/s	4.228559	-1.04136	3.782413	4.707793	0.048627	3.749866	0.661755	2.37363	4.450815
30 m/s	10.13347	12.15723	24.32913	23.64929	-5.31928	22.72971	3.081842	19.91195	7.741633
40 m/s	-4.32095	8.695306	13.07627	0.185092	3.498573	22.57927	6.27331	14.64843	29.79551
50 m/s	6.633146	15.96392	-3.5977	6.351486	11.67599	2.894866	4.784051	-2.78144	-1.01937
60 m/s	-25.9448	-19.7529	-30.3503	-24.7496	-21.9834	-30.2425	-14.9521	-34.2873	-5.72411

Table 5.3 Percentages of difference between model with and without BD at Point 5:
(a) Maximum longitudinal deflection (b) Minimum longitudinal deflection.

(a) Speed	22 % of rail mass			26 % of rail mass			30 % of rail mass		
	Location 1	Location 2	Location 3	Location 1	Location 2	Location 3	Location 1	Location 2	Location 3
10 m/s	-3.35534	-3.42964	-0.98389	-3.50034	-3.46804	-0.97565	-3.74957	-3.45184	-0.98132
20 m/s	-2.07407	-1.81455	-0.15078	-2.35549	-1.84949	-0.52536	-1.33024	-1.85126	0.339537
30 m/s	21.58393	3.728221	27.15768	6.210831	5.230126	8.25202	7.062242	26.17448	1.791124
40 m/s	7.203558	4.025392	-5.36921	0.254624	-6.48197	-1.13674	-0.52648	-7.21093	-1.58631
50 m/s	-6.47186	20.09247	2.486622	-3.31506	2.712303	2.372736	4.360442	11.39531	8.328956
60 m/s	-15.3796	3.36412	8.964696	10.13357	15.43206	-4.41934	-12.8733	-11.6442	-15.5709
(b) Speed	22 % of rail mass			26 % of rail mass			30 % of rail mass		
	Location 1	Location 2	Location 3	Location 1	Location 2	Location 3	Location 1	Location 2	Location 3
10 m/s	-3.00456	-3.38648	-1.25452	-3.58265	-3.19558	-0.75453	-3.95918	-3.17023	-0.68325
20 m/s	-3.66243	-3.15976	1.146182	-2.69088	-4.54382	-3.80017	-0.9477	-4.31756	-1.81014
30 m/s	16.44034	5.606858	22.5626	12.68906	7.335022	4.214197	8.895053	20.86694	-4.86194
40 m/s	-6.09602	-6.35762	-2.50434	-6.55873	-2.65242	10.70337	-3.11169	-3.19859	5.614894
50 m/s	12.56833	17.72045	6.85887	-1.9023	0.457532	1.25301	-3.7055	-1.76775	-2.3264
60 m/s	18.71923	-2.64867	15.60285	18.09562	-2.81461	-1.01407	12.4275	9.697538	23.86417

Table 5.3 Percentage of difference between model with and without BD at Point 5:
(c) Minimum vertical deflection.

(c) Speed	22 % of rail mass			26 % of rail mass			30 % of rail mass		
	Location 1	Location 2	Location 3	Location 1	Location 2	Location 3	Location 1	Location 2	Location 3
10 m/s	-2.20266	0.612491	2.068243	-2.8229	1.101636	2.474555	-4.29363	1.680885	2.10991
20 m/s	-1.40178	-0.20294	1.876744	-5.07808	-0.26445	1.373663	-5.43963	2.276711	1.994513
30 m/s	-5.44028	4.669839	12.48905	-4.63165	-0.45813	-5.05283	-14.6826	11.03329	-4.19257
40 m/s	-4.00567	6.101246	6.217715	-0.40466	3.014915	16.66148	-2.07173	6.830587	10.37618
50 m/s	-0.8787	11.72413	-1.11656	-3.05942	1.37024	5.217729	-0.80229	1.111148	11.23823
60 m/s	1.925886	15.79456	3.632062	16.78083	-3.23917	14.92988	-1.65205	6.368374	-9.45556

Table 5.4 Percentage of difference between model with and without BD at Point 6:

(a) Maximum longitudinal deflection (b) Minimum longitudinal deflection.

(a) Speed	22 % of rail mass			26 % of rail mass			30 % of rail mass		
	Location 1	Location 2	Location 3	Location 1	Location 2	Location 3	Location 1	Location 2	Location 3
10 m/s	-3.2072	-1.42793	1.248552	-3.1234	-0.7991	1.121775	-3.48197	-0.57425	1.069288
20 m/s	0.523489	-7.71674	-4.39209	0.309212	-5.79176	0.028292	-4.4037	-6.45398	2.692797
30 m/s	49.6157	96.52574	132.1681	64.48735	32.78684	121.3391	44.95682	107.0619	32.16832
40 m/s	24.67316	1.685474	36.19154	18.1483	-8.37661	22.32096	-0.0573	19.47948	31.32525
50 m/s	-32.6552	4.317339	-38.0781	-34.1258	2.109998	-37.1851	-27.9092	-36.9408	-22.2601
60 m/s	-39.0112	-37.5591	-43.8641	-30.3322	-47.4021	-48.6768	-46.0807	-40.9089	-38.6762
(b) Speed	22 % of rail mass			26 % of rail mass			30 % of rail mass		
	Location 1	Location 2	Location 3	Location 1	Location 2	Location 3	Location 1	Location 2	Location 3
10 m/s	-2.80588	0.985167	2.680194	-3.2168	1.576666	4.346972	-3.31458	2.612156	4.265974
20 m/s	-4.42339	2.294071	0.251524	-3.1878	1.648744	3.841704	-6.17373	-0.0308	0.971153
30 m/s	-0.24913	15.46313	13.12916	6.0638	1.969088	6.104713	-6.70916	15.26349	3.912516
40 m/s	-3.07534	-5.15631	3.214389	-4.28139	4.060708	6.868508	-11.6584	5.121538	19.29564
50 m/s	-1.07564	2.618279	1.186149	-4.28488	11.99002	6.318771	1.823602	2.577413	2.901151
60 m/s	0.971308	13.89411	12.47254	20.28249	-11.0655	18.24797	0.439329	10.1114	-4.4667

Table 5.4 Percentage of difference between model with and without BD at Point 6:
(c) Minimum vertical deflection.

(c) Speed	22 % of rail mass			26 % of rail mass			30 % of rail mass		
	Location 1	Location 2	Location 3	Location 1	Location 2	Location 3	Location 1	Location 2	Location 3
10 m/s	1.633974	-1.49215	2.272383	1.870961	-0.53392	4.028568	2.852589	0.660798	4.311629
20 m/s	-0.57568	-1.72083	0.245977	-0.66533	-1.90527	0.851768	-0.0278	-1.68178	0.183539
30 m/s	6.864405	23.17907	21.67469	12.61158	2.482858	2.406463	-0.80542	21.58334	5.111937
40 m/s	2.545864	-1.88471	6.808772	3.913103	8.591397	17.36852	-0.57864	8.256538	25.79255
50 m/s	10.01774	12.29763	5.892619	9.718729	-3.68128	8.287701	5.247605	5.280017	13.94125
60 m/s	-2.72566	5.802728	0.48513	19.50291	-19.046	13.01458	-6.94835	-1.67072	-8.25029

(a)

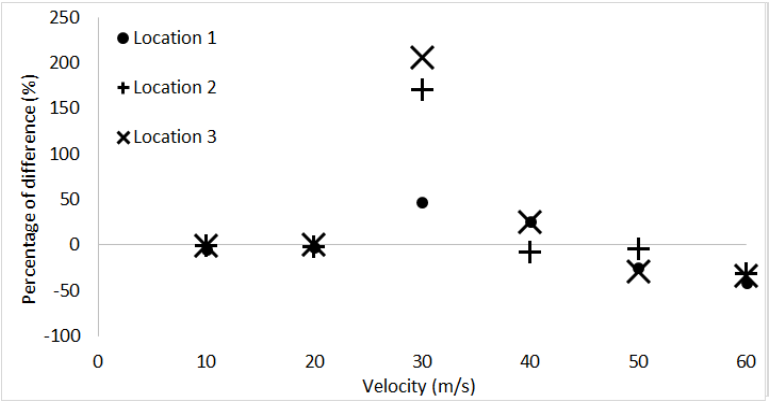

(b)

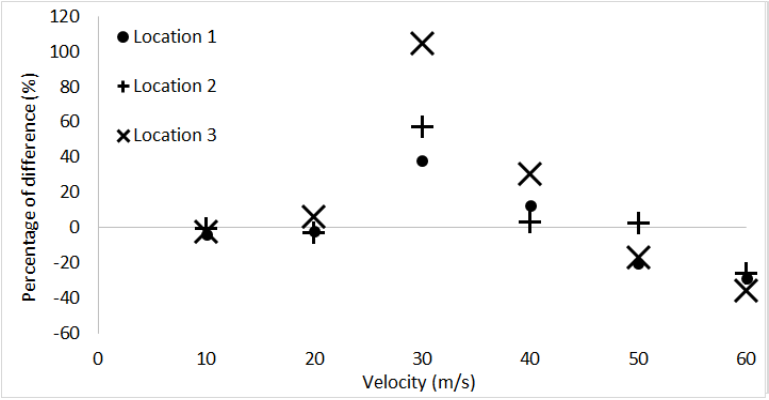

(c)

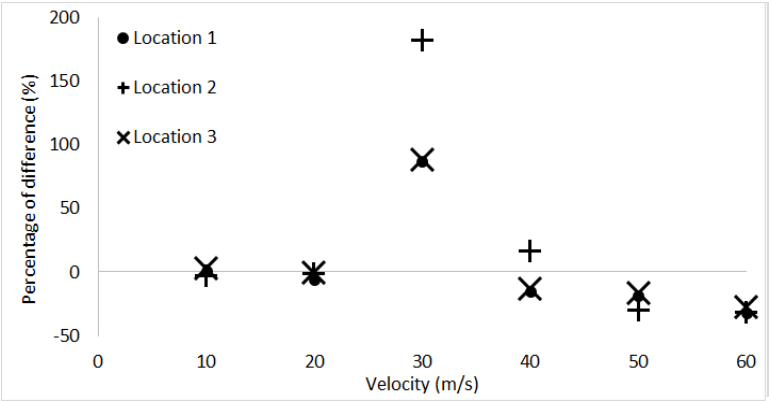

Figure 5.2 Percentage of difference in maximum longitudinal deflection at locations at Point 4 with block dampers of (a) 22%, (b) 26%, and (c) 30% rail mass.

(a)

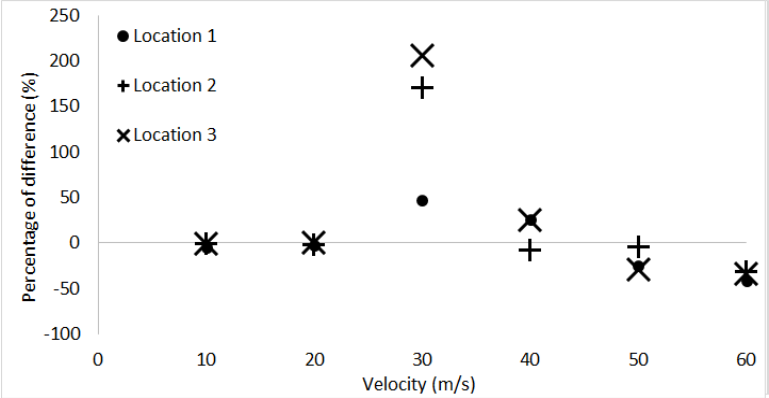

(b)

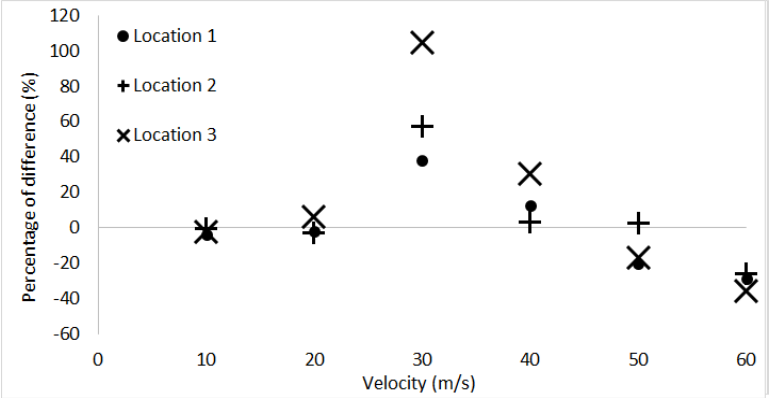

(c)

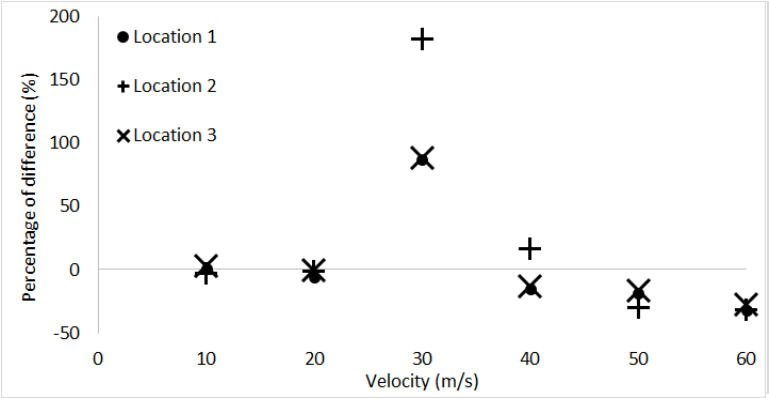

Figure 5.3 Percentage of difference in minimum longitudinal deflection at locations at Point 4 with block dampers of (a) 22%, (b) 26%, and (c) 30% rail mass.

(a)

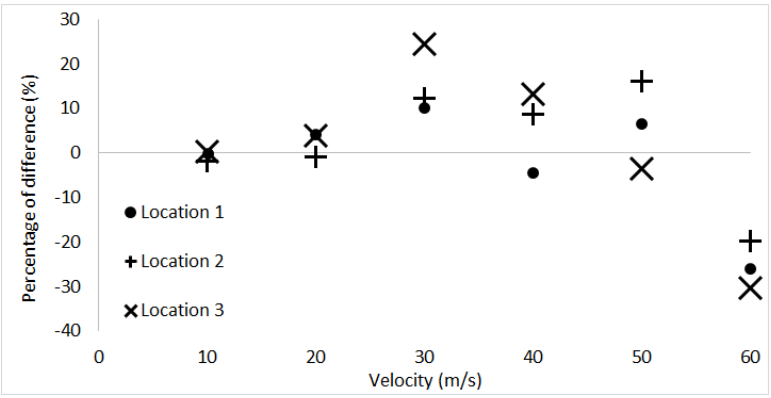

(b)

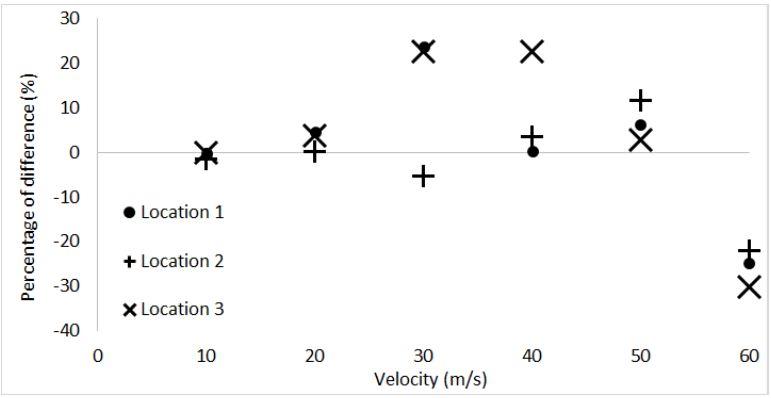

(c)

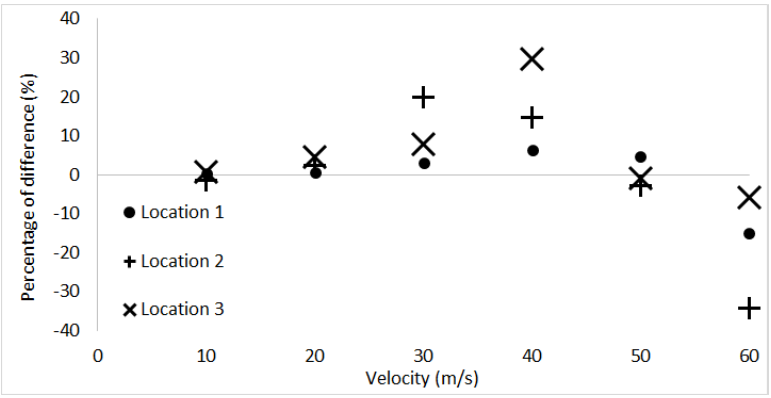

Figure 5.4 Percentage of difference in minimum vertical deflection at locations at Point 4 with block dampers of (a) 22%, (b) 26% , and (c) 30% rail mass.

(a)

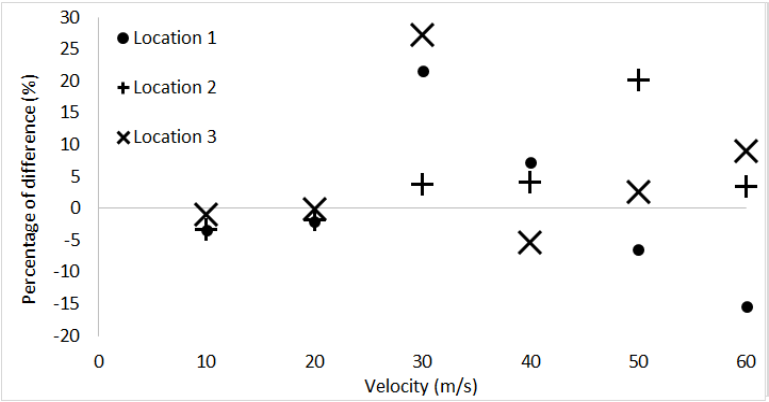

(b)

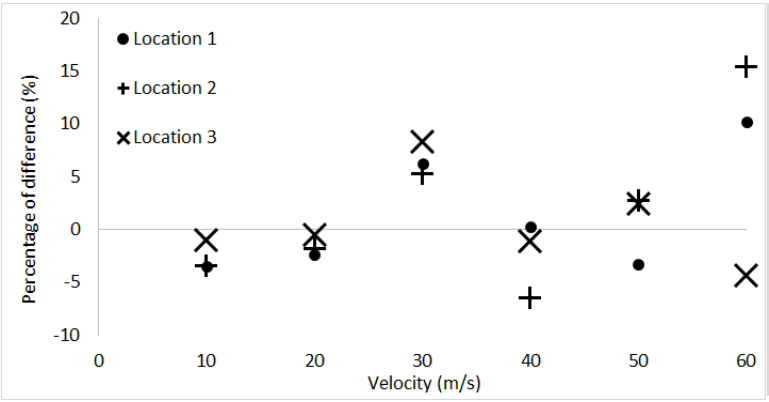

(c)

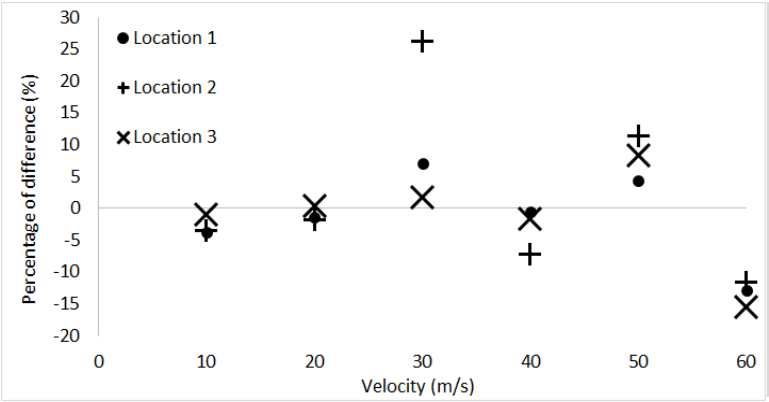

Figure 5.5 Percentage of difference in maximum longitudinal deflection at locations at Point 5 with block dampers of (a) 22%, (b) 26% , and (c) 30% rail mass.

(a)

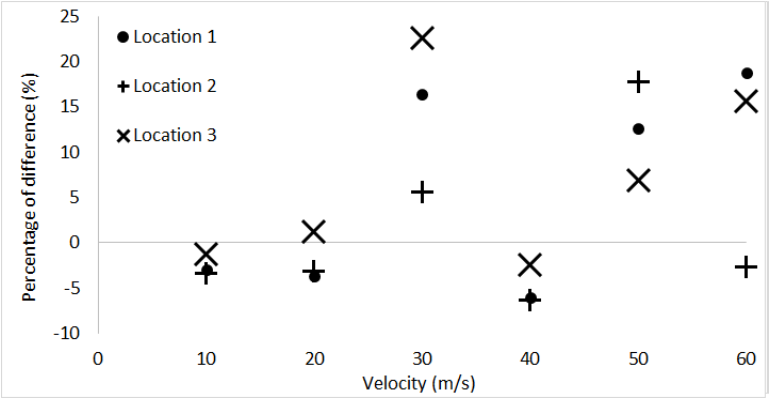

(b)

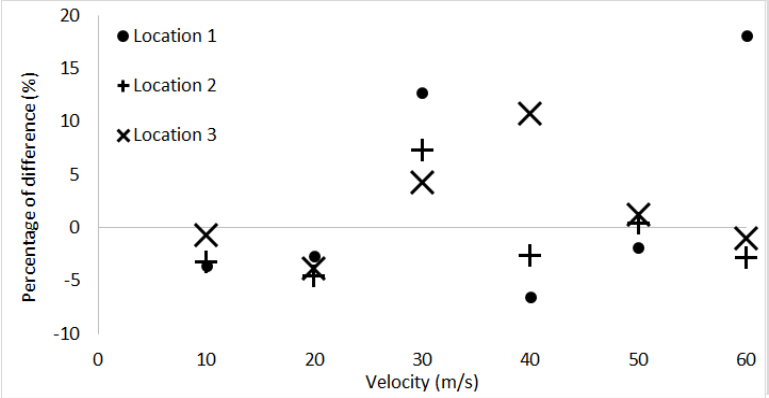

(c)

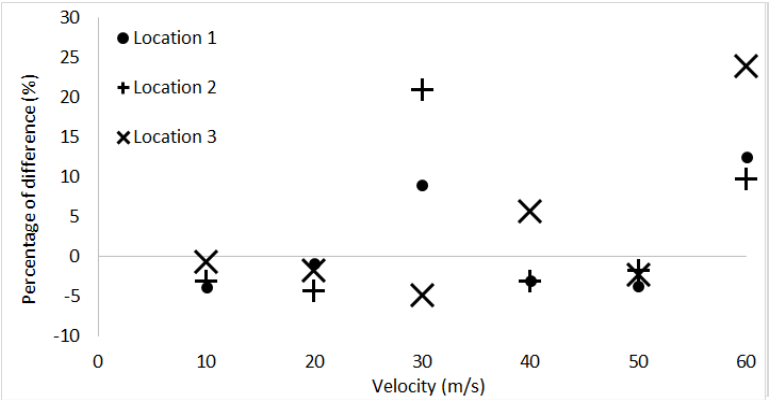

Figure 5.6 Percentage of difference in minimum longitudinal deflection at locations At Point 5 with block dampers of (a) 22%, (b) 26% , and (c) 30% rail mass.

(a)

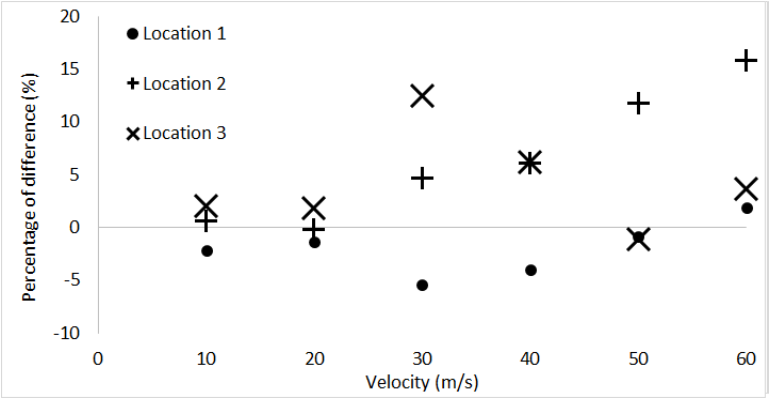

(b)

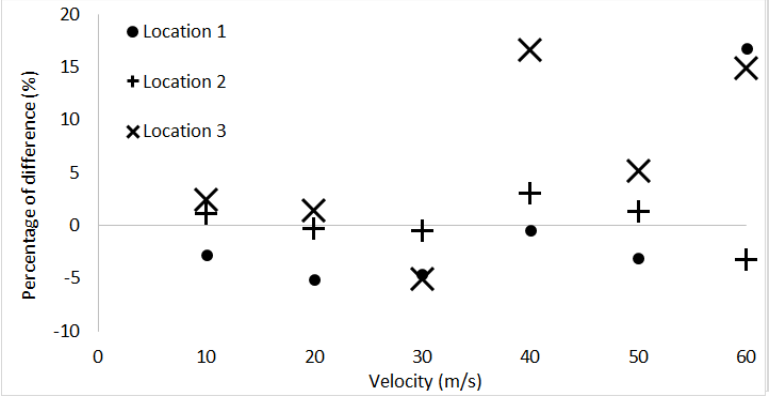

(c)

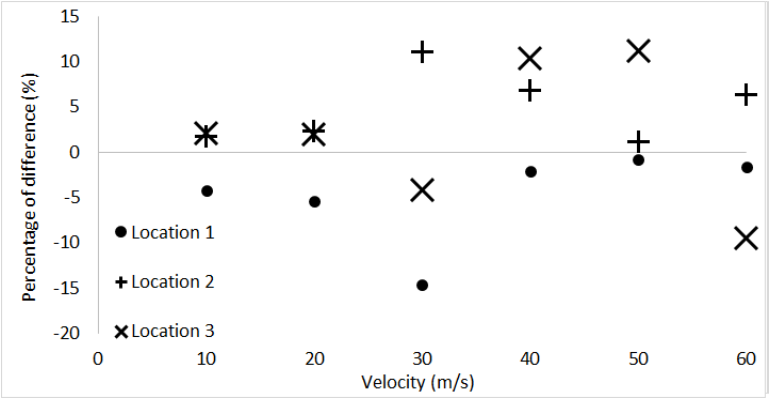

Figure 5.7 Percentage of difference in minimum vertical deflection at locations at Point 5 with block dampers of (a) 22%, (b) 26% , and (c) 30% rail mass.

(a)

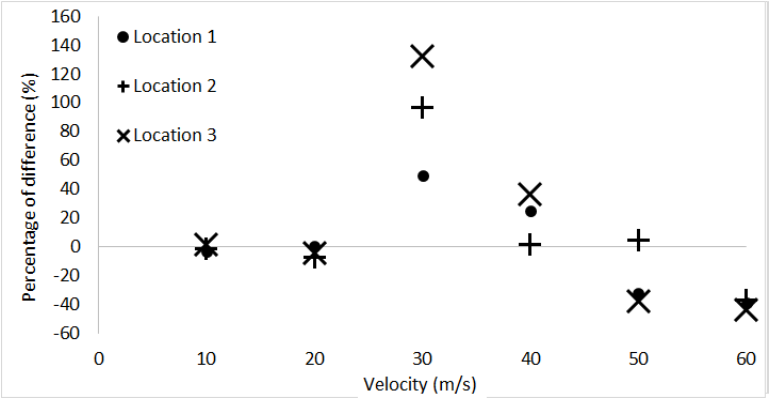

(b)

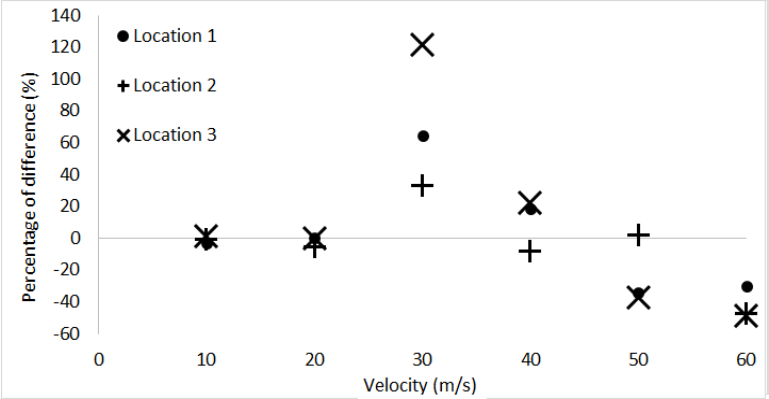

(c)

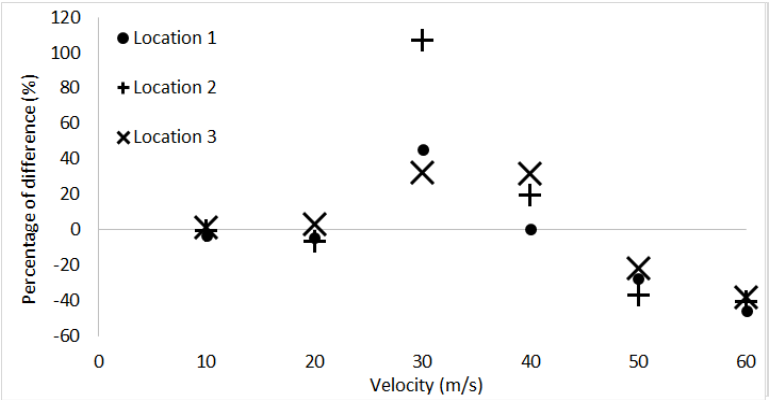

Figure 5.8 Percentage of difference in maximum longitudinal deflection at locations at Point 6 with block dampers of (a) 22%, (b) 26% , and (c) 30% rail mass.

(a)

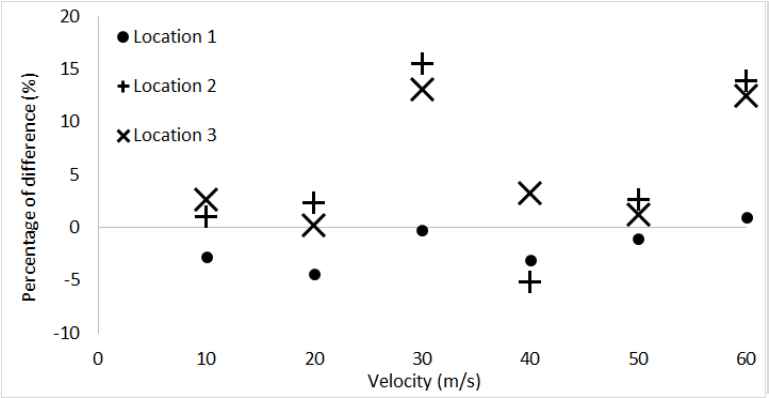

(b)

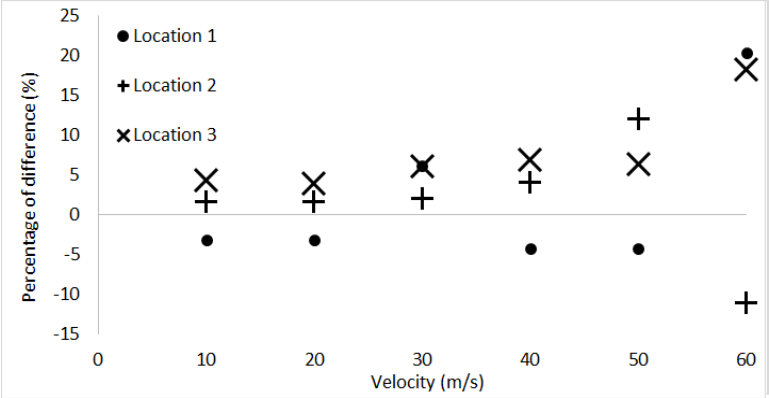

(c)

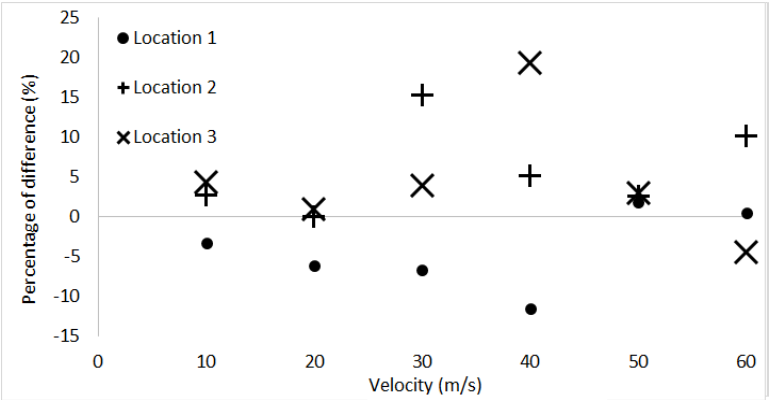

Figure 5.9 Percentage of difference in minimum longitudinal deflection at locations at Point 6 with block dampers of (a) 22%, (b) 26% , and (c) 30% rail mass.

(a)

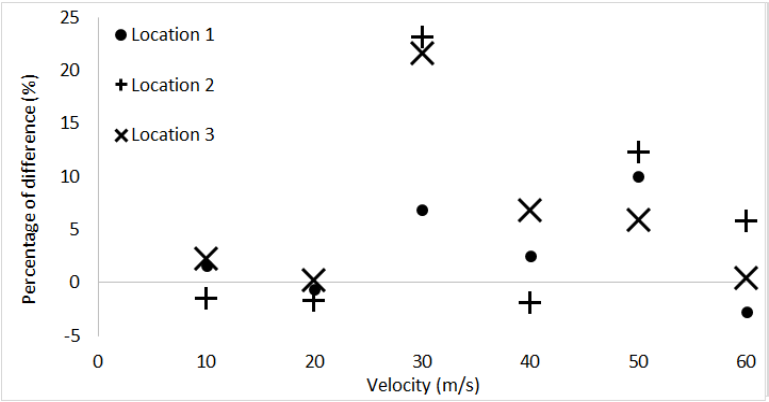

(b)

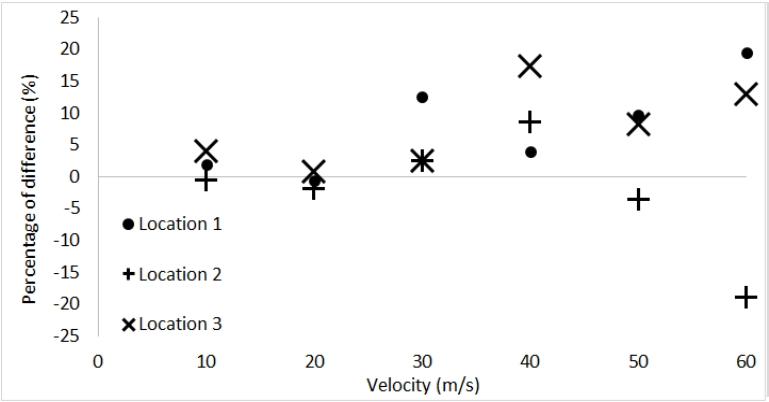

(c)

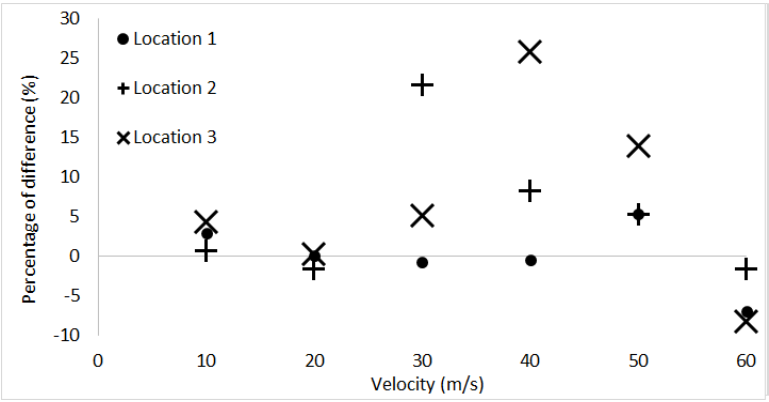

Figure 5.10 Percentage of difference in minimum vertical deflection at locations at Point 6 with block dampers of (a) 22%, (b) 26% , and (c) 30% rail mass.

5.2.2 Effects of Block Dampers with Different Percentages of Rail Mass

After arranged results by locations, in this sub-section, it presents the effects of the total mass of block dampers with respect to rail mass on 3D FE rail model subjected to scaled traveling point. The locations of block dampers are based on the places which are predicted with larger deflections. The difference dimensions of block dampers are used to change the natural frequency. Therefore, the results on Table 5.2 through 5.4 are presented by placing block dampers at same locations and compared with the different mass of block dampers. The height of block dampers is 6 cm, 7cm, and 8 cm. Hence, the total mass of block dampers with respect to rail mass are 22 %, 26%, and 30%, respectively. Figure 5.11 through 5.19 shows the percentages of difference with various block dampers' mass.

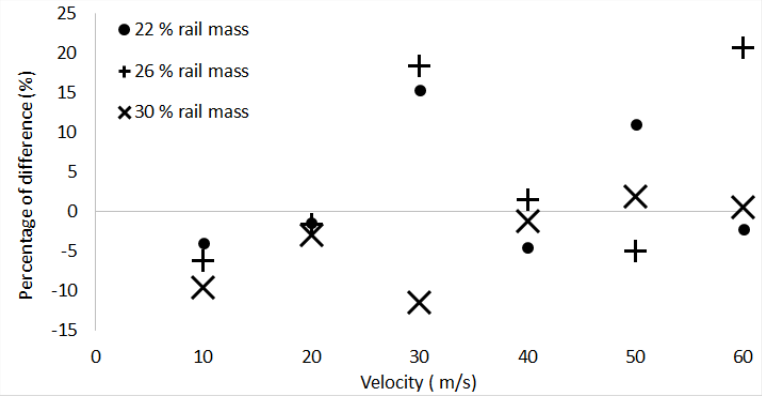

Figure 5.11 (a)

(b)

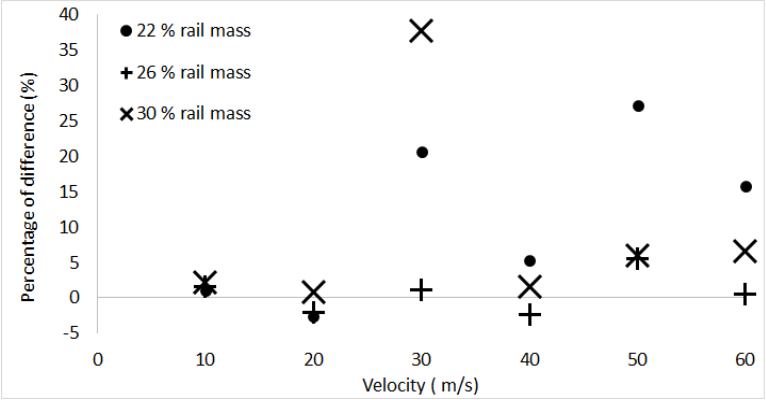

(c)

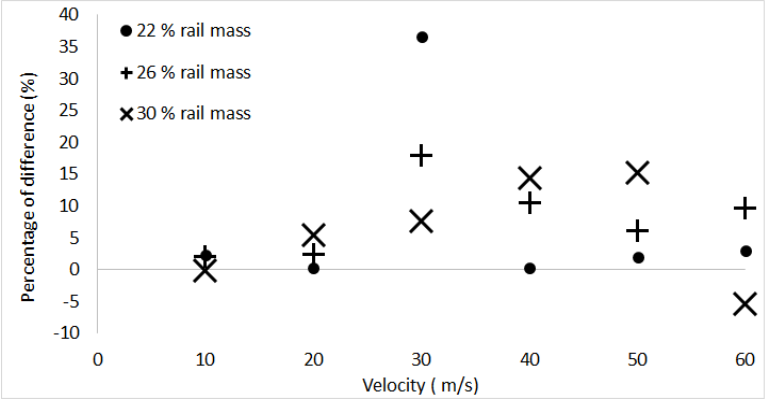

Figure 5.11 Percentage of difference of maximum longitudinal deflection at Point 4. Block dampers with 22% of rail mass (a) Location 1, (b) Location 2, and (c) Location 3.

(a)

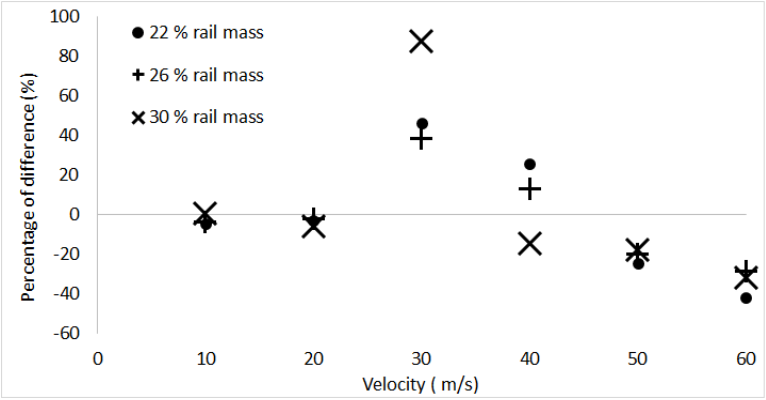

(b)

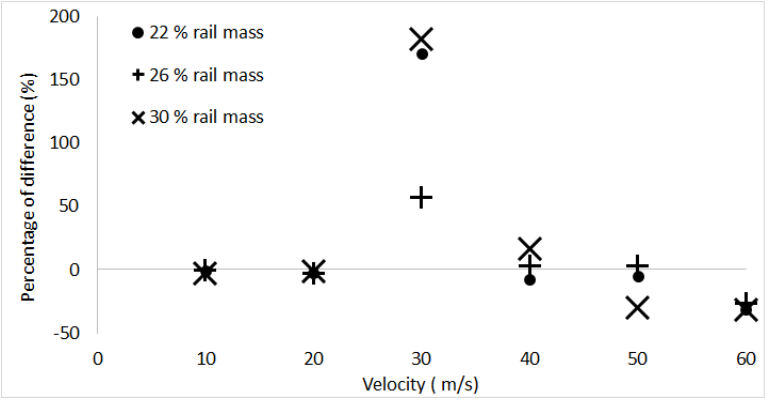

(c)

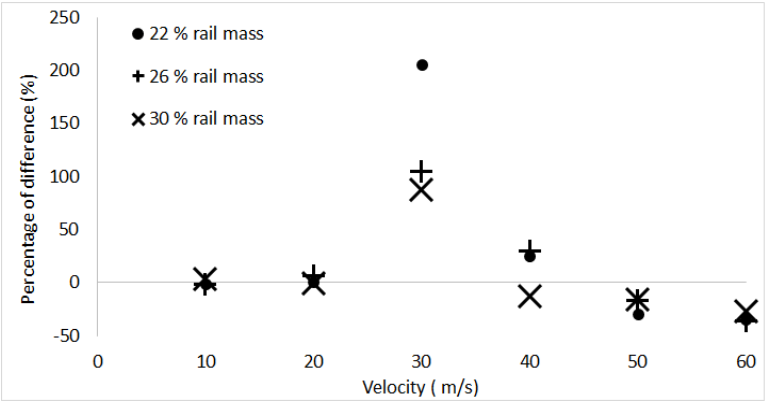

Figure 5.12 Percentage of difference of minimum longitudinal deflection at Point 4. Block dampers with 22% of rail mass (a) Location 1, (b) Location 2, and (c) Location 3.

(a)

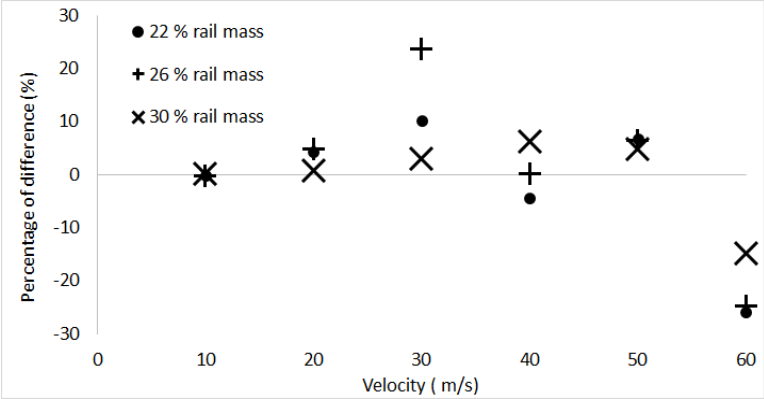

(b)

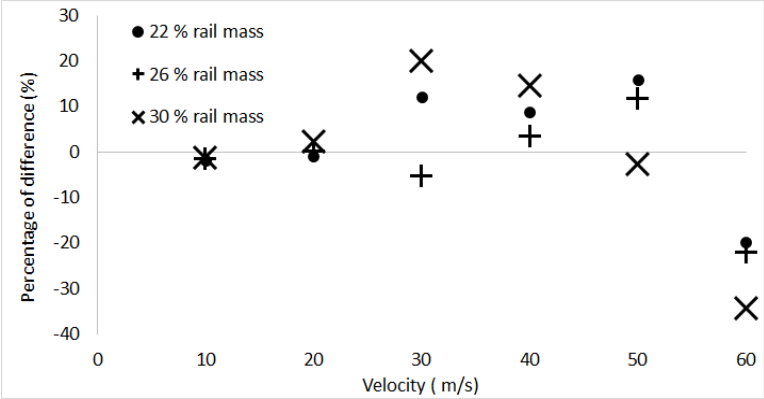

(c)

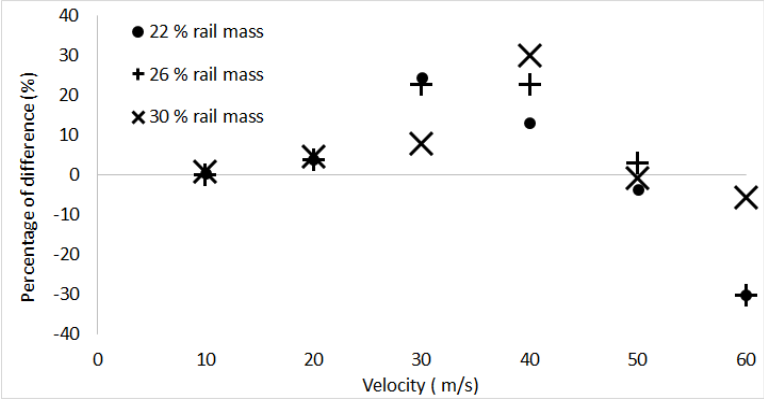

Figure 5.13 Percentage of difference of minimum vertical deflection at Point 4. Block dampers with 22% of rail mas (a) Location 1, (b) Location 2, and (c) Location 3.

(a)

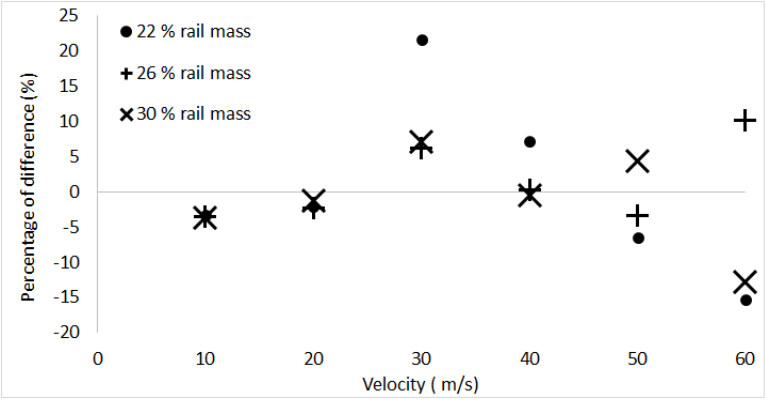

(b)

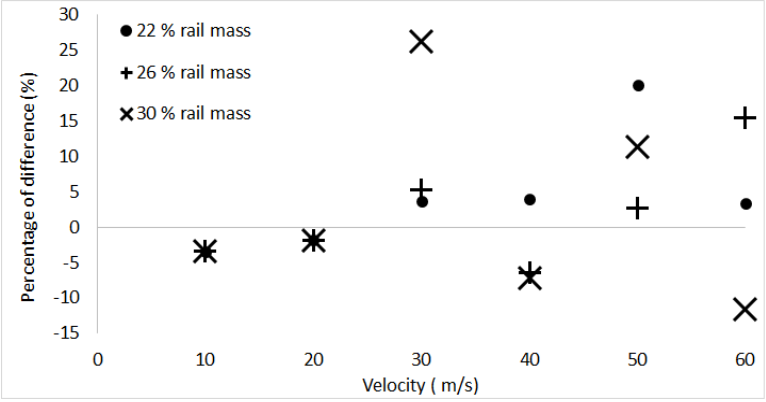

(c)

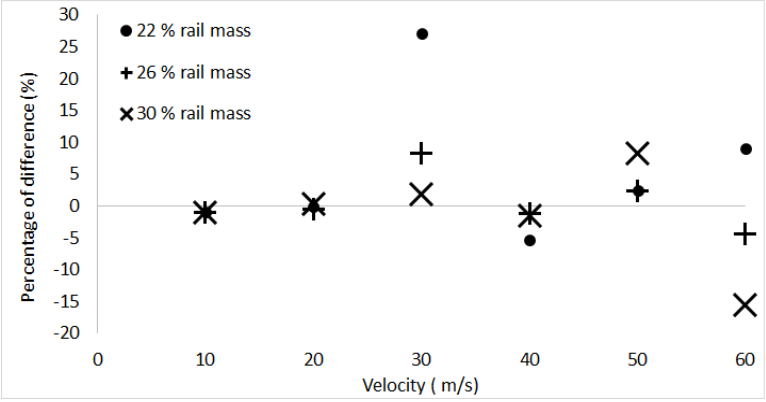

Figure 5.14 Percentage of difference of maximum longitudinal deflection at Point 5. Block dampers with 22% of rail mass (a) Location 1, (b) Location 2, and (c) Location 3.

(a)

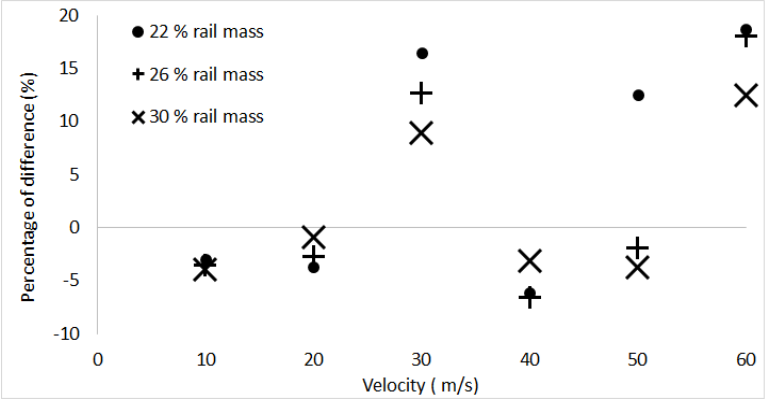

(b)

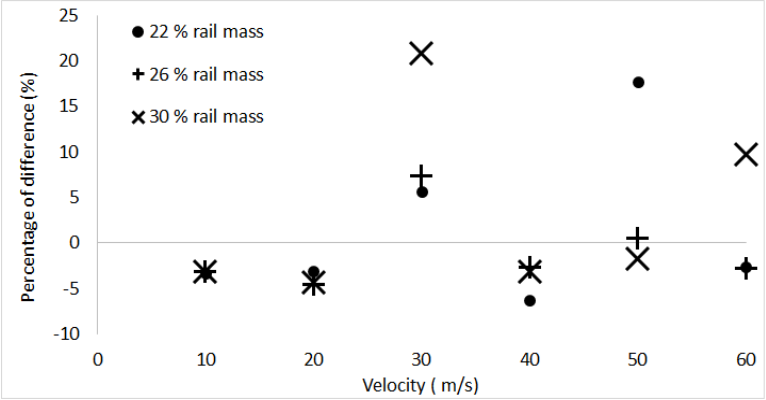

(c)

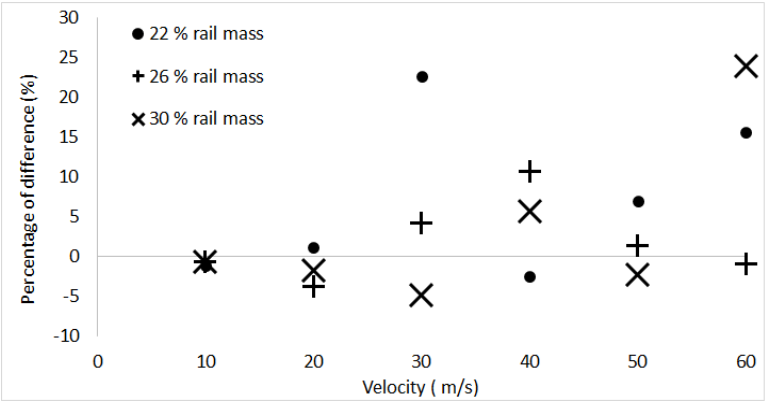

Figure 5.15 Percentage of difference of minimum longitudinal deflection at Point 5. Block dampers with 22% of rail mass (a) Location 1, (b) Location 2, and (c) Location 3.

(a)

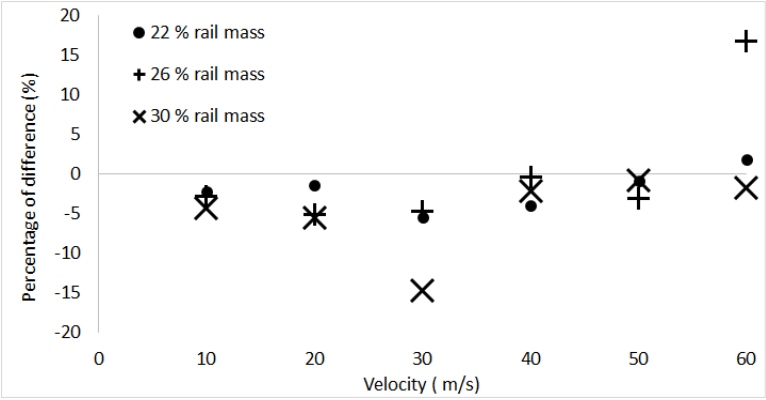

(b)

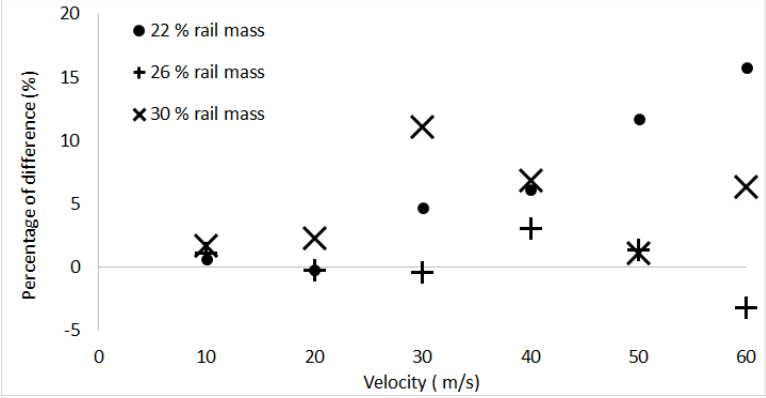

(c)

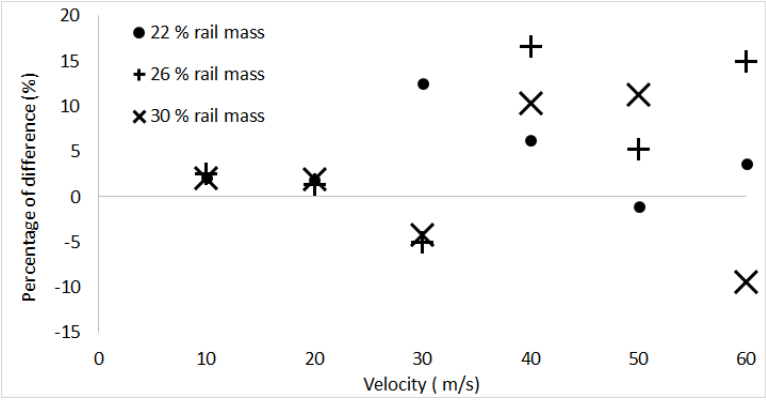

Figure 5.16 Percentage of difference of minimum vertical deflection at Point 5. Block dampers with 22% of rail mass (a) Location 1, (b) Location 2, and (c) Location 3.

(a)

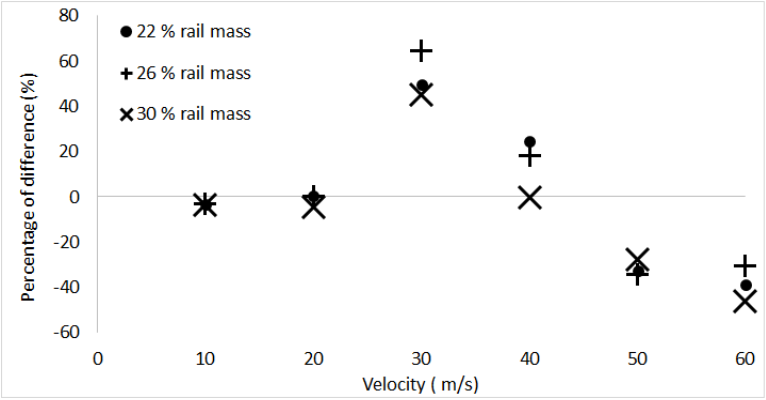

(b)

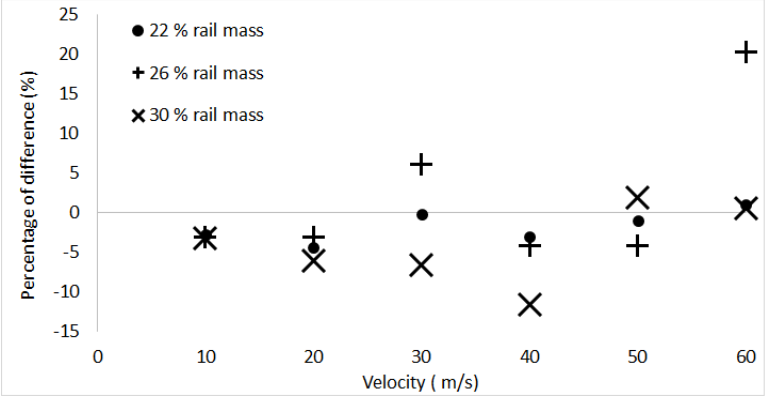

(c)

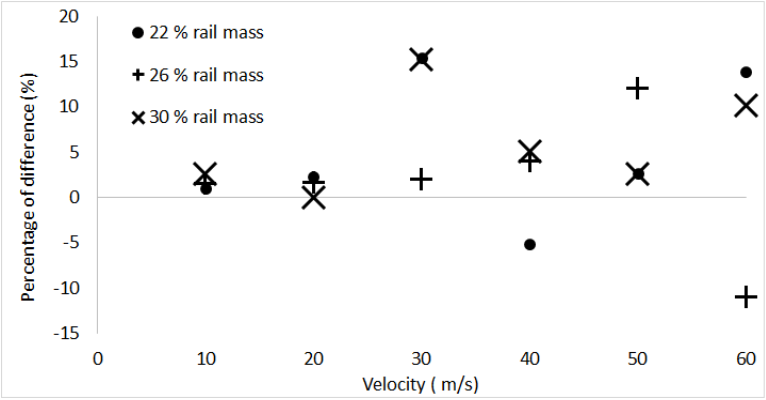

Figure 5.17 Percentage of difference of maximum longitudinal deflection at Point 6. Block dampers with 22% of rail mass (a) Location 1, (b) Location 2, and (c) Location 3.

(a)

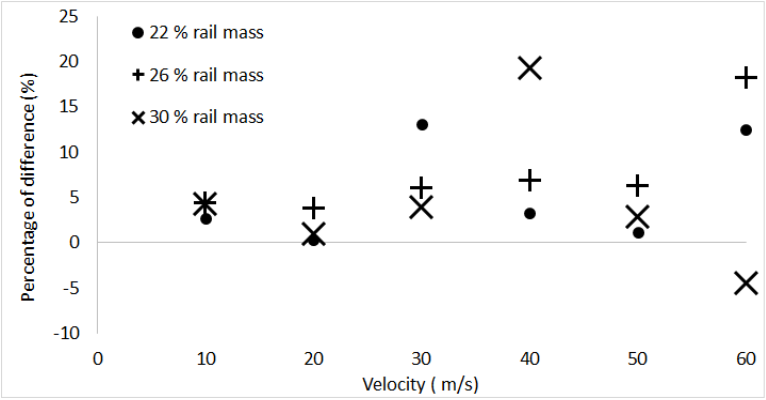

(b)

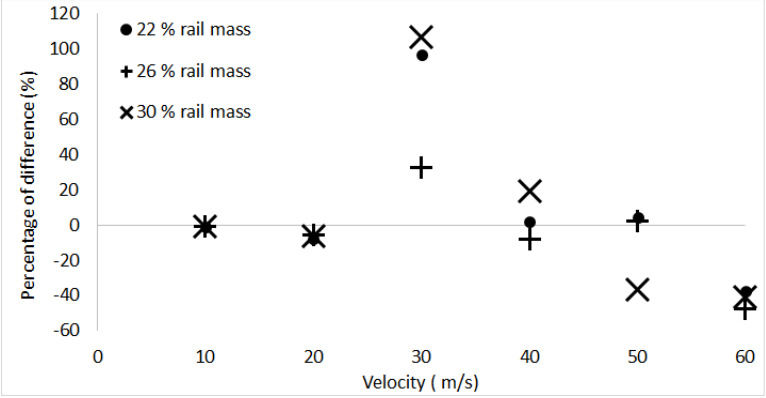

(c)

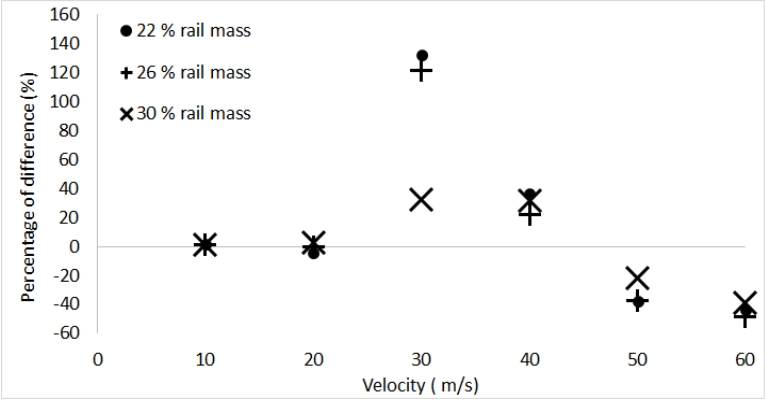

Figure 5.18 Percentage of difference of minimum longitudinal deflection at Point 6. Block dampers with 22% of rail mass (a) Location 1, (b) Location 2, and (c) Location 3.

(a)

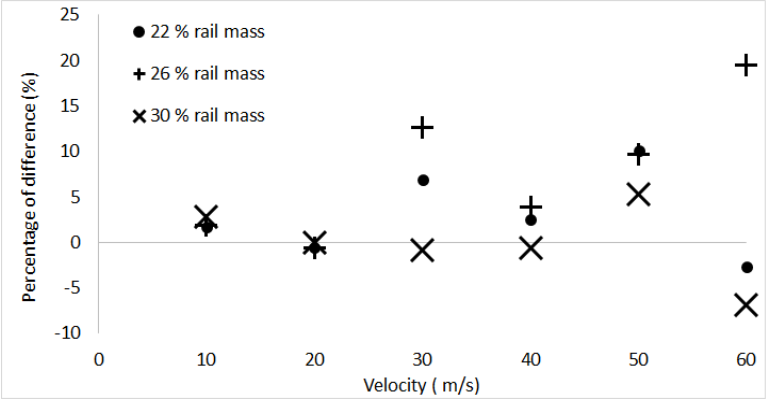

(b)

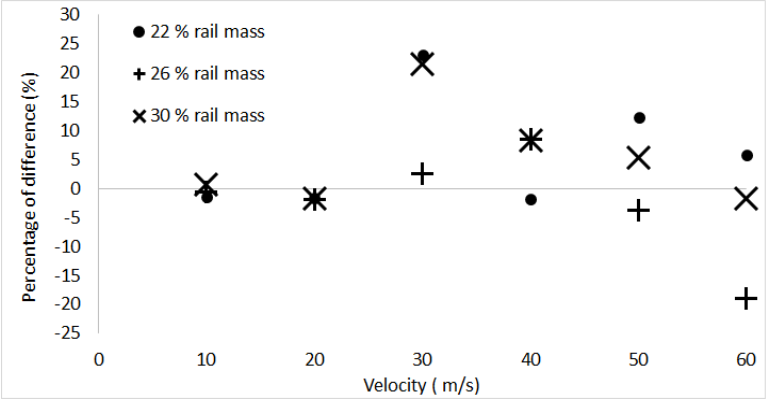

(c)

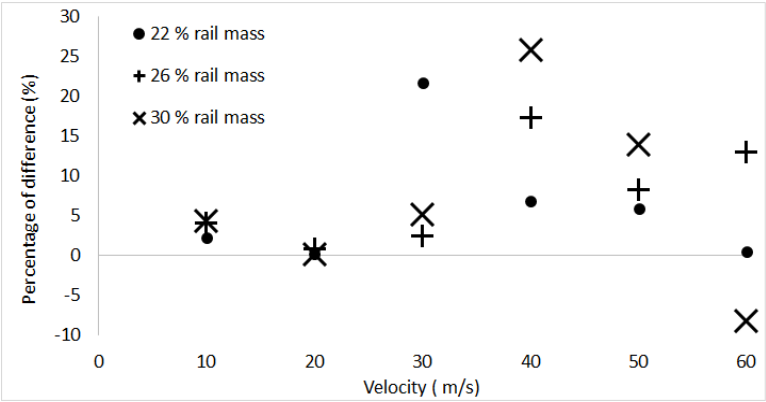

Figure 5.19 Percentage of difference of minimum vertical deflection at Point 6. Block dampers with 22% of rail mass (a) Location 1, (b) Location 2, and (c) Location 3.

5.2.3 Discussion

The results present the quite different in each selected point. When the velocity is up to 30 m/s, the deflections of both direction changed dramatically. The percentage of difference at 10 m/s and 20 m/s seems stable. take point 5 at 30 m/s with 30 % rail mass' block dampers placed on location 1 as an example. (see Figure 5.20) The Figure 5.20 presents the results that before the scaled traveling point load reaches the point 5, it is under oscillating. But, the minimum vertical deflection reduces about 14.6 % of original deflection. In general, the effects of location 1 of block dampers on 3D FE rail model presents better results than the others. At location 1, it is predicted to have the largest deflection based on analytical results and FE beam model presented in Chapter 4. Therefore, adding block dampers at that position can make the effects of traveling point load smaller. In addition, at location 1, the results are mostly better when the mass of block dampers increases. The possible explanation is about natural frequencies. The Table 5.5 presents a case from 3D FE rail mode with the first twelve natural frequencies and shows the results of 22%, 26%, and 30% of rail mass' block dampers placed at location 1 as well. In Table 5.5, it shows the difference with and without block dampers on 3D FE rail model. In addition, the tendency of natural frequency is decreasing while the mass of block damper increases.

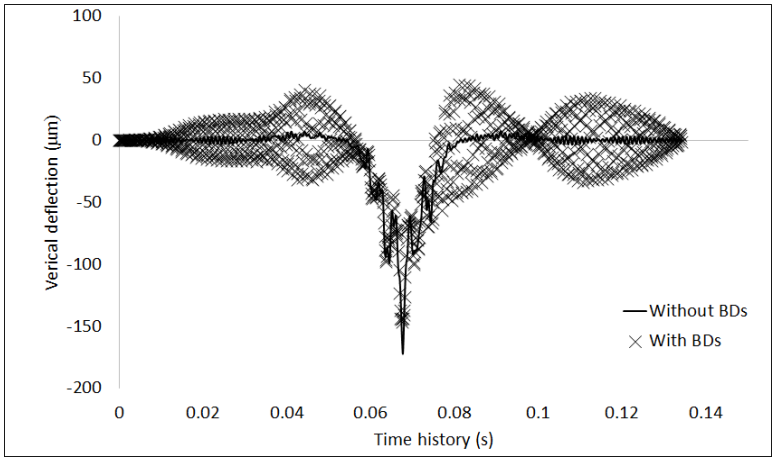

Figure 5.20 Vertical deflection of 3D FE rail model with and without block dampers.

Table 5.5 First twelve natural frequencies of 3D FE rail model and results with block dampers (BD).

(Hz)	Without BDs	22%	26%	30%
1	289	286	283	280
2	303	298	295	291
3	33	328	324	319
4	381	368	362	354
5	432	408	399	386
6	580	576	570	562
7	597	581	573	627
8	655	635	641	637
9	776	700	670	643
10	882	735	689	645
11	998	753	698	800
12	1118	903	847	883

CHAPTER 6 SUMMARY, CONCLUSIONS AND RECOMMENDATIONS FOR FUTURE WORK

6.1 SUMMARY

In the investigation reported presently, in the foregoing five chapters, analytical models based on beam theories for wheel-rail dynamics were studied. These simple analytical models were studied so that the approach to include traveling point load (TPL) was followed. These simple analytical models were validated by the finite element method (FEM) applying corresponding beam theories. To be more realistic three-dimensional (3D) finite element (FE) wheel-rail models were investigated by making use of the commercially available FE package, Abaqus. The dynamics of the interaction between and wheel and rail was examined. The approach of replacing the 3D FE wheel-rail model by a 3D FE rail with TPL was examined so that the computational time could be drastically reduced. The effects of block damper (BD) masses and locations on the dynamic characteristics were studied.

Specifically, in Chapter 1 of this thesis, previous studies on modeling rails by using beam theories and applying traveling load on rails were examined. In addition, previous investigations on modeling wheel-rail interaction by beam elements and 3D solid element were reviewed.

In Chapter 2 theoretical development was presented. Euler-Bernoulli beam (EBB) theory and Timoshenko beam (TB) theory were included and discussed. Analytical solution for the free vibration, traveling point load on simply supported (SS) EBB were also included. In parallel, element stiffness and mass matrices based on the EBB theory, TB theory, 3D solid elements were introduced. The concept of TPL was applied to the 3D

FE wheel-rail problem. Frictions at the contact areas were included in the model.

Chapter 3 provided details steps in performing the 3D FE wheel-rail model. The parameters and materials properties of rail and wheel were presented based on the UIC 60 rail standard. The dynamic responses or interaction of the 3D FE wheel and rail computational model were based on the penalty contact approach available in Abaqus. The solid element used was the 8 nodes brick element.

In Chapter 4, it included two parts. In the first part, results of free vibration and beam subjected to traveling point load between analytical solutions, and corresponding finite element models were included. The second part was concerned with results of comparison between 3D FE rail model with scaled and non-scaled TPL. The dynamic responses in this part were obtained by applying the implicit numerical integration technique.

Chapter 5 dealt with the computed results of the locations and percentages mass of the BD attached to the rail. The 3D FE rail model with scaled TPL was employed. The effects of location and percentage mass of BD on the responses of rail with and without BD were examined. It was observed that the scaled TPL approach gave responses very close to those of the 3D FE wheel-rail model for the vertical deflections. However, the horizontal or friction related responses were not as close.

6.2 CONCLUSIONS

With reference to the computed results presented and observations made in the foregoing chapters, the following conclusions are apparent.

First, the main objectives of (1) providing a computational model using the rail

and TPL in order to circumvent the difficulty of obtaining accurate responses and forces at the contact areas of a wheel-rail system; (2) performing a comparison study between the wheel-rail system and the rail with TPL model; and (3) understanding the dynamic responses of the wheel-rail system with and without block dampers have been successfully accomplished.

Second, a procedure of modeling a rail with a scaled TPL replacing the computationally difficult problem of wheel-rail interaction problem was developed. This procedure can reduce drastically the computational time required in a full wheel-rail interaction model. It also makes the analysis of wheel-rail interaction more simple and provides a means for further investigation of relatively more complex models.

Third, a procedure was developed for the investigation of the effects of rails with and without BD. The effects of locations and percentage mass of the BD on the responses were also studied. For the first time, these effects of BD on the responses of railway were carried out based on the 3D FE rail model with scaled TPL. The general conclusion in this part of the investigation is that with the increase in the percentage of the mass of the BD responses of the rail are reduced. This is important in that it shows the service life of the rail may be lengthened as a result of response reduction.

Fourth, with reference to the above conclusions it is apparent that the analysis of bridges or roads with traveling point load and moving mass to represent bridges or roads under the actions/loading of traveling locomotives or trucks/cars may not be appropriate because most, if not all, current work do not include scaled factor and frictional forces at the contact areas.

6.3 RECOMMENDATIONS FOR FUTURE WORK

The results of the present investigation lead to fourth possible future research directions. The first direction of research work is by using the measured force data at the contact areas and inputting them to a 3D FE rail model so that linear and nonlinear responses at the contacting areas can be efficiently obtained and the damage at these contacting areas can be examined. This is particularly useful in the study and understanding of the corrugation phenomenon in railways or metro subways in major cities over the world.

Second, the concept of replacing the wheel-rail model with a rail and TPL system is simple and computationally efficient. Therefore, further studies should be performed on the more detailed geometrical model of the rail profile. For example, the angle effect of the rail head can be pursued.

Third, the thermal effects on the linear and nonlinear dynamic responses of wheel-rail system replacing by the rail TPL model should be studied. This will lead to the understanding of the amount of damage by the thermal stresses on the rail.

Fourth, the effects of BD on the wheel-rail responses should be investigated with a view to introducing other forms of BD. For example, laminated composite layer or layers between the BD and rail can be introduced so that more reduction on the dynamic responses can be achieved.

APPENDIX 3A

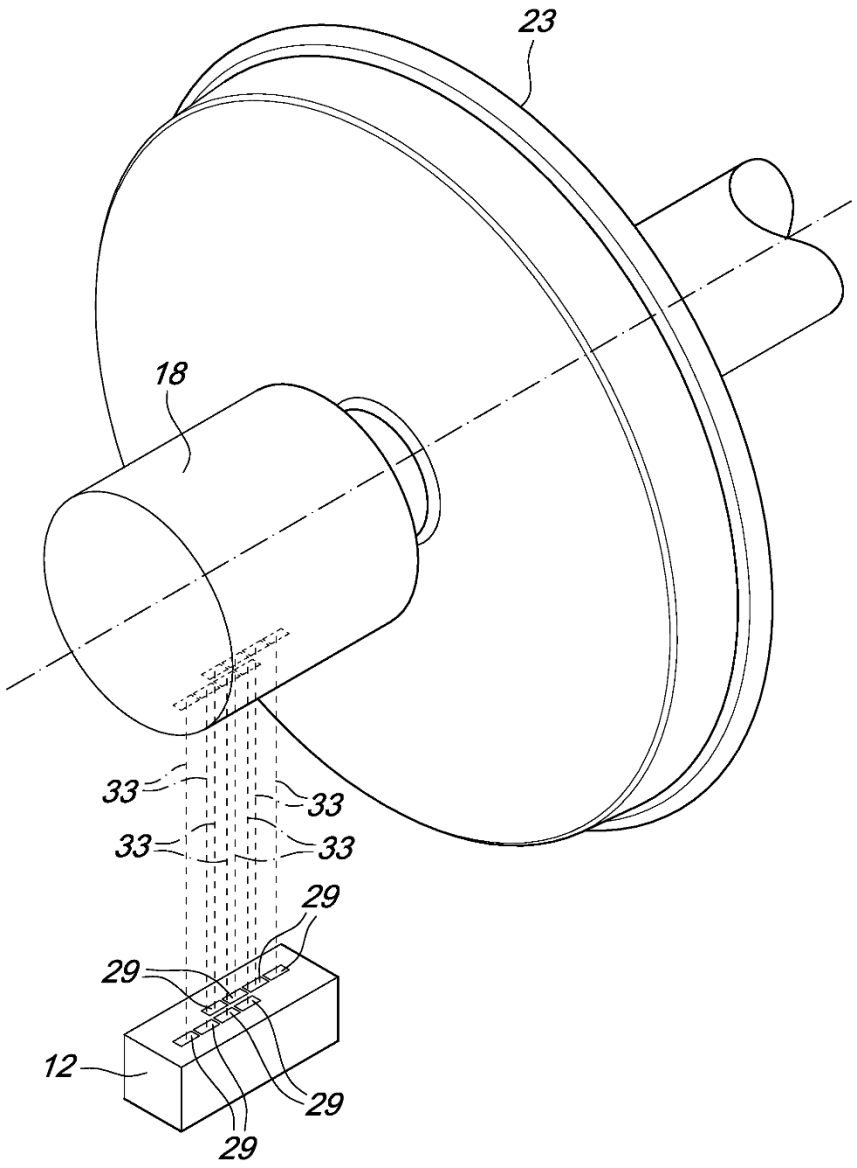

Figure 3A.1 *Detector for detecting train wheel bearing temperature, US 20130032674 A1* [3.8].

APPENDIX 3B

EN 13674-1:2003 (E)

Dimensions in millimetres

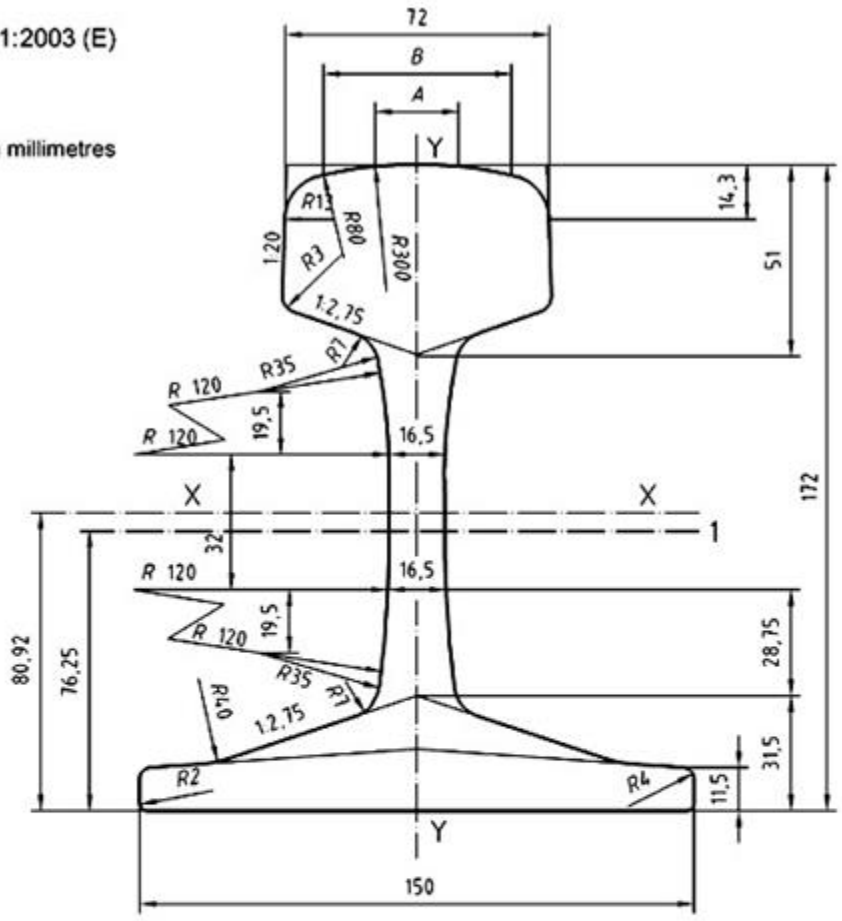

Key

1 Centre line of branding

Cross-sectional area	:	76,70	cm^2
Mass per metre	:	60,21	kg/m
Moment of inertia x-x axis	:	3038,3	cm^4
Section modulus - Head	:	333,6	cm^3
Section modulus - Base	:	375,5	cm^3
Moment of inertia y-y axis	:	512,3	cm^4
Section modulus y-y axis	:	68,3	cm^3

Indicative dimensions : A = 20,456 mm
B = 52,053 mm

Figure 3B.1 De Song Technology Co., Ltd, UIC 60(60E1)[3.9].

REFERENCES

[1.1] Wikipedia, Steam Locomotive, https://en.wikipedia.org/wiki/Steam_locomotive.

[1.2] Wikipedia, Land Speed Record for Rail Vehicles, https://en.wikipedia.org/wiki/Land_speed_record_for_rail_vehicles.

[1.3] T. Dahlberg, "Track Issue", *Handbook of Railway Vehicle Dynamics*, Chapter 6, 2006, Taylor & Francis Group, LLC.

[1.4] L. Frýba, *Vibration of Solids and Structures under Moving Loads*, Chapter 1, 1973, Noordhoff.

[1.5] Y.B. Yang, J.D. Yau, and Y.S. Wu, *Vehicle-Bridge Interaction Dynamics with Applications to High-Speed Railways*, 2004, World Scientific.

[1.6] S.L. Grassie, R.w. Gregory, D. Harrison, and K.L. Johnson, "The dynamics response of railway track to high frequency vertical excitation", *Journal Mechanical Engineering Science*, Vol. 2, No. 2, 1982.

[1.7] B. Mehri, A. Davar, and O. Rahmani, Dynamic Green Function Solution of Beams Under a Moving Load with Different Boundary Conditions, *Mechanical Engineering,* Vol. 16, No. 3, p. 273-279, 2009.

[1.8] M. Ichikawa, Y. Miyakawa, and A. Mastuda, "Vibration analysis of the continuous beam subjected to a moving mass", *Journal of Sound and Vibration*, Vol. 230, Iss. 3, p. 493-506, 2000.

[1.9] J-B. Ayasse and H. Chollet, "Wheel-Rail Contact", *Handbook of Railway Vehicle Dynamics*, Chapter 4, 2006, Taylor & Francis Group, LLC.

[1.10] Y.H. Lin, "Vibration analysis of Timoshenko beams traversed by moving loads", *Journal of Marine Science and Technology,* Vol. 2, No.1, p. 25-35, 1994.

[1.11] P. Ruge, and C. Brik, "A comparison of infinite Timoshenko and Euler-Bernoulli beam models on Winkler foundation in the frequency-and-time-domain", *Journal of Sound and Vibration*, Vol. 304, p. 932-947, 2007.

[1.12] M.H. Kargarnovin, and D. Younesian, "Dynamics of Timoshenko beams on Pasternak foundation under moving load", *Mechanical Research Communications,* Vol. 31, p. 713-723, 2004.

[1.13] R.U.A. Uzzal, R.B. Bhat, and W. Ahmed, "Dynamics response of a beam subjected to moving load and moving mass supported by Pasternak foundation", *Shock and Vibration*, Vol. 19, p. 205-220, 2012.

[1.14] T.X. Wu , and D.J. Thompson, "The effects of local preload on foundation stiffness and vertical vibration of railway track", *Journal of Sound and Vibration*, Vol. 219, Iss. 5, p. 881-904, 1999.

[1.15] T.X. Wu , and D.J. Thompson, "A double Timoshenko beam model for vertical vibration analysis of

railway track at high frequencies", *Journal of Sound and Vibration*, Vol. 224, Iss. 2, p. 329-348, 1999.

[1.16] T.X. Wu , and D.J. Thompson, "Analysis of lateral vibration behavior of railway track at high frequencies using a continuously supported multiple beam model", *Journal of Acoustical Society of Americal*, Vol. 106, Iss. 3, 1999.

[1.17] A. Yavari, M, Nouri, and M. Mofid, "Discrete element analysis of dynamic response of Timoshenko beams under moving mass", *Advances in Engineering Software*, 33, p. 143-153, 2002.

[1.18] T. Ekevid, M.X.D. Ki, and N-E. Wiberg, "Adaptive finite element analysis of wave propagation under moving loads induced by high-speed trains", *European Congress on Computational Method in Applied Sciences and Engineering*, 2000.

[1.19] N.S. Vyas, and A.K. Gupta, "Modeling rail wheel-flat dynamics", *WCEAM*, Paper 233, 2006.

[1.20] A. Sladkowski, and M. Sitarz, "Analysis of wheel-rail interaction using FE software", *Wear*, 258, p. 1217-1223, 2005, Elsevier Ltd..

[1.21] A. Pieringer, W. Kropp, and D.J. Thompson, "Investigation of dynamic contact filter effect in wheel/rail interaction using a 2D and 3D non-Hertzian contact model", *Wear*, 271, p. 328-338, 2011, Elsevier Ltd..

[1.22] K. Nguyenn, J.M. Goicolea, and F. Galbadón, Comparison of dynamic effects of high-speed traffic load on ballasted track using a simplified two-dimensional and full three-dimensional model, Journal of Rail and Rapid Transit, Vol. 228, No. 2, p. 128-142, 2014.

[1.23] V.N. Dinh, K.D. Kim, and P. Warnitchai, "Dynamic analysis of three-dimensional bridge-high-speed train interactions using a wheel-rail contact model", *Engineering Structure*, 31, p. 3090-3106, 2009. Elsevier Ltd.

[1.24] I. Esen and M. Eroglu, "3D finite element analysis of UIC 60 rail and UIC 55 wheel rolling contact and understanding starting mechanism of wear", *2nd International Iron and Steel Symposium (IISS'15)*, 2015.

[2.1] Timoshenko, S., *History of strength of materials*, McGraw-Hill New York, 1953.

[2.2] Timoshenko, S. P., "On the correction factor for shear of the differential equation for transverse vibrations of bars of uniform cross-section", *Philosophical Magazine*, p. 744. 1921.

[2.3] S.M. Abullah, "Free vibrations of simply supported beams using Fourier series", *Al-Rafidain Engineering*, Vol.14, No.2, 2006, University of Mosul.

[2.4] T. Dahlberg, "Track Issue", *Handbook of Railway Vehicle Dynamics*, Chapter 6, p. 145, 2006.

[2.5] D. Dinev, "Analytical solution of beam on elastic foundation by singularity functions", *Engineering*

Mechanics, Vol. 19 (No.9), p. 381-392, 2012

[2.6] H. Hertz, Über die berührung fester elastischer Körper (On the contact of rigid elastic solids). In: *Miscellaneous Papers*. Jones and Schott, Editors, J. reine und angewandte Mathematik 92, Macmillan, London, p. 156, 1896, English translation: H.Hertz.

[2.7] L. Frýba, *Vibration of solids and structures under moving loads*, Chapter 1, 1973, Noordhoff.

[2.8] V. Garg, R. V. Dukkipati, "Six-axle locomotive response model", *Dynamics of Railway Vehicle System*, Chapter 6, Section 3, p. 197. 1984, ACADEMIC PRESS.

[2.9] A. Mehmood, A.A. Khan, and H. Mehdi, Vibration Analysis of Beam Subjected to Moving Loads Using Finite Element Method, *IOSR Journal of Engineering (IOSRJEN)*, Vol. 4, Iss. 5, p. 7-17, 2014.

[2.10] C.W.S. To, A Linearly Tapered Beam Finite Element Incorporation Shear Deformation and Rotary Inertia for Vibration Analysis, *Journal of Sound and Vibration*, Vol. 78, Iss. 4, p.475-484, 1981.

[2.11] G. R. Cowper, The Shear Coefficient in Timoshenko's Beam Theory, *Journal of Applied Mechanics, Vol.33*, Iss. 2, p. 335-340, 1966.

[2.12] P. Wriggers and G. Zavarise, "Computational contact mechanics", *Encyclopedia of Computational Mechanics*, Chapter 6, Volume 2 (Solids and Structures), Edited by Stein, E., de Borst, R., and Hughes, T. J. R., 2004, John Wiley and Sons, Ltd.

[2.13] M. A. Crisfield, *Non-linear Finite Element Analysis of Solids and Structures*, Chapter 23, Volume 2, 1997, Wiley.

[2.14] G.R. Liu and S. S. Quek, *The Finite Element Method*, 2nd Edition, Chapter 9, 2013.

[2.15] R. J. Melosh, "Structural analysis of solids", *Journal of Struct. Div.*, ASCE, vol. 89 (No. ST4), 1963, 205-223.

[2.16] S. Gangulya,, S.Neogyb, A.Nandib, On Lumping of Gyroscopic Matrix in Finite Element Analysis of Rotors, *12th International Conference on Vibration Problems*, ICOVP, 2015.

[3.1] Abaqus, http://www.3ds.com/products-services/simulia/products/abaqus/

[3.2] *Abaqus Documentation 6.14,* sub-section 6.3.3.

[3.3] NDT Resource Center, "Discussion", *The Speed of Sound in Other Materials,* https://www.nde-ed.org/EducationResources/HighSchool/Sound/speedinmaterials.htm

[3.4] R. D. Cook, D. S. Malkus, M. E. Plesha, and R. J. Witt, *Concepts and Applications of Finite Element Analysis*, 3rd Edition, p. 402, 1989, John Wiley & Sons.

[3.5] Crossing Collision/Derailment Via Rail Canada Inc. Passenger Train No 85 Mile 33.54, Goderich-Exeter Railway (GEXR) Guelph Subdivision Limehouse, Ontario". Transportation Safety Board of Canada. 1999-11-09. Retrieved 2008-02-28.

[3.7] Abaqus Documentation 6.14, sub-section 36.1.1

[3.8] A. Agostini, “Detector for detecting train wheel bearing temperature”, US 20130032674 A1, 2013.

[3.9] De Song Technology Co. , Ltd., 60E1 railway steel rail,
http://www.steelrail.cn/uic860-standard-rail/39-60e1-railway-steel-rail.html

[5.1] *Abaqus Documentation 6.14*, sub-section 35.3.1.